MECHANISMS OF PARTICLE MIGRATION

IN ELECTROSTATIC PRECIPITATORS

by

KATHRYN LOUISE BARNES

Submitted in partial fulfilment of the requirements
for the award of
Doctor of Philosophy of Loughborough University of Technology

1987

Supervisor : DR. J.I.T. STENHOUSE

Director of Research : MR. P.J. LLOYD

ACKNOWLEDGEMENTS

I would like to take this opportunity to express my sincere thanks to my Supervisor, Dr. J.I.T. Stenhouse. His continued enthusiasm and guidance have been a source of great inspiration in the completion of this thesis. I must also thank the Department of Chemical Engineering for their support, and I am particularly grateful to my Director of Research, Mr. P.J. Lloyd, in the first instance for recruiting me and subsequently for numerous fruitful discussions.

I acknowledge the financial support of the Science and Engineering Research Council, who provided the funding for my three-year Research Assistantship. I am also indebted to Lodge Cottrell, Birmingham, who generously supplied much of the equipment used in the experimental work.

Thanks are due to Mr. I. Sinclair, for his able assistance with the experimental work, and to Mr. G. Boyden, who produced the excellent photographs included in this thesis.

My thanks would be incomplete without mention of my husband, Nicholas, who has provided a shining example of commitment and dedication. I am especially grateful for his strength and encouragement through the long dark summer of 1985. Finally, and perhaps most importantly, I thank my Mum and Dad for their unfailing love and support throughout my University career. They have always shown enthusiasm and interest in my work, and it is to them that I dedicate this thesis.

SYNOPSIS

Electrostatic precipitators are high efficiency gas cleaning devices widely used in industry for removing particulates from process gases. A major factor affecting their performance is particle migration, which is governed by the complex interaction of electrical and hydrodynamic phenomena. A fuller understanding of these fundamental mechanisms is therefore essential to the development of realistic mathematical models.

The work described in this thesis concentrates on the fluid-particle interactions in a wire-plate system. A pilot-scale rig was built using actual components from an industrial precipitator, allowing realistic conditions to be simulated in the laboratory.

Hot-wire anemometry and laser-Doppler photon correlation techniques were employed to study the time-averaged velocity field. Several designs of wall strengthener were considered, and in each case the effect on the surrounding flow field was investigated using helium-bubble visualisation. The turbulent nature of the fluid was characterised by local dispersion coefficient values and fluctuating velocity components.

Alumina test dust in the size range 1-10 μm was used in the precipitator under a variety of operating conditions, and a technique was established for extracting representative dust samples. The samples allowed simultaneous measurement of concentration and size distribution, from which concentration profile development and collection efficiency information was obtained.

Two alternative numerical models of the precipitator were developed, both incorporating the results from the

fluid flow field experimentation. The first approach was based on the finite difference solution of the convective-diffusion equation, using appropriate boundary conditions. In the second approach, the transport of dust down the precipitator duct was simulated by the step-wise progression of a series of vertical line-sources, whose motion was governed by electrical migration and lateral diffusive spread. The validity of the models was tested by comparison of the predicted concentration profiles with corresponding experimental results.

FIGURES

CHAPTER 3

CHAPTER 4

CHAPTER 6

APPENDIX B

NOMENCLATURE

a = width of strengtheners (m)

A = surface area of collection plates (m^2)

A_p = surface area of particle (m^2)

b = electrical mobility of charge carriers ($m^2V^{-1}s^{-1}$)

c = particle concentration (no. m^{-3})

c_o = concentration of particles along injection axis (no. m^{-3})

c_{in} = inlet particle concentration (no. m^{-3})

C_D = drag coefficient

d = collection plate spacing (m)

d_f = laser-Doppler fringe spacing (m)

d_p = particle diameter (m)

d_e = effective plate spacing (m)

D = diffusion/dispersion coefficient (m^2s^{-1})

D_B = Brownian diffusion coefficient (m^2s^{-1})

D_p = particle dispersion coefficient (m^2s^{-1})

D_x = dispersion coefficient in x-direction (m^2s^{-1})

D_z = dispersion coefficient in z-direction (m^2s^{-1})

D' = asymptotic dispersion coefficient (m^2s^{-1})

e = electron charge (C)

E = electric field (Vm^{-1})

E_{av} = average electric field value (Vm^{-1})

E_o = applied voltage/plate spacing (Vm^{-1})

E_x = electric field in x-direction (Vm^{-1})

E_z = electric field in z-direction (Vm^{-1})

f = frequency of phase modulator (Hz)

F = Fanning friction factor

g = acceleration due to gravity (ms^{-2})

h = grid spacing in x-direction (m)

i = x-direction cell coordinate

I = current (A)

j = z-direction cell coordinate

J = current density (Am^{-2})

k = grid spacing in z-direction (m)

l = Prandtl's mixing length (m)

l_E = Eulerian length scale of turbulence (m)

l_L = Lagrangian length scale of turbulence (m)

l^* = dimensionless length of vortex

l_m = mixing length for mass transfer (m)

L = length of precipitator duct (m)

L_s = length of strengthener arm (m)

L_c = length of filter head extension (m)

m = no. of cells along half wire-to-wire spacing

n = no. of cells across wire-to-plate spacing

N = mean local concentration (no. m^{-3})

q = particle charge (C)

q_s = particle saturation charge (C)

Q = gas volume flow rate through precipitator ($m^3 s^{-1}$)

r = radial distance from line through axis of point source (m)

r_p = particle radius (m)

R = velocity correlation coefficient

R_E = Eulerian correlation coefficient

R_L = Lagrangian correlation coefficient

Re = Reynold's number

Re_p = particle Reynold's number

s = distance from aerosol injection point (m)

s_x = half wire-to-wire spacing (m)

s_z = wire-to-plate spacing (m)

S = particle stopping distance (m)

Sc = Schmidt number

t = time (s)

t^* = time taken for $R \rightarrow 0$ (s)

T = residence time in precipitator duct (s)

T_p = relaxation time of particle (s)

u = fluid velocity surrounding probe head (ms^{-1})

u_x = local fluid velocity in x-direction (ms^{-1})

u' = axial fluctuating velocity (ms^{-1})

v = instantaneous fluid velocity (ms^{-1})

v' = transverse fluctuating velocity (ms^{-1})

v_{sh} = fringe shift velocity (ms^{-1})

v^* = wall friction velocity (ms^{-1})

V = voltage (V)

V_o = voltage applied to discharge electrodes (V)

V_d^+ = dimensionless deposition velocity

w = fluid velocity inside probe head (ms^{-1})

W = particle flux towards surface ($m^{-3}s^{-1}$)

x = axial coordinate (m)

x_c = distance from leading edge of plate at which transition from laminar to turbulent flow occurs (m)

x_{in} = distance from leading edge of plate at which flow becomes fully turbulent (m)

x_o = length scale characteristic of turbulent flow (m)

x_s = distance from precipitator inlet to first strengthener (m)

y = vertical coordinate (m)

z = transverse coordinate (m)

z_b = thickness of laminar boundary layer (m)

α = weighting factor in finite difference scheme

η = efficiency

η_o = mechanical efficiency

δ = relative density of air

ε_o = permittivity of free space (Fm^{-1})

λ = wavelength (m)

μ = viscosity ($Kgm^{-1}s^{-1}$)

ν = kinematic viscosity (m^2s^{-1})

ρ_f = fluid density (Kgm^{-3})

ρ_p = particle density (Kgm^{-3})

CONTENTS

INTRODUCTION

Electrostatic precipitators are gas cleaning devices widely used in industry for removing particles from process gases. The particles become charged by ions from a corona discharge and migrate towards earthed collection plates, due to the presence of an electric field. On arrival, the particles adhere to the plates and are removed by periodic rapping. The dislodged layer of particles falls into hoppers situated beneath the precipitator.

The successful application of electrostatic precipitation dates to the first years of the twentieth century. Oliver Lodge had experimented with precipitators since 1880, but was commercially unsuccessful due to the primitive methods available for producing high-voltage power. In 1907, Frederick G. Cottrell adapted the newly developed mechanical rectifier and high-voltage transformer systems, and built a workable precipitator to enable collection of the acid mist emitted by a sulphuric acid plant. The success of electrostatic precipitation in this field led quickly to its application to other sources of industrial air pollution including copper, lead and zinc smelters (1910) to recover metal oxides from fumes, cement plants (1912), pulp and paper mills (1916), electric utility power plants (1923) and blast furnaces (1930). The largest single application of precipitators is in the removal of flyash from coal combustion.

The advantages of electrostatic precipitators over other gas cleaning devices include high efficiency, low pressure loss and power consumption and a wide workable temperature range. The initial high capital cost of the equipment is offset by low maintenance costs. As the control of particulate emissions from industrial sources becomes more stringent, the need arises for more efficient

precipitators to meet these rigid specifications.

A major factor affecting precipitator performance is particle migration, which is governed by the complex interaction of electrical and hydrodynamic phenomena. Understanding of these individual phenomena is therefore necessary before the important mechanisms affecting particle migration can be identified. The purpose of the work contained in this thesis is to provide further understanding of the fluid-particle interactions in a wire-plate system. Although the importance of other mechanisms in affecting precipitator performance is recognised, a lack of experimental data regarding particle migration is evident. Quantitative analysis of such mechanisms is required so that they can be realistically incorporated into mathematical models.

Chapter 2 describes the pilot-scale precipitator built using actual components from an industrial precipitator. Easy optical and mechanical access to the internal structure has enabled experimental measurements to be performed in the precipitator under realistic working conditions.

An experimental study of the steady state flow field has been carried out using laser-Doppler photon correlation and hot-wire anemometry techniques. The results contained in Chapter 3 have been compared with theoretically predicted velocity profiles, incorporating the wake effect downstream of the discharge electrodes. Several designs of wall strengthener have been considered, and in each case the surrounding flow field was investigated using streak photography of neutral-buoyancy helium bubbles. The analysis has provided a basis for the mathematical simulation of velocity fields in precipitators employing wall strengtheners, for use in mathematical models.

The turbulent nature of the fluid is characterised in Chapter 4, enabling the relative importance of back-mixing on particle migration to be estimated. The significance of turbulent mixing is discussed with respect to realistic interpretation of experimental measurements. Local dispersion coefficient values, determined from the lateral spread of an isokinetically injected aerosol, were obtained for a range of working conditions. A relationship is developed between small-scale dispersion coefficients and r.m.s. fluctuating velocity components, and preliminary attempts are made to verify the relationship.

Dust concentration profile data has been obtained for particle sizes in the range 1-10 μm. Chapter 5 describes the development and use of a sampling device which enables simultaneous measurement of the size distribution and concentration of extracted dust samples. Such results are a useful indication of the extent of back-mixing occurring across the precipitator duct, and have been used to estimate the effect of inlet flow modulation, applied voltage, gas velocity and wall strengtheners on particle collection.

Mechanical efficiency is the fraction of dust collected on the precipitator walls by means of turbulent deposition. Collection by this mechanism will occur regardless of the electrical conditions in the precipitator, but will be affected by the turbulence level in the gas stream. The extent of particle collection by this mechanism has been measured in this work by analysing the dust deposited on samples of aluminium foil, attached to the walls of the precipitator duct. The results have been compared with values found in the literature which were obtained in fully developed flow conditions.

Accurate design methods are necessary to determine the principal sizing and electrical parameters required to

achieve the specified levels of performance. Methods used in practice include design by analogy, use of pilot precipitators, statistical methods, data banks and computerised mathematical models. One of the most widely used methods of design is a semi-empirical approach based on the Deutsch-Anderson equation. This method requires a strong data base containing information on working precipitators with similar performance specifications. The Deutsch-Anderson equation may be expressed as follows

$$\eta = 1 - \exp(-Aw/Q)$$

where η = collection efficiency,
A = collection electrode area (m^2),
Q = gas volume flow rate ($m^3 s^{-1}$),
w = theoretical migration velocity (ms^{-1}),

In practice, the theoretical migration velocity is replaced by an effective precipitation rate parameter, w_e, which is a parameter derived from field experience and pilot precipitator simulations. This value of w_e is then used in the Deutsch-Anderson equation to determine the specific collection area corresponding to the required efficiency.

Theoretically, precipitator design should be possible from first principles if sufficient knowledge of the mechanisms contributing to particle collection is available. In reality, the complex interaction of the mechanisms requires simplifying assumptions to be made before mathematical analysis of the problem is feasible. In Chapter 6, two alternative numerical models of the precipitator have been developed, incorporating the results from the fluid flow field experimentation. The first approach is based on the finite difference solution of the convective-diffusion equation. In the second approach, transport of dust is simulated by the step-wise progression

of a series of vertical line sources down the precipitator duct. The validity of the models is tested by comparing the predicted concentration profiles with corresponding experimental results.

CHAPTER 1

BACKGROUND

Precipitator performance is affected by many mechanisms which combine and interact, making the process of dust removal from process gases difficult to model mathematically. For instance, the electrical conditions are affected by the presence of charged dust particles, but dust concentration is controlled by the electrical and fluid flow properties of the system, as well as other parameters such as reentrainment and the electrical properties of individual particles. Some of the phenomena affecting precipitator performance, such as particle charging, electrical conditions, electric wind, turbulent mixing and turbulent deposition, are of particular interest, and have been reviewed individually in this Chapter. Where possible, the relevance of each mechanism to electrostatic precipitation has been discussed. In addition, brief accounts are given of several attempts to model particle migration and collection using analytical and numerical procedures.

1.1 Particle charging

When aerosol or dust particles are exposed to a unipolar source of ions in an electric field, collisions of ions and particles occur due to the random thermal motion of the ions and their induced motion by the applied electric field. The amount of charge acquired by a particle in an electrostatic precipitator determines the velocity with which it migrates to the collection wall. Fundamental study of particle charging has resulted in the development of increasingly complex theories to describe the phenomenon.

In classical theory, spherical particles are considered to be charged by two processes;

a) field charging - due to the bombardment of particles by ions travelling under the influence of the electric field,
b) diffusion charging - resulting from ionic collisions with particles due to the random thermal motion of the ions.

Field charging is the dominant mechanism for the charging of particles > 0.5 μm diameter, whilst diffusion charging predominates for particles < 0.2 μm diameter. In the intermediate size range, both mechanisms contribute significantly.

Pauthenier and Moreau-Hanot (1932) produced a theoretical and experimental investigation into field charging. For particles > 10 μm diameter, the charging rate was defined as

$$\frac{dq}{dt} = Neb \int_{\theta=0}^{\theta_o} E_o dA_p \qquad (1.1)$$

where q = particle charge (C),
E_o = undisturbed electric field (Vm^{-1}),
N = ion concentration ($no.m^{-3}$),
e = electron charge (C),
θ = angle between point on sphere and electric field (^{o}),
θ_o = limiting angle for charge flow (^{o}),
b = mobility of charge carriers ($m^2V^{-1}s^{-1}$),
A_p = surface area of particle (m^2).

Ions continue to flow to the particle until sufficient charge is acquired for the local electric field to completely counteract the external field, at which point charging ceases. The theoretical limit at which this occurs is known as saturation charge, q_s, given by

$$q_s = 12\pi r_p^2 \varepsilon_o E_o \qquad (1.2)$$

where r_p = particle radius (m).

Substituting this value into equation 1.1 and integrating gives

$$\frac{dn}{dt} = \pi e N b n_s (1 - n/n_s)^2 \qquad (1.3)$$

where n_s = no. of charges on particle at saturation

Thus the total charge acquired by an initially uncharged particle in time t is

$$n = n_s \pi N e b t / (\pi N_o e b t + 1)$$

White (1951) derived a description of diffusional charging using an analogy with the kinetic theory of gases, giving rise to the charging rate

$$\frac{dn}{dt} = \pi r_p^2 \, v N \exp(-ne^2/r_p kT) \qquad (1.4)$$

where v = r.m.s. velocity of ions (ms^{-1}),
T = temperature (^oK),
k = Boltzmann constant.

As the potential of the particle increases due to its acquired charge, the probability of ion impact decreases until the diffusional charging rate becomes insignificant. For an initially uncharged particle, White integrated equation 1.4 to obtain

$$n = \left[\frac{r_p kT}{e^2}\right] \ln (1 + (\pi r_p v N e^2/kT)t) \qquad (1.5)$$

In deriving this charging equation, White assumed that the mean free path of the ions λ, was small compared to particle radius r_p. Liu, Whitby and Yu (1967) tested this assumption by measuring the charge acquired by DOP at low pressure, thus allowing the ratio r_p/λ to be varied from 1-66. Positive corona conditions were used to avoid free electron charging. The results demonstrated the independence of particle charge and the ratio r_p/λ down to a value of 1. The values agreed well with diffusional charging predictions if it was assumed that the ions were emitted from the corona in clusters.

Hewitt (1957) performed a series of experimental tests on DOP aerosol, using positive charging conditions. Comparing the results with values predicted by summing equations 1.3 and 1.4, the following conclusions were drawn:

a) For a given charging field there is a particle size corresponding to minimum mobility.
b) Measured particle charge depends on the product Nt.
c) Results agree with diffusional charging theory predictions for zero electric field conditions.
d) For small particles, the effect of the electric field is greater than accounted for by theory.
e) The most difficult particles to precipitate are those in the size range 0.1 - 0.2 μm.

Penney and Lynch (1957) used both cylindrical corona and uniform parallel plate charging geometries to investigate the difference between positive and negative charging conditions. In both cases they found the measured charge to be greater than the theoretical predictions by a factor of 2. For the case of negative cylindrical corona geometry, increasing voltage appeared to increase the charge imparted to the particles much more rapidly than with positive corona. The high charging rates associated with

negative corona conditions were assumed to be a result of free electron charging.

Although no quantitative method of incorporating free electron charging into theoretical models has yet been established, an experimental investigation of the phenomenon has been made by DuBard, McDonald and Sparks (1983). Since industrial precipitators generally use negative coronas due to their higher sparkover voltage, further study of free electron charging is essential. It is possible that this mechanism explains the discrepancy between predicted charge values and those experienced by particles in an electrostatic precipitator.

Liu and Yeh (1968) found the magnitude of field and diffusional charging contributions to be comparable for submicron particles in a moderately high electric field with $Nt = 10^7$ (ions/cc). They subsequently proposed a new theory which took into account the considerable effect of electric field on the charging of submicron particles. The charging process was divided into two regimes depending upon the magnitude of the charge q already residing on the particle.

i) $q < q_s$

Contrary to previous predictions, Liu and Yeh assumed diffusional charging to occur in the shaded region of Figure 1.1, causing enhanced particle charging, particularly at low electric field values. The modified charging equation was given by

$$\left(\frac{dn}{dt}\right)_I = \pi e N b n_s (1-n/n_s)^2 + \frac{N v \pi r_p^2}{2}(1+n/n_s)$$

ii) $q > q_s$

In this case, no electric field lines enter the

particle, and any further charging of the particles was assumed to occur due to the random thermal motion of the ions. This charging rate can be calculated from the estimated ion concentration N_a surrounding the particle given by,

$$N_a = N\exp(-e\Delta V/kT)$$

where $\Delta V = V_a - V_o$ (V),

V_a = electric potential at particle surface for $\theta=0$ (V),

V_o = electric potential at r_o (V).

Assuming uniform ion concentration N_a over the rest of the particle surface, the charging rate is

$$\left(\frac{dn}{dt}\right)_{II} = \pi r_p^2 N v \exp(-e\Delta V/kT)$$

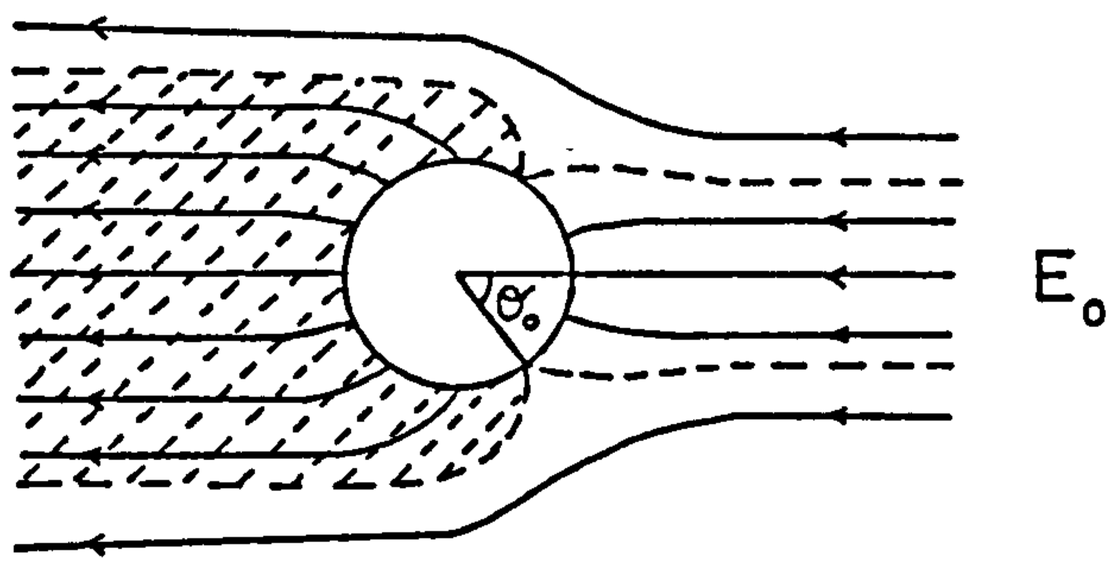

Fig. 1.1 Field-enhanced diffusional charging

The total charging rate was given by the sum of the individual rates. Comparison of theoretical predictions with the experimental data of Hewitt shows good agreement for small particles, but only for unrealistically low values of v and b.

Smith and McDonald (1976) took the theory of Liu and Yeh a stage further by dividing the particle surface into three regions, as shown in Figure 1.2, and estimated the probability that ions reach the particle surface in each of regions I, II and III. The applied electric field was considered to affect the charging rate in two ways;

a) ions gain kinetic energy from the applied field, aiding them in overcoming the repulsive force of the charged particle.
b) the ion distribution near the particle may be altered.

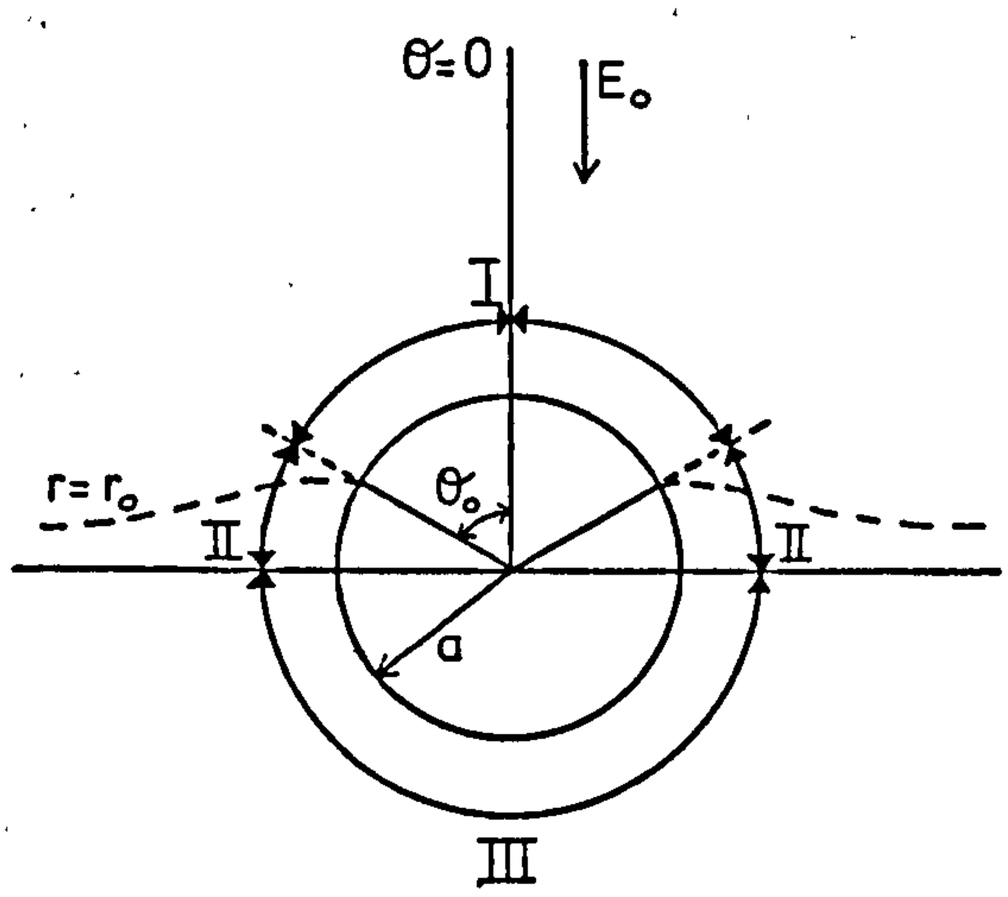

Fig. 1.2 Charging regions as defined by Smith and McDonald (1976)

In Region I, the charging rate is limited by the rate at which ions are brought into the system by the external field, and is equivalent to the field charging rate described by equation 1.3. In Region II, charging occurs due to ion diffusion enhanced by the applied electric field resulting in a charging rate of

$$\left(\frac{dn}{dt}\right)_{II} = \frac{v}{4}\int_{\theta}^{\pi/2} N_a(2\pi r_p^2 \sin\theta)d\theta$$

o

In Region III, the electric field due to particle charge and the external electric field are in the same direction, and a steady state charge density system prevails. The ion density near the particle in this region is barely affected by changes in external electric field values, and the classical diffusional charging equation 1.4 is applicable.

To enable comparison of theoretical predictions of particle charge with experiment, accurate values of v and b are required. Smith and McDonald decided to use the same values as Hewitt - $v=500\ ms^{-1}$ and $b=1.6x10^{-4}\ m^2V^{-1}s^{-1}$. Their theoretical predictions tended to overpredict charge values for particles in the size range 1-5 μm, particularly for low electric field conditions, where diffusional charging theory produced best predictions. Excellent agreement occurred for particles < 1.4 μm diameter.

The above theories of Liu and Yeh, and Smith and McDonald are only approximate, employing a variety of assumptions and simplifications. Liu and Kapadia (1978) calculated the combined effects of field and diffusional charging in the continuum regime (where $d_p > \lambda$), using a numerical solution technique. The solution of the

macroscopic ion diffusion equation,

$$D \nabla^2 N + b \nabla N . \nabla V = 0$$

where D = diffusion coefficient ($m^2 s^{-1}$),

yields a particle charging rate which was numerically integrated to obtain particle charge as a function of time. Although the results agree well with the experimental results of Hewitt and Smith et al., the limiting factor for this type of calculation is the computing time required. For cases of high electric field values extrapolation is necessary, since the time required to solve the system using an iterative method would be prohibitive.

Until 1978, the most reliable and comprehensive experimental data on particle charging was generally considered to be that obtained by Hewitt (1957). A subsequent investigation into the charging of fine particles by Smith et al. (1978) provided new data, some of which overlapped Hewitt's work with good agreement. Some of the parameters studied included ion density-time, dielectric constant, electric field, particle diameter and mobility of the charge carriers. Also detailed in the paper was a review of previous charging work.

A parameter of great significance when considering particle charging in electrostatic precipitation is the charging time constant, T. If the value of T is sufficiently small, particles may be considered charged to their limiting value on entry into the precipitator duct. In this case, the rate of increase of particle charge is not important and only the limiting charge value need be considered. The high ion density field maintained in an electrostatic precipitator justifies the use of equation 1.2 for calculating the charge on particles with diameter

greater than 1 μm.

Robinson (1972) experimentally determined values of the effective charging time T' from the downstream location of the maximum precipitate density along a tubular precipitator. Comparison of T' with the theoretical value of T calculated from

$$T = 4\varepsilon_o/Neb$$

showed T' to be significantly smaller. Robinson suggested the relationship

$$\frac{T'}{T} = \frac{w}{w}e$$

Using values for the parameters representative of conditions in a precipitator, the charging time constant corresponds to a distance of approximately 5mm. This provides further validation for the use of equation 1.2 in calculating particle charge.

1.2 Electrical conditions

1.2.1 Theoretical modelling of electric field

The electric field in the interelectrode space serves a three-fold purpose;

a) to generate the ions from the corona discharge,
b) to provide the driving force that causes the ions to collide with the particles.
c) to generate the force necessary for collection of the particles.

The field has two contributing factors - the applied voltage divided by the wire-plate spacing, and the space charge component due to the presence of ions and charged particles. Ideally, a model used to calculate the electrical conditions in a precipitator should be capable of describing the electric field for both clean and dust-laden conditions.

The expressions used to describe the field are the Poisson equation and the current continuity equation, namely

$$\nabla^2 V = -\rho/\varepsilon_o$$

and

$$\nabla.\underline{J} = \nabla.(\rho b\underline{E}) = 0$$

where b = charge carrier mobility ($m^2V^{-1}s^{-1}$),
ρ = space charge density (Cm^{-3}),
$\underline{J}$ = current density (Am^{-2}),
V = electric potential (V),

Cooperman (as later published by McDonald et al.(1977)) showed the presence of space charge to cause an increase in the field near to the collection plates. The approximate

analytical solution, derived to describe the field for a wire-plate precipitator, assumed the space charge to be evenly distributed across the duct. The resultant field V(x,z) was a combination of two terms, the first describing the effect of the electrostatic field and the second the space charge density, giving

$$V(x,z) = V_o \left[\sum_{m=-\infty}^{\infty} \ln \frac{\cosh[\pi(x-2ms_x)/2s_z] - \cos(\pi z/2s_z)}{\cosh[\pi(x-2ms_x)/2s_z] + \cos(\pi z/2s_z)} \Big/ \sum_{m=-\infty}^{\infty} \ln \frac{\cosh(\pi ms_x/s_z) - \cos(\pi r/2s_z)}{\cosh(\pi ms_x/s_z) + \cos(\pi r/2s_z)} \right]$$

$$+ \frac{Js_x}{bV_o} \ln(d/r)(s_z^2 - z^2)$$

where V_o = applied voltage (V),

s_z = wire-plate spacing (m),

s_x = one-half wire-wire spacing (m),

r = radius of corona wire (m),

d = a geometry factor depending on ratio of s_x and s_z.

x = distance measured from electrode along duct (m),

z = distance measured from electrode across duct (m).

Since exact analytical solutions are unavailable for the wire-plate geometry, numerical solutions have been developed. The majority of these models assume that the motion of all charge carriers can be represented by a single effective mobility. Leutert and Bohlen (1972) divided the precipitator duct into a fine grid structure and suggested the following procedure:

(i) Compute an initial estimate for the potential field, V(x,z) from Cooperman's electrostatic expression (zero space charge).

(ii) Compute ρ at every point using the finite difference form of the current continuity equation.

(iii) Recompute V(x,z) using the finite difference form of Poisson's equation.

(iv) Repeat steps (ii) and (iii) until the desired convergence criterion is satisfied.

(v) Compare the measured current density value with the computed value, $J = b\rho E_z$. If they are in agreement, the solution is valid. If not, the initial space charge density value at the corona wire must be adjusted accordingly, and the iterative procedure repeated from step (ii).

McDonald, Smith, Spencer and Sparks (1977) based their numerical technique for calculating electric field values on the above procedure. To enable a solution for the finite difference form of the Poisson and current continuity equations to be calculated, an initial estimate of the space charge density near the corona wire, ρ_c, was required. McDonald et al. used an expression derived earlier from discharge theory, where

$$\rho_c = \frac{2s_x J_p}{brf[30\delta + 9(\delta/r)^{1/2})} \times 10^{-3}$$

where δ = relative density of air,

J_p = average current density at plate ($Ampm^{-2}$),

r = radius of corona wire (cm),

f = roughness factor of wire

= 1 for a smooth wire.

This is actually the space charge density value at the boundary of the ionised sheath surrounding the discharge

electrode, but can be assumed equivalent to the point charge density located at the centre of the corona wire.

McDonald et al. suggested a method of including the effect of particle space charge density, whereby ion mobility and particle mobility are combined to obtain an effective mobility value. To use this method, reliable information on effective mobility as a function of particle size distribution and loading is required. Initial tests showed the introduction of particles to cause an increase in the electric field at the plate, and this effect becomes more pronounced as the effective mobility decreases.

Although rigorous analytical solutions are not yet available, Moseley, McDonald and Sparks (1981) derived semi-empirical expressions using analytical approximations. The potential in the wire-plate system was evaluated by assuming the charge near the corona wire to be distributed as in a wire-cylinder geometry, and near the collection plate as for parallel geometry. The space charge effects of the particles were taken into account by evaluating the effective current density, J_{eff}, due to both the ions and the charged particles,

$$J_{eff} = b_{eff}(J_i/b_i + J_p/b_p)$$

where $b_{eff} = (b_i\bar{\rho}_i + b_p\bar{\rho}_p)/(\bar{\rho}_i + \bar{\rho}_p)$

b = mobility ($m^2V^{-1}s^{-1}$),

$\bar{\rho}$ = average charge density (Cm^{-3}),

Suffices i and p refer to ions and particles respectively.

Moseley et al. claim their model to be accurate to within 3% for low current density values, but with significant deviations for high values. Attempts to use this algorithm for calculating electric field values in Chapter 6 were

unsuccessful. No further work has been published by the authors on this procedure.

Pude, Hughes and Coventry (1983) developed an analytical model based on the assumption that the current density field becomes collinear with the Laplacian potential field, $\phi(x,z)$. The effect of this is two-fold:

a) The current density, J(x,z) can be calculated from $\phi(x,z)$.
b) The direction of the current flow, and hence the electric field, is in the direction of $\phi(x,z)$.

Calculations of electric field using this model show that, for small discharge electrode dimensions, the current density is uniform along the earthed collection plate. As the current is increased the charge increases proportionally, and an accumulation of charge occurs at the discharge electrode. High electric field and current density values are required for maximum charging and collection conditions, but values are limited by interelectrode and deposited dust layer breakdown.

Electrical conditions may be disrupted when electrostatic precipitators are used to collect dusts with high electrical resistivity. Particles tend to retain their charge on collection and eventually breakdown of the interstitial space in the dust layer occurs. Thus positive ions will be emitted into the duct, causing a reduction of the net charge acquired by particles. Lawless and Sparks (1980) outlined a procedure for calculating the electric field values in the presence of both positive and negative ions. The number of calculations was reduced by numerically integrating Maxwell's equations and the current continuity equation.

Particle space charge may have a significant effect on particle migration, particularly at the precipitator inlet where dust concentration is high. Unfortunately, the inclusion of particle space charge into electric field calculations is complicated by the inherent dependence of particle space charge on dust concentration. Experimental investigation is required to assess whether this effect is important enough to be included into mathematical models.

1.2.2 Experimental measurement of electrical conditions

Experimental measurements of the potential field and space charge density surrounding the discharge electrodes were originally made by measuring the charge acquired by a ball when shot or dropped through the corona region. Serious weaknesses in this method occur as a result of the uncertainty of measurement location and also the nullifying effect of opposite sign charges, producing erroneous results in bipolar surroundings.

Penney and Matick (1960) developed an electrostatic probe consisting of a fine wire supported by a frame, forming a shield to protect the wire from extraneous potential regions through which it was passed. Errors incurred due to the charging of the probe by surrounding ions were proportional to field strength and wire diameter. Penney and Matick performed a series of measurements on electric fields designed to represent conditions in an electrostatic precipitator. They consistently found the electric field value to be a maximum opposite the corona wire. Accurate measurements could only be made for potential fields which were uniform over the length of the probe wire.

Singh, Coventry amd Dalmon (1981) developed a corona probe incorporating a fine carbon fibre, capable of

producing a corona discharge for a small potential difference with respect to its surroundings. A variable potential, applied to the probe via a thin insulated connection, was adjusted to give zero current conditions. At this point, the probe tip matched the potential of the surrounding field. Measurements were found to cause least disturbance to the field if the probe was inserted along equipotential surfaces. Coventry and Hughes (1982) used this device for making quantitative and qualitative assessments of different discharge electrode geometries, for a variety of dust loadings. The variation of corona discharge along the length of an electrode was investigated visually, using an image intensifier system, and current density values were measured at the collection plate surface. The results indicated the presence of a highly non-uniform discharge from a twisted square electrode, whilst the discharge emitted by the sawtooth electrode was fairly uniform.

The investigation by Coventry and Hughes into the effect of dust coatings on the discharge and collection electrodes provided an extension to the work of Rinard, Rugg, Patten and Sparks (1981) who measured V-I characteristics for several combinations of dirty/clean, plate/wire conditions.

1.3 Electric wind

Electric wind is caused by the movement of gas, induced by the repulsion of ions from the vicinity of the high electric field surrounding a discharge electrode. Its presence was first reported by Hauksbee (1709) who experienced a weak blowing sensation on holding a charged tube to his face.

Ramadan and Soo (1969) solved the current continuity

and momentum equations, and were able to compute secondary flow components. They postulated a peak velocity for electric wind in an electrostatic precipitator greater than the mean flow velocity (i.e. 3 ms^{-1}). Flow visualisation experiments were performed using kerosene smoke as a tracer (<7 μm diameter).

Robinson (1976) observed the formation of vertical circulatory cells in a precipitator duct as shown in Figure 1.3. An increase in the level of turbulence was observed for gas velocities less than 3 ms^{-1} at levels of negative corona current typically encountered in electrostatic precipitators.

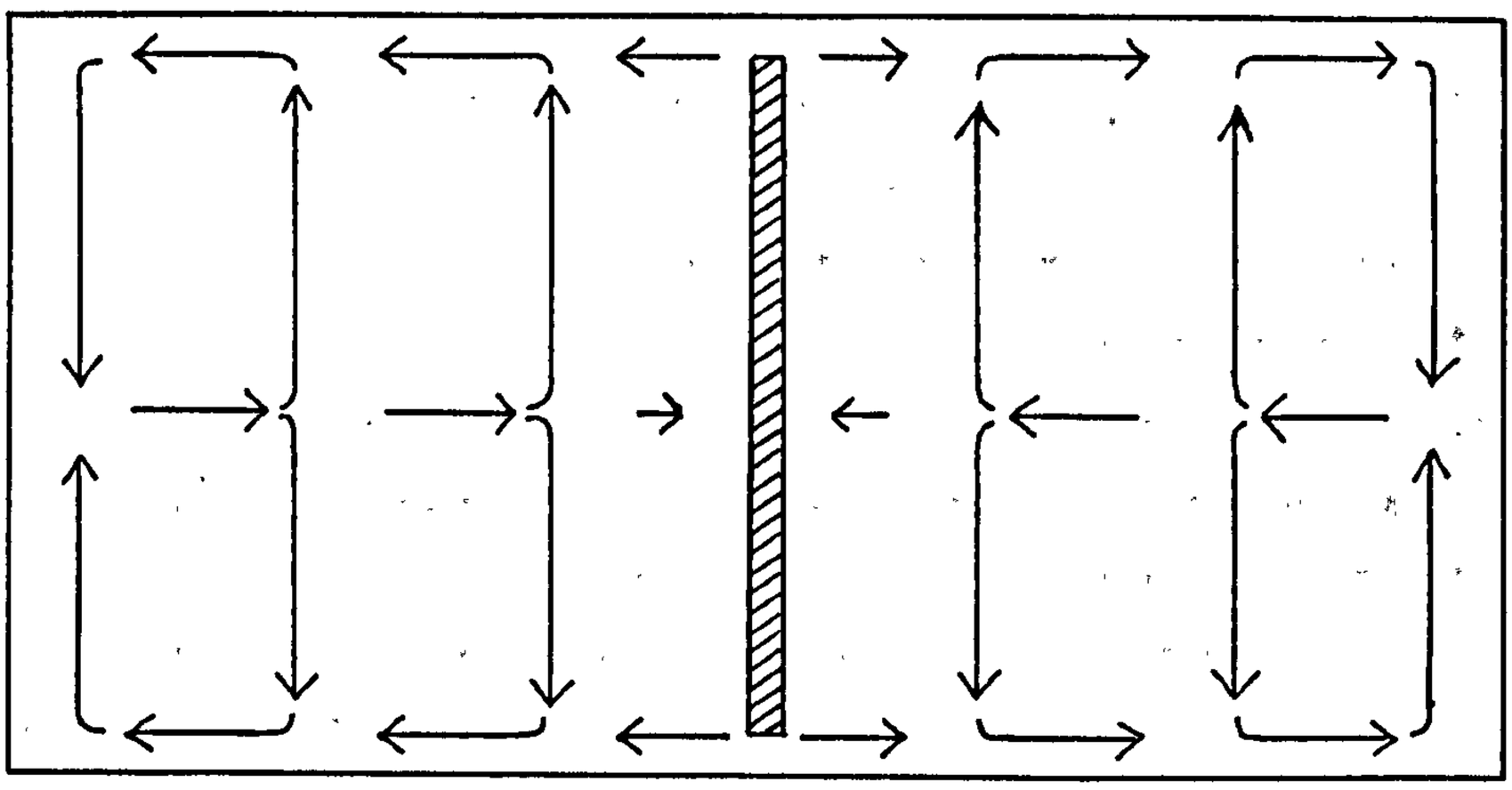

Fig. 1.3 Vertical circulatory cells (Robinson)

Schlieren optical techniques and oil mist cine films were employed by Yamamoto and Velkoff (1981) to confirm their numerical simulation of the electrohydrodynamic (EHD) flow in a precipitator. Flow interactions were modelled

using a dimensionless form of the Navier-Stokes equation, expressed in terms of the vorticity-stream function. Finite difference approximations were integrated over small time intervals until a steady state system was obtained.

Figure 1.4 shows the secondary flow field predicted by Yamamoto and Velkoff for increasing values of the mainstream velocity U_o.

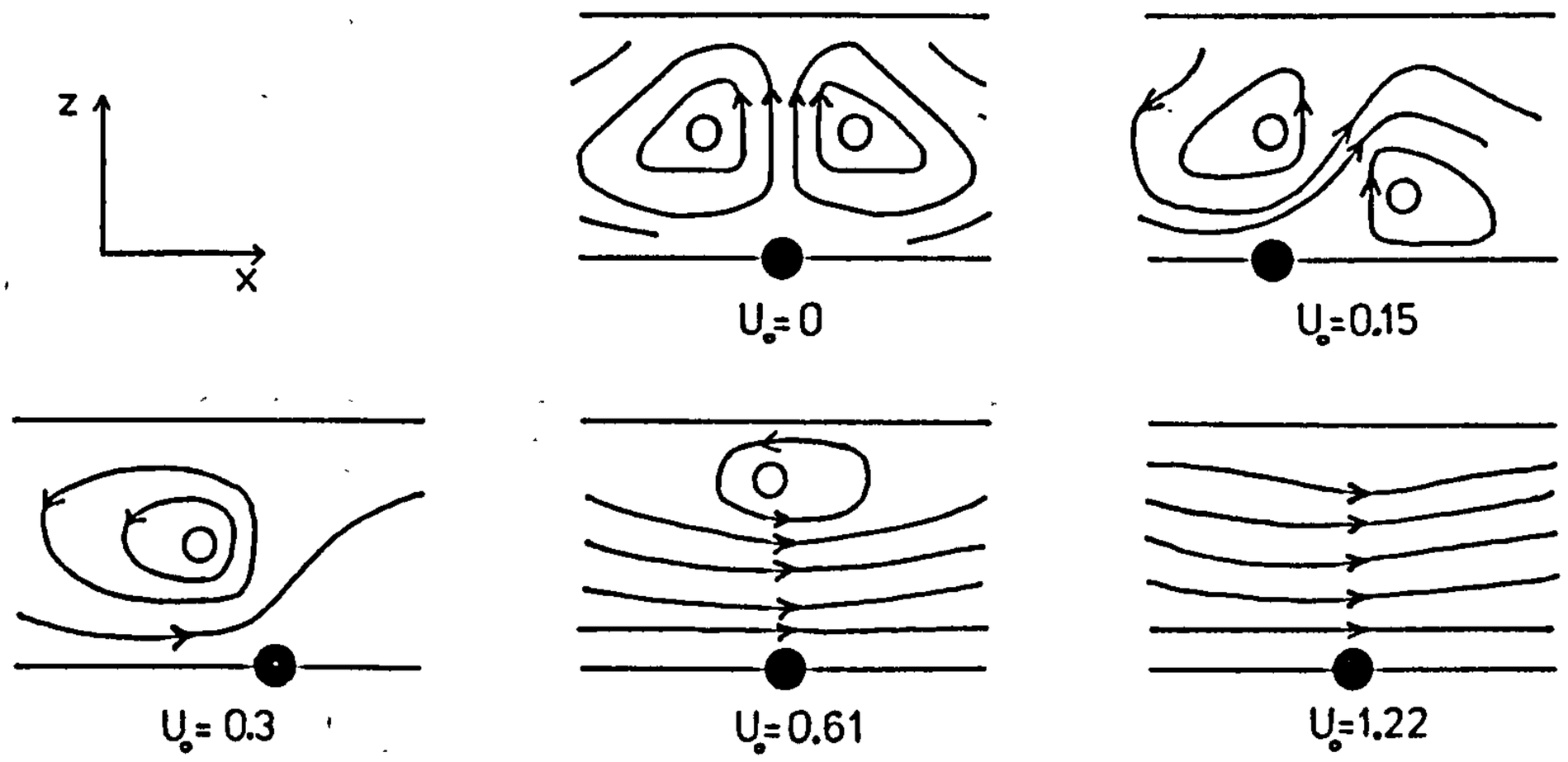

Fig. 1.4 Predicted effect of secondary flow field with increasing mainstream velocity, U_o

The pair of major circulatory cells are shifted downstream and eventually a single counter-clockwise cell is formed. For Re > 7200, the interaction zone becomes insignificant. At low Re values the increased shear stress occurring downstream of the discharge electrodes, due to the circulatory cell, may cause reentrainment. A particle entering the duct would be moved towards the discharge electrode, after which it would be pushed back towards the collection wall. In a multi-wire configuration, the

particles would perform a zig-zagging motion and a large portion of cross-sectional flow area would be blocked off by the induced circulatory cells. The experiments performed by Yamamoto and Velkoff were for a positive corona discharge, and the non-turbulent secondary flow caused by the electric wind was observed in the horizontal x-z plane only. Monitoring of current density distributions showed them to be unaffected by gas velocity, even for values as high as 9 ms^{-1}.

An attempt to resolve the findings of Yamamoto and Velkoff, and Robinson was made by Leonard, Mitchner and Self (1983). Flow interaction in the x-z plane was determined by the ratio of the electric body force to the inertial force, $(I/\rho_f lbU_o^2)$ where l is the electrode length (m). Schlieren and laser-Doppler anemometry (L.D.A.) results indicated recirculating flow in the horizontal plane, as predicted by Yamamoto and Velkoff, but only for values of $(I/\rho_f lbU_o^2)$ greater than those found in industrial precipitators. Hot-wire anemometry was used to detect turbulence intensity levels in a positive, single-wire precipitator. The results showed turbulence generation occurring near the endwalls of the precipitator for moderate values of linear current density. As the current density increased, the boundaries of the turbulent flow region migrated inwards towards the centre of the channel.

Smoke-wire visualisation allowed the induced vortical motion in the y-z plane to be observed, as hypothesized by Robinson. This secondary flow was assumed to arise as a result of corona quenching by the insulating endwalls of the precipitator, and only became turbulent for $(I/\rho_f lbU_o^2) > 1.34$. It was emphasised that the wind tunnel used in Robinson's experimental work had a small aspect ratio (3:1), and the endwall effects would have extended to the centreline. Leonard et al. suggested that in a full-scale

precipitator, with an aspect ratio between 30-60:1, the endwall effects would be negligible. Smoke tests were also performed for the negative corona case. In contrast to the positive case, turbulence and increased mixing was produced throughout the precipitator for velocities less than 2 ms^{-1}. At mean velocities greater than 2 ms^{-1}, no mixing above that produced by the wakes of the discharge electrodes was observed. Turbulence production was caused by local secondary flows, which are unstable due to the nature of the localised corona tufts formed by negative coronas.

Stock and Crowe (1976) used a grid method to calculate ion-gas momentum coupling, and hence the electric wind, for a wire-tube precipitator. This approach included particle-gas momentum coupling, particle transport and electric field calculations. For the wire-tube configuration, the model predicted a net deficit of momentum in the core and a surplus near the wall due to particles moving by electrostatic attraction to the wall, carrying with them their axial momentum. The electrodynamic secondary flow had the opposite effect, increasing the gas velocity near the centre and decreasing it near the wall. These two opposing effects counterbalanced each other resulting in an unaffected velocity profile. However, in a wire-plate precipitator, Stock and Crowe estimated the effect of electric wind to be much greater.

Bernstein and Crowe (1981) developed a corresponding model for a wire-plate precipitator. The numerical simulation used to describe the flow was originally developed at Imperial College, London, and includes the time-averaged conservation equations of mass and momentum and a two-equation turbulence model. The solution of the EHD model was obtained by finite difference methods and allowed the effect of straight wall strengtheners to be examined theoretically. Smoke visualisation was employed

for a negative electrode precipitator to confirm the predictions of the numerical simulation. Qualitative agreement with the observed flow patterns was obtained, and note made that whilst the electric wind may increase the particle migration velocity, the recirculating flow may also contribute to reentrainment.

Thomsen, Larsen, Christensen and Christiansen (1982) have provided useful experimental data on electric wind produced under negative electrode conditions. L.D.A. was used to study the electric wind produced by discharge electrodes with different geometries. The horizontal flow distortions as observed by Yamamoto were found to disappear for mean gas velocities at or above 1 ms^{-1}. However, the turbulence produced by the vertical rolls of vorticity, as suggested by Robinson, persisted up to gas velocities of 2 ms^{-1}.

Athwal, Coventry and Hughes (1983) have recently provided further information into the velocity components of gas flow around transverse sawtooth discharge electrodes. An increase of 0.32 ms^{-1} in the z-direction velocity component due to the electric wind was measured, using L.D.A.. The presence of a vertical component of gas velocity at the wall was predicted, but they were not able to measure it due to the limitations imposed by L.D.A. measurement volume requirements.

A more fundamental study of a point-plane configuration by Athwal et al., showed the electric wind velocity to be almost proportional to the applied voltage with a magnitude of approximately 2 ms^{-1}. Similar studies performed by Sato (1980) allowed the contribution of the electric wind to particle velocity to be subtracted. The resulting particle velocity was due only to the Coulomb force, and was used to obtain accurate particle mobility and charge values.

Negative corona discharges are generally used in industrial precipitators since their sparkover voltage is higher than for positive coronas. Unfortunately, reproducible experimental results are difficult to obtain for negative coronas due to their random tuft-like structure. Ideally, a three-dimensional solution is required to account for electric wind. It is only fairly recently that experimental investigations into the effect of electric wind on particle migration have been carried out. From the literature it is evident that further work is necessary to resolve opposing viewpoints on the subject - some workers believe that electric wind has a negligible effect at gas velocities encountered in precipitators, whereas others suggest that it is an important effect and is responsible for high mixing coefficients. Since no simple way of realistically including the effect of electric wind into a mathematical model has yet been developed, the mechanism has not been included in the models of Chapter 6. However, its significance in explaining some of the experimental results has been recognised.

1.4 Turbulent mixing

Much attention has recently been drawn to the importance of the mixing action of the turbulent gas stream on particle migration in electrostatic precipitators. Although the effect of different levels of turbulence has been studied theoretically, a lack of experimental evidence remains. The term generally used to quantify turbulent mixing is the diffusion coefficient. Although difficult to measure in practice, this parameter is widely used for calculating the transfer of material in turbulent flow situations.

1.4.1 Mathematical description of turbulent mixing

Theoretical investigation into turbulent diffusion was initiated by Taylor (1954), who drew analogies between molecular and turbulent diffusion using a velocity correlation coefficient $R(\Delta t)$, defined by

$$R(\Delta t) = \frac{\overline{v(t)v(t+\Delta t)}}{\overline{v^2}}$$

where v = instantaneous velocity (ms^{-1}),
$\overline{v^2}$ = mean square velocity (m^2s^{-2}).

Kalinske and Pien (1944) used Taylor's definition of the mean spread of particles released into a uniform field of turbulence to obtain the relationship

$$\frac{d(\overline{z^2})}{dt} = 2\overline{v^2}\int_{\Delta t=0}^{\infty} R\, d(\Delta t) \qquad (1.6)$$

where $\overline{z^2}$ = mean square distance travelled in the direction of fluctuating gas velocity component (m^2).

If the gas is moving with a mean velocity of U_o in the x-direction, then time t can be replaced by x/U_o. As the distance x increases, the velocity correlation decreases, and for large values of x, $R \rightarrow 0$. Thus the integral term can be represented as

$$\int_{x=0}^{\infty} R \, dx = \text{a constant} = x_o$$

The parameter x_o is a length scale characteristic of the turbulent flow field. Substituting the integral term into equation 1.6 yields

$$\frac{d(\overline{z^2})}{dx} = \frac{2\overline{v^2}x_o}{U_o^2} \qquad (1.7)$$

Assuming the turbulent diffusion process to be analogous to molecular diffusion, the following expression was deduced

$$D = \frac{U_o}{2} \frac{d(\overline{z^2})}{dx} \qquad (1.8)$$

Substituting the derivative term in equation 1.7 into equation 1.8 for large x yields

$$\overline{z^2} = \frac{2D}{U_o}(x-x_o) \qquad (1.9)$$

from which D may be calculated. The value of diffusion coefficient thus calculated is only representative of the full range of eddy sizes if $x>2x_o$ (see Section 4.1.1). Clearly, the scale of scrutiny under which turbulent mixing is observed is of paramount importance to the interpretation of experimental results.

Although the measurement of turbulent mixing is of great interest in many fields of work, relatively little information has been reported in the literature. Most of

the methods used to determine the extent of mixing in a gas stream have involved the measurement of a dispersed tracer. Kalinske and Pien (1944) determined z^2 values downstream of a hydrogen chloride/alcohol point source, by assuming that the material would spread from the source according to the Normal Law

$$c/c_o = \exp(-\overline{z^2}/2z^2)$$

$$z^2 = -4.606\overline{z^2}\log(c/c_o)$$

where c = conc. of trace material (no. m^{-3}).

Therefore, plotting relative concentration values c/c_o against z on semi-logarithmic paper resulted in a straight line with slope $-4.606\overline{z^2}$. From this value of $\overline{z^2}$, D may be obtained from equation 1.8. Rearranging equations 1.7 and 1.8 gives

$$x_o = DU_o/\overline{v^2} \qquad (1.10)$$

from which a minimum value of x_o can be determined using an estimated maximum value of D. Conversely, an estimate of the characteristic length scale x_o may be determined if the diffusion coefficient is known.

Briller and Robinson (1969) described a similar method for measuring turbulent mixing, which does not assume prior knowledge of the concentration distribution of the dispersed medium. The standard deviation, σ, of the average transverse particle displacement values was measured as a function of distance downstream from the source. Turbulent diffusion coefficient values were then obtained from the relation

$$D = \frac{1}{2}\frac{d(\sigma^2)}{dt}$$

1.4.2 Turbulent mixing in electrostatic precipitators

The convective-diffusion equation has been used in various attempts to model particle transport in an electrostatic precipitator. To obtain a realistic solution, prior knowledge of the turbulent diffusion coefficient, D, is required. In most models uniform mixing is assumed throughout the duct (the Deutsch model assumes an infinite value of D), although it is known that turbulent diffusion vanishes at the collection plate and is affected by the internal geometry of the precipitator duct.

The extent of mixing is dependent on the turbulence level and the corresponding characteristic length scale of the gas stream in the precipitator duct. This may vary by orders of magnitude throughout the precipitator, particularly with the inclusion of flow modulation pipes and wall strengtheners. An additional complication arises due to possible variation of diffusion coefficient with particle size (see Section 1.4.3).

Pyle et al. (1980) used methods similar to Kalinske and Pien to measure the turbulent mixing in a precipitator. The vertical and horizontal spread of a point source of 1 μm latex aerosol particles were measured across the precipitator exit, and values of diffusion coefficient were calculated from

$$D = \overline{z^2}/2T$$

where T = residence time in the duct

= U_o/L (s)

This method can only determine an estimate of the diffusion coefficient, since in the case of a real precipitator the residence time T is not well defined. The coordinate system of the precipitator duct used by the authors (shown in

Figure 1.5) has been adopted throughout this thesis.

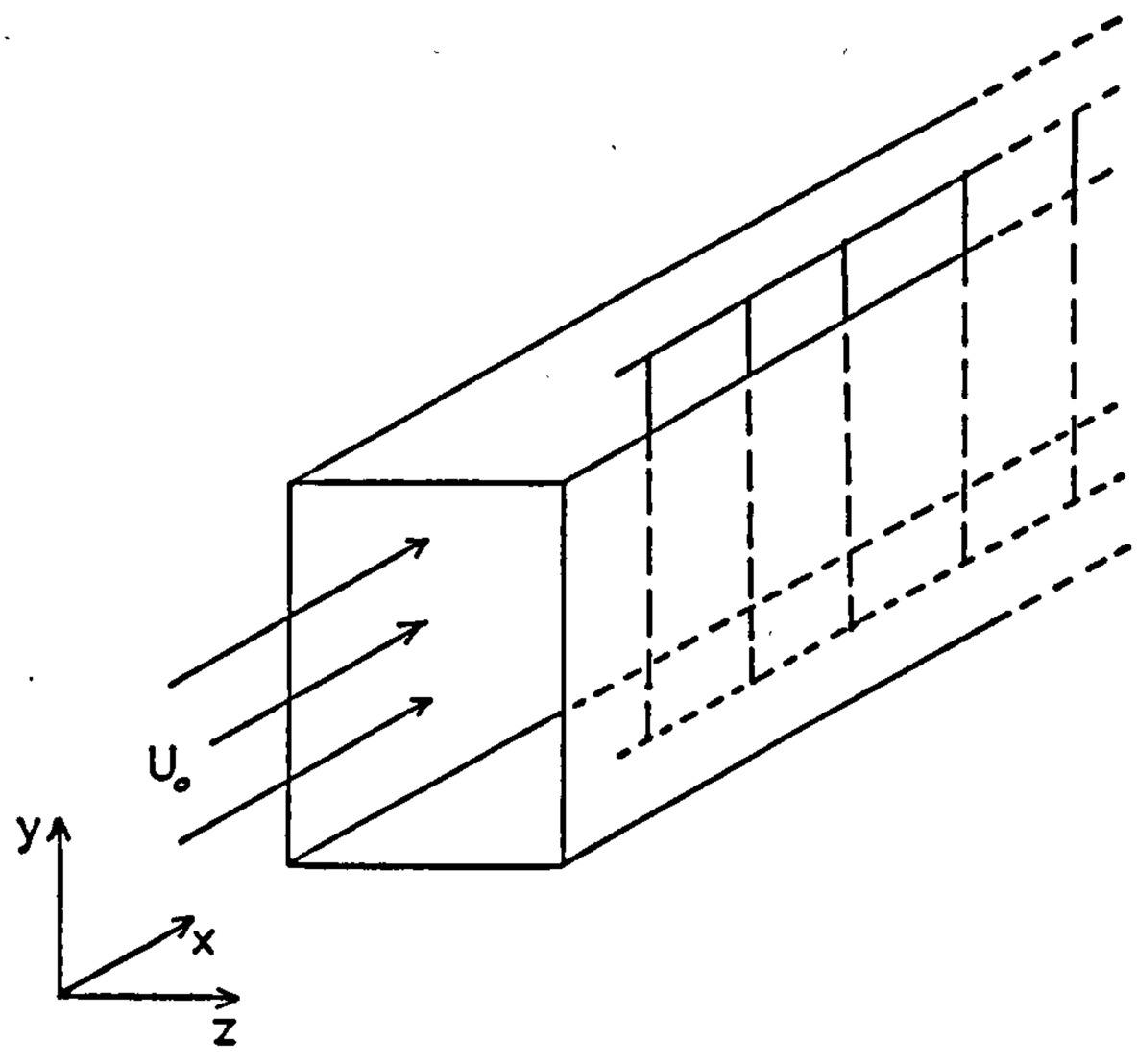

Fig. 1.5 Coordinate system of precipitator duct

Pyle et al. studied the effects of electrode geometry applied voltage and particle size on the average diffusivity in a straight duct system. The results showed an increase in D_z from 8.02×10^{-4} to 13.3×10^{-4} $m^2 s^{-1}$ for 0 and 50KV applied voltage respectively. No explanation of this result was given, but the increase in D_z may be due to electrostatic repulsion of charged particles or electric wind. Insignificant change of D_y occurred under the same conditions, which may imply independence of the model precipitator to 3-D effects such as vertical electric wind. The effect of particle size on turbulent diffusion appears to be dependent on the direction of measurement. D_z is relatively unaffected by particle size, whilst D_y decreases

Diffusion coeff. (m^2s^{-1})	Origin of value	Reference
$2.6x10^{-3}$	Dhanak's relationship $D=0.07U_o d(f)^{1/2}$	Williams and Jackson (1962)
$1.66x10^{-3}$	As above	Feldman et al. (1976)
$10\text{-}20x10^{-4}$	Expt. measurements	Pyle et al. (1980)
$2.2x10^{-3}$	Kay's relationship $D=150$	Leonard et al. (1980)
1.0	Guess	Vincent (1980)
0.1	Back-calculated from N(T)	Maclennan et al. (1981)
$5.0x10^{-4}$	-	Eschbach et al. (1981)
$7x10^{-4}$	$D=6.37x10^{-7}(Re-4000)^{2/3}$	Lawless et al. (1982)
$<<5x10^{-3}$ - $>>10^{-2}$	Limiting cases C-D equation	G. Cooperman (1984)

Table 1.1 Range of diffusion coefficient values used in the literature

from approximately 17.5×10^{-4} to $11.0 \times 10e^{-4}$ $m^2 s^{-1}$ for an increase in particle diameter from 1.0 to 4.5 μm. The significance of these results was not discussed in terms of the effect on precipitator efficiency.

Similarly measured values of average diffusivity were used to evaluate a solution to the convective-diffusion equation (Pyle et al.,1981). The results were then compared to theoretical predictions of the Deutsch equation and to experimental collection efficiency results measured for submicron latex spheres. Various levels of turbulence were obtained in the duct by the insertion of different mesh size grids, followed by a plane of cylindrical rods at the inlet. Although it appeared from the experimental results that the efficiency increased at higher turbulence levels, this was a false impression since whilst D increased by 43%, the mean gas velocity decreased by 23%. It was this decrease in gas velocity which caused the increase in efficiency.

The confusion over the appropriate value of diffusion coefficient to be used in mathematical modelling of electrostatic precipitators is reflected in the wide range of values employed by various workers. Table 1.1 shows some of these values and their method of origin. Clearly, quantitative measurement of gas stream turbulence in electrostatic precipitators is urgently required.

1.4.3 Particle diffusivity

The inertia of a particle causes it to have a finite response time to passing turbulent eddies. Peskin (see Boothroyd, 1971) defined the resultant decrease in particle diffusivity, D_p, as compared to eddy diffusivity, D, in terms of the impulse response parameter, K, and the Lagrangian and Eulerian scales of turbulence l_L and l_E respectively. If K=0 then the particle follows the fluid

motion perfectly and D_p=D. Particles with large values of K do not respond to the fluid motion, and the corresponding reduction in particle diffusivity may be calculated from the expression

$$\frac{D_p}{D} = 1 - \left(\frac{l_L}{l_E}\right)^2 \frac{3K^2}{K+2} + O(1/l_E^4) \qquad (1.11)$$

where $K = \frac{\sqrt{\pi}}{18} Re_p \frac{\rho_p d_p}{\rho_f l_L}$

This equation is displayed in graphical form (ref. Soo (1967), p.58). Calculations using this expression are difficult since a general relationship between l_L and l_E has not yet been established. For a fixed value of K, the ratio D_p/D will be close to unity for small values of l_L/l_E. The graph shows that for K<0.1 then $D_p/D \approx 1.0$.

Vincent and Maclennan (1980) deduced from equation 1.11 that, for a fixed value of l_L/l_E, the response of the particle to the turbulent fluctuations depends on the relative values of particle relaxation time T_p and 1/v (where l is the integral length scale). Since l_L increases with U_o, and l_E is of the order of s_z, then

$$1 - \frac{D_p}{D} \propto \frac{U_o^2 r_p^2}{s_z^2} \qquad (1.12)$$

This expression implies that a reduction in particle diffusivity could be obtained by increasing the precipitator mainstream gas velocity. Unfortunately, this would also have the effect of decreasing the residence time of particles in the precipitator, thus decreasing the efficiency.

Information is required on the possible variation in diffusivity with particle size of the test dust in

concentration measurements described in Chapter 5. For a 10 μm diameter particle of alumina dust carried by a 2 ms^{-1} turbulent gas stream (15% turbulence intensity), the following relationship between K and l_L is obtained,

$$K = 6.9 \times 10^{-4} (l_L)^{-1}$$

For the worst case of $l_L/l_E=1$, this relationship can be used to estimate the ratio D_p/D as a function of l_L. Figure 1.6 shows the results for a 10 μm diameter alumina particle. The graph shows that for the particle diffusivity to be within 10% of the eddy diffusivity value, l_L must be at least 2.5 mm. Calculations described in Chapter 3 show l_L to be of the order of several centimetres - hence $D_p=D$ is a justified assumption.

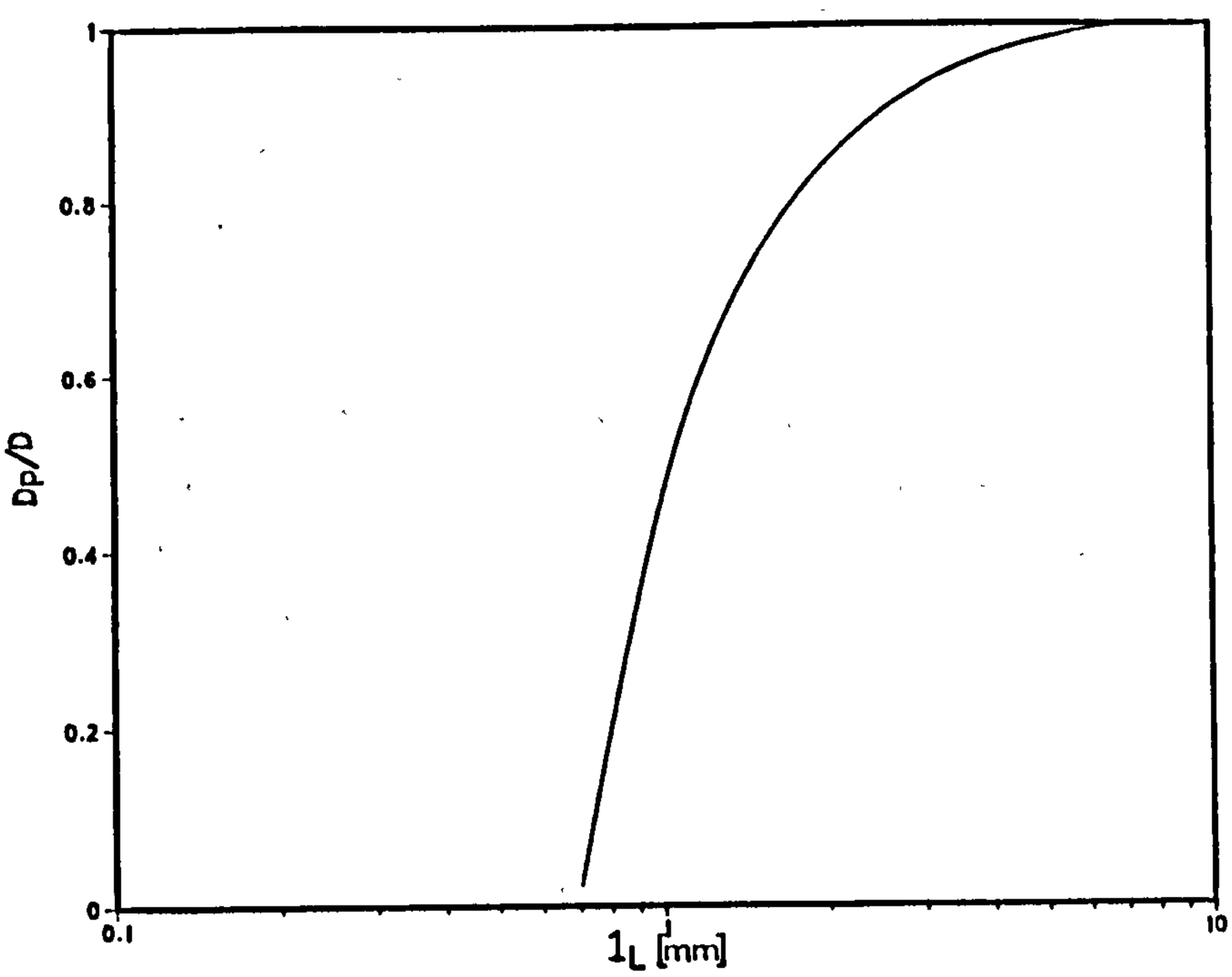

Fig. 1.6 D_p/D versus $\log(l_L)$ for 10μm particles of alumina

Further support of the equivalence of D_p and D for alumina dust in the size range 1-10 μm is obtained by comparing estimates of the particle relaxation time T_p and effective eddy passage time, t. If $t>T_p$ then the particle will occupy the eddy for sufficient time for it to acquire the same velocity as the eddy. In such a case, $D_p/D \approx 1.0$. An estimate of t may be calculated from the expression

$$t = l/v'$$

where l = eddy size (m),

v' = r.m.s. fluctuating velocity.

Figure 1.7 enables an eddy size to be calculated which will cause a particle, with aerodynamic diameter d_p, to follow its motion. Eddy length versus t lines are plotted for three different turbulence intensity levels ranging from 1.5 to 50% for a 2 ms^{-1} mean flow velocity. Also indicated on the graph is the value of t corresponding to the Kolmogorov length scale. It appears that even at 15% turbulence the eddy passage time of the smallest eddies is sufficiently long for the particles to follow the fluid motion, so $D_p \rightarrow D$.

In general, the dust precipitated by industrial precipitators contains particles of a much larger size than considered in this work. Soo et al. (1960) have shown that for glass beads in the size range 50-200 μm

$$0.02 < D_p/D < 0.06$$

suggesting that particle diffusivity may be drastically reduced for large particles. The improved collection efficiency of larger particles in an electrostatic precipitator is usually justified by their increased electrical migration velocity. From the above

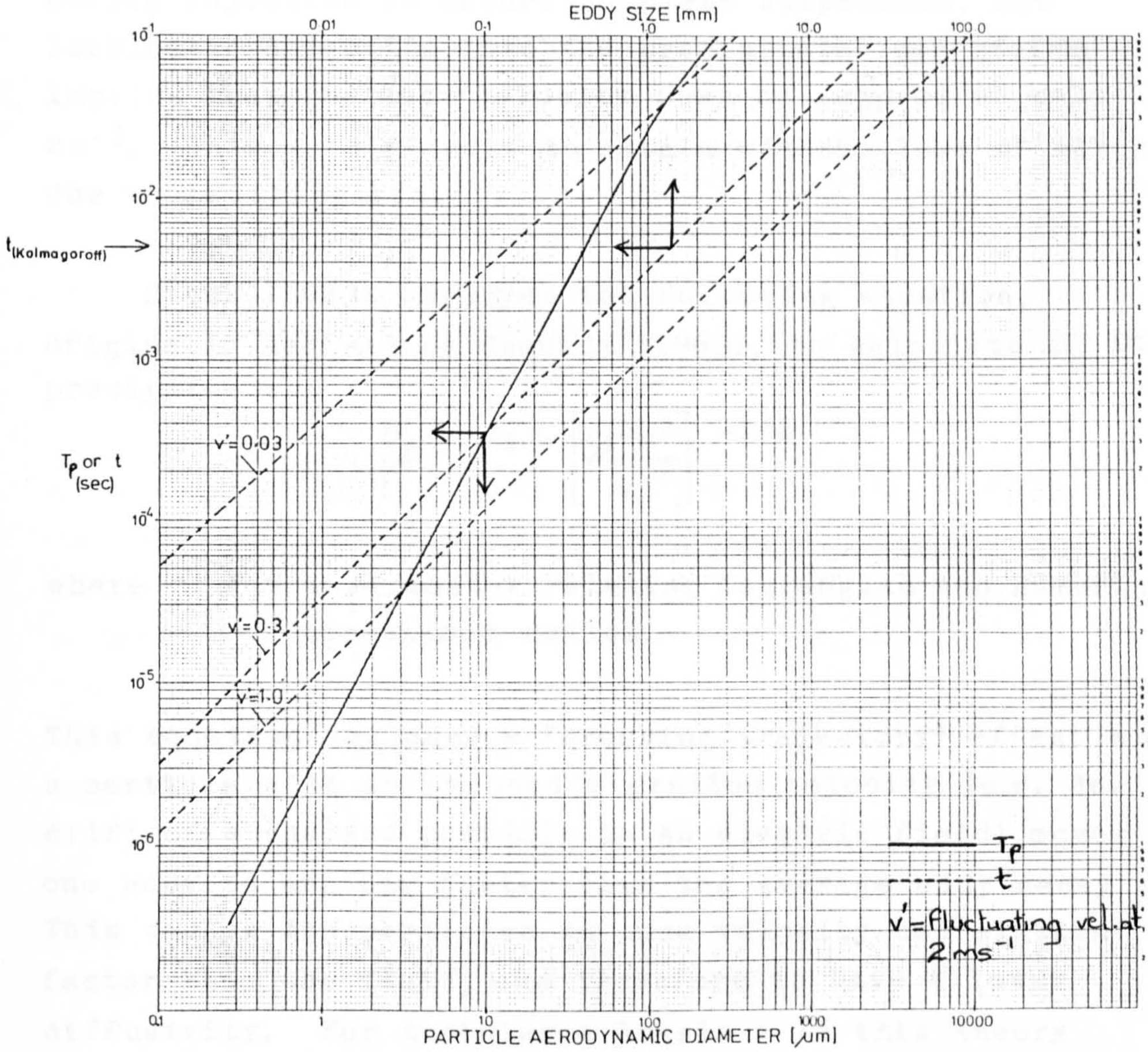

Fig. 1.7 Comparison of particle relaxation time, T_p, and eddy passage time, t.

considerations, it appears that reduced diffusivity may also play an important role in the enhanced collection of large particles. This effect requires further experimental investigation. Unfortunately, practical difficulties arise when the technique used for measuring the diffusivity of eddies or small particles is applied to larger particles.

Dusts such as alumina or flyash require high shear fields during injection to ensure complete dispersion, but isokinetic injection into the precipitator gas stream implies that the dust velocity must be reduced to only 1-2 ms^{-1}. This is difficult to attain without loss of material due to settling etc..

Stock (1983) employed the following equation, originally derived by Csanady (1963), to calculate D_p in a precipitator.

$$\frac{D_p}{D} = 1 + \left[\frac{4\beta^2 w^2}{v'^2}\right]^{-1/2}$$

where β = a parameter relating Lagrangian and Eulerian turbulence scales.

This equation includes a "crossing trajectory" effect where a particle with an imposed migration velocity (e.g. due to drift of a charged particle in an electric field) moves from one eddy to another faster than the average eddy decay rate. This causes the particles to lose velocity correlation faster than the fluid, and therefore to have a lower diffusivity. For turbulence levels > 4% this theory predicts a negligible deviation of the ratio D_p/D from unity. Since turbulence levels in electrostatic precipitators are frequently as high as 15%, this effect can be neglected.

1.5 Turbulent deposition

The transport of particles from the turbulent flow stream inside a precipitator duct to the collection walls is of primary importance in the study of electrostatic precipitation. Particle deposition occurs in general as a result of the following;

a) electrostatic migration of charged particles in an electric field,
b) deposition of the particles due to the turbulent nature of the gas flow field.

The second mechanism occurs with or without the presence of an electric field and is the cause of mechanical collection. Potter (1981) has reported mechanical efficiency values as high as 30-70%, but omitted details of the conditions under which the measurements were made. The mechanisms by which turbulent deposition occurs are of obvious interest, especially if this sizeable fraction of collected dust is to be accounted for in theoretical models. Papavergos and Hedley (1984) provide a detailed review of theoretical and experimental studies of turbulent deposition.

The transport rate of particles to the wall is usually expressed in terms of the dimensionless deposition velocity V_d^+, defined as

$$V_d^+ = \frac{W}{v^* N}$$

where W = particle flux towards surface ($m^{-2}s^{-1}$),
N = mean local aerosol concentration.

Freidlander and Johnstone (1957) proposed a model to describe turbulent deposition whereby particles are transported from the turbulent core towards the wall by turbulent diffusion, and then projected through the laminar sublayer with a velocity equal in magnitude to the local r.m.s. radial fluid velocity, v'. Before reaching the wall, the particle travels a distance S, commonly known as the stopping distance, where

$$S = v'T_p$$

The values of V_d^+ for three regions, $S^+<5$, $5<S^+<30$ and $S^+>30$ were derived in terms of the dimensionless stopping distance, S^+.

Subsequent work by Liu and Ilori (1974) attributed the underestimation of deposition values calculated using the theory of Freidlander and Johnstone to their assumption of $\varepsilon_p = \varepsilon_m$, where ε_p is the particle diffusivity and ε_m is the eddy viscosity of momentum. Consequently, they attempted to derive an expression for the variation of ε_p through the turbulent boundary layer. Using the relationship

$$\varepsilon_p = \varepsilon_m + v'^2 T_p$$

they improved the fit of their model with experimental data, particularly for $2 < T_p^+ < 20$. The results also predicted higher deposition rates where the flow was not fully developed.

Owen (1960) produced a theory similar in many ways to that of Freidlander and Johnstone. Diffusivity was taken as being proportional to eddy viscosity, rather than equal to it, and particle diffusion was assumed to occur up to a distance $y^+ = l^+$ from the wall, after which free-flight took place. A value of $l^+ = 1.6$ was chosen by Owen.

A further modified version of Freidlander and Johnstone's theory was developed by Davies (1965). Rather than using a constant initial particle projection velocity, Davies assumed that the initial free-flight velocity started at a distance $y^+ = S^+ + r_p^+$ with magnitude equal to the local turbulent fluctuation velocity. The theory considered three regimes; diffusive, transitional and inertial. In the transitional regime, deposition occurred as a result of both diffusive and inertial mechanisms. Despite this logical extension to Freidlander and Johnstone's model, including a

more reasonable estimate of the initial free-flight velocity, the analysis presented by Davies disagreed with experimental data by as much as two orders of magnitude.

Beal (1970) attempted to develop a general theory to cover a size range of 0.1-100 μm, without classifying particles into regimes as described by Davies. A constant initial free-flight velocity, defined by half the axial velocity, was chosen to obtain a reasonable fit with experimental data. The inverse deposition velocity was expressed as a sum of the resistances from the turbulent core to $y^+ = S^+ + r_p^+$ and for $y^+ < S^+$. Although the method for calculating the free-flight velocity was unrealistic, predictions using this theory appear to fit experimental data more satisfactorily than previous theories.

Sehmel (1971) initially proposed a theoretical model similar to Davies' analysis except for the empirical expression for eddy diffusivity. Poor agreement with experimental values led to the proposal of new concepts:

a) Particles are deposited to the wall with an effective particle diffusivity arising from inertial and turbulent diffusional effects and residual lift forces due to the shear near the wall.
b) Free-flight particle velocity values can be back-calculated from experimental data and correlated with relaxation time to obtain

$$U_p^+ = 1.49(T_p^+)^{-0.49}$$

where U_p^+ = dimensionless initial projection velocity towards surface.

Unfortunately, this equation opposes the intuitive idea of how U_p^+ should vary with T_p^+. As T_p^+ decreases, one would

expect the particle to become detached from the eddy closer to the wall, and subsequently possess a smaller U_p^+. This new theory enabled prediction of deposition values to within approximately 24% of experimental data.

Following the observations made by Kim, Kline and Reynolds (1971) of turbulent "bursts" through the laminar sublayer, Cleaver and Yates (1975) developed a new approach to particle deposition assuming the particles to be carried right up to the wall by these fluid downsweeps. In abandoning the free-flight model, the difficulty of calculating a relevant initial injection velocity was avoided. Particle trajectories within a downsweep were computed to enable estimation of the percentage of particles approaching the wall. Two methods of modelling the flow within the downsweep were considered - two-dimensional stagnation point flow and a flow model based on Laufer's data.

Taking into account the influence of axial flow on deposition as shown in Figure 1.8, Cleaver and Yates derived the following expression,

$$N^+ = A_c/2 + (1-A_c)A_a(U_a/v^*)$$

where N^+ = dimensionless deposition flux,
A_a = % axial capture of a downsweep,
A_c = % downsweep capture area,
U_a = mean axial convection velocity (ms^{-1}),
v^* = friction velocity (ms^{-1}).

The analysis stresses the importance of the ratio of particle to fluid density. Cleaver and Yates suggested that insufficient attention to the value of this ratio may explain the scatter of data in previous experimental studies.

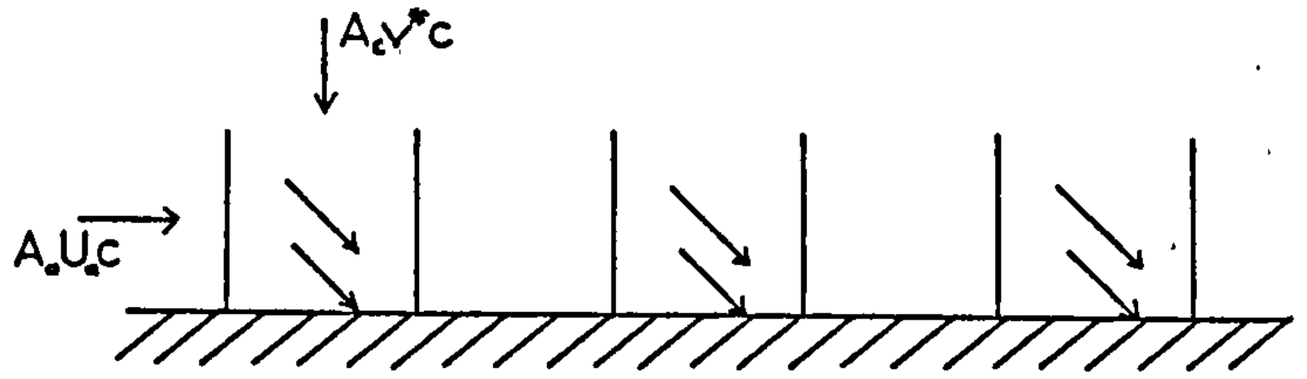

Fig. 1.8 Influence of axial flow on turbulent deposition

Probablistic theories such as this provide better physical insight into the actual mechanisms of collection than free-flight models, as well as giving satisfactory agreement with experimental data. Subsequent work by Cleaver and Yates (1976) enabled them to predict the effect of turbulent "bursts" on reentrainment. A critical wall shear stress τ_{wc} was defined, below which reentrainment would not occur. An important implication of this theory is the dependence of N on the time taken to measure deposition. Graphs of N vs v^* may be used to estimate dynamic adhesion forces, which are important in such problems as redeposition, where the phenomena are controlled by adhesion.

Wood (1981) studied deposition to both rough and smooth surfaces. Deposition rates were found to be extremely sensitive to surface roughness, even for hydraulically smooth surfaces (i.e. sublayer scale). Deposition rate equations were derived, assuming that particles were caught when they reached the level of effective roughness height. These were found to agree with experimental data only when the dimensionless height of the roughness element, $k^+ < 5$ i.e. the hydraulically smooth regime. Lack of reliable experimental data for rough surfaces prevented further verification of the theory.

Davies (1983) also investigated deposition to rough surfaces and found deposition to be approximately ten times that onto smooth surfaces. The following expression was proposed for small particles (i.e. $T_p^+ < 0.22$)

$$V_d^+(\text{smooth}) = 0.075Sc^{-2/3}$$

$$V_d^+(\text{rough}) = 0.080Sc^{-1/2}$$

The experimental independence of V_d^+ on surface roughness for large particles ($T_p^+ > 33$) was attributed to the inertial effect providing sufficient z-directional penetration for the particles to be carried through the laminar sublayer. The larger particles are brought close to the surface by jumping down streamlines, as shown in Figure 9, and inertial collection by the roughness element then occurs.

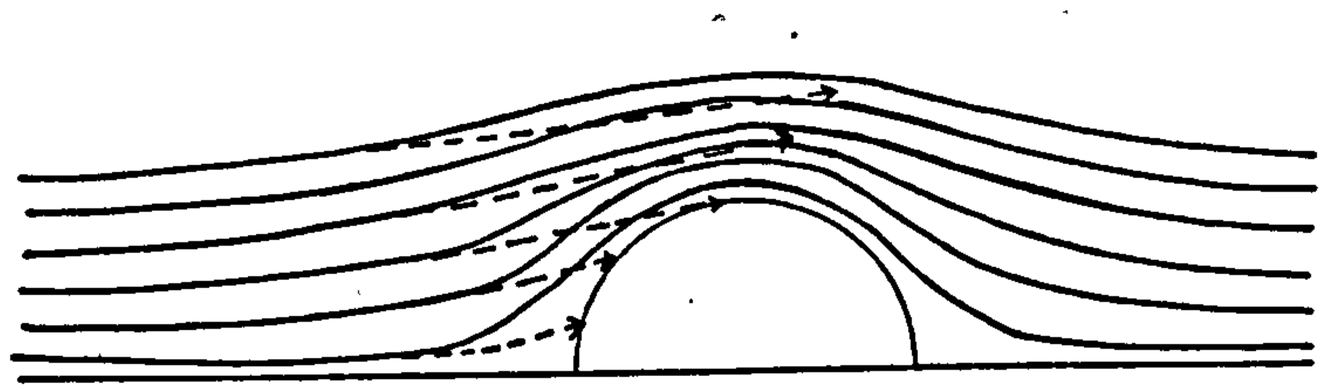

Fig. 1.9 Inertial impaction of large particles on roughness elements

Although the theories mentioned above can predict turbulent deposition under ideal conditions, they may not be applicable in the case of electrostatic precipitators, where fully developed flow is probably never achieved and and disturbances such as wall strengtheners exist. Further experimental investigation of mechanical deposition in precipitators is therefore required before the collection mechanism can be realistically incorporated into mathematical models.

1.6 Mathematical modelling of precipitator performance

An accurate mathematical model capable of describing the process of electrostatic precipitation is useful for;

a) designing precipitators by calculation from first principles,
b) optimising operating conditions,
c) predicting trends caused by variation of design parameters,
d) accurate sizing of precipitators to avoid costly under- or over-sizing.

Information provided to the precipitator designer usually consists of chemical and size analyses of the dust, estimated inlet concentration and required efficiency. Recently, additional guides as to the minimum specific collection area and rapping forces for the electrodes have been included (Darby, 1981).

The following review of mathematical models has been split into two sections. The first section deals with analytical modelling and includes fairly simple expressions for efficiency, usually based on the assumption of an exponential fall in dust concentration down the precipitator duct. The second section deals with the numerical solution of the differential equation describing particle motion in the precipitator. Validation of theoretical models requires comparison of predicted results with experimental data measured under realistic working conditions. Although efficiency measurements obtained from industrial precipitators exist in abundance, there remains a lack of information on concentration profile development along the duct. Such information is required so that a qualitative comparison with predicted values can be used to check that mechanisms have been modelled accurately, and that any

agreement in efficiency values is not fortuitous.

1.6.1 Analytical methods

In the event of laminar flow conditions in an electrostatic precipitator, all particles would theoretically be caught in a finite length, L, defined by

$$L = \frac{U_o s_z}{w_{min}}$$

where w_{min} = minimum electrical migration velocity of any particle in the precipitator (ms^{-1}).

In practice, flow conditions in the majority of precipitators are turbulent, which causes the particles to be back-mixed across the duct. A simplistic mathematical model which describes this idealised situation is the Deutsch-Anderson expression (as described in Introduction) which is still in common use for precipitator size calculations. Although this expression has been used as a design tool for many years, it is based on several simplifying approximations, some of which are not realised in practice:

a) The particles are considered to be fully charged immediately on entering the system.
b) Turbulent and diffusive forces cause the particles to be uniformly distributed over any cross-section of the duct.
c) The particles always move towards the wall at their terminal electrical velocities and are not affected by the transverse velocity of the gas stream.
d) Particles are sufficiently separated so as not to affect each other.
e) All particles have migration velocities defined by the balance between electrical and aerodynamic drag forces,

$$w = qE/(6\pi\mu r_p)$$

f) Any interaction between neutral gas molecules and ions i.e. electric wind, can be neglected.

g) There are no non-ideal effects such as reentrainment, uneven gas flow distributions, sneakage or back corona.

In practice, the non-ideal effects are incorporated into an empirical or effective migration velocity value, w_e. This value bears no relationship to the theoretical value w, and is calculated from test efficiencies obtained during operation. This method of precipitator design can only be reliably used where similar systems are already in operation, so that an empirical calculation of w_e can be obtained. Cooperman (1973) presented a nomogram capable of predicting the effective migration velocity from known values of efficiency, volume flow rate and collection area. This provides a simple and quick method for calculating w_e, providing an answer with accuracy to within 1.5%. Ideally, a model would be developed which could incorporate all the physical mechanisms occurring in a precipitator. Design could then start from first principles and new designs such as wide-plate and pulse energised precipitators could be studied.

Oglesby and Nichols (1978) derived an equation similar to the Deutsch-Anderson equation which introduced particle concentration and a gas distribution parameter, such that

$$\eta = 1 - \exp(-(N_\delta/N)(A/U_oQ)w)$$

where N = particle conc. in gas stream ($no.m^{-3}$),

N_δ = particle conc. in boundary layer ($no.m^{-3}$),

Q = quality factor of the gas flow.

Robinson (1967) attempted to include the erosion of

collected dust and a non-uniform concentration profile, whilst retaining the simplicity of an exponential relationship. The efficiency equation contained three terms, the first taking account of dust non-uniformity, the second and third describing variable and constant erosion terms,

$$P = w\chi c - \alpha w\chi c - \beta w\chi c_o$$

where P = net flux of particles to the wall ($Kgm^{-2}s^{-1}$),
c = average particle conc. ($no.m^{-3}$),
c_w = particle conc. near to the wall ($no.m^{-3}$),
c_o = input particle conc.($no.m^{-3}$),
α = mass of dust eroded/mass of dust precipitated,
β = mass of 'problem' dust eroded/mass of total dust precipitated,
$\chi = c_w/c$ is a measure of the cross-section conc. uniformity.
w = precipitate flux/unit dust conc. at wall.

'Problem' dust refers to an apparently unprecipitable fraction of dust which occurs, for example, in the case of low resistivity dust, where the particles are repeatedly precipitated and eroded until they finally escape from the end of the precipitator. If the constant erosion term is omitted the equation becomes exponential, from which Robinson concluded a that uniform cross-sectional dust distribution is not essential for the existence of an exponential concentration decay along the duct.

The effect of turbulence was modelled by Cooperman (1971) using an empirically determined parameter, f, defined as

$$f = \frac{\left(\frac{\text{turbulence-induced particle transport}}{\text{away from wall}}\right)}{\left(\frac{\text{electrostatic-induced particle transport}}{\text{towards wall}}\right)} \qquad (1.13)$$

The precipitation process was described by the differential equation,

$$\frac{d^2c}{dz^2} - \frac{U_o}{D}\frac{dc}{dz} - (1-f)\frac{wc}{s_z D} = 0$$

with $c = c_o$ at $x = 0$, and $c \longrightarrow 0$ as $x \longrightarrow \infty$.

Dimensionless quantities $A = s_z U_o/2D$, $B = (1-f)s_z w/2D$ and $l_c = L/s_z$, were used to express the collection efficiency as,

$$\eta = 1 - \exp(A - (A^2+2B)^{1/2})l_c$$

where L = overall treatment length of the precipitator (m).

The implications of this result include a reduction in the migration velocity by a factor (1-f). Consequently this equation predicts that the efficiency should always be less than that predicted by the Deutsch-Anderson equation. Practical difficulties arise in attempting to use this method due to the introduction of unknown parameters f and D. Leonard et al. (1980) have questioned the introduction of the parameter f on physical grounds. They attributed the reduced efficiencies obtained in practice to non-ideal effects such as reentrainment, sneakage etc..

Gooch and McDonald (1976) described a mathematical model capable of calculating efficiency as a function of particle size and operating conditions. The Deutsch-Anderson equation was applied to each incremental length and then summed to give an overall efficiency. The effect of gas sneakage was accounted for by including a term C in the exponent defined by

$$C = \frac{\text{ideal value of w (no sneakage)}}{\text{apparent value of w (with sneakage)}}$$

The model tended to overpredict performance at low current density and gas velocity values, and underpredict for high values.

Further empirical parameters k_1 and k_2 were introduced by Potter (1978,1981) who described an extended Deutsch equation,

$$\log(1-\eta) = \log(1-\eta_o) - k_1 V_o - k_2 d_p \propto V^2$$

where η_o = mechanical efficiency,
V_o = corona initiating voltage (V),
$\propto$ = specific collection area (m^{-1})

k_1 and k_2 are constants dependent on the temperature, viscosity of the carrier gas, and dielectric properties of the particles.

The first term on the right-hand side was introduced to represent mechanical collection. The second term accounted for the collection of the small number of particles posessing a natural charge, under the influence of applied field value too weak to initiate a corona discharge. The final term applied only in the presence of corona charging of the particles. The customary expression of precipitability as an effective migration velocity was replaced by a semi-logarithmic plot of collection efficiency against $\propto V^2$, described as the performance line. A slight bending over of the line at high efficiencies indicated an increase in collection of fines.

Although the fraction of dust collected by mechanical deposition was found by Potter to be as high as 70%, no experimental investigation of this mechanism in electrostatic precipitators has yet been reported. Of particular interest is the variation of mechanical

deposition with particle size, which may aid in determining whether collection is due to residual particle charge or turbulent deposition.

Industrial precipitators generally rely on baffles, spaced periodically along the duct, to strengthen the walls. Depending on their design, these strengtheners tend to reduce dust erosion at the expense of increasing turbulence within the duct. Vincent (1971a,1971b,1980) suggested that entrapment of the dust in the stationary or quasi-stationary vortices formed in the wakes of strengtheners may result in an increase in efficiency. His mathematical analysis of the situation assumed that a particle, having performed a single effective revolution in a vortex, would lag behind an untrapped particle by a time interval, t_d. During this time, the particle was considered as occupying a mean stationary position at the centre of the vortex as shown in Figure 1.10. The effect of the electric field would be to sweep the particle to the collection wall. If the time taken for the particle to reach the wall was less than detention time t_d, Vincent assumed that the particle was collected.

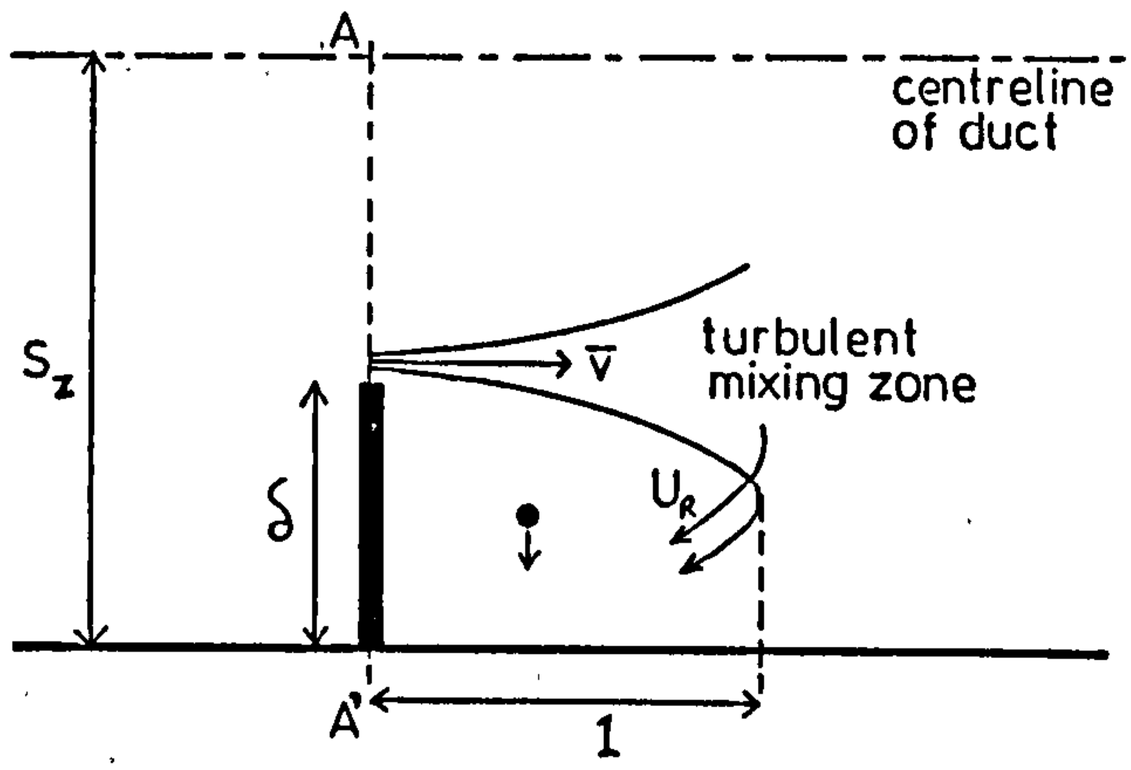

Fig. 1.10 Entrapment of dust in vortex formed downstream of strengthener

The mean air flow through AA' is given by

$$U_o = \frac{v}{(1-\delta/s_z)}$$

where v = mean velocity of reentrained air back into mainstream

δ = distance strengthener protrudes into duct (m).

The fraction of air (and hence dust), ϕ, entrained into the vortex is,

$$\phi = \frac{v(1/2s_z)}{U_o(1-\delta/s_z)}$$

where 1 = length of vortex (m).

The detention time, t_d, for a particle performing a single revolution of a vortex is,

$$t_d = \frac{(U_o+U_R)}{U_R U_o}$$

where U_R = mean air recirculation velocity inside vortex (ms^{-1}).

For particle collection to occur,

$$r_p \geq \frac{\delta}{\beta} \frac{U_R U_o}{21(U_o+U_R)} = a_c$$

where a_c is the critical particle size for collection.

$\omega = \beta r_p$

Vincent superimposed this vortex collection directly onto conventional Deutsch-type collection. The results showed that collection efficiency is enhanced by the presence of wall strengtheners, although in practice a major

contribution may have been due to reduced reentrainment.

Subsequent work of Vincent and Maclennan (1980,1981) resulted in a description of collection efficiency based on gas treatment time. This approach retained the simplicity of an exponential expression and embodied all the complicated fluid mechanical processes into a single determinable or measurable treatment time function, N(T). For isotropic, random turbulence, N(T) is a normal distribution (see Figure 1.11), and hence the probability of treatment time in the turbulent core p(T), is

$$p(T) = \left[\frac{h_1(1-\beta)}{\sqrt{\pi}}\right] \exp(-h_1^2(T-T_o)^2)$$

where $h_1 = U_o/(4D_pT_o)^{1/2}$,

T_o = mean gas treatment time (s).

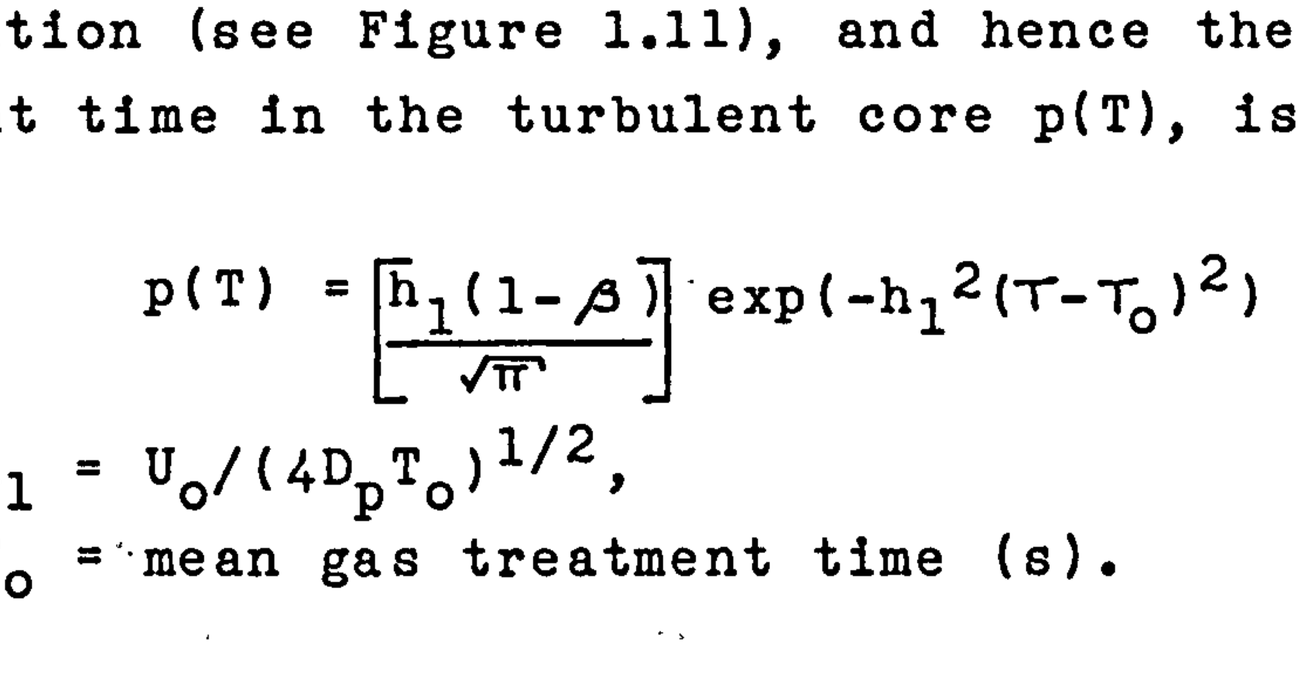

Fig. 1.11 Gas treatment time function, N(T) in a precipitator duct

The probability of treatment time for the entrained gas q(T), is

$$q(T) = \frac{\beta}{t_R} \exp(-(T-T_o)/t_d)$$

The total probability of treatment times, N(T), is given by

$$N(T) = \underbrace{p(T)}_{\text{for all } T} + \underbrace{q(T)}_{\text{for } T>T_o}$$

Wall strengtheners have two effects on the shape of N(T);

a) the graph becomes skewed towards larger T, resulting in higher predicted efficiencies,
b) the graph is broadened, resulting in a decrease in efficiency due to the exponential form of the efficiency equation.

The discrepancy between the theoretical and effective migration velocity values was accounted for in the function N(T). This was obtained experimentally by observing the decay of smoke-filled cavities. For monosized particles, and n sets of strengtheners, the collection efficiency was defined as

$$\eta = 1 - \gamma^n \exp(-\alpha T_o(1-\phi))$$

where $\gamma = \beta/(1+\alpha t_d) + (1-\beta)\exp(\alpha^2/4h_1^2)$

From this work, Vincent (1971b,1972) went on to describe the possibility of including a grid-type device onto the end of precipitators, to increase the efficiency without significantly increasing their overall length.

Although analytical models are relatively simple to apply, their use is limited to predicting precipitator performance where similar designs already exist, so that fitting parameters such as w_e and f can be estimated. Progress in the modelling of precipitators can only advance if quantitative descriptions of the mechanisms affecting

particle migration are realistically incorporated.

1.6.2 Numerical modelling

Inaccurate assumptions implicit in the derivation of the Deutsch equation have resulted in limitations to its application. The most obvious objection to this type of model lies in the assumption of infinite transverse mixing, resulting in a uniform concentration profile across the duct. Also, non-ideal phenomena such as reentrainment, non-uniform particle distribution across the inlet, sneakage and electric wind cannot be included as individual mechanisms, but only as empirical corrections to the Deutsch exponent. Numerical simulation of precipitator operation overcomes some of the above problems, but introduces others such as discretisation errors and limitations imposed by computer storage space.

Williams and Jackson (1962) deduced from the earlier concentration measurements of Rose and Wood (1956) that dust is not perfectly mixed across a precipitator duct, but is remixed at a rate controlled by the turbulence in the gas stream. Based on this assumption, they developed the turbulent mixing theory where the dust concentration c, may be obtained from the mass balance of a rectangular element,

$$D \frac{\partial^2 c}{\partial z^2} - w \frac{\partial c}{\partial z} - U_o \frac{\partial c}{\partial x} = 0$$

with $D \frac{\partial c}{\partial z} = wc$ on the centreline, and $\frac{\partial c}{\partial z} = 0$ at $z = 0$

This is known as the convective-diffusion equation. Values of w were back-calculated from precipitators with known efficiencies, and D in the turbulent core was calculated from the expression

$$D = 0.071 U_o s_z (F)^{1/2}$$

where F = Fanning friction factor.

The efficiency was shown to increase along the length of the precipitator due to a build-up of particles close to the wall.

Feldman, Kumar and Cooperman (1976) used a similar approach to Williams and Jackson, but introduced into their boundary conditions the particle flux factor, f, as defined by equation 1.13, so that

$$D \frac{\partial c}{\partial z} = fwc \quad \text{at } z = 0$$

The convective-diffusion equation was solved numerically for cases of f = 0, 0.5 and 1 where f = 0 and f = 1 correspond to zero and total reentrainment respectively.

Extension of this model by Stock and Eschbach (1981) allowed particle migration velocities, w, to be calculated from first principles. The electric field calculations included particle space charge, but assumed the effect of ion space charge to be negligible. Also, electric field gradients in the x-direction were ignored, giving

$$E(z) = E_o + \int_{z.o} (q_p/\varepsilon_o) dz$$

where $q_p = 18 \varepsilon_o c(z) E_o / d_p \rho_p$ (Cm^{-3}),
E_o = applied voltage/wire-plate spacing (Vm^{-1}),
c(z) = particle conc. $(no.m^{-3})$.

This model involves an iterative procedure, since c(z) must be known (or estimated) before E(z) can be calculated.

Stock and Eschbach used their numerical scheme to predict a decrease in efficiency due to the introduction of wall strengtheners. The velocity profiles for this geometry were generated by a numerical code, as used by Barriga (1978). Subsequent work by Eschbach and Stock (1981) suggested that increasing the dust loading in a precipitator increased its efficiency. Hence, it may be possible to increase plate spacing and thus reduce specific collection area, resulting in cheaper precipitators.

Leonard, Mitchner and Self (1980) provided a detailed analytical examination of the collection region of a two-stage precipitator, as shown in Figure 1.12. Particle motion was described by the convective-diffusion equation, including longitudinal and axial diffusion terms,

$$U_o \frac{\partial c}{\partial x} + w_e \frac{\partial c}{\partial z} - D\left[\frac{\partial^2 c}{\partial x^2} + \frac{\partial^2 c}{\partial z^2}\right] = 0 \qquad (1.14)$$

where w_e is the net particle velocity towards the collection plate due to electrical drift and turbulent diffusion given by,

$$w_e = w - \frac{D}{c}\frac{\partial c}{\partial z}$$

The electric field for such a configuration is uniform (not taking account of space charge effects), and only provides a crude approximation to a wire-plate system.

Equation 1.14 was solved using a separation of variables technique for both boundary conditions $c = 0$ and $\frac{\partial c}{\partial z} = 0$ at the collection wall. Leonard et al. showed that using $c = 0$ as the boundary condition predicted a mechanical efficiency far in excess of the expected value for their system, and therefore chose $c = 0$ as the more suitable

condition. The corresponding value of mechanical efficiency for a wire-plate system can be calculated to give a value close to that observed by Potter (1981), suggesting that the boundary condition is better represented as a combination of terms,

$$\frac{\partial c}{\partial z} + (1-\alpha)c = 0$$

where α is a constant with dimensions of length.

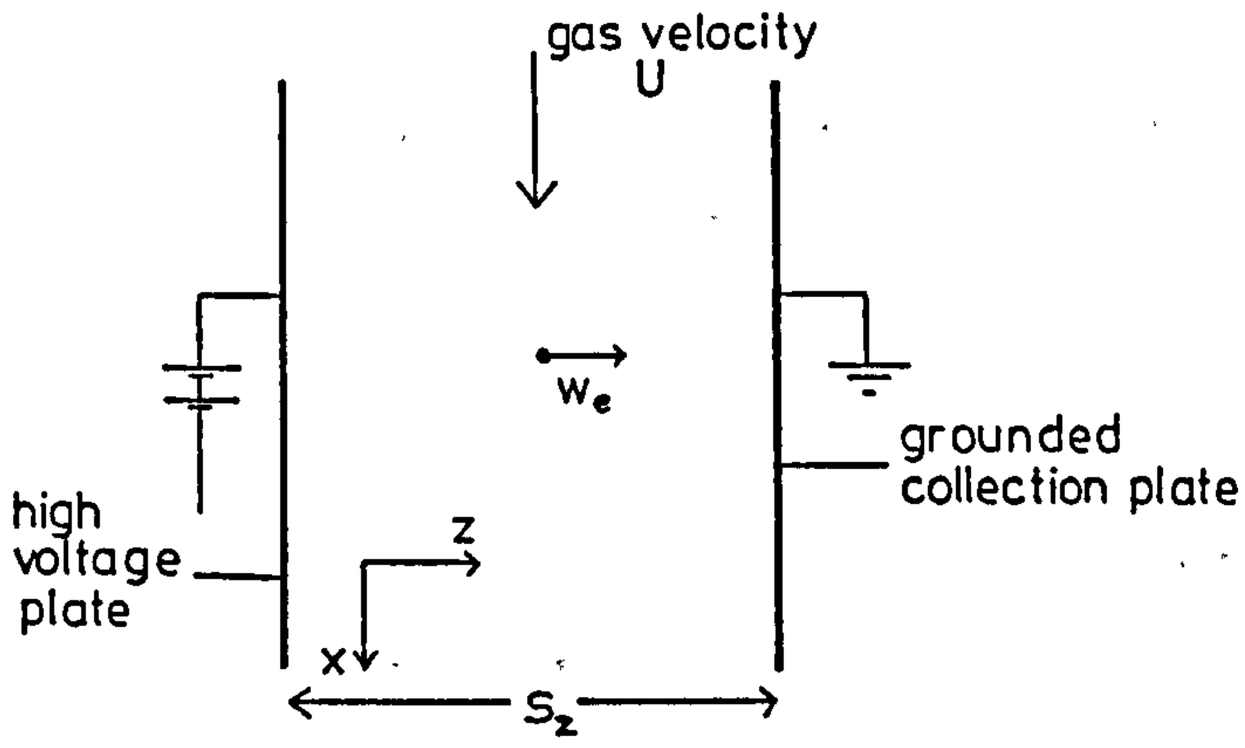

Fig. 1.12 Collection region of a two-stage precipitator

Numerical solution of the convective-diffusion equation using a Crank-Nicholson finite difference scheme showed the efficiency for finite values of D to be greater than that for infinite diffusion (Deutsch limit). This was suggested to be as a result of the higher particle concentration near the wall providing an increased flux of particles i.e. $c(d)w_e > cw_e$. In practice, higher efficiencies are not realised, probably due to non-ideal effects such as

reentrainment, sneakage and back-ionisation. Also, the diffusion coefficient in a typical wire-plate precipitator may be an order of magnitude greater than expected due to the effect of wall strengtheners, discharge wires and electric wind. Leonard et al. found the choice of a suitable value of D to be a major problem, and suggested using the relationship,

$$D = 150\ (\mu/\rho_f) = 2.25\times10^{-3}\ m^2/s$$

where μ = viscosity ($Kgm^{-1}s^{-1}$),
ρ = density (Kgm^{-3}).

A recent paper by Adam (1985) has emphasised the need for careful interpretation of the results of such numerical models. Spurious oscillations or "wiggles" of the numerical solution, due to the errors incurred during discretization of the differential equations, may cause concentration values to appear negative. An explanation of this phenomenon and methods for its elimination are explored by Adam.

Llewelyn (1982) started with an identical equation to that of Leonard et al., but retained full generality of the boundary conditions and diffusion coefficient values. The solution was found to be almost independent of longitudinal diffusion, so a simplified convective-diffusion equation was considered, namely

$$U_o \frac{\partial c}{\partial x} + w \frac{\partial c}{\partial z} = D_z \frac{\partial^2 c}{\partial z^2}$$

A solution was derived by substituting the scaling transformation c = (const) x exp(-wz/2) to eliminate the diffusion term, and using separation of variables techniques. Results predicted by the model suggested that

the precipitator efficiency could be increased by reducing lateral diffusion. The conflict with the theoretical predictions of P. Cooperman were shown to be due to his extremely high lateral diffusion coefficient value (0.1-1.0 $m^2{}_s{}^{-1}$).

G. Cooperman (1984) provided an extension to the theories of Leonard et al., Deutsch and P. Cooperman in the form of a generalised unifying theory. The convective-diffusion equation used by Leonard et al. was taken as a starting point, but with the theoretical migration velocity w_z replacing w_e. The solution was obtained for the set of boundary conditions as imposed by Feldman et al., including $D\frac{\partial c}{\partial z} = fwc$ at $z = 0$.

In terms of the three dimensionless parameters as defined by Cooperman, plus an additional parameter $\gamma = D_z/D_x$, the full general solution was

$$1-\eta = (\text{const}) \exp((\alpha-(\alpha^2+ \lambda_1{}^2+\beta^2/\gamma)^{1/2}))$$

where const = 1 ..... for $\beta/\gamma << \pi/2$

= $((2\pi)^{1/2}\ \gamma/\beta)^3 \exp(\beta/\gamma)$ ... for $\beta/\gamma >> \pi$

and $\tan \lambda_1 = \left(\frac{\beta}{\gamma}\right) \frac{2\ \lambda_1(1-f)}{1^2-(1-f)\beta^2/\gamma^2}$

Cooperman then succeeded in reducing this solution for various values of D_x and D_z with the following results:

a) $D_z >> 10^{-2}$ - P. Cooperman's equation, where efficiency is independent of transverse mixing, D_z.

b) $D_z >> 10^{-2}$ and $D_x << 1.8$ - Deutsch equation, where efficiency is independent of both D_z and D_x.

c) $D_z \approx D_x << 4x10^{-4}$ - Equation of Leonard et al., where efficiency is independent of longitudinal mixing, D_x.

G. Cooperman favoured the expression originally presented by P. Cooperman (1971), and suggested electric wind as the cause of such high effective diffusion coefficients. A new method was prescribed for practical sizing of precipitators, employing theoretical migration velocities and back-calculating diffusion coefficient values from measured efficiencies. Depending on the magnitude of D_z and D_x, the most suitable limiting form of the general equation could be used to calculate the optimum precipitator size. Cooperman assumed the calculation of migration velocity to be accurate since it is based on the verified Coulomb's and Stokes' laws. Whilst this is true, calculation of migration velocity also requires knowledge of particle charge which is not so easily defined. Consequently, theoretical migration velocity values cannot be obtained as confidently as suggested.

In suggesting this method, Cooperman has transferred the "fudge-factor" qualities of the effective migration velocity (as used in the Deutsch expression) to the diffusion coefficients. This may be avoided by acquiring knowledge of turbulent mixing in the duct. Any discrepancies between theoretical and measured efficiencies must then be accounted for by other non-ideal effects such as reentrainment, sneakage etc..

Samuel (1981) developed a novel but complex numerical simulation of the coupled electro-aerodynamic phenomena occurring within a precipitator. The model simulated the following mechanisms without the use of differential equations,

a) corona space charge density in the presence of air flow,
b) charging of particles and their subsequent drift in the electric field,
c) interaction amongst charged particles.

The major objection to this theory is the assumption of a fully developed Poisueille velocity profile in the duct, a consequence of which is that any turbulence-induced phenomena are neglected.

A combination of theoretical and empirical expressions were used by Lawless, Dunn and Sparks (1981) to calculate the progression and collection of particles along a precipitator duct. They assumed the inlet concentration to be a series of adjacent particle sources with finite breadth, $(z_2-z_1)_{x=0}$, which were capable of diffusing in a transverse direction only. After time t, the spread of the sources was calculated from the following expression:

$$c(z,w,t) = c_o/2\ (\mathrm{erf}((z_1-(z-wt))/(4Dt)^{1/2}) - \mathrm{erf}((z_2-(z-wt))/(4Dt)^{1/2}))$$

where $t = h/U_o$ (s),

h = grid spacing in x-direction (m),

U_o = gas velocity

w = particle source velocity in z-direction (ms^{-1}).

The concentration arriving at the next grid is assumed to be evenly distributed, and acts as source for the next time interval, t. Particles reaching the wall are assumed to be collected.

This type of model allows for the inclusion of empirical data such as turbulent diffusion coefficients and velocity profiles, without the additional complications of finite difference methods. It also presents the possibility of keeping a record of particle history which may be important when dealing with non-uniform electric field conditions. The computer storage space necessary for such calculations would be very large.

CHAPTER 2

DESCRIPTION OF PILOT SCALE PRECIPITATOR

2.1 Precipitator duct

A pilot scale rig was designed to simulate an industrial precipitator as closely as possible. The aim of the project was to investigate mechanisms affecting particle motion in a precipitator. The experimental methods used to achieve this required easy access to internal components of the precipitator and stringent safety precautions. The basic components of the rig had been assembled for a previous project, but extensive modifications were required before experimental work could be carried out.

Figure 2.1 shows a plan of the room in which the rig was built, and includes some of the safety devices described in Section 2.3.

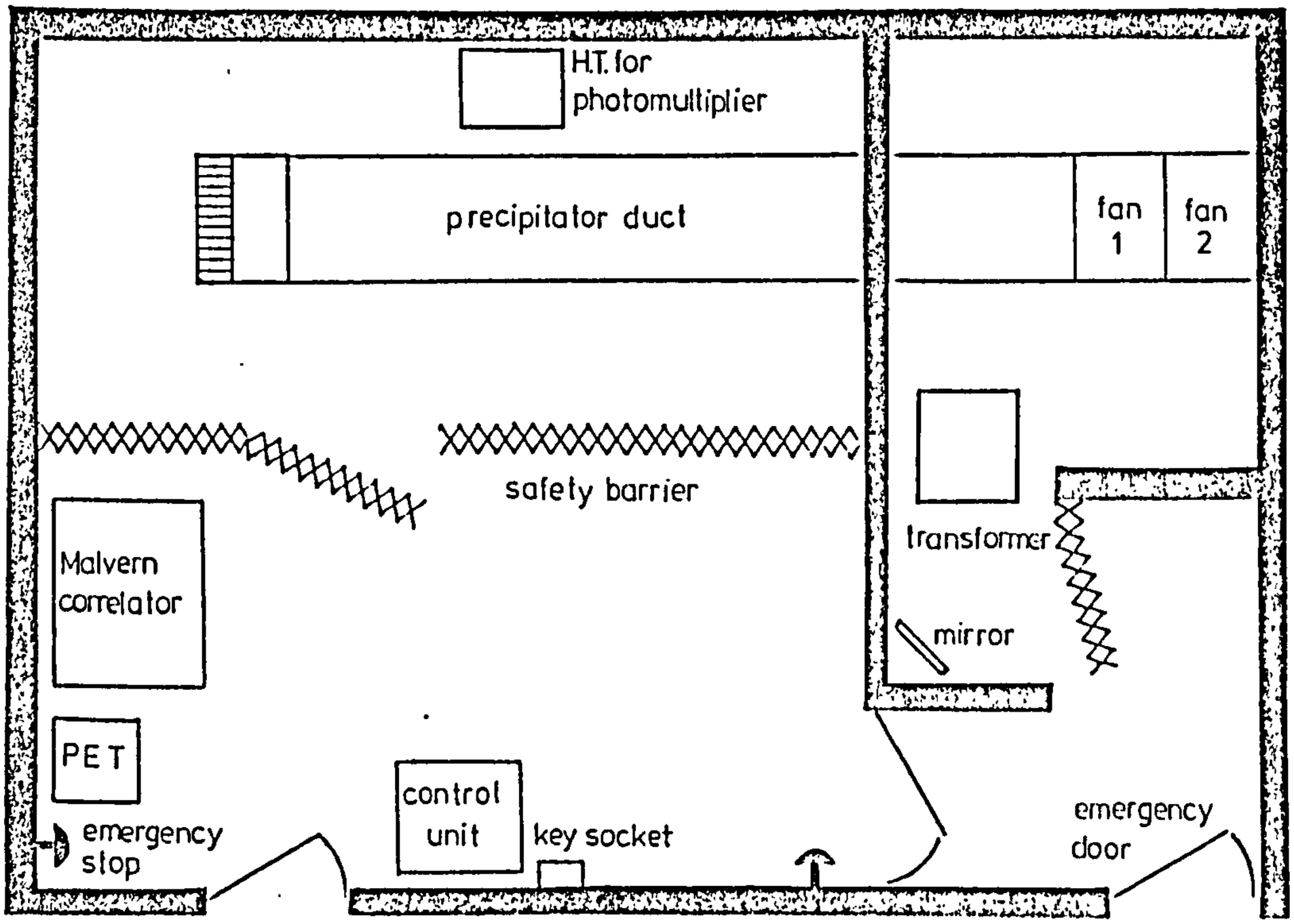

Fig. 2.1 Plan of laboratory containing pilot-scale precipitator

Figure 2.2 shows the internal components of the precipitator. The precipitator walls (dimensions 3 x 0.5m), L-shaped wall strengtheners (dimensions 35 x 50 mm) and discharge electrodes were supplied by Lodge Cottrell Ltd.. Various designs of discharge electrodes were used, including twisted square and sawtooth geometries. The electrodes were spaced at 0.23 m intervals along a support bar, which was filed smooth to prevent spurious corona discharge. The support bar was suspended from several removable glass plates (dimensions 0.5 x 0.5 x 0.01m) which were placed along the top of the precipitator. The bolts used to fix the support bar to the glass plates were completely covered in silicone rubber to contain any corona discharge. Glass plates were also fixed with silicone rubber to the underside of the duct, providing electrical insulation as well as a transparent medium for flow visualisation techniques.

The spacing between the duct walls could be varied, but for the purposes of this work it was fixed at 0.3 m. The incorporation of wall strengtheners, spaced at 0.9 m intervals along the duct walls, allowed experiments to be conducted both with and without strengtheners. A wooden support frame was built around the precipitator walls. To simulate the operation of an industrial precipitator, the flow of gas was maintained down both sides of the earthed duct walls. This also had the advantage of minimising any disturbance to the flow field, caused by the presence of holes in the walls. Legs were attached to the support frame, raising the duct 1 m from the ground.

Uniform flow conditions across the inlet were obtained by inserting a honeycomb mesh to break up any large scale eddies. The diameter of the individual hexagonal structures was 10 mm. Space was left behind the mesh for the optional insertion of vertical pipes. In industrial precipitators,

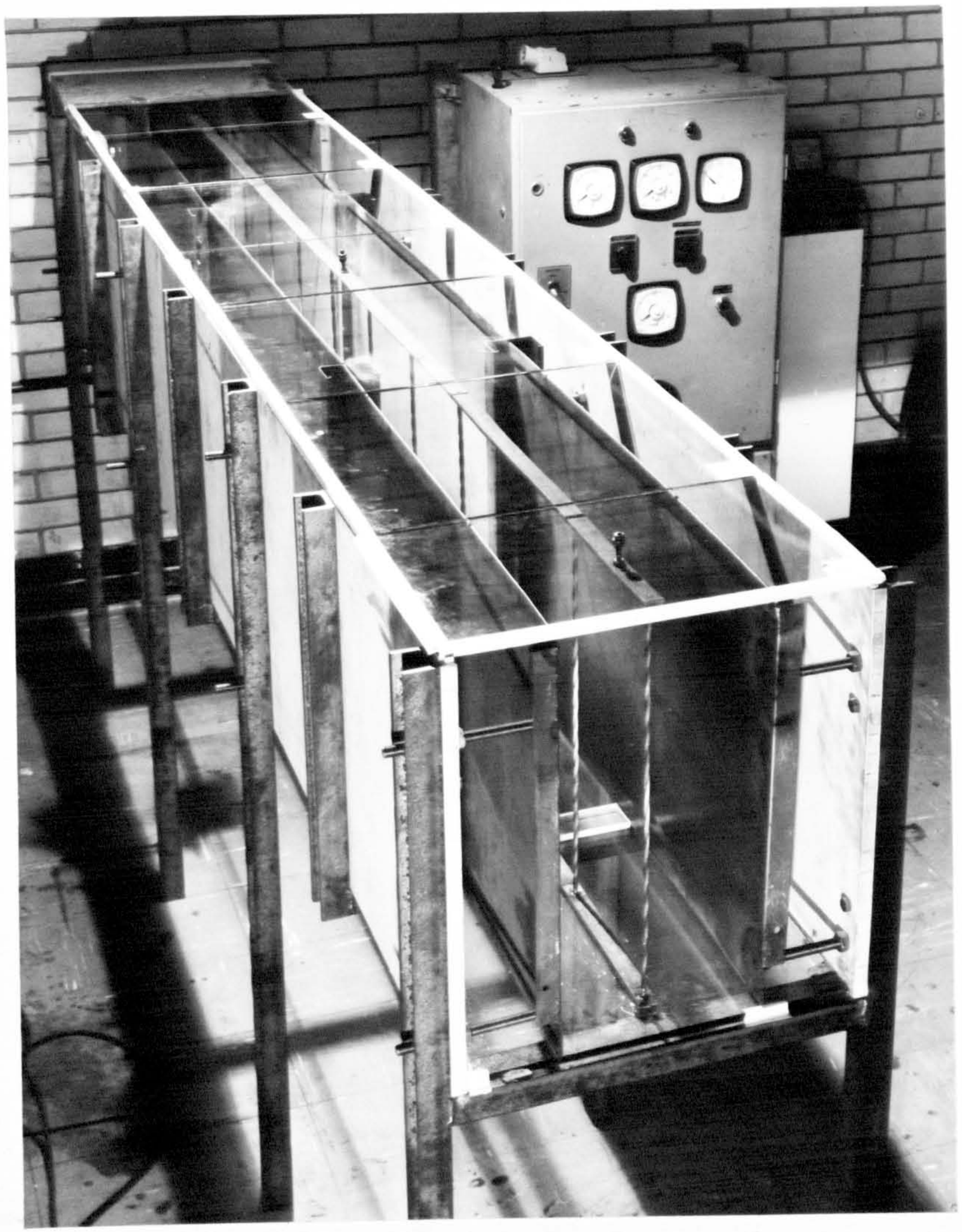

Fig. 2.2 Precipitator duct and power supply control unit

Fig. 2.5 Mechanical earthing device and transformer

such pipe arrangements are used to induce uniform flow conditions across the precipitator entrance, to prevent overloading a particular region. These flow modulation pipes are known to introduce turbulence into the precipitator and so their effect on performance is of interest.

Locations in the duct at which a range of experimental measurements were made throughout the work are shown in Figure 2.3.

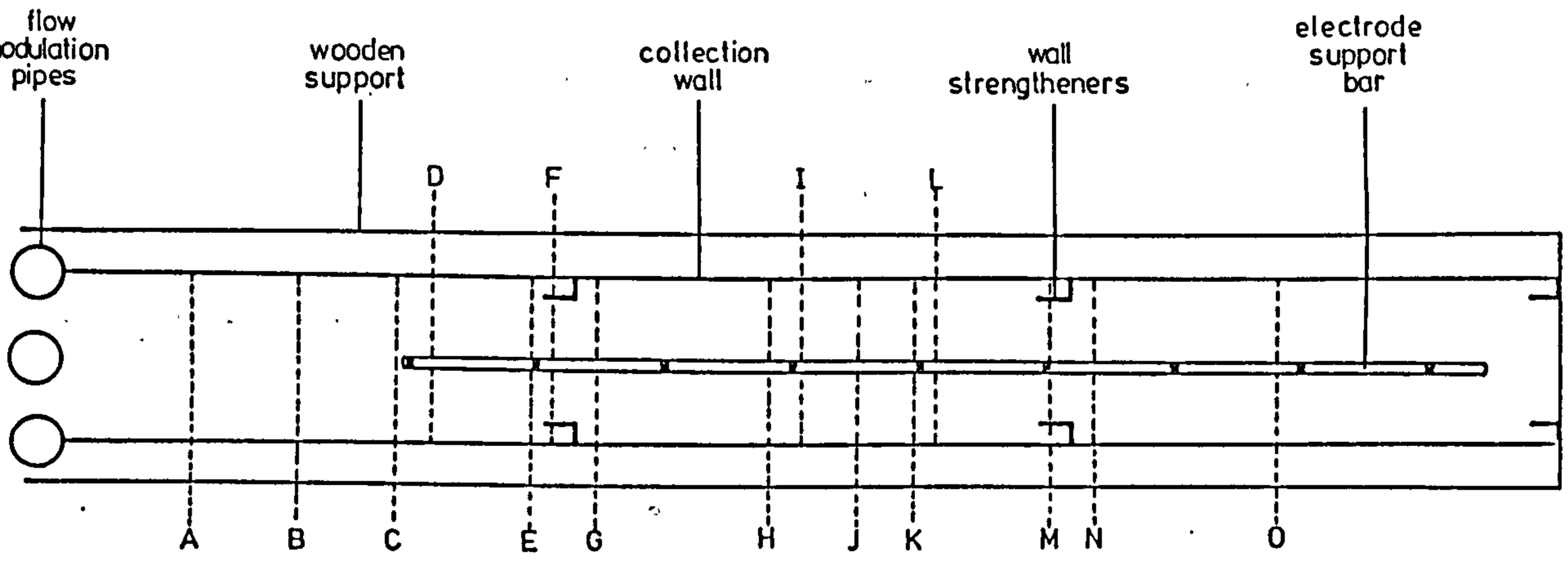

Fig. 2.3 Location of measurement positions in the precipitator duct

Positions A - O are described more precisely in Table 2.1.

A - 230 mm downstream of flow modulation pipes
B - 200 mm upstream of 1st electrode
C - 20 mm upstream of 1st electrode
D - 40 mm downstream of 1st electrode
E - 10 mm upstream of 2nd electrode
F - 40 mm upstream of 1st strengthener
G - 40 mm downstream of 1st strengthener
H - 350 mm downstream of 1st strengthener
I - 20 mm downstream of 4th electrode
J - Midway between 4th and 5th electrodes
K - 20 mm upstream of 5th electrode
L - 640 mm downstream of 1st strengthener
M - 40 mm upstream of 2nd strengthener
N - 40 mm downstream of 2nd strengthener
O - 40 mm upstream of 8th electrode

Table 2.1 Location of measurement positions along precipitator duct

Positions defined in Table 2.1 with respect to the strengtheners refer to the stem of the strengtheners.

Two fans were connected in series with a bag filter downstream of the precipitator. One of the fans was throttle controlled, enabling gas velocities of 1 - 6 ms^{-1} to be obtained in the duct. The filtered air expelled by the fans was released outside the building. Periodic removal of particles caught by the filters was carried out by shaking the bags.

2.2 Electrical components

The oil-submerged transformer and rectifying equipment, also supplied by Lodge Cottrell Ltd., were capable of providing voltages of -100 KV to the discharge electrodes.

In practice, electrical breakdown across the precipitator duct occurred at voltages approaching -70 KV. Consequently, most experiments were performed at -65 KV. A voltage divider, in the form of 40x10 MOhm resistors in series, was installed across the H.T. supply. This allowed the potential drop across a single 10 MOhm resistor to be used as a measure of the total voltage applied to the discharge electrodes. The dimensions of the voltage divider were sufficient to prevent sparkover, and all soldered joints were covered in a layer of silicone rubber to prevent spurious corona discharge.

Two diodes were soldered in opposite directions across the voltmeter terminals as protection against a current surge in the event of a sparkover. Figure 2.4 shows the characteristic V-I curve for the twisted square discharge electrodes. Ripple on the rectified voltage was measured, and found to be less than 10%.

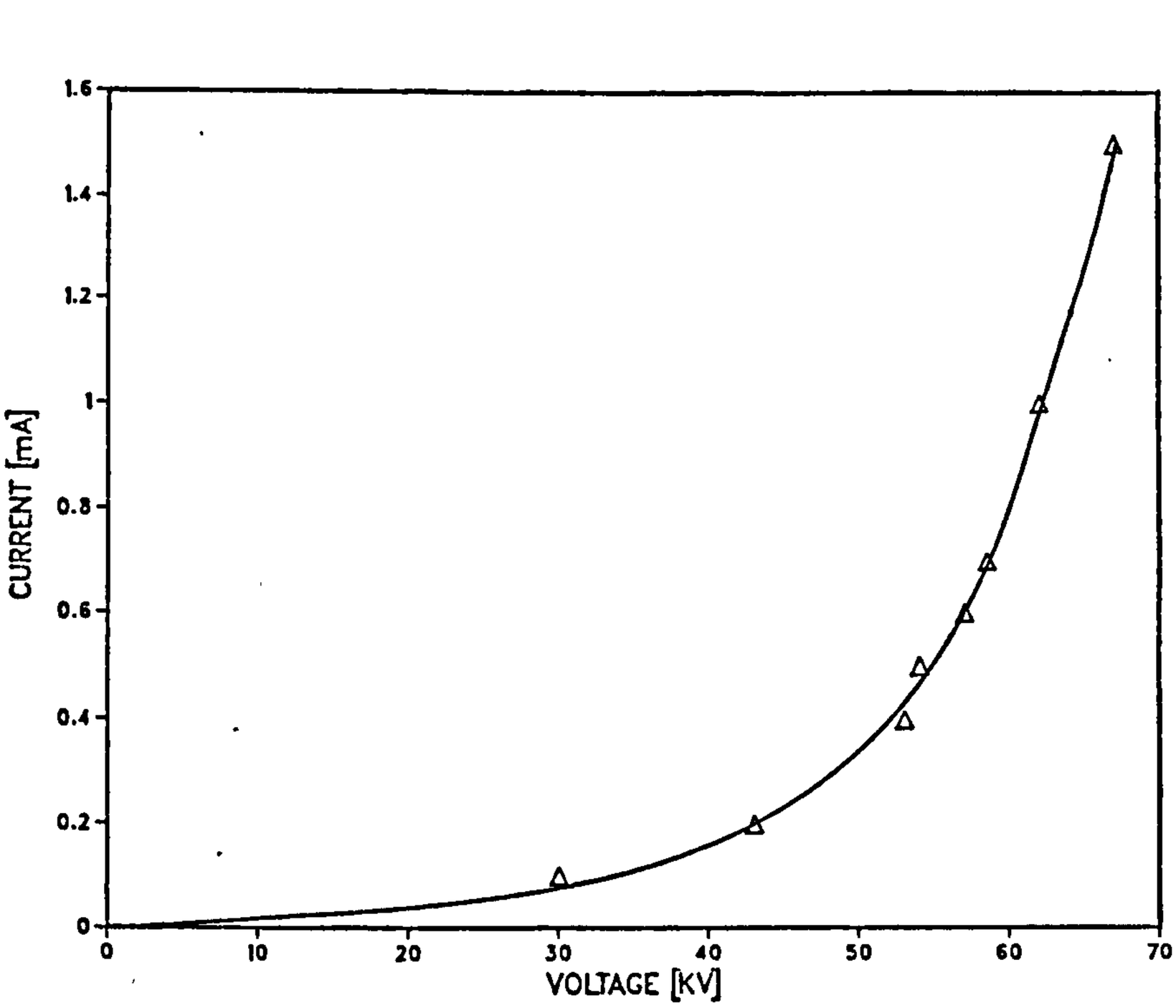

Fig. 2.4 V-I characteristics of twisted square discharge electrodes

2.3 Safety devices

Safety devices installed in the rig included a mechanical earthing system (as shown in Figure 2.5), interlock barriers and two emergency stop buttons. The earthing device consisted of a d.c. solenoid, which when activated (by turning the isolation switch on) lifted the earthed arm away from the output terminal of the transformer. Turning the isolation switch off caused the arm to fall back onto the transformer and the system to be safely earthed. It was necessary to ensure that the distance between the raised earthed arm and the transformer terminal was sufficient to prevent sparkover. Since the transformer was situated behind safety barriers in a separate room, a strategically placed mirror was required to check the earthing system for failure before entering the transformer section.

A safety barrier of height 1.4 m was built around the precipitator duct and transformer sections of the rig. An Interlock system was devised to ensure that the key for the isolation switch could only be removed from its socket if the keys for both gates were already in their sockets. The keys could only be removed by shutting and locking the gates. Emergency stop buttons were situated at convenient positions so that all electrical equipment, except the room lighting and fans, could be turned off immediately.

2.4 Additional features

A platform was built above the precipitator duct, as shown in Figure 2.6, capable of supporting the helium-cadmium laser and photomultiplier tube (hereafter referred to as P.M.T.). Two-dimensional movement of the platform allowed accurate positioning of the laser and P.M.T. for laser-Doppler photon correlation work. Motion across the

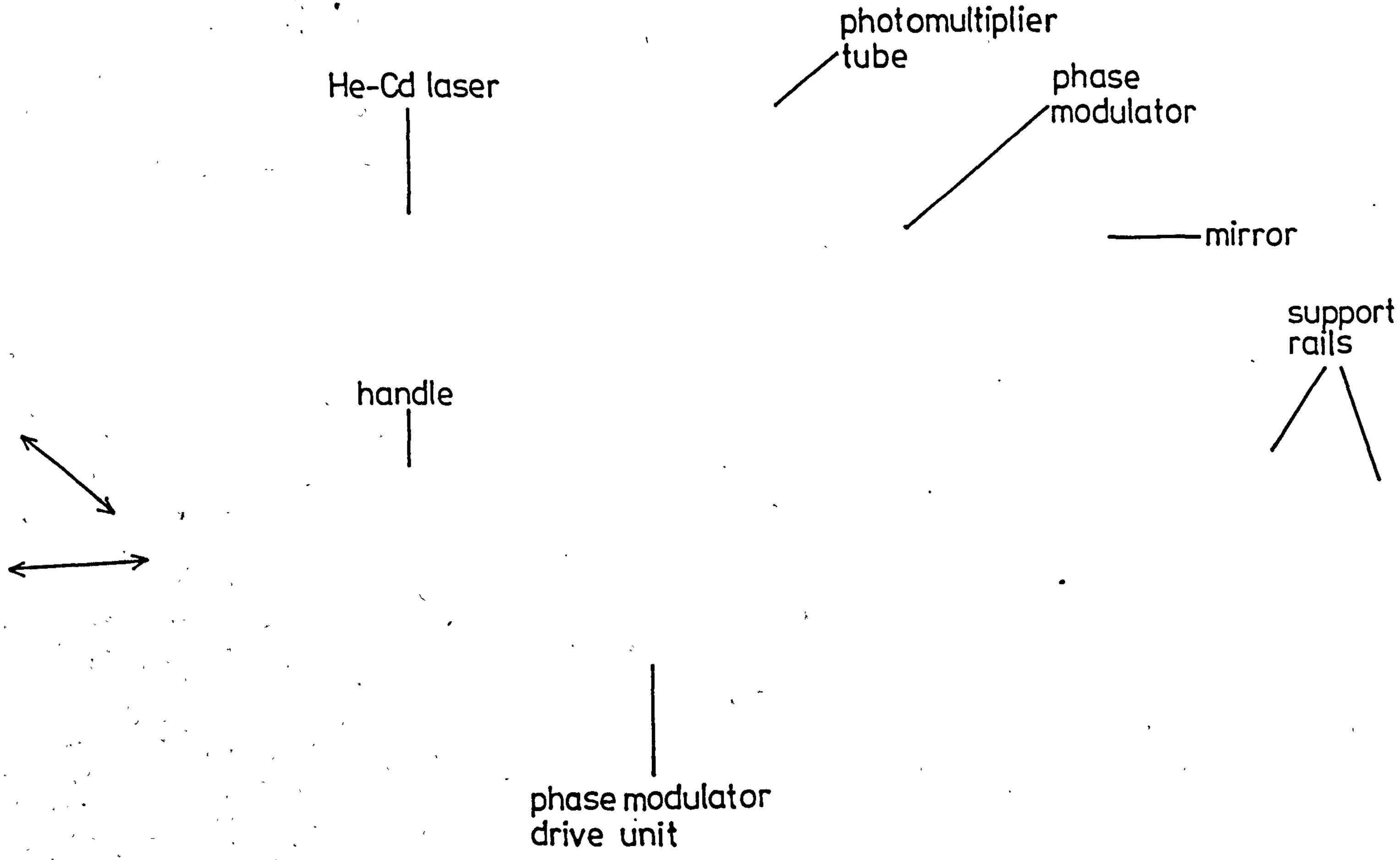

Fig. 2.6 Laser-Doppler photon correlation equipment

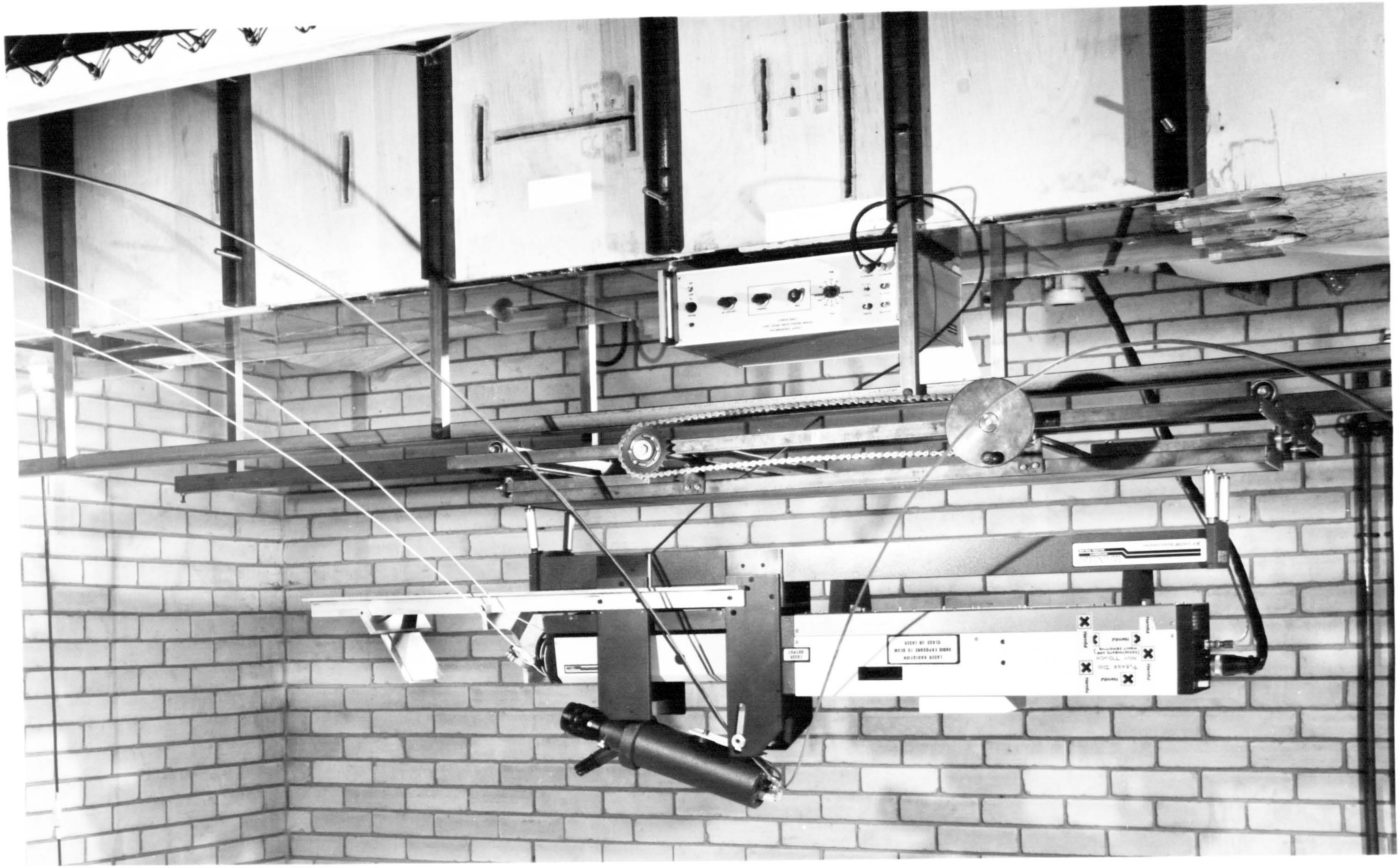

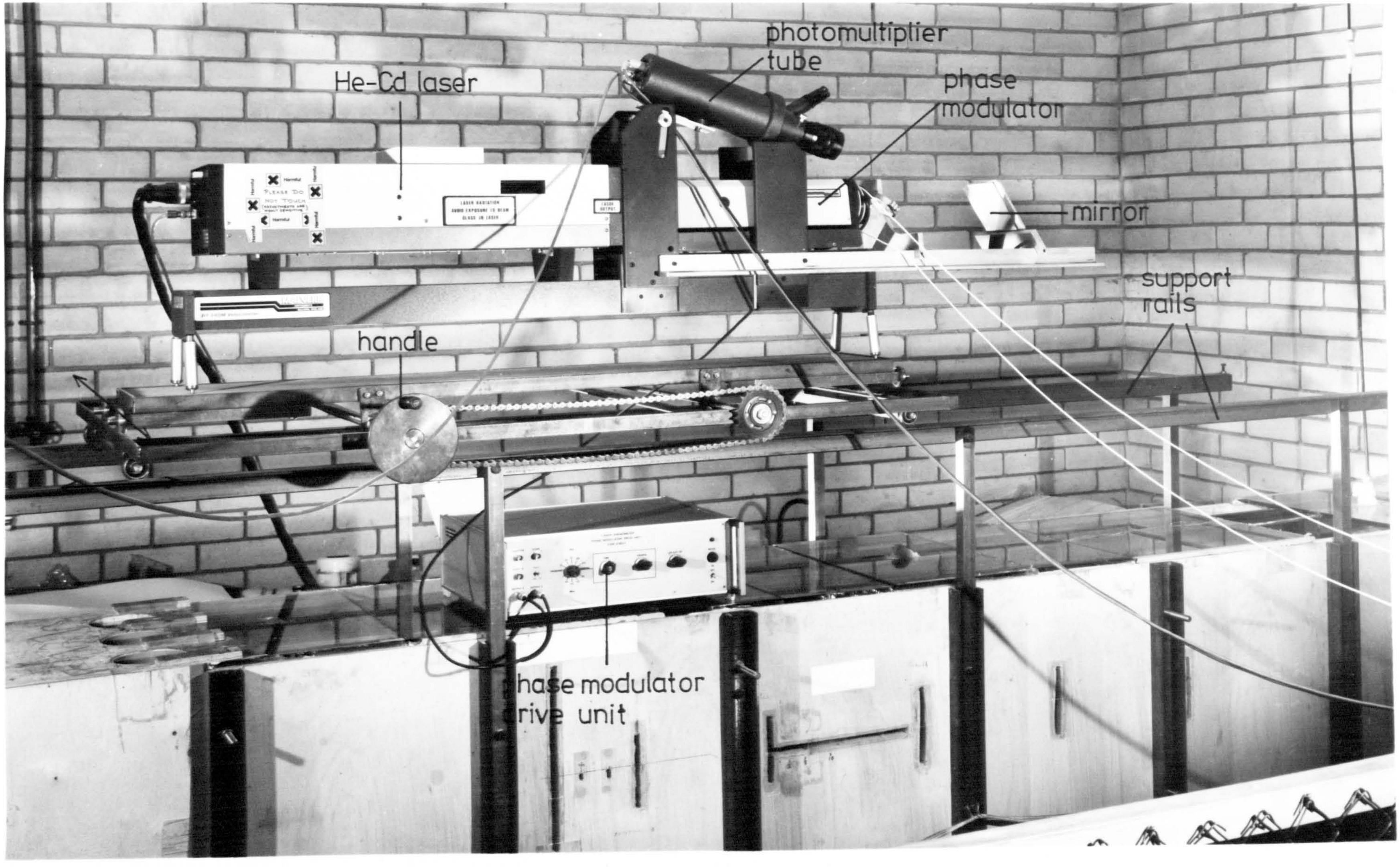

Fig. 2.6 Laser-Doppler photon correlation equipment

duct was controlled by a screw mechanism, which could be operated from the safe side of the barrier. The platform was capable of traversing the duct in 1.54 mm steps, each increment corresponding to a single turn of the handle. The platform was supported by a substantial frame built onto the rig to minimise the transmission of vibrations. Two horizontal rails, extending along the length of the duct, were bolted to the legs of the rig. The frame was supported on these rails by a system of wheels, allowing movement of the frame along the duct.

CHAPTER 3

STEADY STATE VELOCITY FIELD

3.1 Introduction

The gas velocity field is one of the most important factors affecting particle migration in an electrostatic precipitator. An increase in the mean gas velocity may produce some or all of the following effects;

a) reduction of particle residence time in the duct,
b) masking of the electric wind effect,
c) enhancement of dust re-entrainment from the duct walls,
d) change in the velocity fields associated with discharge electrodes, flow modulation pipes and wall strengtheners.

The effect of wall strengtheners on precipitator efficiency has been the subject of much debate over recent years. Although the strengtheners are expected to increase local levels of turbulence, Vincent (1971a,1980) has suggested that particle capture in the vortices formed downstream of strengtheners may be a cause of significant dust collection.

The work described in this chapter is a study of the steady state velocity field in the precipitator and how it is affected by the presence of discharge electrodes, flow modulation pipes and wall strengtheners. In several cases, comparisons are made between experimental data and theoretical predictions of velocity profiles. Flow visualisation techniques have been used to compare the effects of differently shaped wall strengtheners on the surrounding flow field. A simple method has been suggested for incorporating the flow field into a numerical model.

An advantage of numerical modelling over more traditional analytical approaches lies in the ability to incorporate local values of parameters such as gas velocity, electric drift velocity, dispersion coefficient and possibly electric wind. To use the numerical models to their full potential, realistic values of these parameters must be included. The work reported here was carried out to obtain such information.

3.2 Experimental procedures

In the following sections three experimental procedures used for measuring the velocity field in the precipitator duct will be described.

3.2.1 Hot-wire anemometry

Velocity profiles across the precipitator duct were measured using a DISA constant temperature hot-wire anemometer. This technique relies on a change in the rate of cooling of a hot wire when placed in a moving stream of fluid. As the temperature of the wire changes, so does its electrical resistance. A current passing through the wire is constantly modified to maintain the wire at a constant temperature. The magnitude of this compensating current is related to the instantaneous velocity of the fluid in a direction perpendicular to the axis of the wire. The DISA mean value unit averages the signal over a suitable time interval, enabling a mean velocity value to be determined. The incorporation of a linearising unit results in proportionality between the 0 - 10 V digital reading produced by the hot-wire anemometer and the fluid velocity.

A single-wire probe calibrated for a 0 - 10 ms^{-1} flow was inserted into the probe support and mounted through a hole cut in a perspex sheet. The perspex sheet was cut to

the same size as the glass plate it replaced to avoid any disturbance of the flow. A heavy stand was used to hold the probe support in a fixed position, thereby minimising the transmission of vibrations from the duct to the probe. The axis of the probe was positioned normal to the direction of gas flow and mean velocity values were measured over 100 second intervals. To minimise end effects, all velocity measurements were made in the horizontal plane bisecting the duct i.e. 250 mm below the top glass plates. Investigation of the velocity values in the boundary layer close to the walls was carried out by attaching a micrometer stepping device to the probe support, capable of delivering 0.1 mm steps.

The frequency distribution of eddy fluctuations in the turbulent flow was estimated from a trace of fluid velocity versus time. This was obtained by passing the linearised hot-wire anemometer signal through a high speed ultra-violet oscillograph recorder. Analysis of the trace permitted the determination of an average eddy frequency from which an estimate of the scale of turbulence could be made. To ensure that vibrations were not being transmitted from the duct, the probe support was inverted as in Figure 3.1.

Although still resting on the perspex sheet, the support was positioned so that the probe was outside the duct. With the gas inside the duct moving at a velocity of 2 ms^{-1}, a trace of the velocity fluctuations was recorded with the ultra-violet oscillograph recorder. Any vibrations experienced by the probe would have resulted in an oscillating signal. Since no such signal was observed, it was assumed that vibrations had been sufficiently damped by the use of a heavy support stand.

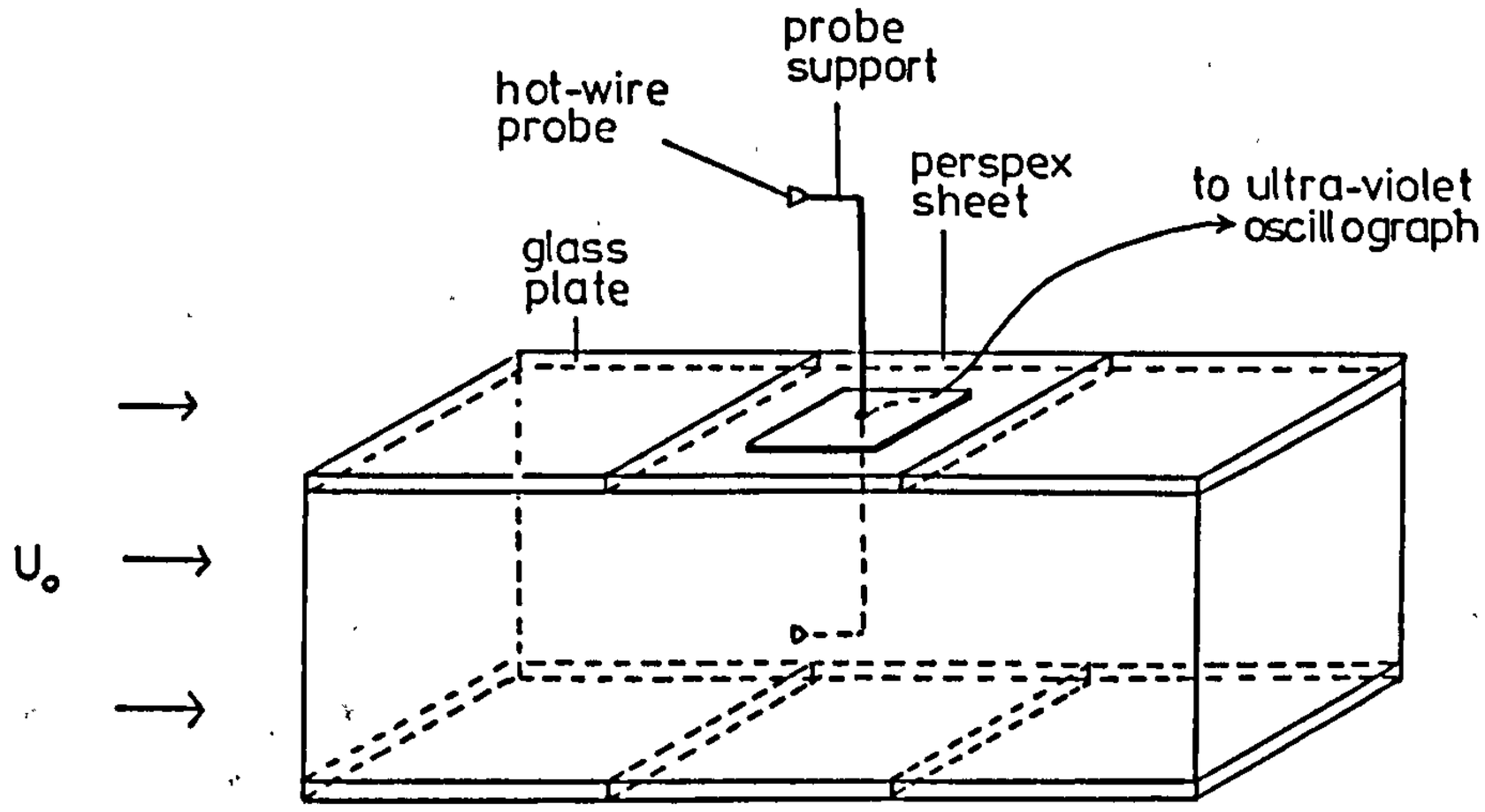

Fig. 3.1 Arrangement of hot-wire anemometer probe to test for vibration of duct

3.2.2 Laser-Doppler photon correlation

Average velocity and turbulence intensity profiles across the precipitator were measured using laser-Doppler photon correlation. This is a non-intrusive method which is ideal for measuring velocity and turbulence intensity values in hostile environments such as those found in a precipitator. Light from a 40 mW helium-cadmium laser was passed through a rotating beam splitter as shown in Figure 2.6. The resulting component beams were reflected into the duct by a front-silvered mirror angled at 45°. The region in which the laser beams crossed, producing an interference pattern in the form of a set of fringes, is known as the sensing zone. Location of the 1 mm^3 sensing zone could be accurately defined, and its motion was controlled by the screw mechanism described in Section 2.4.

The ability of the beam splitter to rotate through 360° allowed orthogonal velocity components to be measured, without realignment of the optics. The fringe spacing d_f depends on the angle between the component beams θ, and the wavelength of the light λ, so that

$$d_f = \lambda \sin\theta$$

To calculate a value of d_f the crossover point for the component beams was determined and the beam separation B measured at a distance A beyond the crossover point, as in Figure 3.2. An estimate of d_f was then obtained from the above equation where, for small θ, $\sin\theta \rightarrow B/A$.

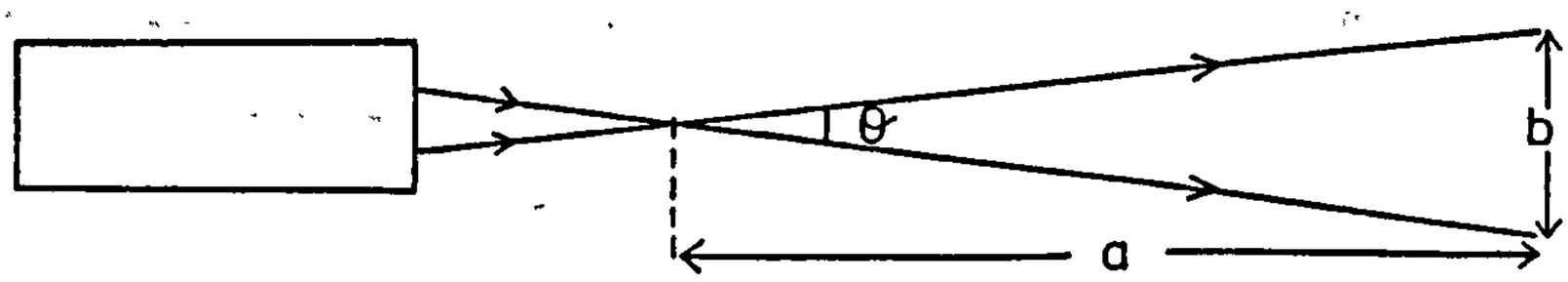

Fig. 3.2 Measurement of laser beam crossover angle, θ

Seeding of the flow was provided by the injection of a submicron corn oil aerosol (see Section 4.1.2.1). The relaxation time of the aerosol particles was sufficiently small to ensure close representation of the gas flow. As the aerosol particles travelled through the interference fringes, the back-scattered light was received by the P.M.T. mounted on top of the laser, as a series of light pulses. This information was transmitted to a Malvern Instruments Ltd. 7023 correlator which displayed the corresponding 96-channel autocorrelation curve.

The shape of the autocorrelation curve depends on the relationship between incoming data and that at subsequent times. Any random background noise which masks the signal will correlate to a constant value. This method of signal processing has the advantage of high sensitivity at low seeding particle densities, and is therefore ideal in back-scattering arrangements where the light intensity received by the P.M.T. is low. The use of back-scatter mode eliminates the need to realign the P.M.T. for every movement of the laser, thereby speeding up the rate at which measurements could be made.

Analysis of the autocorrelation function was performed using a computer program obtained from Malvern Instruments Ltd.. The program was modified to interface correctly with existing hardware. The first 48 channels of data were transferred from the correlator through an IEEE interface to a Commodore PET. The output from the program consisted of mean velocity and turbulence intensity values for each correlation curve.

The method of data analysis was valid for flow fields with turbulence intensity levels up to 15%. To aid in the measurement of highly turbulent flow fields, a phase modulator was incorporated into the laser-Doppler system. This imposes a temporal variation of sawtooth form onto the phase angle of one of the output beams, resulting in a linear motion of the fringe pattern across the sensing zone. If the fringes are arranged to move in the opposite direction to the mean gas flow, an apparent increase in the mean gas velocity occurs, resulting in a lowering of the turbulent intensity value. For the purposes of this work, a frequency shift of 0.2 MHz was found to reduce the effective turbulence levels sufficiently. This corresponds to an imposed fringe velocity v_{sh} of 4.32 ms^{-1}, as given by

$$v_{sh} = f d_f$$

where f = frequency of phase modulator (Hz).

3.2.3 Flow visualisation

Photographs and cine film of illuminated helium bubbles travelling along the precipitator duct provided a useful method for quantitative and qualitative analysis of the flow structure surrounding the wall strengtheners.

The helium bubbles were produced by an Armfield generator fed with a mixture of air, helium and soap solution. To ensure accurate representation of the flow field, neutrally buoyant bubbles were required. These were obtained by controlling the flow rates of helium and soap solution so that the weight of the soap in each bubble was offset by the low-density helium.

Optical access into the precipitator was provided by means of a mirror positioned at 45° above the duct. A 1 KW spotlight and two 2 KW photographic lamps were required in illuminating the bubbles sufficiently to produce high-contrast streak photographs. The lamps were positioned at a downstream location inside the duct to provide 90° illumination. Black velvet was draped at convenient locations in the duct to minimise background illumination.

3.3 Theoretical description of velocity fields

To include the effect of velocity into numerical models, a method for simulating realistic flow fields in the precipitator duct is required. The following section introduces some theoretical models capable of generating velocity profiles for various conditions. The predictions from these models are then compared with experimental

results enabling an assessment of their suitability to be made.

3.3.1 Flow over a flat plate

As a first approximation, the precipitator plates may be considered as flat, sharp-edged plates situated in a uniform stream of fluid with velocity U_o parallel to the plates, as shown in Figure 3.3. Since the fluid adjacent to the plate is necessarily at rest, the local velocity u_x must increase from zero at the plate to U_o at some point far out into the fluid stream. The region of fluid within which $u_x < 0.99U_o$ is known as the boundary layer. As the fluid progresses downstream from the leading edge of the plate, an increasing amount of momentum is lost from the fluid through the drag at the plate. The subsequent thickening of the laminar boundary layer may be described by the following relationship

$$z_b = 5(x\nu/U_o)^{1/2} \qquad (3.1)$$

where z_b = boundary layer thickness (m).

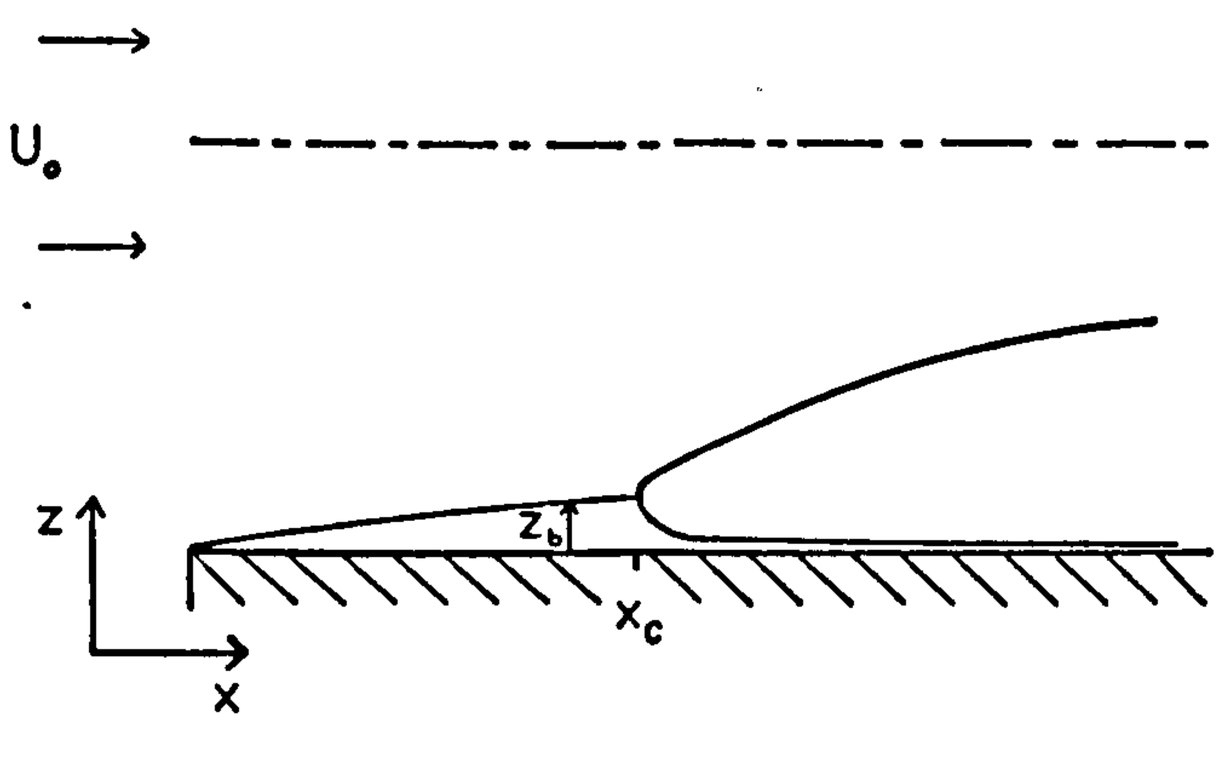

Fig. 3.3 Boundary layer development for flow over a flat plate

If the mainstream velocity is sufficiently high the velocity gradient in the boundary layer induces turbulence. Experiments have shown that for $Re_b > 1500$ (where Re_b is the Reynold's number based on the width z_b of the boundary layer), the boundary layer becomes unstable and eventually turbulent. Substitution of z_b from equation 3.1 gives the distance from the leading edge, x_c, at which the transition occurs as

$$x_c = 10^5 \nu / U_o$$

For rough plates or a blunt leading edge, this critical distance downstream x_c is decreased.

Davies (1972) has shown that the thickness of the turbulent boundary layer and the inherent velocity profiles may be described by the following relationships,

$$z_b = 0.376x(Re_x)^{-1/5} \qquad (3.2a)$$

$$u_x = U_o(z/z_b)^{1/7} \qquad (3.2b)$$

where $Re_x = U_o x/\nu$

At a distance x_{in} downstream from the duct inlet, the velocity profile becomes fully developed and remains the same for the rest of the duct (see Figure 3.4). An estimate of the minimum inlet length x_{in}, may be obtained by assuming that the turbulent boundary layer extends to a distance halfway across the duct at $x = x_{in}$. Substituting $z_b = s_z$ into equation 3.2a yields

$$x_{in} = 2.82s_z(Re)^{0.25} \qquad (3.3)$$

The effect of rough plates or a blunt leading edge will be to reduce the value of x_{in}, but no satisfactory method for correcting the inlet length has yet been developed.

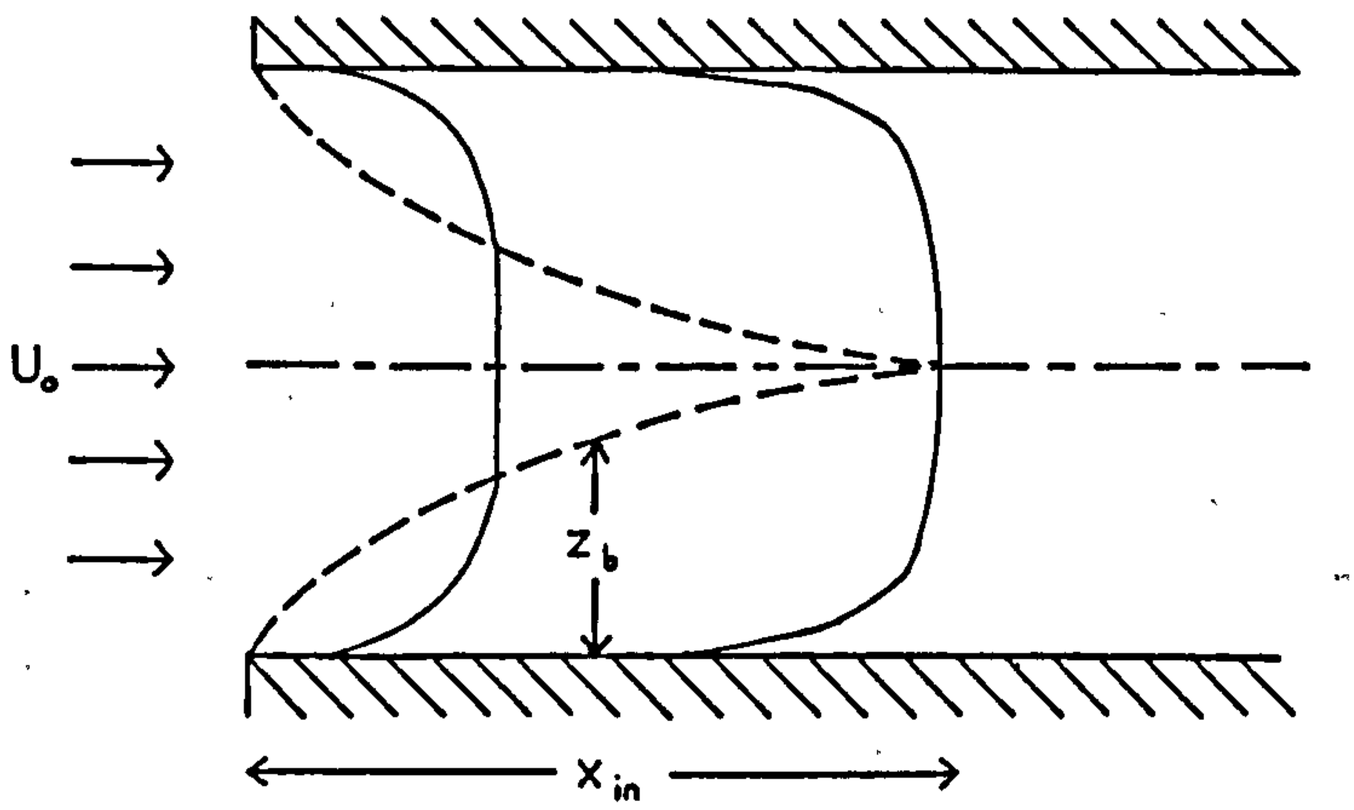

Fig. 3.4 Fully developed flow

Once fully developed turbulent flow has become established, the velocity profile across the duct may be described by the following expressions, known collectively as the Universal velocity profile,

$$u_x^+ = z^+ \qquad \text{for } z^+ < 5$$
$$u_x^+ = 5\ln(z^+) - 3.05 \qquad \text{for } 5 < z^+ < 30$$
$$u_x^+ = 2.5\ln(z^+) + 5.5 \qquad \text{for } z^+ > 30$$

The dimensionless velocities and distances, u_x^+ and z^+ are defined by

$$u_x^+ = u_x/v^* \quad \text{and} \quad z^+ = zv^*/\nu$$

where v^* = friction velocity (ms^{-1}).

3.3.2 Flow around a cylinder

The flow field in an electrostatic precipitator is complicated by the presence of discharge electrodes, flow

modulation pipes and wall strengtheners. Theoretical models describing the flow field downstream of a cylinder may be useful in predicting the velocity profiles for such obstructions.

The fluid velocity in the wake of a cylinder is lower than the mainstream velocity. This velocity depression is caused by a loss of fluid momentum due to the drag on the cylinder. Schlichting (1962) derived an expression describing the velocity profile in a two-dimensional wake behind a single body of diameter a (see Figure 3.5). The theory was based on Prandtl's mixing length hypothesis and consequently predicts a wake of finite width. For large values of x, where $U_o - u_x$ is small,

$$\frac{U_o - u_x}{U_o} = \frac{(10)^{1/2}}{18\beta} \left(\frac{x}{C_D a}\right)^{-1/2} (1-(z/b)^{3/2})^2 \qquad (3.4)$$

where b = half-width of wake (m),

β = 1/b

l = Prandtl mixing length (m),

z = transverse distance from axis of wake (m),

U_o = undisturbed velocity (ms^{-1}),

C_D = drag coefficient

= 1.41 for a cylinder.

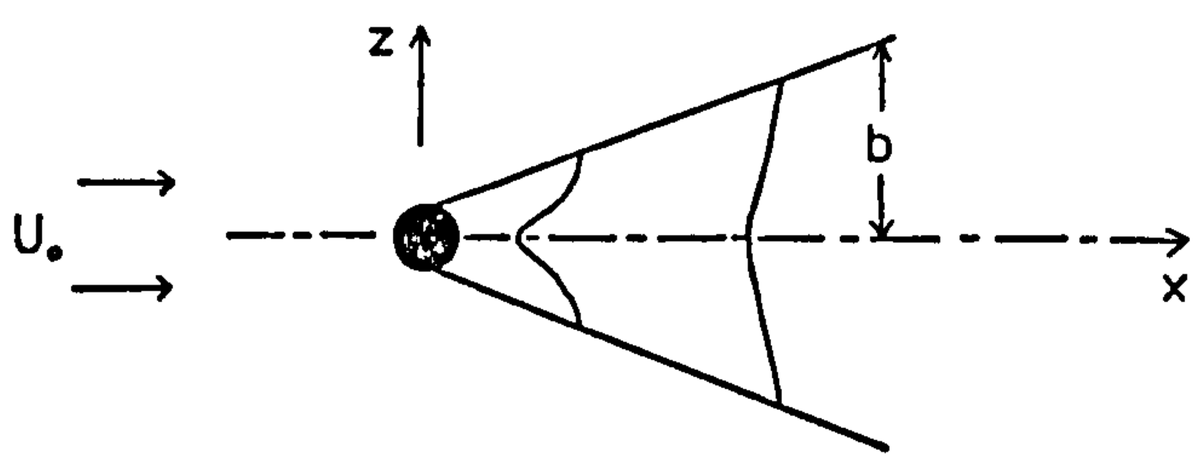

Fig. 3.5 Velocity profiles in the downstream wake of a cylinder

A value of 0.18 for β has been determined experimentally by Schlichting from measurements of b against x for wakes behind cylinders of different diameters. Davies uses a value of 0.22 for β in the theory of turbulent jets.

Brauer (1982) showed through theoretical and experimental investigation, that different types of vortices are formed downstream of a cylinder, depending on the Reynold's number Re_a, associated with the cylinder diameter;

$6.23 < Re_a < 50$ - steady double vortex (see Figure 3.6)
$50 < Re_a < 160$ - unsteady double vortex
$160 < Re_a$ - unsteady single vortex.

For a single 5 mm diameter discharge electrode in a 2 ms^{-1} velocity field, $Re_a = 667$ suggesting the presence of an unsteady single vortex. In this case there will be periodic formation and detachment of the vortices.

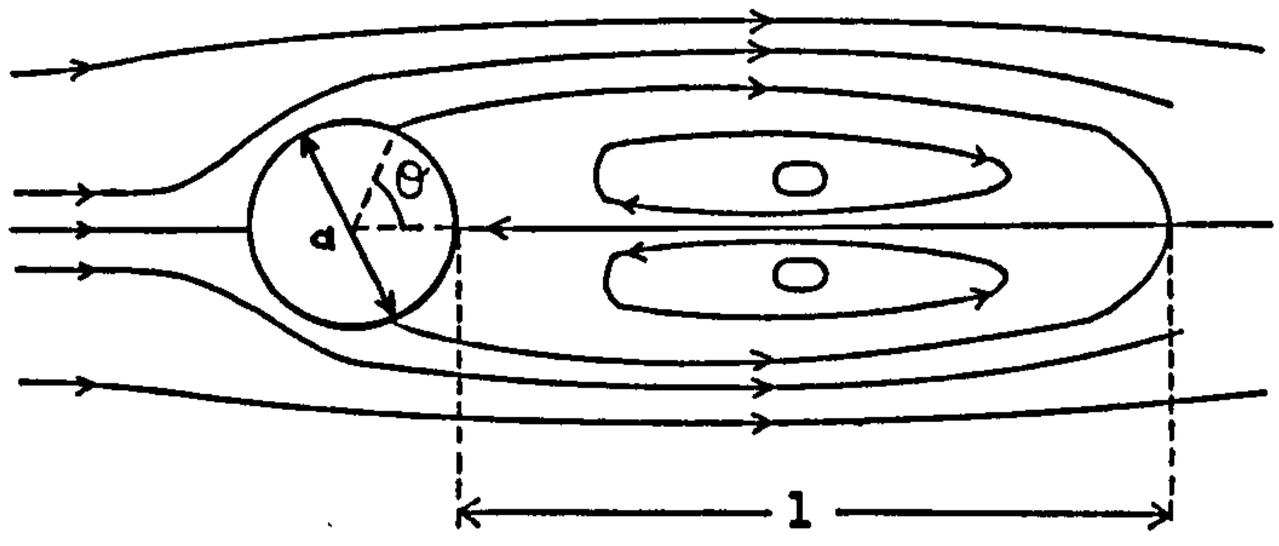

Fig. 3.6 Steady double vortex formation downstream of a cylinder

Brauer determined empirical expressions for the angle θ, at which the fluid separates from the cylinder wall, and the dimensionless length of the vortex $l^+ = l/a$ such that

$$\theta = 40.4(\ln[Re_a] - 1.83)^{0.436}$$

$$1^+ = 0.12Re_a - 0.748$$

For Re_a = 667, as calculated for a single 5 mm discharge electrode, this yields $\theta = 79^o$ and 1 = 0.2 m. For an axial spacing of 0.23 m down the duct, this calculation shows that the vortex almost extends downstream to the next electrode.

3.3.3 Flow past a row of cylinders

Sclichting showed that the wake formed behind a row of cylinders of diameter a, and pitch λ, is closely related to the wake behind a single cylinder (see Figure 3.7).

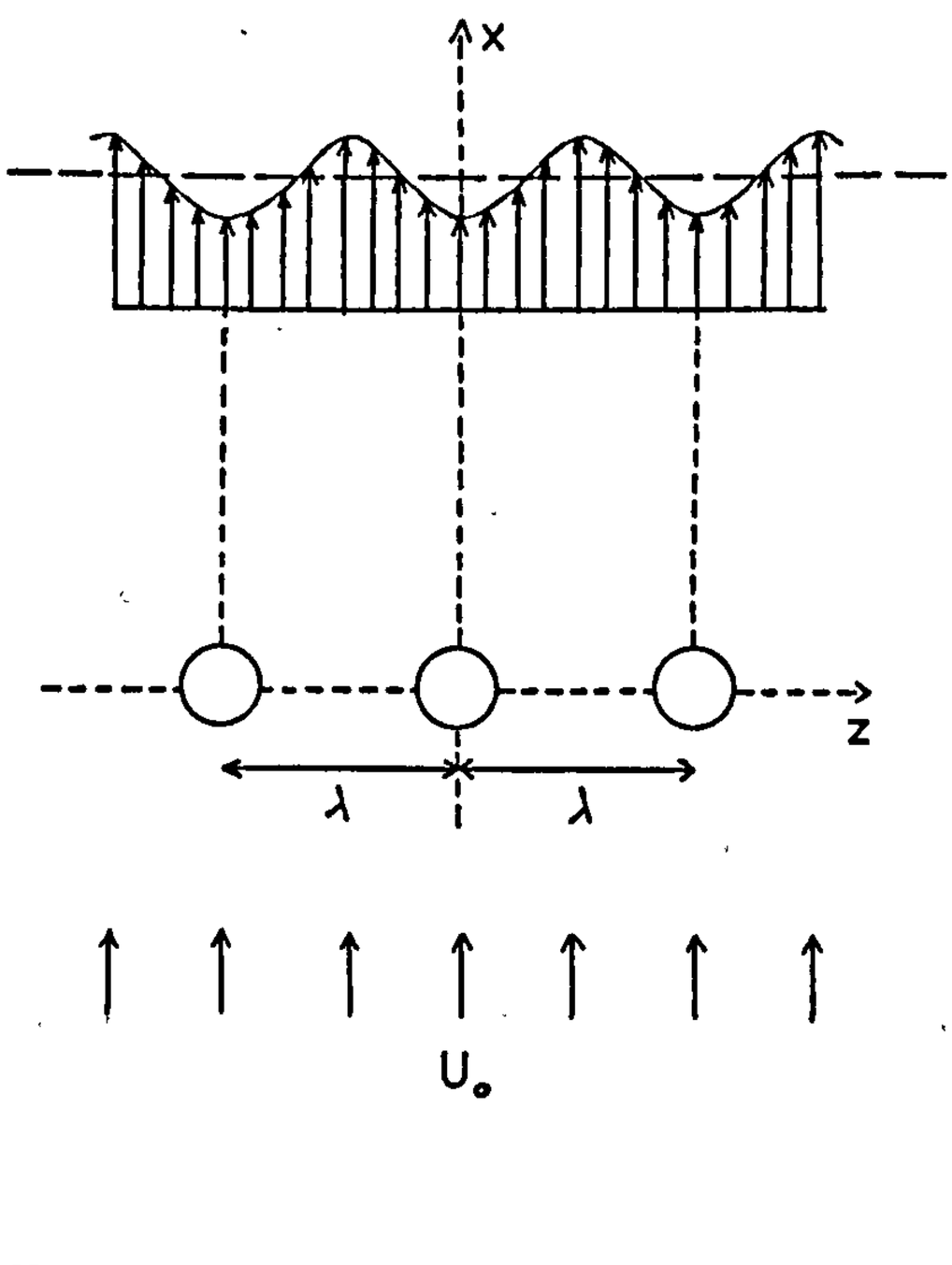

Fig. 3.7 Velocity profiles downstream of a row of cylinders

As expected, the velocity distribution is a periodic function of z, with period λ . For $x/\lambda > 4$, the velocity profile was expressed as follows:

$$\frac{U_o - u_x}{U_o} = (1/8\pi^3)(\lambda/1)^2(\lambda/x)\cos 2\pi(z/\lambda) \qquad (3.5)$$

This equation suggests that for a given distance downstream x, as the ratio $\lambda/1$ increases, the velocity depression becomes more pronounced. Schlichting used a value of $1/\lambda = 0.103$ for the case where $\lambda/a = 8$.

An attempt has been made to use this theory to predict the velocity profiles downstream from the flow modulation pipes at the inlet of the precipitator. Approximating the mixing length as half the distance between the pipe edges gives

$$1 = 0.5(\lambda - a)$$

$$\Rightarrow \quad 1/\lambda = 0.5(1 - a/\lambda)$$

Substituting a = 0.1 m and λ = 0.152 m into this equation yields a value for the ratio $1/\lambda = 0.17$. Velocity profiles were calculated at distances of 0.1 and 0.6 m downstream from the flow modulation pipes. As the flow progresses downstream, Davies suggested that the mixing length will increase according to the following,

$$1^2 = 10\,\nu\, x/U_o$$

This relationship was used to calculate a value of $1/\lambda$ =0.416 at x=0.6 m from the ratio $1/\lambda$ estimated at x=0.1 m.

Barriga (1978) studied the flow field surrounding a straight wall strengthener, and compared the results with the predictions of various computational fluid dynamic models. A maximum in turbulence intensity was found to

occur in the recirculation zone at a distance downstream equivalent to the height of the strengthener. For strengtheners spaced at realistic distances along the duct, the flow structure was shown to remain unaltered from cell to cell after the 5th strengthener. Barriga suggested that the amount of turbulence produced by the wall strengtheners overwhelms the effect of the inlet flow conditions on the recirculation zone. Investigation of the numerical flow field solution showed the recirculation zone between the 6th and 7th strengtheners to extend a distance three times the strengthener height.

3.4 Results and discussion

The following results were measured at locations referred to in Figure 2.3. The integration time over which the velocity values were averaged was similar for both hot-wire anemometry and laser-Doppler photon correlation techniques, but the laser-Doppler method was much slower at producing results due to the necessary transfer and analysis of data in the computer. On the other hand, the fine wire probes used by the hot-wire anemometer were extremely delicate, and renewal was costly. Also, since a DISA r.m.s. velocity analyser was unavailable, reliable turbulence intensity data could only be supplied by the laser-Doppler technique. Taking these points into consideration, hot-wire anemometry was employed for the majority of the velocity profile work where mean axial velocity components were required. Laser-Doppler photon correlation was used in cases where more detailed analysis of the flow structure was required, such as turbulence intensity and transverse velocity components.

3.4.1. Effect of flow modulation pipes

Velocity profiles were measured at Position B in the duct with and without the 0.1 m diameter flow modulation pipes installed. Velocity values were obtained across the whole width of the duct using the DISA hot-wire anemometer. Comparison of the profiles in Figure 3.8 shows that the flow modulation pipes remove velocity gradients, resulting in a flat profile.

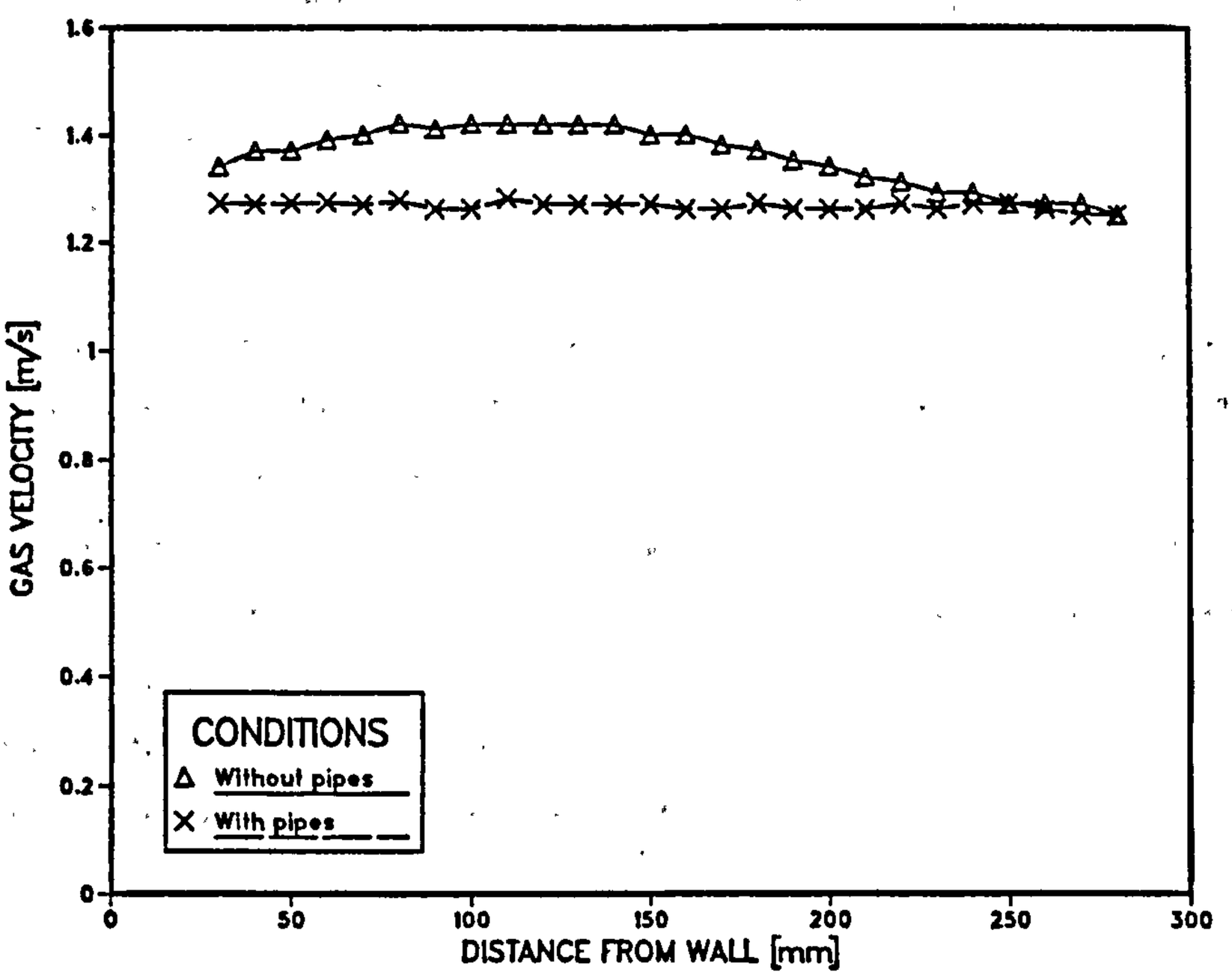

Fig. 3.8 Effect of flow modulation pipes on velocity profile

Since any disturbance to the flow field as predicted by Schlichting in equation 3.5 has disappeared at a distance of approximately 0.4 m downstream from the flow modulation pipes, the inlet velocity profile was assumed to be uniform. The pressure drop across the pipes causes a reduction in the average velocity from approximately 1.35 to 1.27 ms^{-1}.

3.4.2 Simple flat plate system

Following the experimental procedure described for hot-wire anemometry in Section 3.3.1, a detailed velocity profile was measured at Position K. The mainstream gas velocity was approximately 1.4 ms^{-1}, and as with all hot-wire anemometry measurements, the applied voltage was zero. With the 0.1 m flow modulation pipes installed, but without the wall strengtheners, the velocity profile was as shown by the solid curve in Figure 3.10. The velocity gradient close to the wall is very steep with the turbulent core appearing to start at $z^+ = 970$. The velocity depression at the centre of the duct can be attributed to the cumulative wake effect behind the discharge electrodes.

Calculation of the inlet length x_{in} from equation 3.3 shows the transition to fully developed turbulent flow to occur at a distance of approximately 5.5 m from the inlet. Due to the presence of the flow modulation pipes and slightly rough walls, this is likely to be a considerable overestimate of x_{in}. To verify whether this is the case or not, theoretical velocity profiles assuming $x > x_{in}$ and $x < x_{in}$ were compared to the experimental data for $x = 1.5$ m.

a) $x > x_{in}$

In the case of fully developed turbulent flow, the velocity profile may be described by the Universal velocity profile, as defined in Section 3.3.1.

b) $x < x_{in}$

The thickness of the developing turbulent boundary layer may be calculated from equation 3.2(a) where

$$z_b = 0.376x(Re_x)^{-1/5}$$
$$= 0.0527 \text{ m}$$

Substituting this value into equation 3.2b enables velocity values to be calculated.

Comparison of the theoretical and experimental velocity profiles close to the wall is shown in Figure 3.9. The theoretical velocity profiles are shown as broken lines. Although discrepancies occur around the region $50 < z^+ < 100$, the agreement between the Universal velocity profile and the experimental data for small values of z is good.

To incorporate the velocity depression downstream of the discharge electrodes, the expression derived by Schlichting (equation 3.4) was applied. To estimate the cumulative effect of several electrodes in series, the velocity profile resulting from the first electrode was used as the flow field incident onto the second electrode. Repeating this procedure for the first four electrodes allowed the velocity profile corresponding to a position 20 mm upstream of the 5th electrode to be calculated. Table 3.1 shows the velocity values calculated in this way for β = 1.0. Such a high value of β is justified by the presence of the twisted-square profile discharge electrodes. These will cause a greater disturbance to the flow than smooth cylinders, as assumed in the theory.

Figure 3.10 shows the complete velocity profile calculated from the superposition of Schlichting's wake profile and the Universal velocity profile, compared with the experimental data. It is considered that the predicted velocity field adequately describes the experimental values for a straight-wall system, with no strengtheners.

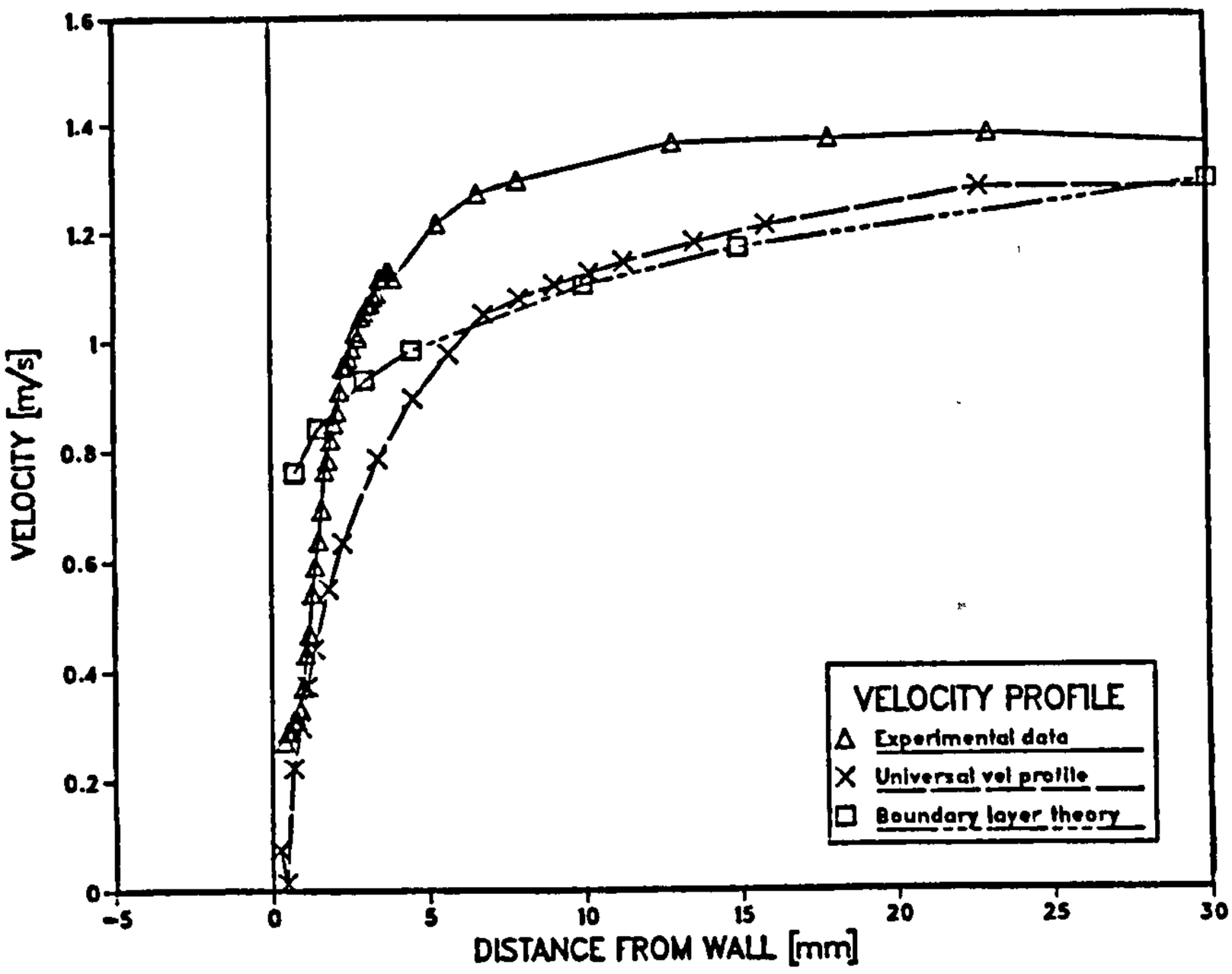

Fig. 3.9 Comparison of experimental and theoretical velocity profiles, close to wall

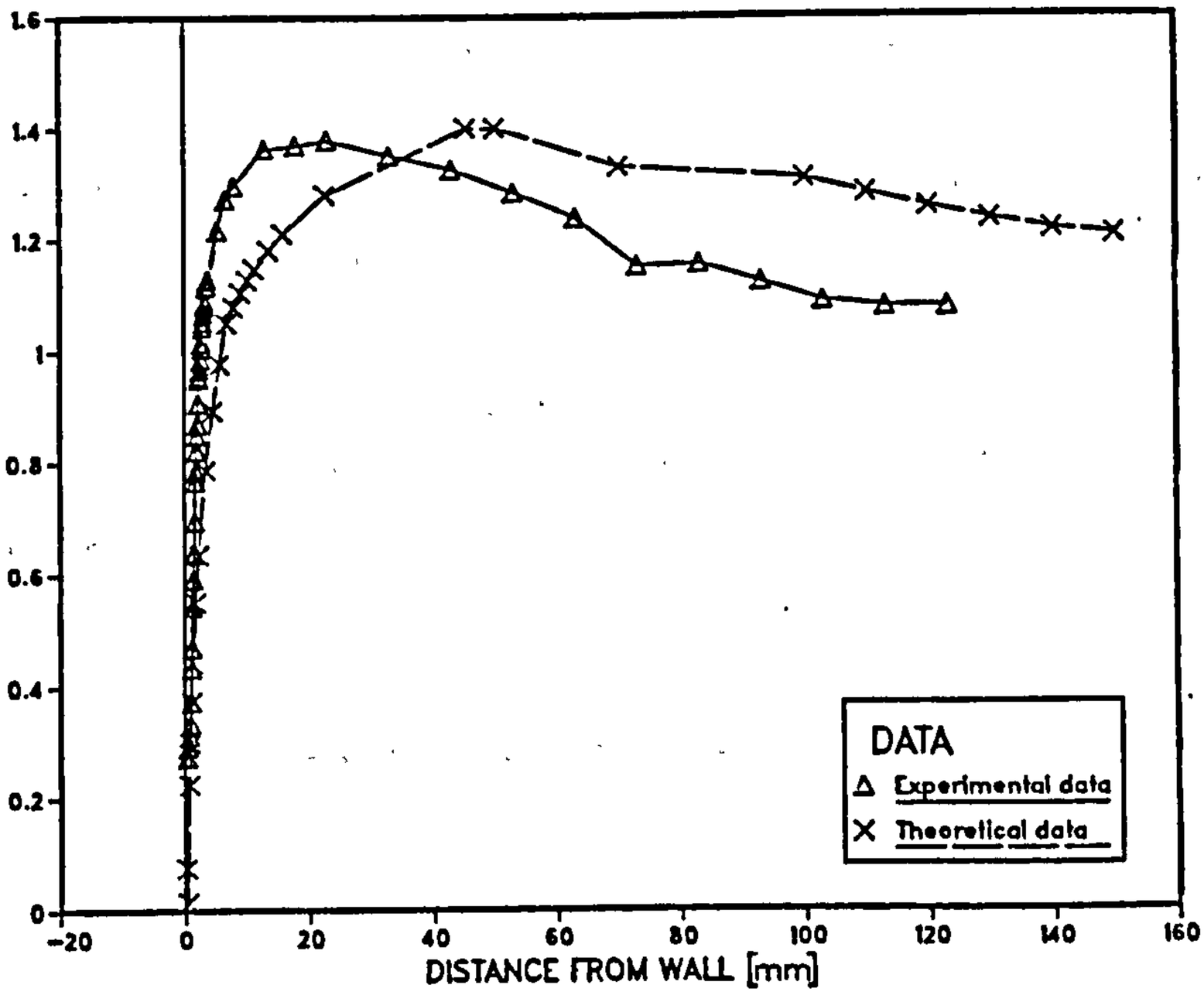

Fig. 3.10 Comparison of experimental and theoretical velocity profiles, including wall effect

Distance from wall (mm)	Velocity (ms^{-1})
50	1.384
70	1.356
100	1.305
110	1.287
120	1.270
130	1.254
140	1.242
150	1.235

Table 3.1 Velocity profile in wake of discharge electrode

3.4.3 Effect of wall strengtheners

Less detailed velocity profiles were measured throughout the duct with the wall strengtheners present. The results are displayed in Figure 3.11. The profiles shown on the right hand side of the duct correspond to those measured using hot-wire anemometry (see Section 3.2.1), and those on the left hand side were measured using laser-Doppler photon correlation (see Section 3.2.2). In practice, both sets of data were measured on the same side of the duct. The average velocity was set to 2 ms^{-1} and the base line of each curve corresponds to the position at which the measurements were made. At positions G and J, where velocity profiles have been determined using both measurement techniques, excellent agreement between the results is shown.

The results in Figure 3.11 show that by the time the gas flow reaches the first discharge electrode, the velocity in the wake of the flow modulation pipes has flattened off as predicted by equation 3.5. As the flow approaches the

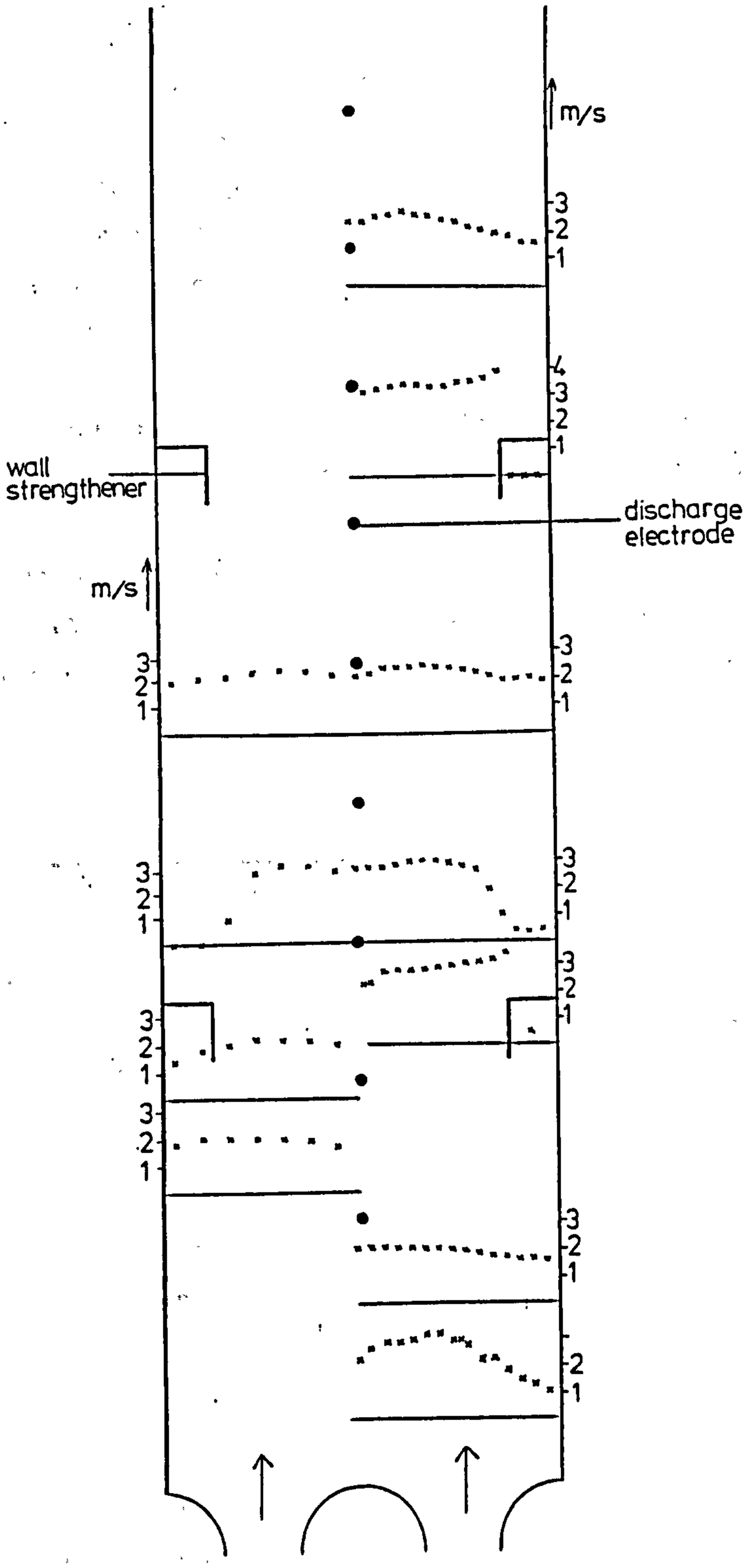

Fig. 3.11 Velocity profiles across precipitator duct

wall strengtheners, the velocity near the wall begins to decrease. In the highly turbulent region encompassed by this type of strengthener, the axial flow component is virtually zero. The velocity in the adjacent core of the flow increases to compensate for the effectively reduced cross-sectional area. In the downstream wake of the strengtheners, the axial velocity remains virtually zero, but the flat velocity profile recovers before the flow encounters the next strengthener. The wake effect of the discharge electrodes is small compared to that of the strengtheners.

For the purposes of modelling the flow field, a flat velocity profile provides an adequate description, except in the regions surrounding the strengtheners. To take account of the increase in mainstream velocity that occurs across the duct between the strengtheners, a sinusoidal curve has been theoretically imposed along the precipitator walls, as shown in Figure 3.12.

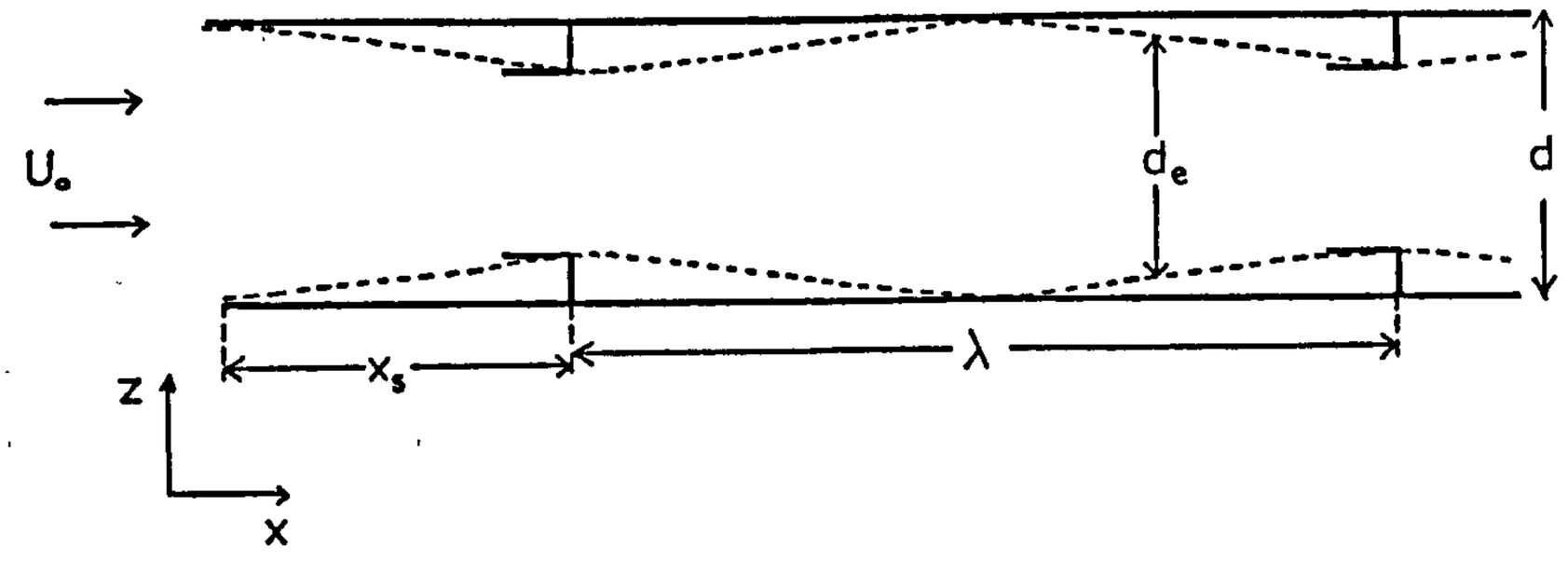

Fig. 3.12 Simulation of velocity profiles along precipitator duct

The curve has period λ and amplitude a/2, where λ is the spacing of the strengtheners along the duct, and a is

the distance the strengtheners protrude into the duct. The mainstream velocity in the region confined by the curves is assumed to be inversely proportional to the distance between the curves d_e at that point, where

$$d_e = a\sin(2\pi/\lambda(x+x_s) - \pi/2) + 2s_z$$

and d_e = effective plate spacing (m),

x_s = distance from inlet to first wall strengthener (m),

s_z = half plate-to-plate spacing (m).

Knowledge of the velocity U_o for a straight duct, allows the mean velocity u_x at any downstream position x to be calculated from

$$u_x = 2U_o s_z/d_e$$

The flow field in the zones downstream of the wall strengtheners is investigated further in Section 3.4.5.

3.4.4. Effect of electric wind

Much effort has recently been made into establishing the nature of electric wind produced by the discharge electrodes in electrostatic precipitators, and in assessing its effect on particle motion. Although it is not the purpose of this work to study electric wind in detail, some idea of the importance of the phenomenon in affecting the velocity profile data is required, to ensure realistic interpretation of the experimental results. Axial and transverse velocity profiles were measured accordingly at Position I, where the effect of electric wind was expected to be most significant. The wall strengtheners and flow modulation pipes were removed to enhance any indication of electric wind.

Figures 3.13 and 3.14 show the results of the axial and transverse velocity measurements respectively. Application of -65 KV to the electrode appears to increase the axial velocity component by less than 12%. The velocity difference between the curves increases as the wall is approached. Figure 3.14 shows a marked change in the values of transverse velocity components when the voltage is applied. These results all indicate the presence of electric wind effects.

An alternative explanation for the change in velocity with the application of -65 KV is the possibility of the laser-Doppler seeding particles acquiring an electric charge. The increase in velocity would then correspond to a migration of the charged particles in the electric field. A similar method of injecting the aerosol into the precipitator duct was employed in the technique for measuring dispersion coefficients, as discussed in Chapter 4. Tests showed that the aerosol plume did not significantly drift towards the collection walls when the voltage was applied to the discharge electrodes. Consequently, the change in velocity observed here must be due to the effect of electric wind. This could be verified by measuring the axial velocity component adjacent to the discharge electrode, where $E_x=0$. Thus, any change in axial velocity could only be a direct consequence of the hydrodynamics of the system.

Whilst modelling of the complex phenomenon of electric wind has been omitted from the mathematical models of Chapter 6, its effect on experimental results has been acknowledged.

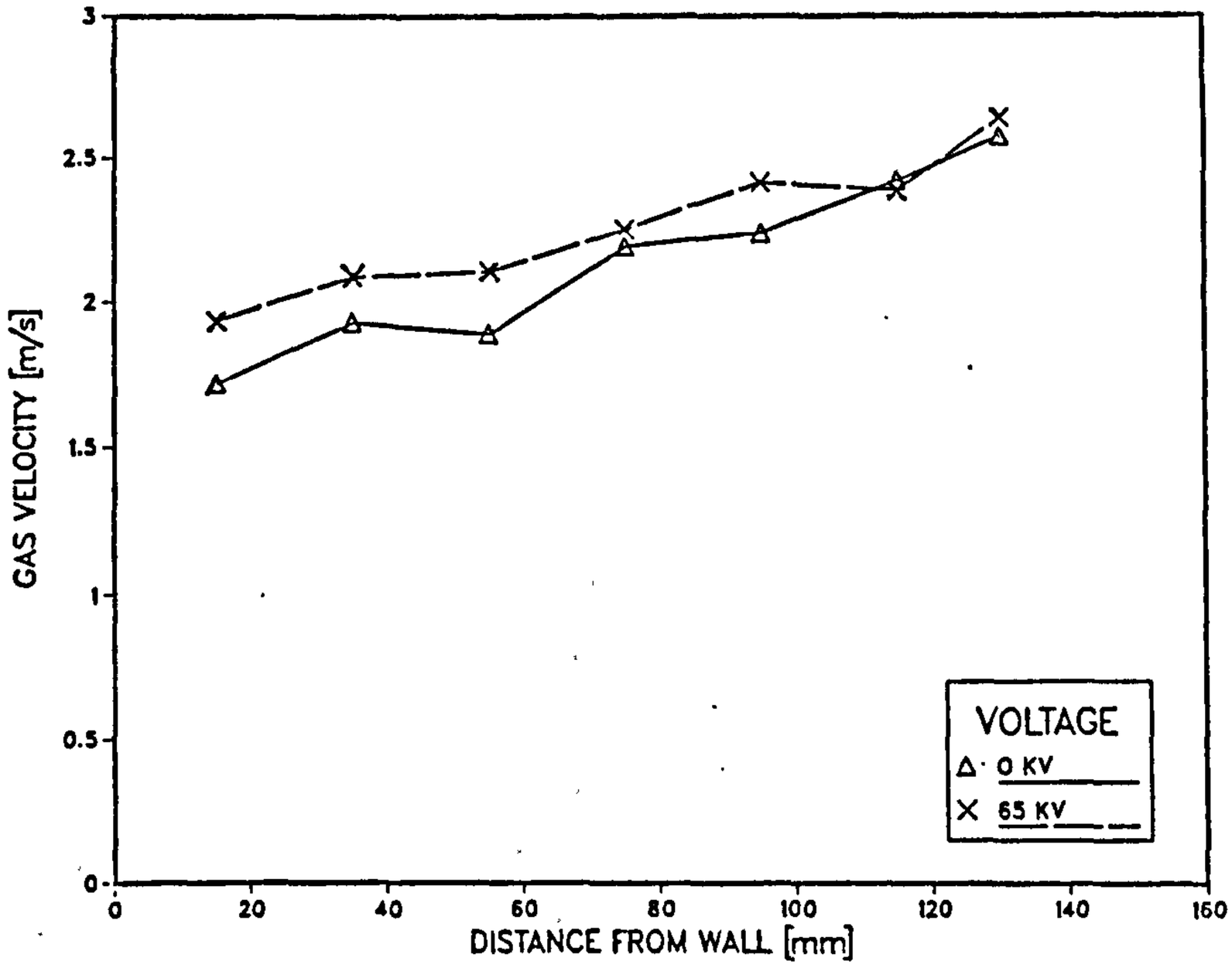

Fig. 3.13 Effect of applied voltage on axial velocity component

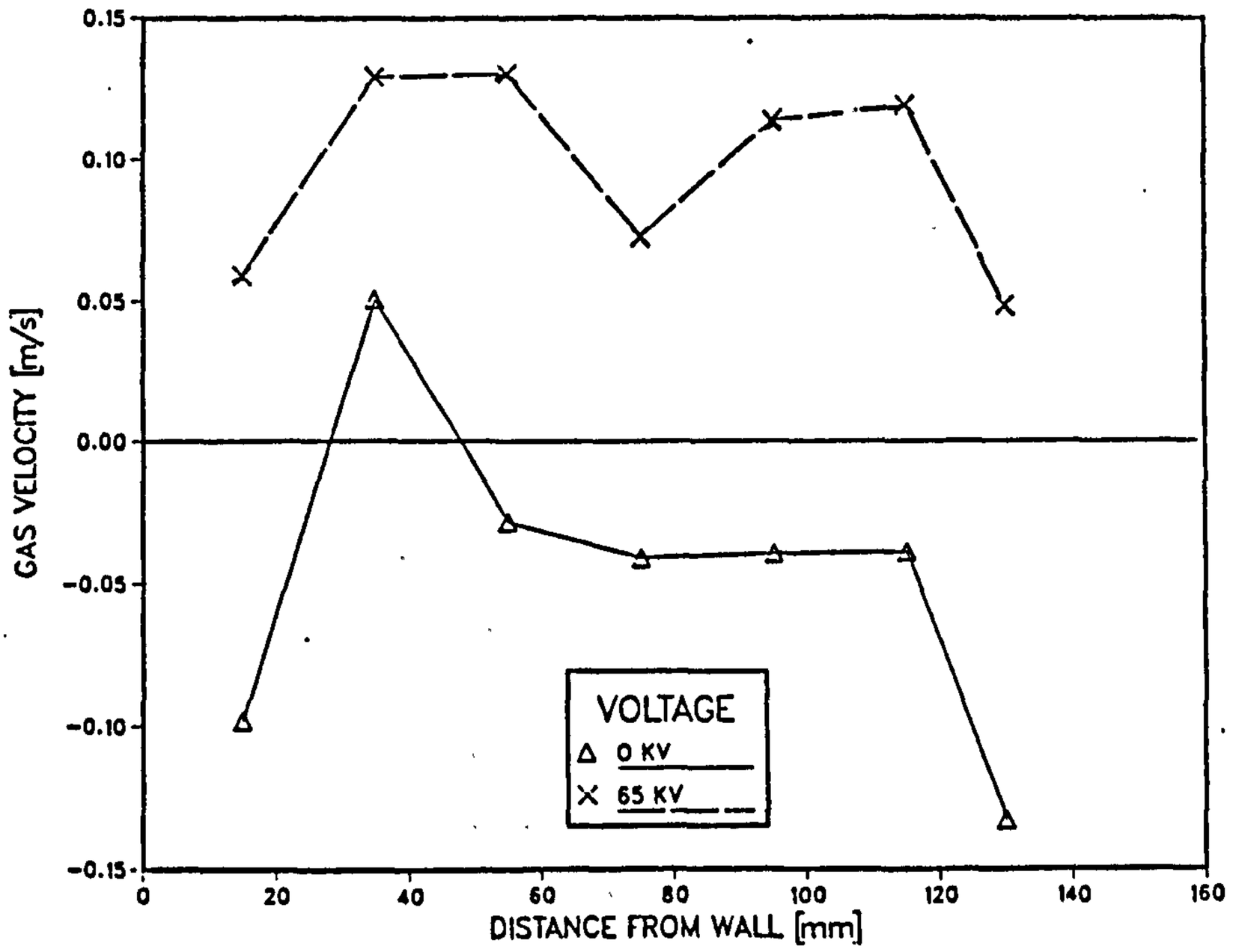

Fig. 3.14 Effect of applied voltage on transverse velocity component

3.4.5 Flow visualisation

Streak photographs were taken of neutral-buoyancy helium bubbles flowing around wall strengtheners with dimensions as shown in Figure 3.15. The strengtheners were positioned at 1 m intervals along the duct wall, and a camera exposure time of 1/15th of a second was used. Figures 3.16(i)-(viii) show the streak photographs for the eight different strengthener designs. The arrow underneath each photograph indicates the direction of the mainstream velocity. A cine film of the helium bubbles was also taken, using a film speed of 65 frames/sec.

Analysis of the photographs by Koumartzakis (1984) has enabled classification of the different strengthener geometries, based on the length of wake developed in the region downstream of the first strengthener. The series 3,4,5 and 6 are strengtheners of similar shape, but different arm lengths, L_s. According to the results in Table 3.3, the wake behind the strengthener may be reduced in size by increasing the length of this arm.

Strengthener set no.	Length of wake (m)
3	0.46
4	0.37
5	0.30
6	0.25

Table 3.3 Length of wake downstream of different electrode designs

For a given camera exposure time, the streak length in the photographs is proportional to the bubble velocity. Using this principle, Koumartzakis was able to calculate

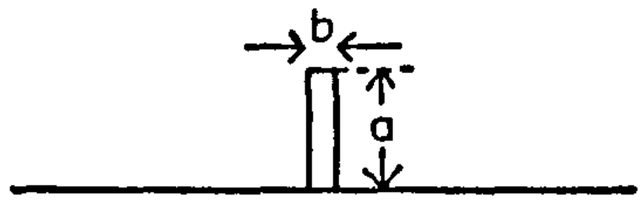

Set no. 1

a=35mm
b=10mm

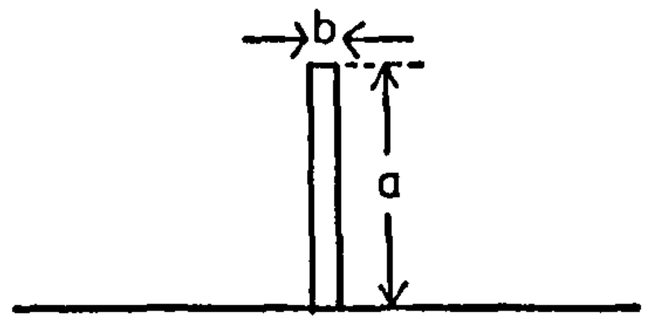

Set no. 2

a=70mm
b=10mm

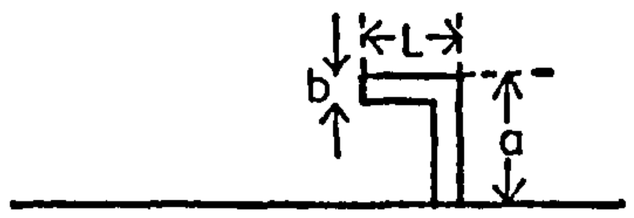

Set no. 3

a=35mm
b=10mm
L=25mm

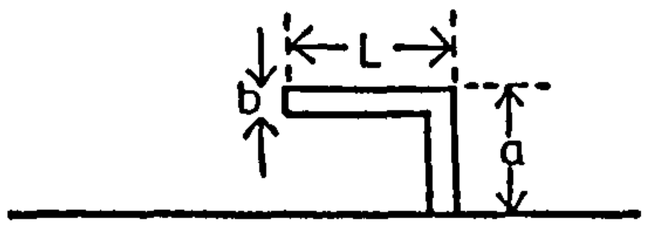

Set no. 4

a=35mm
b=10mm
L=50mm

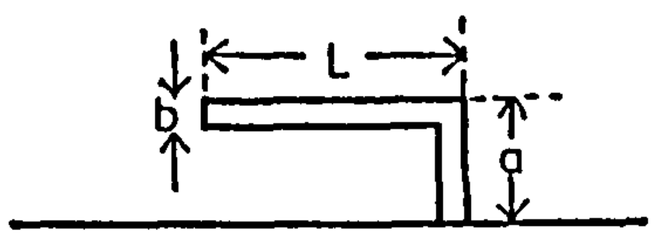

Set no. 5

a=35mm
b=10mm
L=75mm

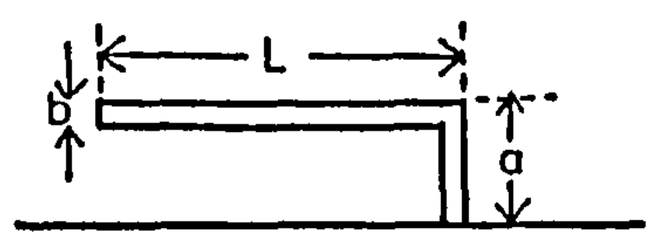

Set no. 6

a=35mm
b=10mm
L=100mm

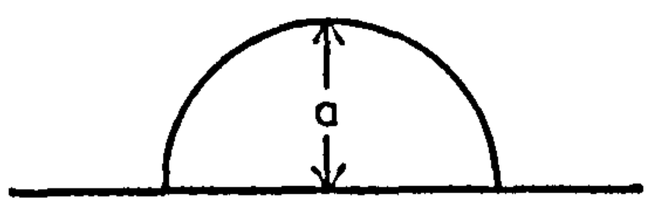

Set no. 7

a=50mm

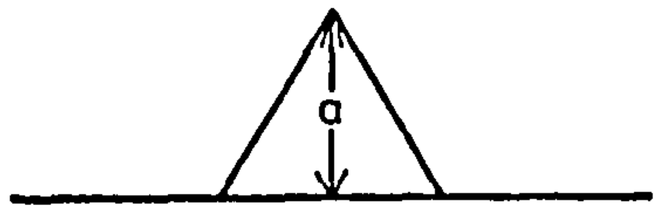

Set no. 8

a=50mm

Fig. 3.15 Dimensions of wall strengtheners

CONTAINS CLEAR OVERLAYS

OVERLAYS SCANNED SEPERATELY AND OVER THE RELEVANT PAGE.

Fig 3·16 i) Streak photographs of neutral-bouyancy helium bubbles

ii)

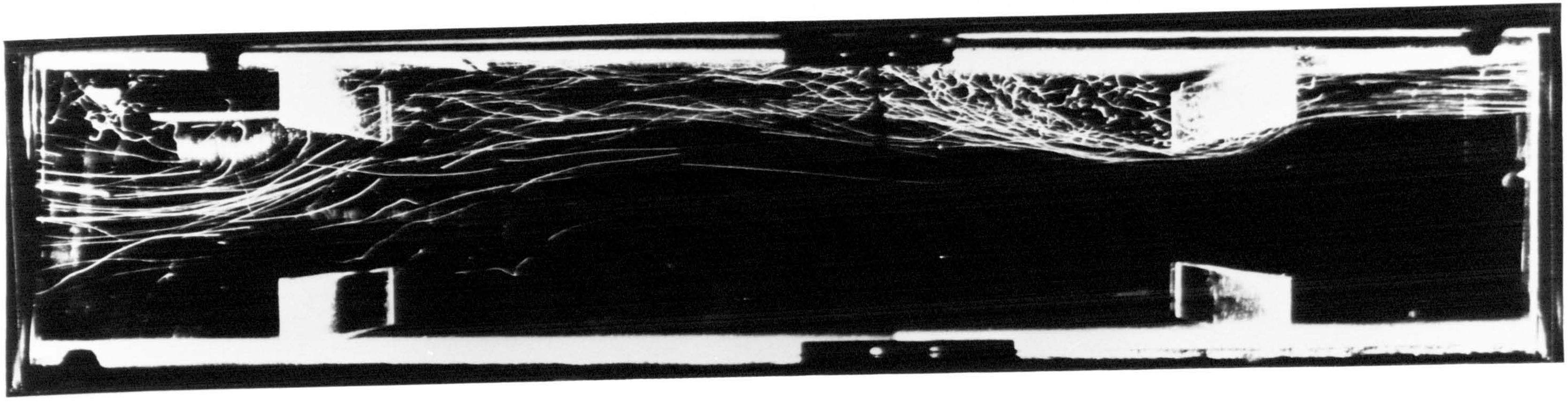

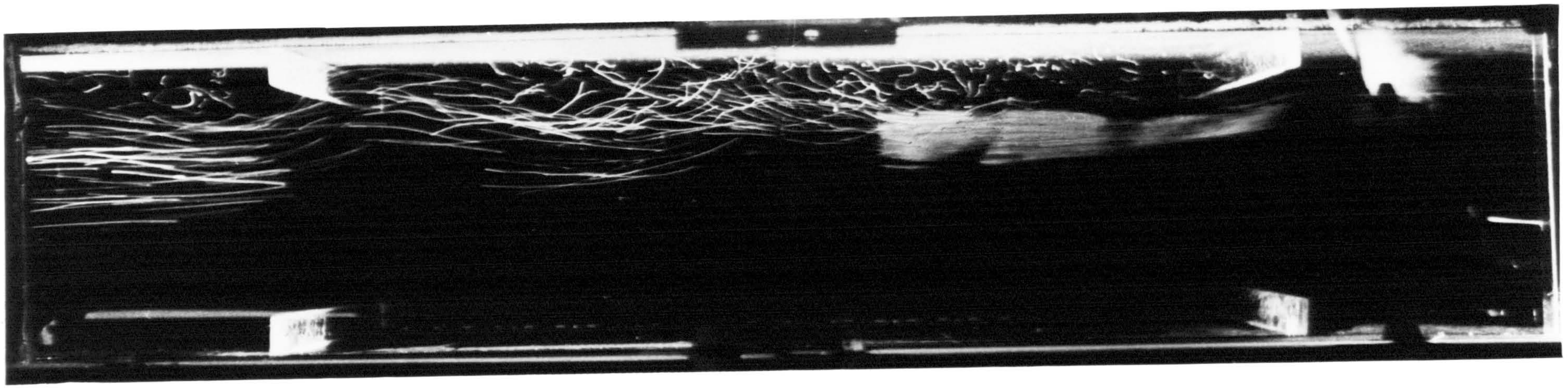

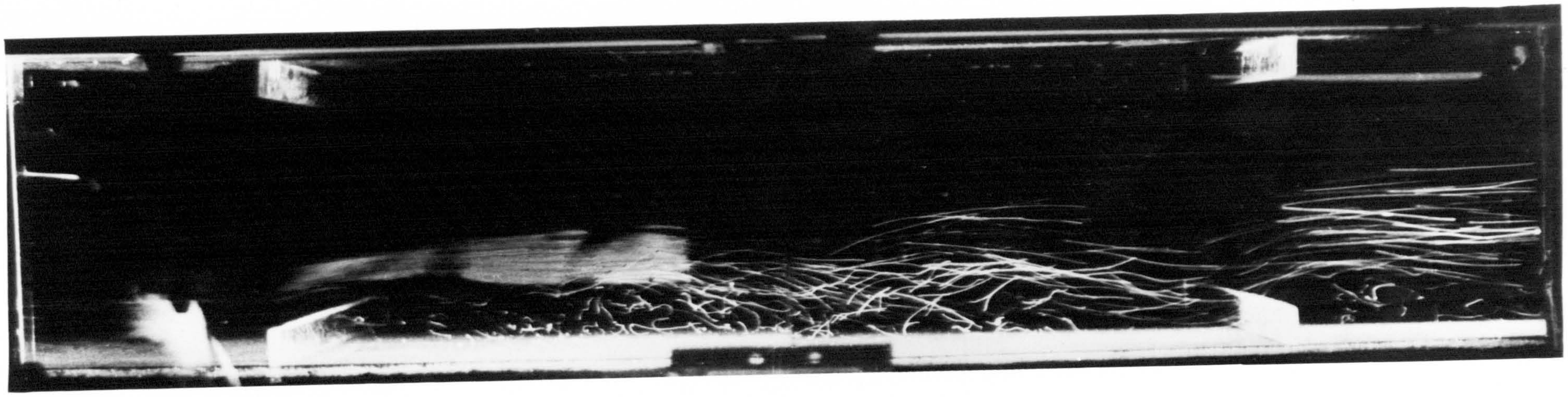

1

Fig 3-16 i) Streak photographs of neutral-bouyancy helium bubbles

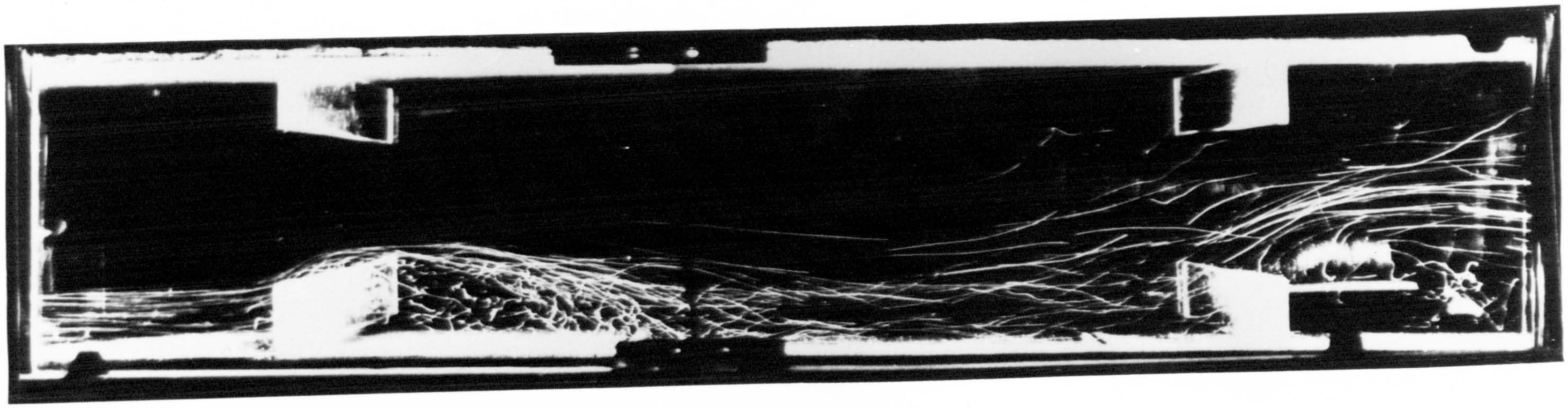

ii)

2

iii)

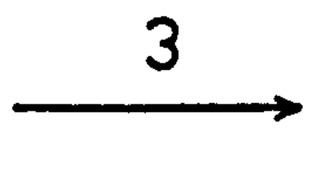

iv)

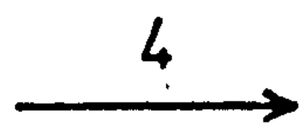

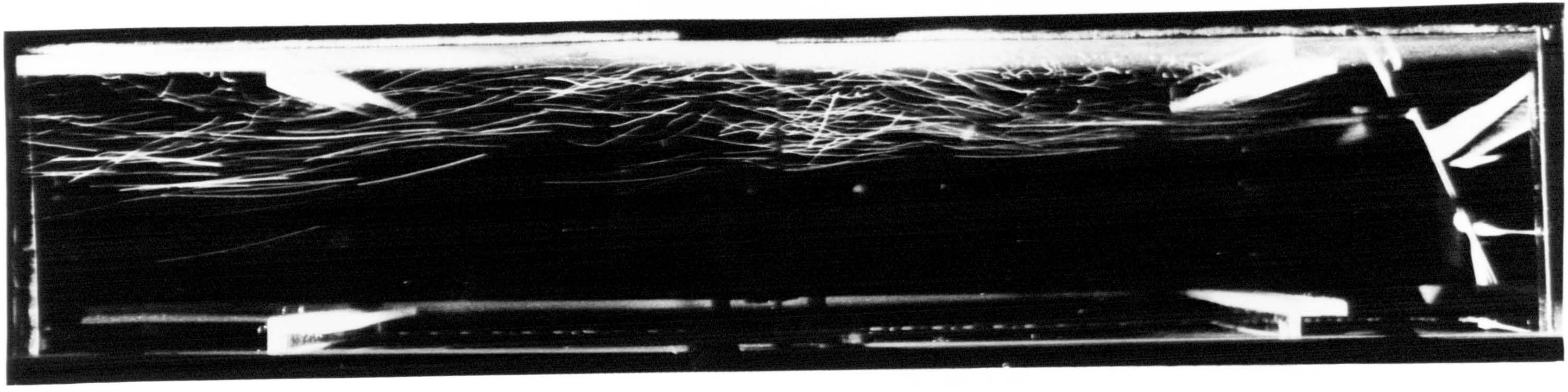

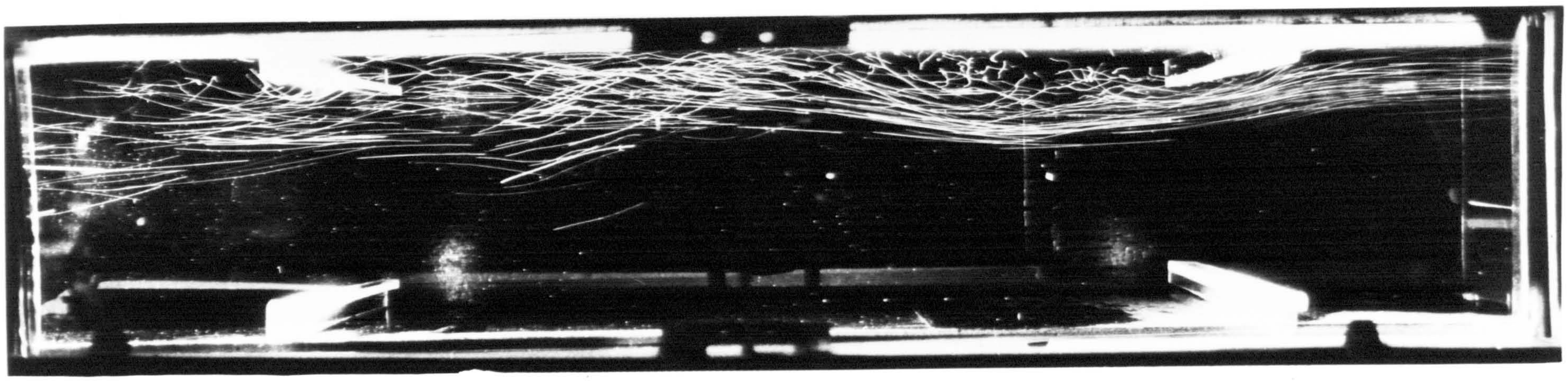

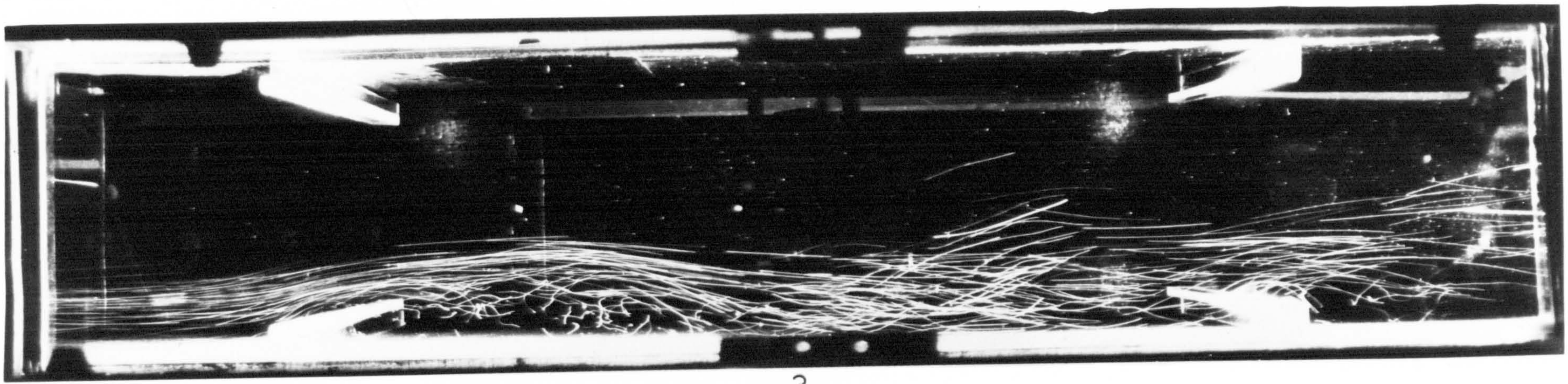

3

iii)

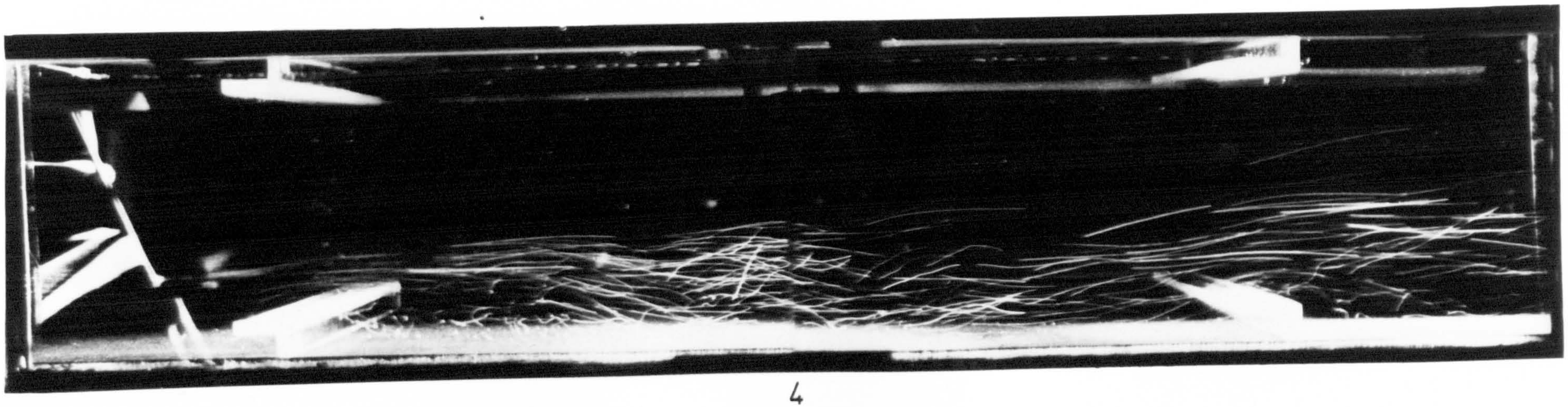

4

iv)

v) 

vi) 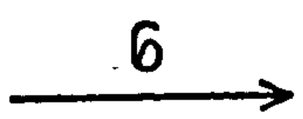

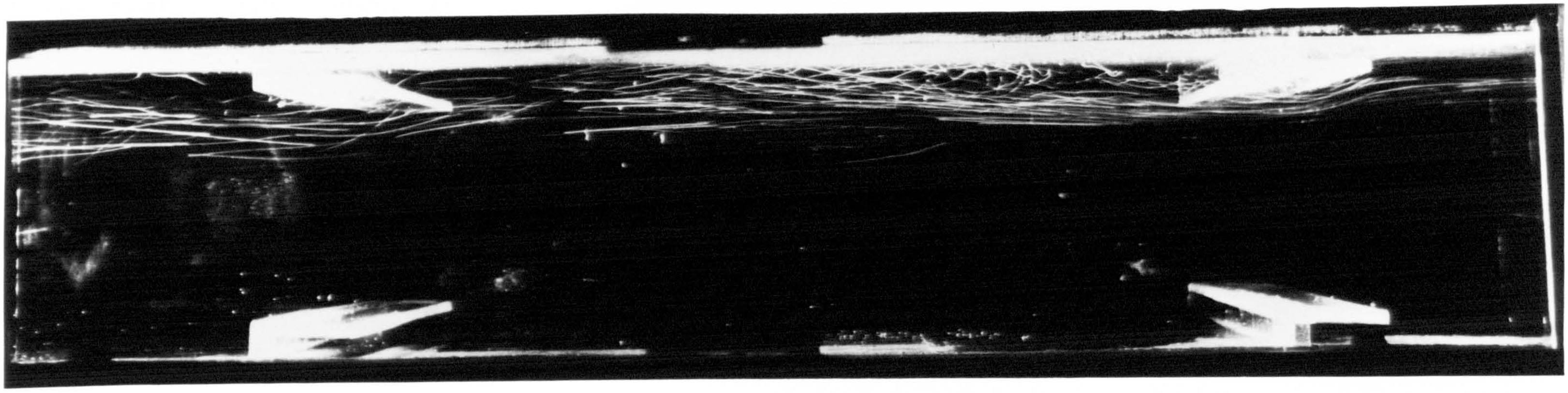

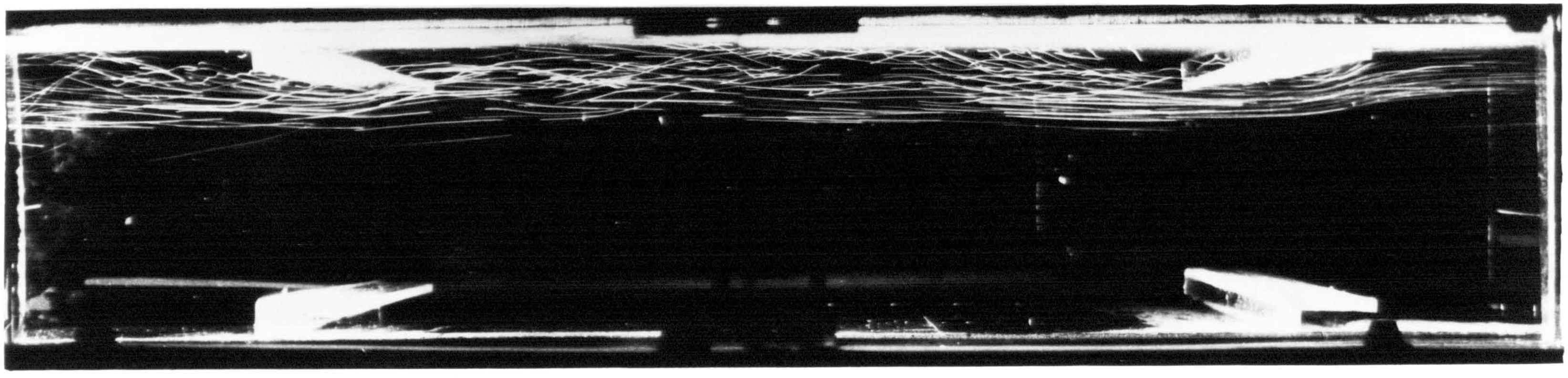

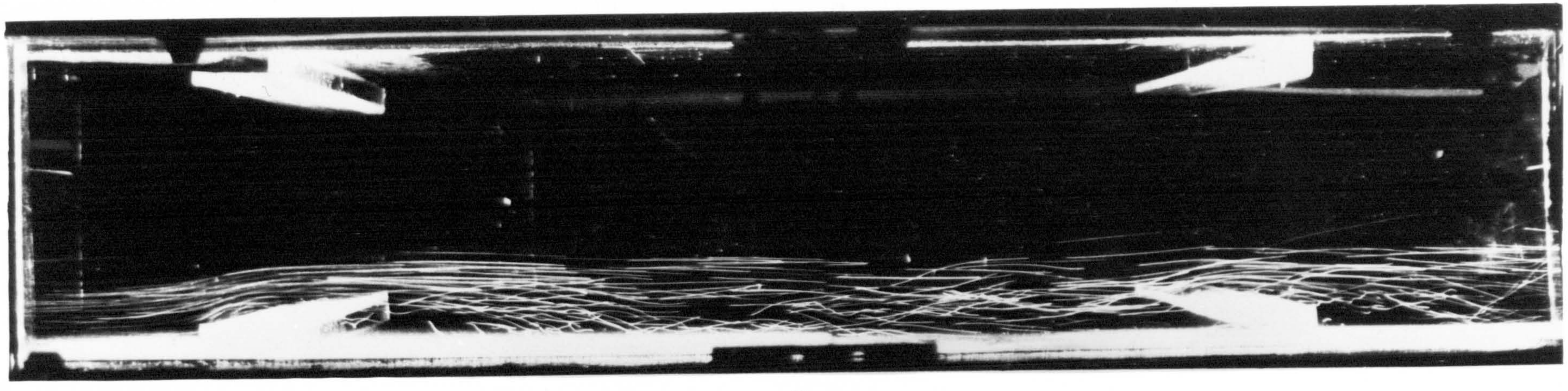

v)

5

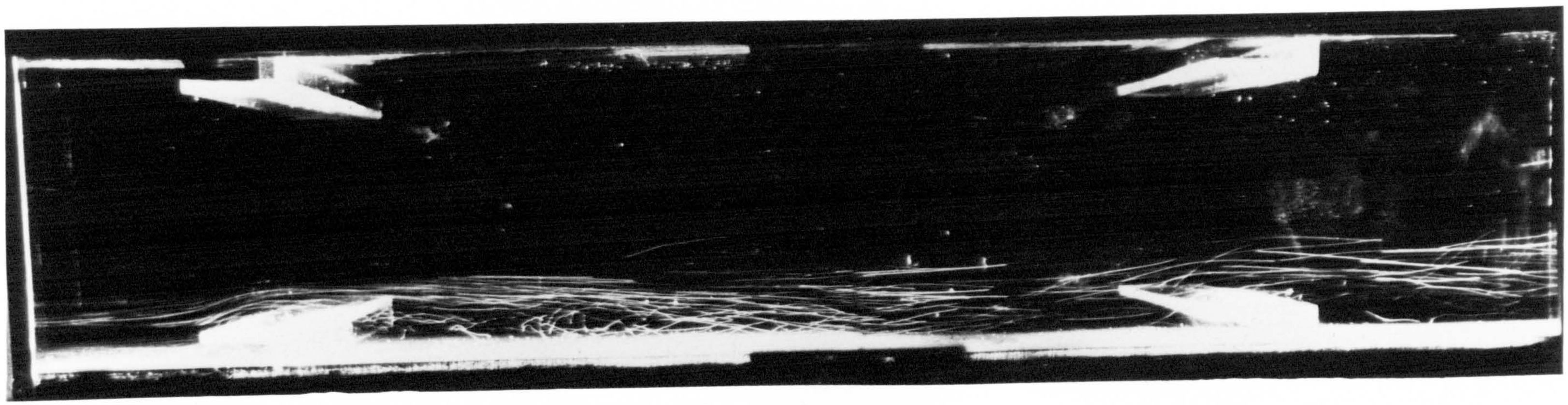

6

vi)

104

7

vii)

8

viii)

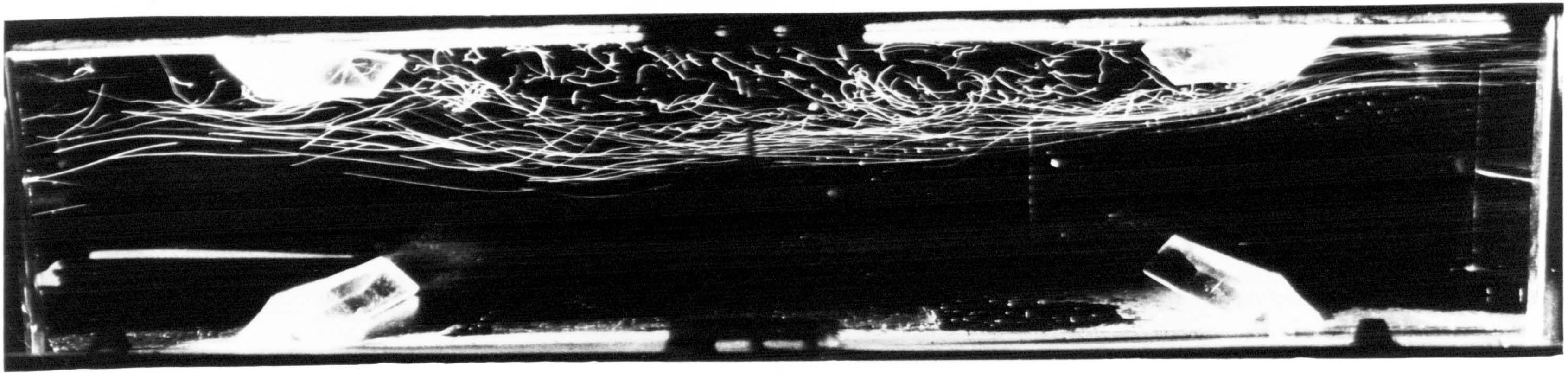

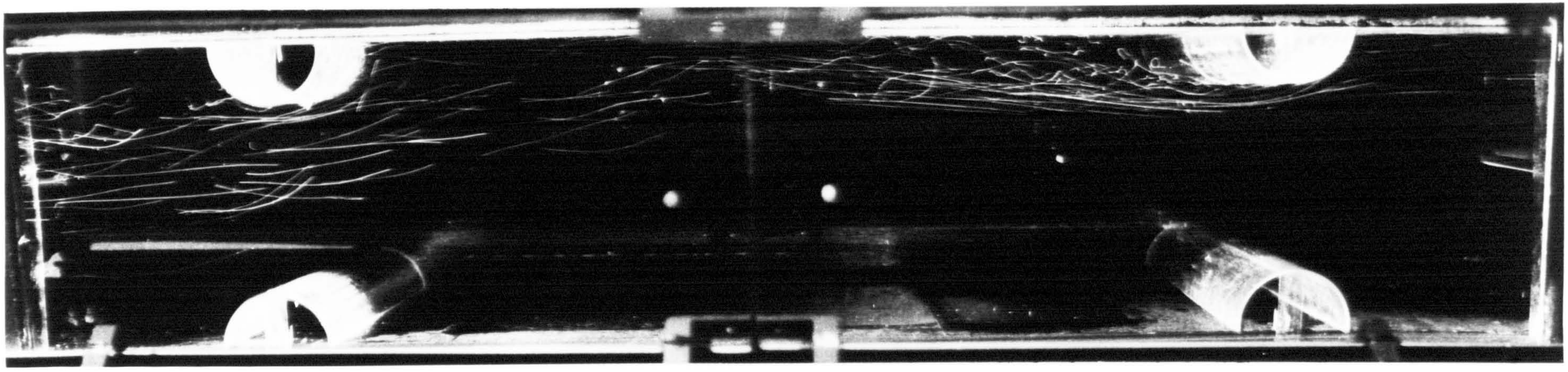

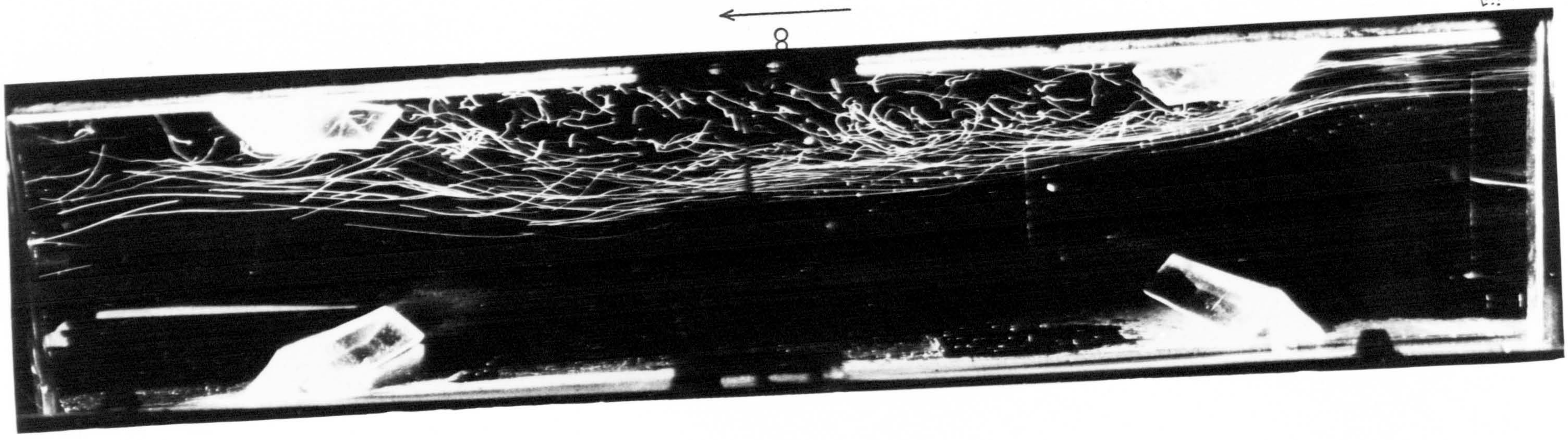
8
VIII

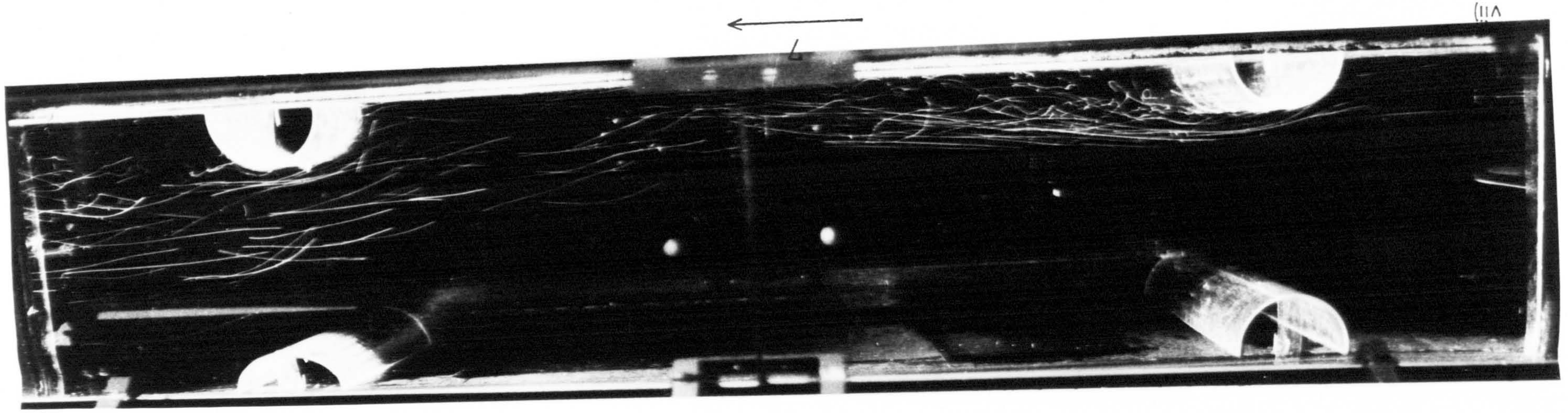
4
VII

velocity values in the regions surrounding the strengtheners. Frame-by-frame analysis of the cine film taken under similar conditions produced the information required to determine particle residence time distributions N(T), as described by Vincent and Maclennan (1980, 1981). These local velocity values and N(T) distributions were used in calculating precipitator efficiency.

A progressive shortening of the wake length behind a strengthener, by increasing the strengthener arm length L_s, may influence precipitator efficiency in three ways;

a) reduction of turbulence,
b) increase in mainstream velocity between the strengtheners,
c) residence time in the smaller wakes is reduced.

The first of these factors implies an increase in efficiency, whilst the second and third are likely to reduce efficiency. A balance of these effects determines the overall precipitator efficiency. The work carried out by Koumartzakis led to a choice of optimum strengthener design as described by Set 4 or 5 (see Figure 3.15).

CHAPTER 4

TURBULENT MIXING AND FLUCTUATING VELOCITIES

Measurements of dispersion coefficient and fluctuating velocity components have been obtained for a range of conditions in the precipitator duct. The significance of mixing in turbulent flows is discussed to enable realistic interpretation of the experimental measurements. An expression is developed relating the small-scale dispersion coefficient and the r.m.s. transverse fluctuating velocity, and preliminary attempts to verify the relationship are made.

4.1 Turbulent mixing

Although the characteristics of particle charging and electrical conditions in a precipitator are well documented, relatively little is known about the hydrodynamics and fluid-particle interactions. The success of numerical models in predicting the conditions in an electrostatic precipitator relies on a realistic description of all these fundamental processes affecting particle motion.

The parameter commonly used in fluid mechanics to describe turbulent mixing is the dispersion coefficient. The aim of the work described in this section was to measure local dispersion of the gas at various positions and conditions in the precipitator, and to elucidate the importance of mixing as a mechanism.

4.1.1 Significance of dispersion coefficient measurement

Attempts to model turbulent mixing have in general drawn on analogies between the eddies in the turbulent fluid and the molecules in the process of molecular diffusion.

Although this analysis has proved useful in the general understanding of eddy diffusion, care is required in the interpretation of related experimental data. Unlike the case of molecular diffusion, in turbulent mixing the scale on which observations are made is often comparable to the size of the eddies. It is essential that experimental measurements are made which are indicative of the relevant length scales.

An instantaneous picture of an aerosol plume would reveal a meandering behaviour, with the width of the plume gradually growing downstream from the source. At distances far downstream, longer time averages of the concentration are required to encompass the meanderings caused by the large-scale eddies. Figure 4.1 shows the effect of different sized eddies on a packet of aerosol having dimensions indicative of the width of the aerosol plume. Eddies larger in size than the packet dimensions tend to transport the packet intact, whereas smaller eddies tend to disperse it. Further downstream from the source, where the plume is wider, larger and larger eddies become effective in causing dispersion, and the smaller eddies become increasingly ineffective.

This suggests that to incorporate the dispersive effect of the full range of eddy sizes, the concentration profile must be measured at a distance sufficiently far downstream of the aerosol source. Kalinske and Pien (1944) recommended that a distance downstream of $x > 2x_o$ be used where x_o is a length scale characteristic of the turbulence (see Section 1.4). In cases where this condition is not satisfied, the profile of the distribution will remain Gaussian, and the standard deviation of the profile will be representative of the transverse fluctuating velocity distribution.

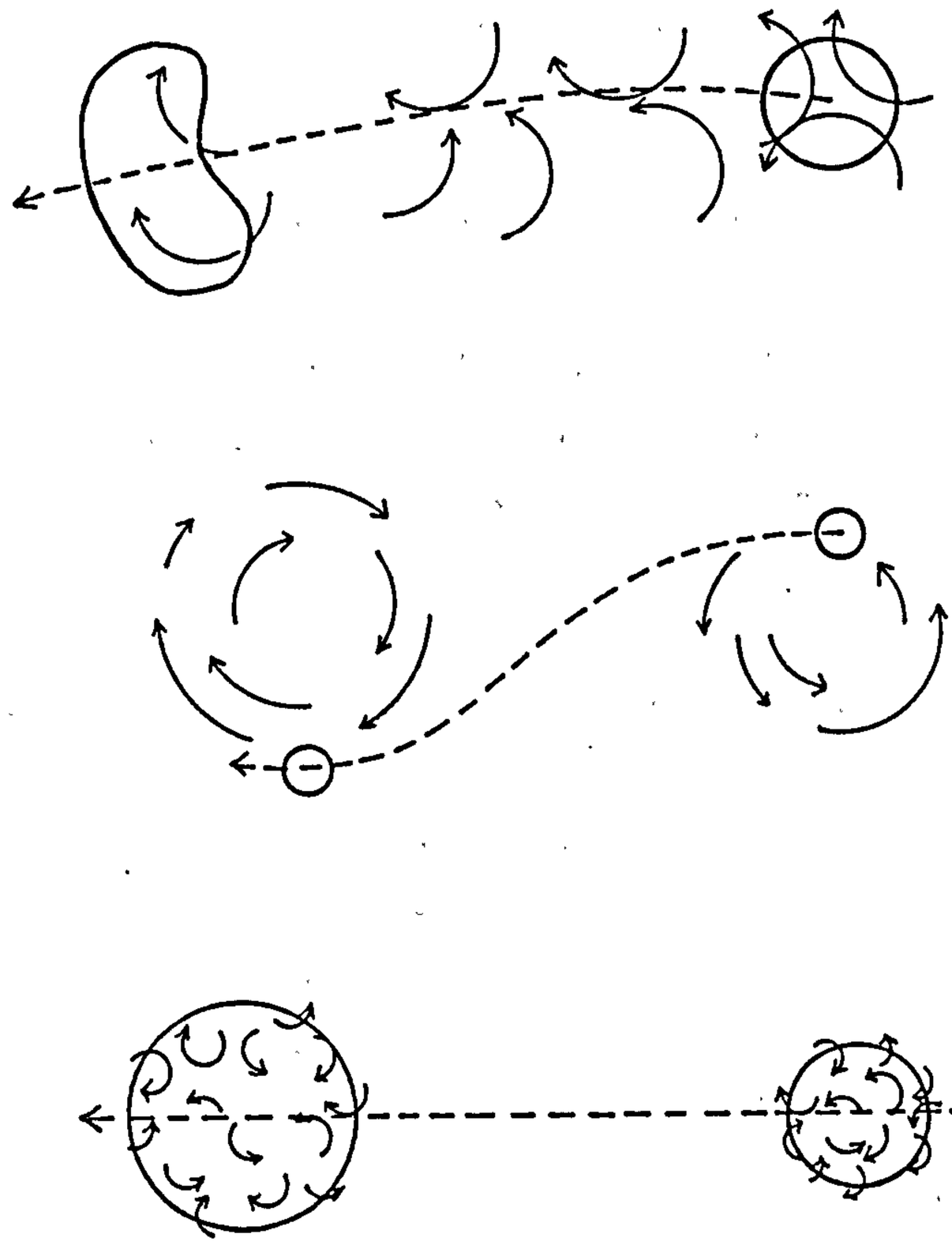

Fig. 4.1 Dispersion of aerosol in turbulent flow

It is important to recognise this fact when interpreting much of the so-called "turbulent diffusion" work reported in the literature. In cases where some large eddies are present, the aerosol plume may not have experienced the dispersive effect of the full range of eddy sizes. A more appropriate description of the results would be in terms of a "dispersion coefficient", indicating that the mechanism causing the material to spread is not proper turbulent diffusion as defined by Taylor (1921). In the following work, the term "diffusion coefficient" is used only with reference to systems where the spread of material

is due to the dispersive effect of the full range of eddy sizes.

Wilson (1904) derived an equation for heat conduction downstream of a continuous point-source of heat in an infinite fluid stream moving with uniform velocity U_o, as shown in Figure 4.2. Towle and Sherwood (1939) replaced the thermal conductivity by the concept of a dispersion coefficient D. According to Hinze (1959) this is justified since neither heat nor mass transfer is affected by interactions between packets of fluid in turbulent motion, and therefore the eddy exchange for heat and mass are interchangeable. Assuming the source to be injecting material at a rate of W moles/sec, the concentration on a plane at a distance x downstream from the injection point may be determined from

$$c = \frac{W}{\sqrt{4\pi Ds}} \exp[-U_o(s-x)/2D] \qquad (4.1)$$

where s = distance from injection to measurement point (m).

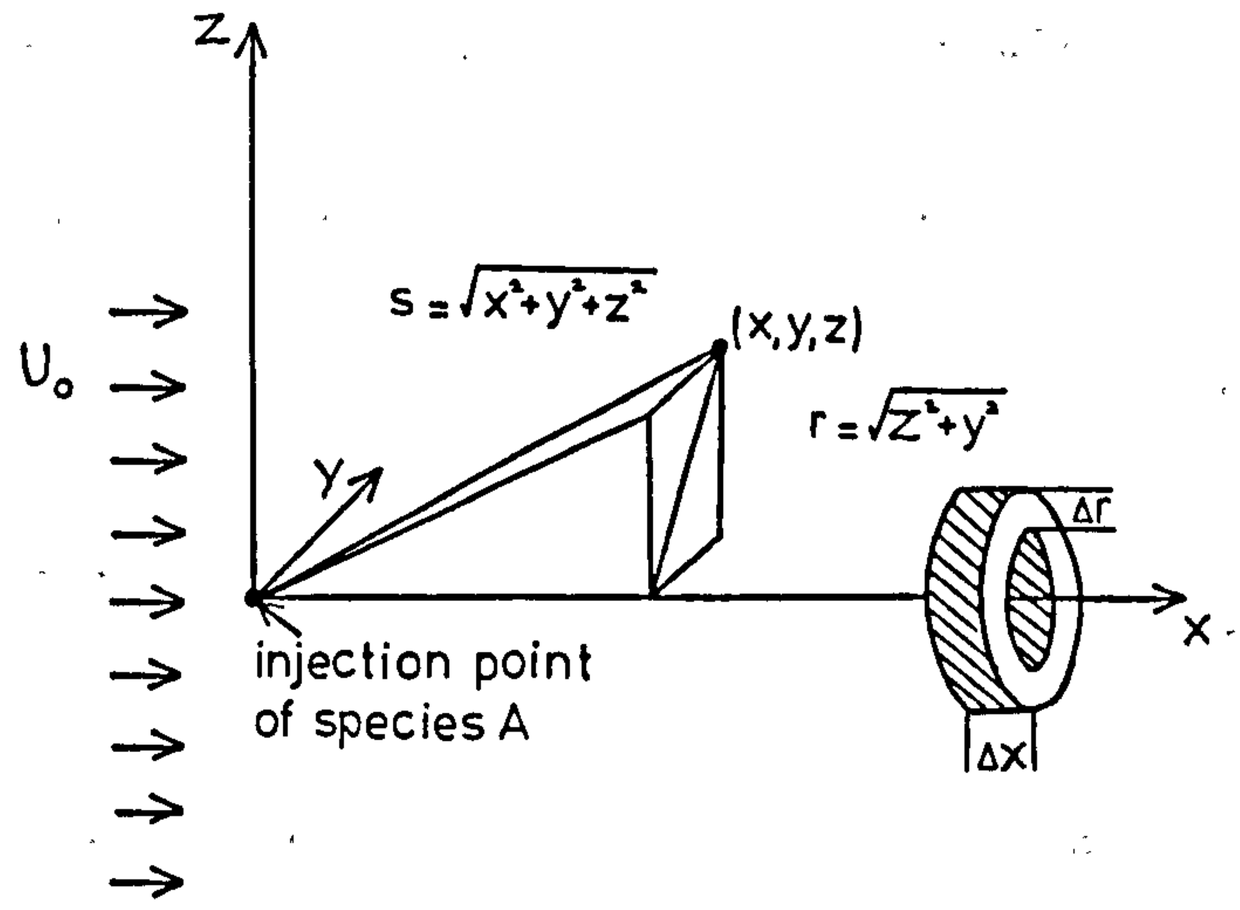

Fig. 4.2 Spread of isokinetically injected aerosol into mainstream gas flow

Application of this expression provides a useful method for calculating dispersion coefficient values from a single concentration profile measurement. Comparison of experimental and theoretical concentration profiles, assuming the above equation adequately describes the dispersion process, allows the most suitable value of D to be calculated. This method was chosen to analyse the concentration profile data obtained as described in Section 4.1.2. A more detailed explanation, including the computer algorithm used to calculate D, may be found in Appendix A.

4.1.2 Experimental procedure for measuring dispersion coefficient

In this work, dispersion coefficient values were measured in the pilot scale precipitator for a range of conditions. An aerosol was injected into the duct through a narrow glass pipe. The concentration profile of the diffusing aerosol was measured 50 mm downstream of the source using a light scattering method. The experimental profiles were then compared with theoretical predictions, and a least squares fit method applied (see Appendix A) to evaluate the corresponding dispersion coefficient, D.

4.1.2.1 Aerosol generation and injection

A corn oil aerosol was injected into the gas flow of the precipitator to provide sources for light scattering. The aerosol was produced by a condensation generator similar in design to that described by Liu et al. (1966) (see Figure 4.3). Required properties of the aerosol included the following;

a) the relaxation time of the aerosol particles must be sufficiently small for the particles to follow the flow closely,

b) the aerosol must be in the size range 0.1-1.0 μm where particles have minimum electrical mobility,
c) evaporation must be insignificant in the time taken to travel from the injection point to the measurement zone,
d) non-hazardous.

The aerosol was produced from a mixture with the following composition;

75% iso-propyl alcohol,
20% corn oil,
5% acetone,
methylene blue dissolved to saturation.

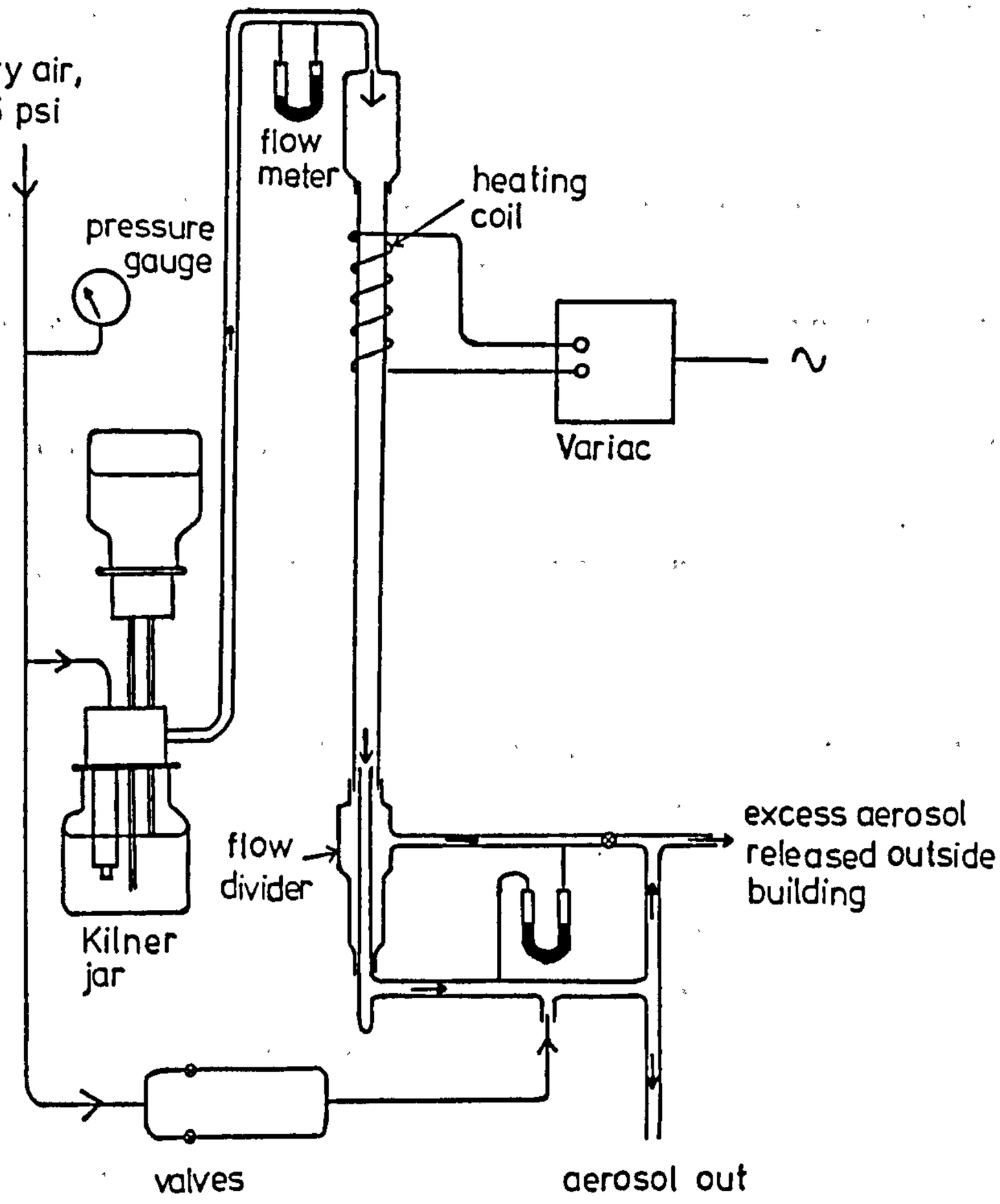

Fig. 4.3 Schematic diagram of aerosol generator

The vapour pressure of corn oil is of the order of 10^{-5} mmHg at 250°C. At room temperature, the vapour pressure will be substantially lower, and calculation of the evaporation rate as suggested by Shaw (1978) shows that evaporation of the aerosol will be negligible. The mixture was atomised to form droplets which were then heated in the Pyrex glass tube section. Using corn oil with such a low vapour pressure resulted in evaporation of the volatile solvents only. This produced an aerosol with reduced homogeneity, but one sufficient for the purposes of this work. The methylene blue provided nuclei for the volatile solvents to recondense on. Since corn oil and iso-propyl alcohol are immiscible, acetone was required to encourage uniform mixing of the components.

To stabalise the aerosol flow over long periods of time, several factors of the Liu et al. generator design were changed. These included;

a) the incorporation of a reservoir tank to maintain the level of generation mixture,
b) an increasein diameter of some of thepipestoprevent blocking,
c) omission of the mesh screen prior to the Pyrex glass tube,
d) reduction of compressed air pressure from 35 to 15 p.s.i..

An aerosol with size distribution in the range 0.1 - 1.0 μm was required for the experimental work. This size range incorporates the minimum in the electrical mobility of the particles. The effect of the electric field on the aerosol particles in the precipitator would then be minimised, enabling measurements representative of the aerodynamics in the duct to be made. Size analysis of the aerosol was made using a Whitby electrical mobility analyser

(for d_p < 0.3 μm) and a Royco optical analyser (for d_p < 3.0 μm). The results for cumulative area % undersize are shown in Figure 4.4, and show the corn oil aerosol to be in the required size range.

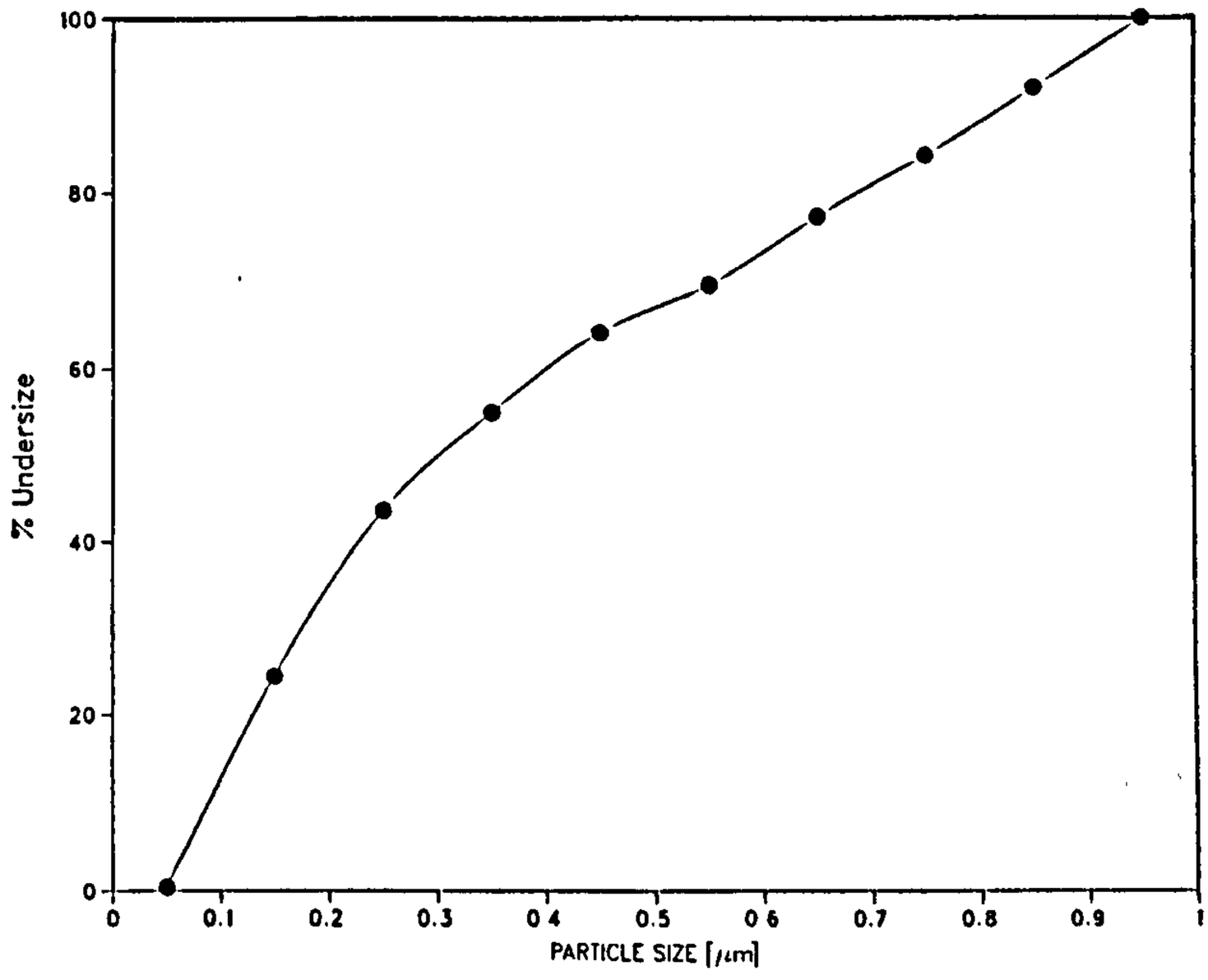

Fig. 4.4 Cumulative area %-undersize for corn oil aerosol

The aerosol was injected into the precipitator duct through a glass pipe with 1 mm bore. The pipe was inserted through the honeycomb mesh at the duct inlet and supported by insulating threads downstream. Three threads were used at each support position to achieve maximum stability without undue complication of the pipe realignment procedure. A rotameter controlled the flow rate of the aerosol and was adjusted to maintain isokinetic injection into the gas flow. Initially a stearic acid aerosol was used, but preliminary tests showed a tendency for the aerosol to deposit in the rotameter and injection pipe.

Frequent stripping and cleaning of the system were then required to avoid blockage.

4.1.2.2 Illumination and detection of the aerosol

Several glass-covered slits were installed in the walls of the wooden support and precipitator at positions G, H, L and N as shown in Figure 2.3, so that the aerosol plume could be illuminated from outside the duct. A vertical ribbon of light from a projector lamp was used to illuminate a cross-section of the aerosol plume, 50 mm downstream from the injection point. The light was passed through a slit cut in aluminium foil and focussed in the region of the diffusing aerosol. The height of the light ribbon was greater than the width of the aerosol plume, so that the scattered light was constant for a small vertical drift of the aerosol. A photomultiplier tube was positioned horizontally above the measurement zone, as shown in Figure 4.5, and a 45^{o} mirror was used to reflect the scattered light from the aerosol to the detector. A 1 mm vertical slit was cut in an aluminium foil sheet and positioned across the front of the P.M.T.. This allowed the ribbon of light to be observed in 1 mm slices, so that a more accurate concentration profile could be obtained.

Focussing of the P.M.T. optics at the measurement zone was aided by the use of a target, as shown in Figure 4.6. The P.M.T. was mounted on a rigid support frame and was capable of traversing the duct by means of a screw mechanism. The pitch of the screw was 1.54 mm so that a half-revolution of the handle moved the photomultiplier tube in 0.77 mm steps across the duct. The perspex handle, 1 m in length, enabled adjustment of the P.M.T. position from the safe side of the barrier.

A Malvern Correlator 7023 attached to the P.M.T. was

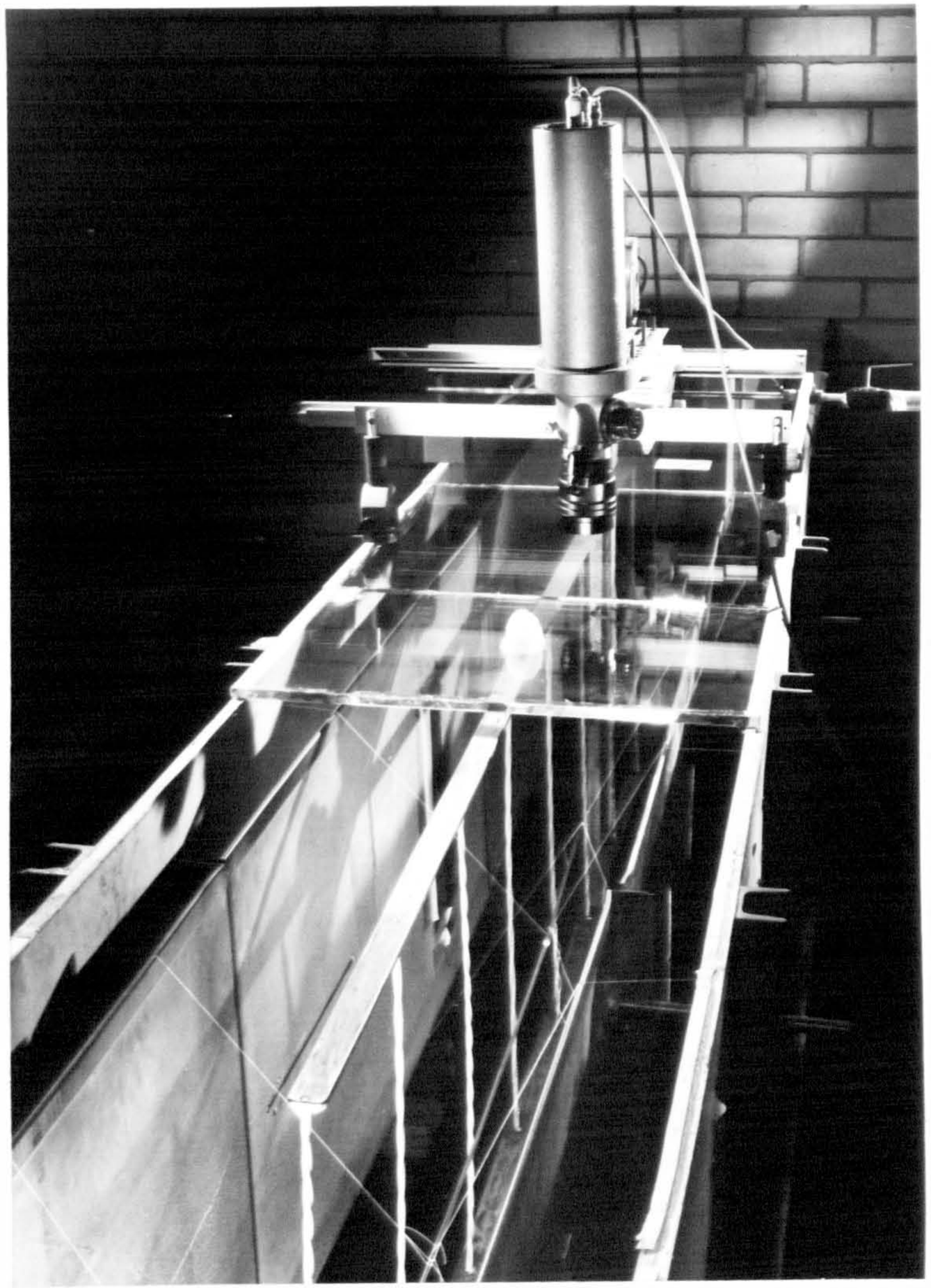

Fig. 4.5 Arrangement of P.M.T. above precipitator duct

Fig. 4.6 Use of perspex rod to locate sensing zone

used as a memory to store the concentration profile data. Each channel stored the sum of a 45 second integration of the incoming signal. This time interval was chosen as sufficient to average out the temporal fluctuations in the count. The correlator trigger was set manually to allow traversing of the P.M.T. between each reading.

After each complete scan of the aerosol plume, the aerosol generator was turned off and a background scan performed to take account of the spurious light present in the duct. The results were transferred to a Commodore PET 4032 via an IEEE interface, from which the dispersion coefficient value was calculated as explained in Appendix A. To maximise the signal-to-noise ratio, it was necessary to reduce the background light to a minimum. This was accomplished by turning off all room lighting and fixing strips of black velvet material to the floor and walls of the duct to absorb the reflected light.

4.1.3 Initial assessment of mixing in the precipitator

An initial measurement of dispersion coefficient with distance downstream from the injection point was required before an assessment could be made of the type of mixing occurring at 50 mm from the injection point. This was done in a straight duct system with the discharge electrodes and wall strengtheners removed. The light ribbon was projected across the duct at Station H and the distance x varied by moving the injection point further upstream. Figure 4.7 shows the values of dispersion coefficient measured for various values of x. Also shown are the results of similar measurements made at Station N. The triangles and crosses represent the experimental values of dispersion coefficient measured at positions H and N respectively.

The results show a definite upward trend of the

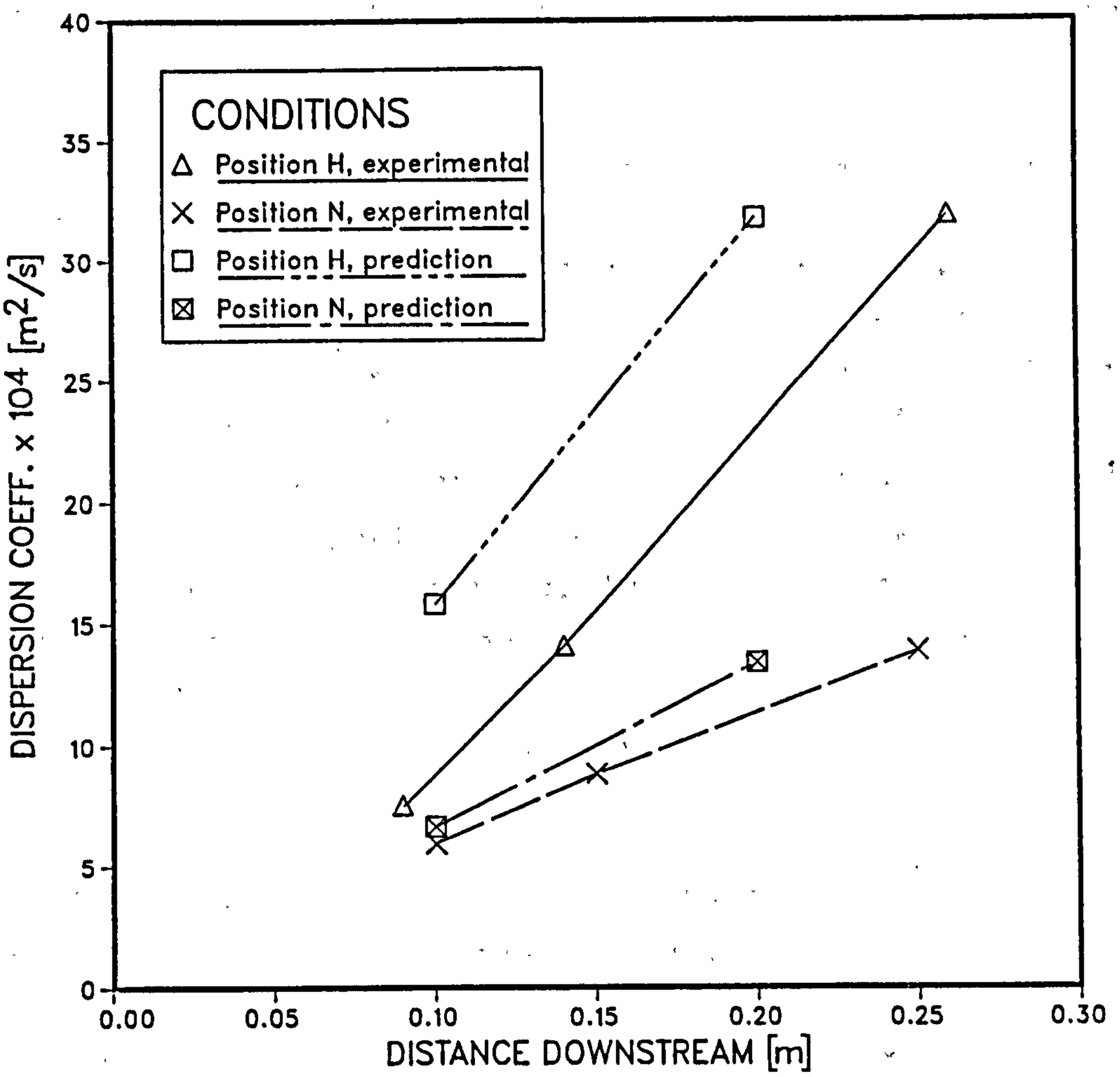

Fig. 4.7 Dispersion coefficient versus distance downstream from injection point

dispersion coefficient with distance downstream from the injection point. This suggests that either the average diffusion coefficient between the injection point and measuring zone varies with distance downstream, or that the correlation coefficient described in Section 1.4.1 is non-zero over the distances measured. Since the magnitude of dispersion coefficient values are similar at Stations H and N, for equivalent values of x, the second of these suggestions is most likely. This corresponds to the region where $x < 2x_o$.

Towle and Sherwood (1939) obtained a similar trend in their measurement of hydrogen and carbon dioxide concentration profiles in a long cylindrical duct. They attributed the increase in dispersion coefficient to the disturbance of the flow by the injection pipe. This is an unlikely explanation since a disturbance would increase the local dispersion coefficient, implying a decrease of D with distance from the injection pipe. To aid in the interpretation of their results, Towle and Sherwood defined an asymptotic value of dispersion coefficient D', where

$$D' = \frac{\Delta(Dx)}{\Delta x} \approx D + x\frac{dD}{dx} \qquad (4.2)$$

Hinze (1959, pp.341) suggested that the increase in D was due to the grid located upstream of the injection point. Just downstream of the grid, the scale of turbulence will be reduced causing a decrease in the turbulent mixing. In this case, the asymptotic value D' represents the mixing that would occur with no grid present. The approximation becomes more accurate for large values of x, where the gradient term becomes smaller and $D' \longrightarrow D$. Due to the linear nature of the data in Figure 4.7, it may be assumed that the measurements correspond to values of x less than x_o. Application of equation 4.2 to these results would require

careful interpretation due to the large gradient term.

To estimate the characteristic length scale of the turbulent flow, a measure of the Lagrangian integral length scale was required, l_L. In the Lagrangian description, the variation of a property connected with a given packet of fluid is considered during the motion of the fluid packet through the flow field. A value of l_L has been defined by Taylor in terms of the Lagrangian correlation coefficient, $R_L(\Delta t)$ which is difficult to measure experimentally. Photographic techniques may be employed, although they tend to be tedious and involve averaging over many particles. Alternatively, Taylor's theory may be used to calculate $R_L(\Delta t)$ from concentration profiles measured at various distances downstream from a point source of material. A more detailed description of this method may be found in Kalinske and Pien (1944). The procedure involves double differentiation of empirical data and is prone to large errors.

A much easier parameter to measure is the Eulerian correlation coefficient $R_E(\Delta t)$, and the corresponding Eulerian integral length scale l_E defined as

$$l_E = v' \int_{\Delta t=0}^{\infty} R_E(\Delta t)\, d(\Delta t)$$

where $R_E(\Delta t) = v(t)v(t+\Delta t)/v'^2$.

A value for $R_E(\Delta t)$ may be calculated from the fluctuating velocity trace of a hot-wire anemometer, obtained as described in Section 3.2.1. The numerator is the product of the velocity at pairs of points, separated by an interval corresponding to time Δt. If $R_{E\ t}(\Delta t)$ is plotted against Δt for various values of Δt, a correlation curve as shown in Figure 4.8 is obtained, from which l_E may be calculated. For a sufficiently large time interval Δt^*, the correlation coefficient falls to zero and the Eulerian length scale may

be defined as

$$l_E = v' \int_{\Delta t=0}^{t^*} R_e(\Delta t) d(\Delta t)$$

This procedure has been performed on a hot-wire anemometer trace measured at the centre of the duct with similar conditions as those used in obtaining the results of Figure 4.7. A Vanguard/Minc was programmed to store the coordinates of the numerous points on the velocity trace. From the calculations, a value of l_E = 0.118 m has been determined. At present, no theoretical relationship between the l_L and l_e has been established although various empirical relations have been determined.

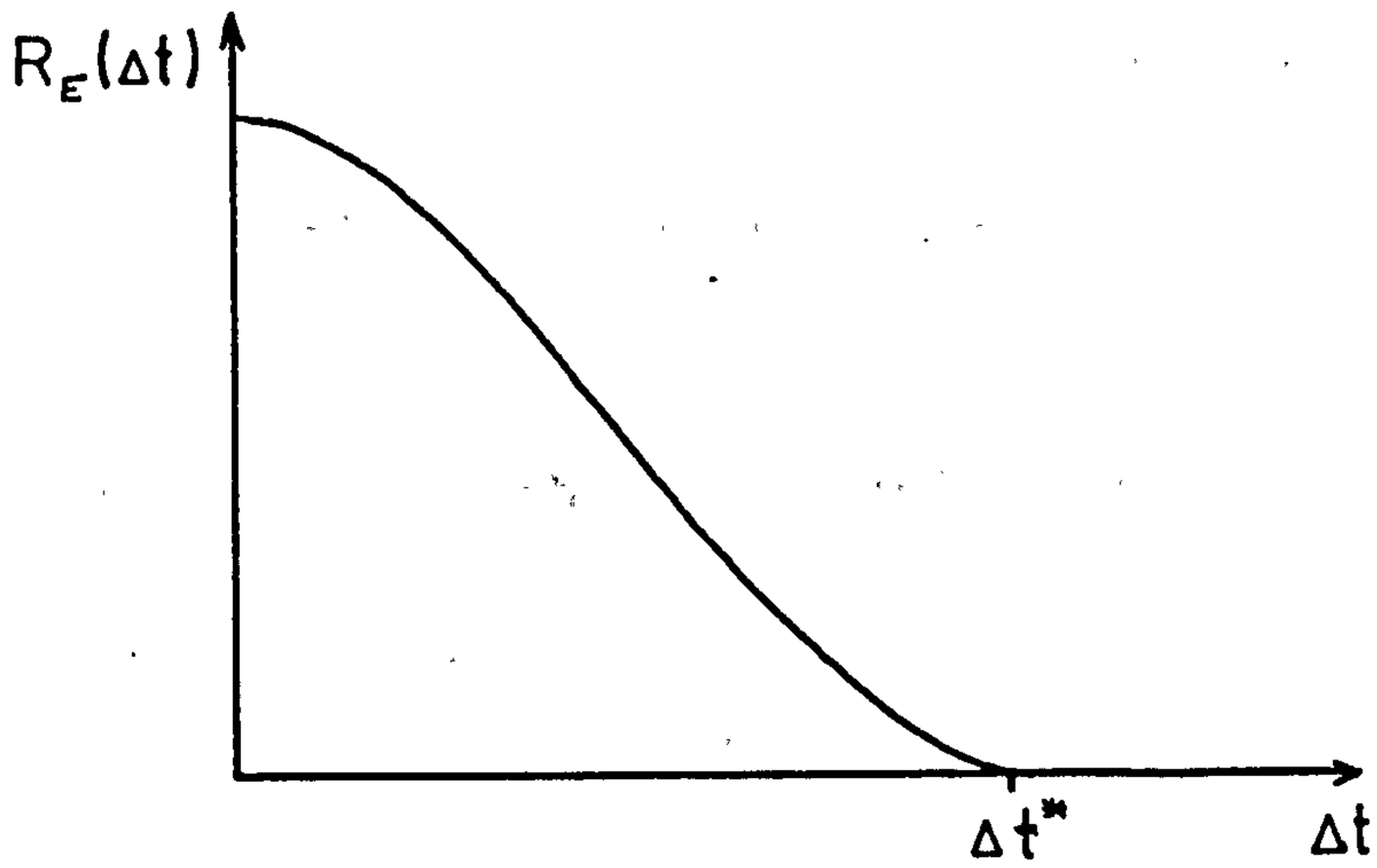

Fig. 4.8 Example of a correlation coefficient curve

The above calculations suggest that to obtain diffusion coefficient values representative of the full range of eddy sizes, concentration profiles would have to be measured at least 0.25 m downstream from the injection point. Such values are not sufficiently localised for the requirements of this work. Consequently, dispersion coefficients have been determined corresponding to a much smaller length scale of 50 mm.

Seinfeld (1985) emphasised the importance of the mean square displacement of the aerosol from a line through the source, parallel to the mean flow. This quantity represents the width of the aerosol plume from which the variance σ_z^2 may be calculated. In a stationary, homogeneous turbulent flow, the variance of the concentration distribution σ_z^2 at locations close to the source can be described by

$$\sigma_z^2 = \sigma_u^2 t^2 \qquad (4.3)$$

where σ_u^2 = variance of the fluctuating velocity distribution.

According to Crank (1956), the two-dimensional spread of a point source may be described by the expression

$$c(t) = \frac{1}{\sqrt{4\pi Dt}} \exp(-r^2/4Dt) \qquad (4.4)$$

For small values of r, this expression reduces to Wilson's equation 4.1 since

$$\begin{aligned} r^2 &= s^2 - x^2 \\ &= (s+x)(s-x) \\ &\approx 2x(s-x) \end{aligned}$$

Equating the exponential term in equation 4.4 with that describing a Gaussian curve yields the following relationship

$$\sigma_z^2 = 4Dt$$

Substituting σ_z^2 from equation 4.3 yields

$$\begin{aligned} D &= \sigma_u^2 t/2 \\ &= \sigma_u^2 x/2U_o \end{aligned}$$

Hence, for small values of x, a graph of D versus x should produce a straight line with slope $\sigma_u^2/2U_o$.

Since the r.m.s. transverse fluctuating velocity v' is by definition mathematically equivalent to the standard deviation of the distribution, the dispersion coefficient can be described in terms of v' and the distance downstream from the source as follows:

$$D = (v')^2 x/2U_o \qquad (4.5)$$

The application of this expression is discussed further in Section 4.2.3.3.

4.1.4 Results and discussion

Experimental conditions investigated were;

a) gas velocity,
b) applied discharge electrode voltage,
c) position in duct,
d) inlet flow modulation,
e) presence of wall strengtheners.

Four downstream locations G, H, L and N were available for measuring dispersion coefficients. A DISA constant-temperature hot-wire anemometer was used to determine local gas velocity values in the duct (see Section 3.2.1). As flow conditions were generally turbulent, mean velocity values were used. These were obtained by averaging the velocity over a 100 second interval.

4.1.4.1 Reproducibility

To obtain confidence in the dispersion coefficient measurement technique, reproducibility tests were performed

at Position N with a gas velocity of 1.5 ms^{-1}. The 0.1 m flow modulation pipes were installed, and the wall strengtheners removed. Six scans of the aerosol plume were made, and dispersion coefficient values were determined from the concentration profiles as explained in Appendix A. Table 4.1 shows the results of the tests.

Result no.	Dispersion Coeff. (m^2/s x 10^4)
1	1.29
2	1.32
3	1.53
4	1.57
5	1.50
6	1.38

Table 4.1 Results of reproducibility tests

Results 1-5 were taken within five hours of each other, and result 6 was taken three days later. The mean value of the results is 1.43 x 10^{-4} m^2s^{-1} ($\pm$ 10%).

4.1.4.2 Effect of anisokinetic injection

To obtain dispersion coefficients truly representative of the fluid flow in the precipitator, the velocity of the injected aerosol must equal that of the mainstream gas flow. Since flow conditions in the duct were turbulent, this requirement could never be satisfied. The best that could be achieved was for the aerosol injection velocity to equal the time-averaged mainstream velocity.

To test the effect of anisokinetic injection on the apparent dispersion coefficient, measurements were made for a range of injection velocities at a constant mainstream gas velocity. The measurements were made at Position N, and to

accentuate the effect, the tests were performed in the absence of flow modulation pipes and wall strengtheners. Table 4.2 shows the results of the measurements made with a mainstream gas velocity of 1.5 ms^{-1}.

Aerosol Vel. (ms^{-1})	Dispersion Coeff. x 10^4 (m^2s^{-1})
0.32	0.940
1.50	0.403
2.25	0.323

Table 4.2 Results of anisokinetic injection tests

The results suggest that anisokinetic injection is a non-linear effect which is more apparent at low velocities.

4.1.4.3 Effect of applied voltage

The effect of discharge electrode voltage on dispersion coefficient was measured at Position N with wall strengtheners and flow modulation pipes installed. The aerosol injection pipe was positioned 0.1 m from the duct wall and the applied voltage was increased from zero to a value near the sparkover threshold. The dispersion coefficient values measured for a range of voltages are shown in Figure 4.9.

The results show an increase in dispersion coefficient of 75% between 0 and -65KV. This may be accounted for by either an increase in turbulence due to the presence of electric wind, or the electrostatic repulsion of the charged aerosol droplets. This second effect was minimized by choosing an aerosol in the size range coinciding with the minimum electrical mobility. If the particles had acquired sufficient levels of charge to cause electrostatic repulsion, the centre of the plume would have drifted

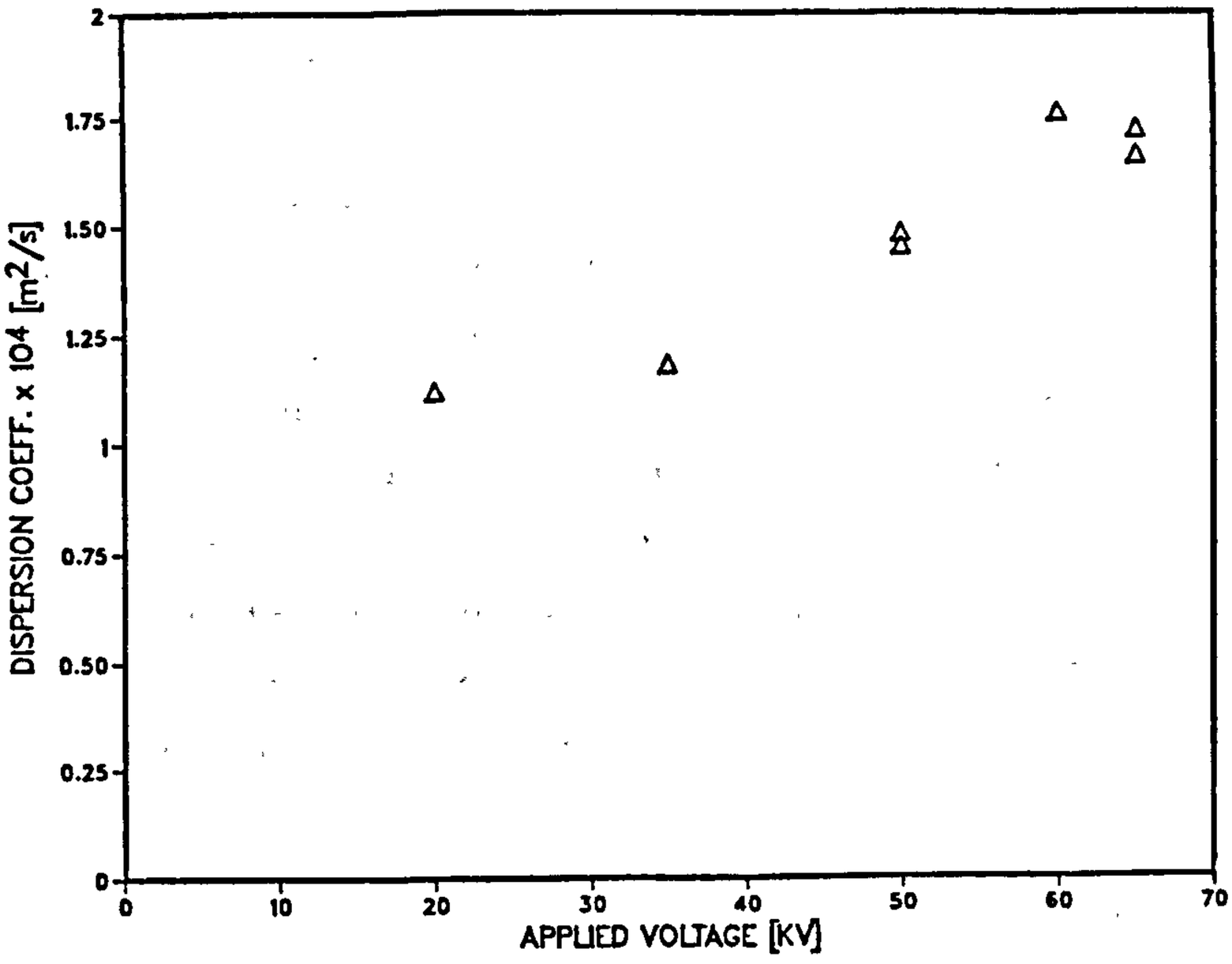

Fig. 4.9 Effect of applied voltage on dispersion coefficient

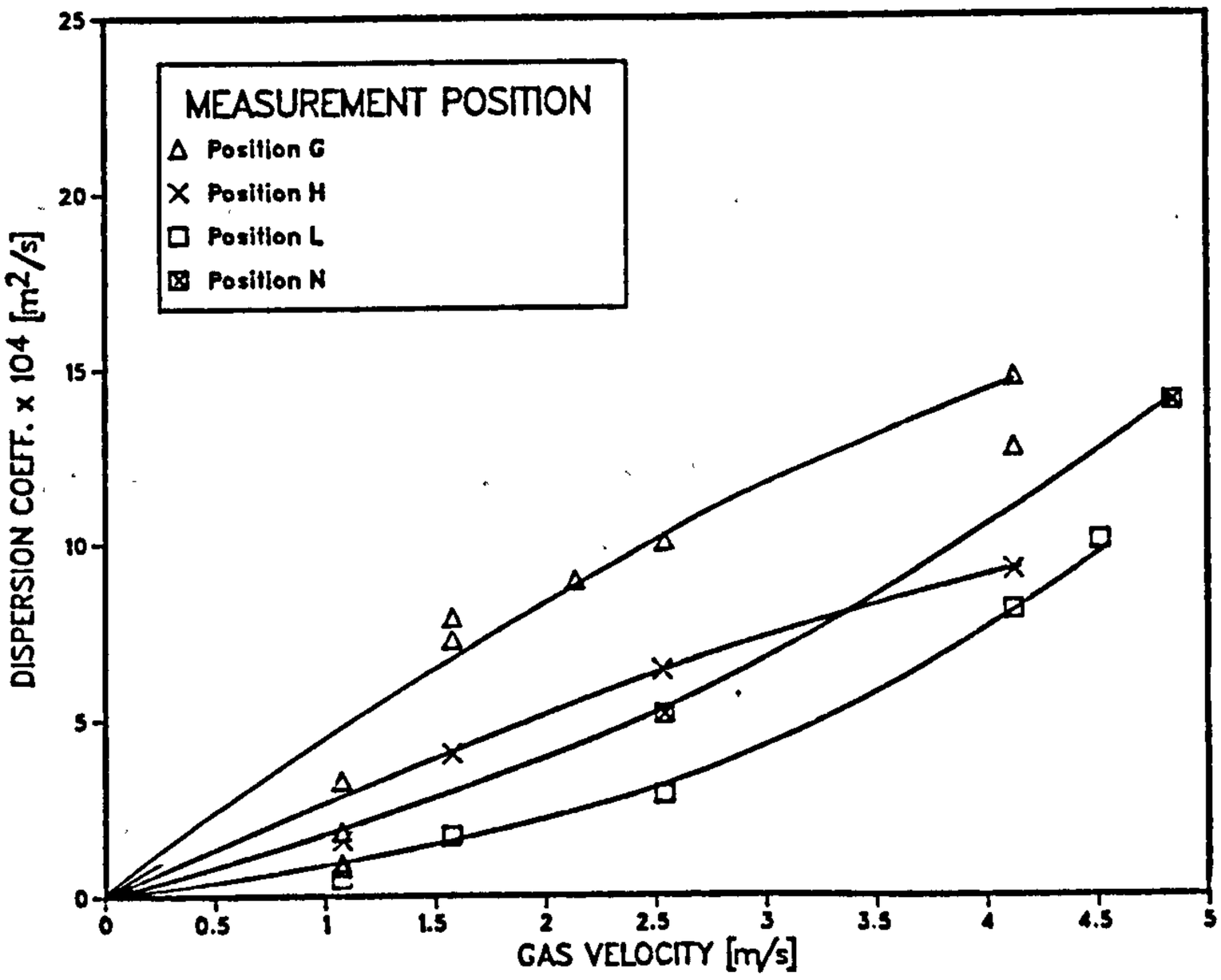

Fig. 4.10 Effect of gas velocity on dispersion coefficient

towards the precipitator walls. Since no such drift was observed, the increase in D was attributed to the effect of the electric wind.

The turbulence induced by the electric wind is essentially due to an effective two-dimensional jet emanating from the discharge electrode. Yamamoto and Velkoff (1981) suggested the formation of large-scale circulation currents in the precipitator duct, as shown in Figure 1.4. Although the currents increase back-mixing of the fluid, their influence on particle motion comprises a steady-state convective drift. As such, their effect should not be included in a dispersion coefficient.

4.1.4.4 Effect of gas velocity

Dispersion coefficient values were evaluated at Stations G, H, L and N for a range of gas velocities with the strengtheners and flow modulation pipes installed. The injection pipe for all measurements was positioned 0.12 m from the duct wall, and an applied voltage of -65KV was maintained.

For fully developed flow in a smooth pipe, Blausius determined an empirical relationship describing the friction factor ϕ such that

$$\phi = 0.04(Re)^{-0.25} \qquad (4.6)$$

Considering the pressure drop down pipes, the friction velocity v^* may be defined as

$$v^* = U_o\phi^{0.5} \qquad (4.7)$$

Substituting ϕ from equation 4.6 into equation 4.7 yields

$$v^* = 0.2U_o Re^{-0.125}$$
$$\propto U_o^{0.875}$$

Davies has shown that v^* is equivalent to the transverse fluctuating velocity v' in the turbulent fluid fairly close to the wall. Hence,

$$v' \propto U_o^{0.875} \qquad (4.8)$$

In Section 4.1.3 it was shown that the dispersion coefficient could be described in terms of v' such that

$$D \propto v'^2/U_o$$

Substituting v' from equation 4.8 gives

$$D \propto \frac{(U_o^{0.875})^2}{U_o}$$
$$D \propto U_o^{0.75}$$

Figure 4.10 shows that this relationship agrees closely with the profiles observed at Stations G and H.

The results also indicate a decrease in D with distance downstream, except at Station N. The larger values of D close to the duct inlet are due to the effect of the 0.1 m flow modulation pipes. The unexpected increase in D at Station N may be explained by the close proximity of the wall strengtheners.

4.1.4.5 Dispersion coefficient profile across the duct

(i) Without strengtheners

A dispersion coefficient profile across the precipitator duct was measured at Station N with 0.1 m flow modulation pipes installed. Initial tests were performed

with no wall strengtheners or applied voltage at a gas velocity of 1.5 ms^{-1}. The results displayed in Figure 4.11 show the value of D to decrease significantly as the wall is approached, with a factor of 2.3 between the values at 20 and 117 mm from the wall. Measurements were then made with an applied voltage of -65 KV which increased the value of D by about 70% (note the similarity to the increase observed in Section 4.1.4.3).

An identical experiment was carried out at a gas velocity of 2.6 ms^{-1}. The results displayed in Figure 4.12 show a similar decrease in D towards the collection wall. The higher velocity measurements showed no appreciable change in D when a voltage of -65 KV was applied.

A feasible explanation of these results is that at low velocities, electric wind may play a significant part in turbulence production thereby causing an increase in dispersion coefficient. At higher velocities the effect of electric wind is much less significant.

(ii) With strengtheners

A similar experiment to that described above was performed with wall strengtheners installed. A comparison of dispersion coefficient profiles measured at Station G (with strengtheners) and Station N (without strengtheners) is shown in Figure 4.13. The measurements were made at a gas velocity of 1.5 ms^{-1} in the presence of the 0.1 m flow modulation pipes.

The results show the wall strengtheners to have a drastic effect on the magnitude of D, particularly at locations close to the wall. Towards the centre of the duct, the dispersion coefficients measured with and without strengtheners are similar. This suggests that the effect of

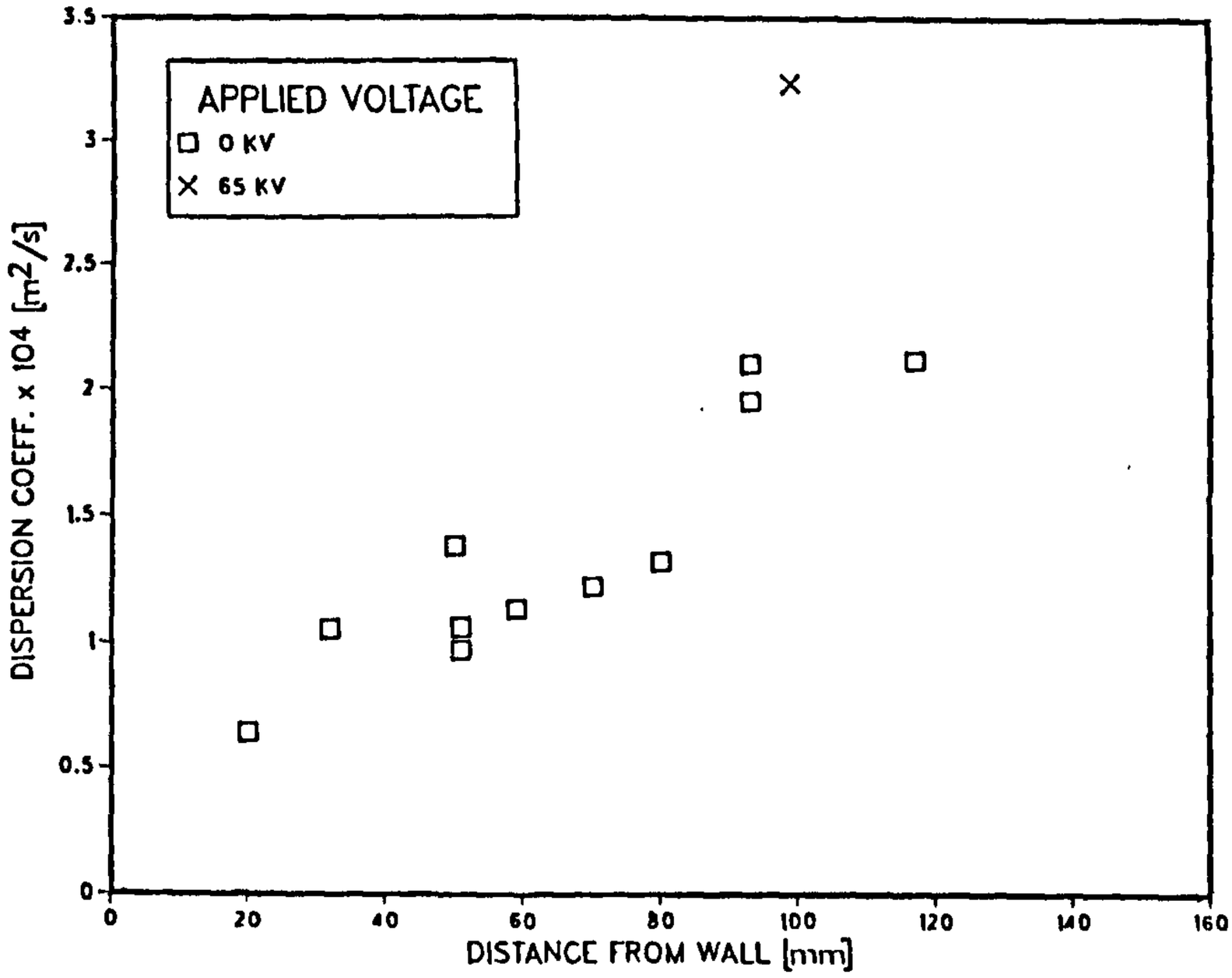

Fig. 4.11 Dispersion coefficient profile across precipitator duct (U_o=1.5 ms^{-1})

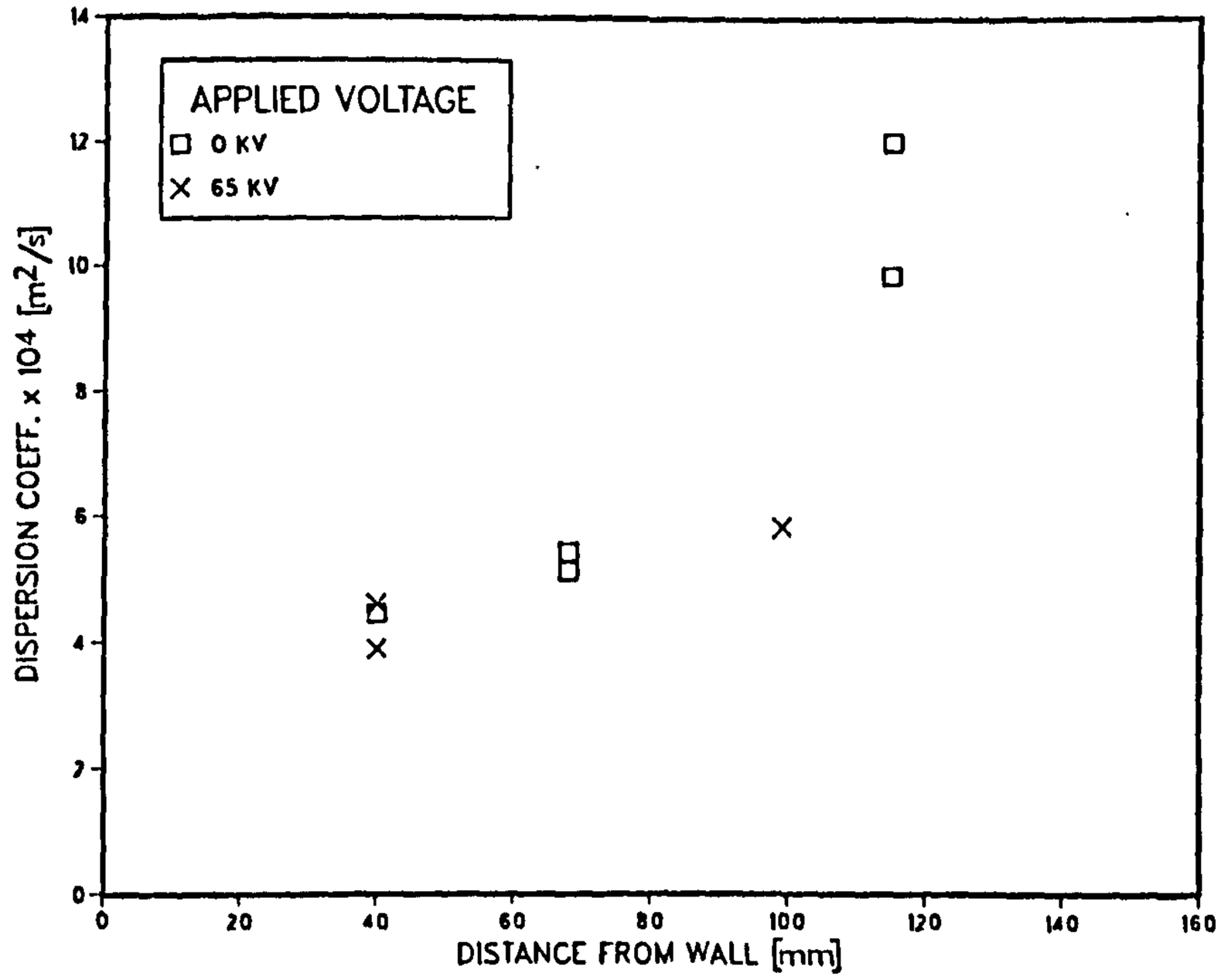

Fig. 4.12 Dispersion coefficient profile across precipitator duct (U_o=2.6 ms^{-1})

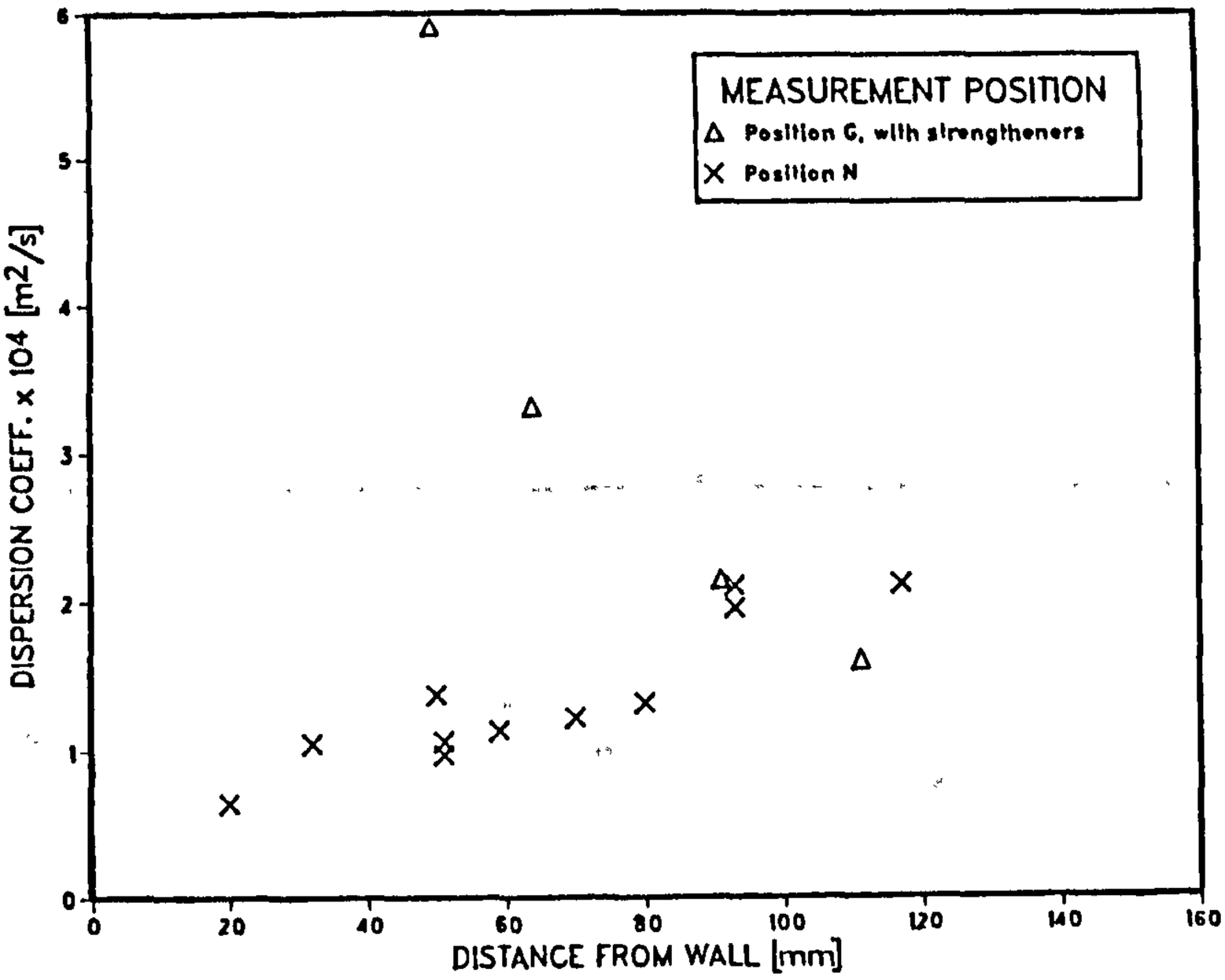

Fig. 4.13 Effect of wall strengtheners on dispersion coefficient profile

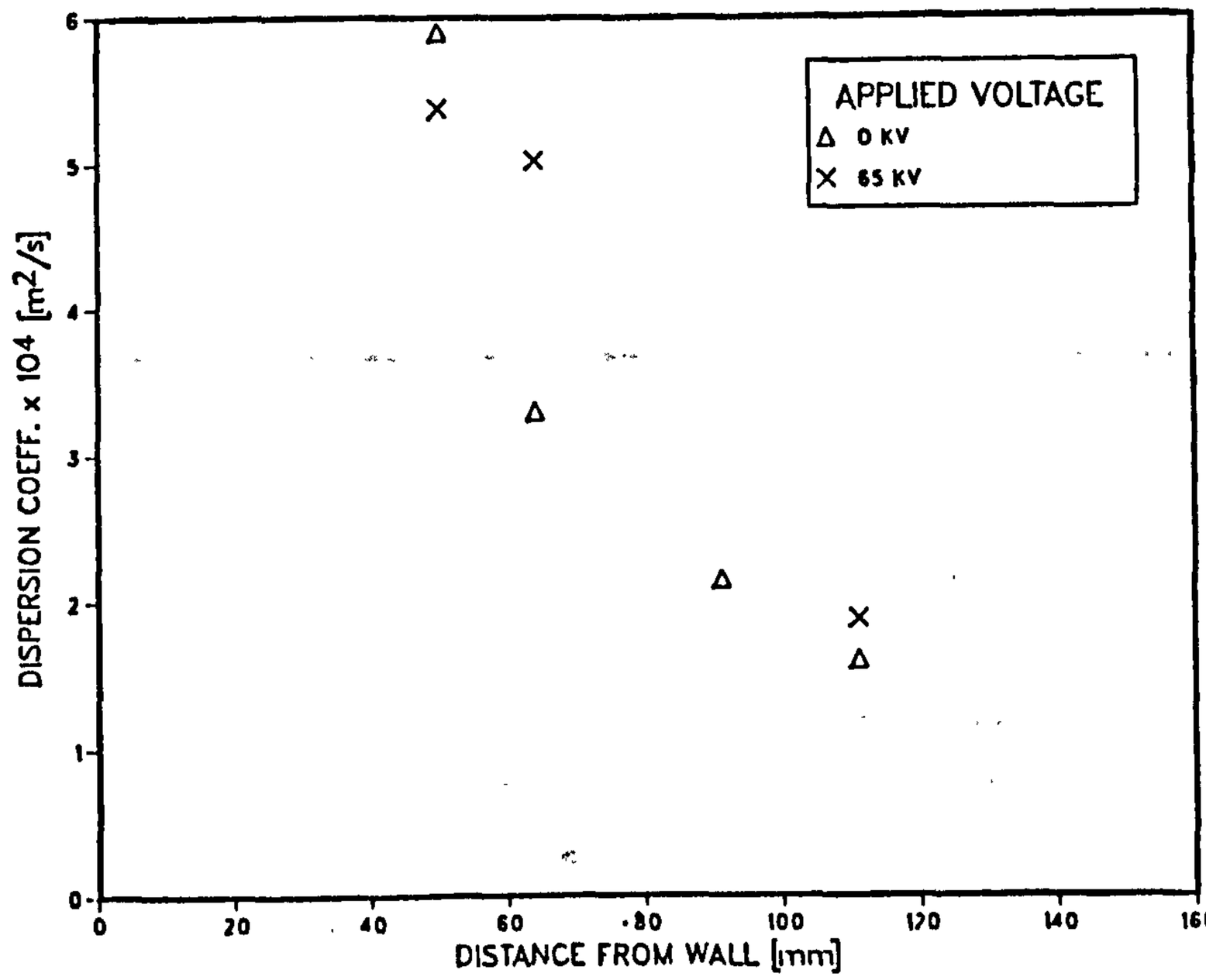

Fig. 4.14 Effect of applied voltage on dispersion coefficient profile (with wall strengtheners)

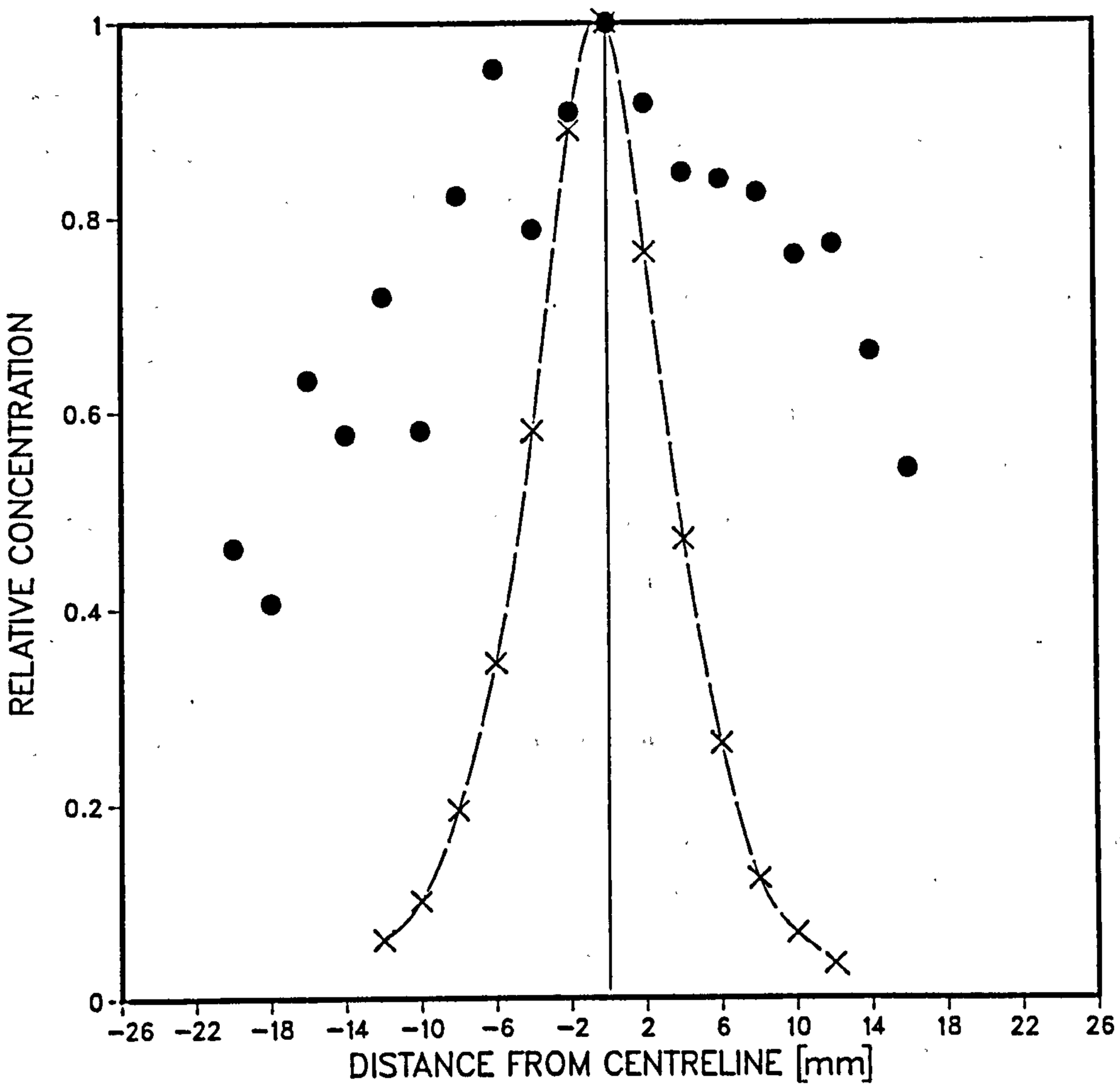

Fig. 4.15 Comparison of a typical aerosol concentration profile (×) with that downstream of a wall strengthener (●)

the strengtheners is localised, but important with respect to collection conditions at the wall.

Figure 4.14 shows the effect of applied voltage on the dispersion coefficient profile at Station G with strengtheners present. The effect is negligible when compared to that of the strengtheners.

To measure the concentration profile of the aerosol behind the wall strengthener, the injection pipe was inserted through a hole cut in the downstream edge of the strengthener. A comparison of the resulting profile was made with that obtained at a typical measurement location 0.1 m from the duct wall, as shown in Figure 4.15. The central line corresponds to the position of the injection pipe, and the data represents the spread of aerosol 50 mm downstream of the injection point. The results indicate that the flow in this region would not be well characterised by a dispersion coefficient value, since the concentration profile is not well described by a Gaussian distribution curve.

4.1.4.6 Effect of inlet flow modulation

Dispersion coefficient values were measured for a range of turbulence conditions in the precipitator duct. All measurements were made with a gas velocity of 1.5 ms^{-1} and an applied voltage of -65KV at Position H. Turbulence conditions were controlled by the presence of wall strengtheners and flow modulation pipes. The results are shown in Table 4.3.

Pipe diameter (m)		Wall	Dispersion Coeff.
0.05	0.1	Strengtheners	(m^2s^{-1} x 10^4)
No	No	No	0.323
Yes	No	No	0.365
Yes	No	Yes	0.492
No	Yes	No	4.65
No	Yes	Yes	7.58

Table 4.3 Dispersion coefficient values for various turbulence conditions

From the results it appears that the flow modulation pipes produce the greatest influence on the dispersion coefficient values. Changing the pipe diameter from 0.1 to 0.05 m decreases the values of D by more than a factor of 10, whereas the introduction of wall strengtheners increases D by less than a factor of 2. It must be remembered though that these measurements were taken at a position 0.12 m from the wall where the effect of the wall strengtheners will be minimal.

Insufficient literature on the flow field downstream of a series of pipes, such as those found at the precipitator inlet, is available for the purpose of theoretical predictions. A simple approximation might be to simulate the pipes by two adjacent two-dimensional jets. The main objections to this type of model are;

a) two-dimensional turbulent jet theory suggests that diffusion coefficient values increase with distance downstream. This contradicts the results found in Section 4.1.4.4,
b) insufficient information is available on the effect of adjacent jets.

More work needs to be done in this area, since the inlet turbulence conditions in a precipitator determine initial back-mixing of the dust, which encourages uniform charging of the particles.

4.2 Fluctuating velocity components

4.2.1 Background

In fully developed turbulent flow there is a wide spectrum of eddy lengths. The largest eddies, of a size comparable to the diameter of the duct, are responsible for much of the mass transfer that occurs in turbulent motion. Prandtl defined a mixing length l as the mean distance of travel of the packets of fluid before they become indistinguishable with the fluid at a new position (see Davies (1978)). Drawing on analogies with viscous flow, Prandtl was able to equate the product of the mixing length l, and the mean transverse fluctuating velocity component v' to the eddy viscosity such that

$$\nu_E = v'l$$

This eddy viscosity is responsible for the transport of momentum in turbulent flows. Limitations to the accuracy of this approach become more obvious when the transport of mass is investigated in a similar way. The whole spectrum of eddies and their interactions contribute to the mass flux, and the concept of pulses of fluid moving instantaneously in a linear fashion is seen to be a considerable oversimplification.

The complicated interactions have been conveniently accounted for by replacing the Prandtl momentum mixing length l with a mixing length representative of mass transfer l_m to obtain

$$D = v' l_m$$

The ratio D/ν_E depends on the physical properties of the system and the intensity of turbulence and is generally found to be greater than unity. In the wake downstream of a cylinder, the ratio may approach a value of 2. Many authors have investigated the relationship between D and ν_E under different conditions of flow.

In both of the above cases, knowledge is required of the transverse fluctuating velocity component, v'. To characterise the flow in an electrostatic precipitator and gain insight into the extent of back-mixing occurring, profiles of axial and transverse fluctuating velocity components, u' and v', were measured in the duct. The ratio of these values at a given position indicates the extent of fluid isotropy. Measurements of v' were made at Stations H and N, in an attempt to correlate dispersion coefficient and r.m.s. transverse fluctuating velocity values as described in Section 4.1.3.

4.2.2 Experimental procedure for measuring fluctuating velocity components

Fluctuating velocity components were measured using the laser-Doppler photon correlation technique as described in Section 3.2.2. Measurements were made at Positions D, F, G, I and J, as displayed in Figure 3.11, corresponding to the measurement locations of the time-averaged velocity profiles, measured by laser-Doppler photon correlation.

4.2.3 Results and discussion

4.2.3.1 Time-averaged and fluctuating velocity components

(i) Axial

Figures 4.16 and 4.17 show profiles of time-averaged and r.m.s. fluctuating axial components of velocity across the precipitator duct at Positions D, F, G and I. The results obtained at Position J have been omitted to avoid over-crowding of the graphs. Due to their similar locations, the results at Position J were found to be very similar to those at Position I.

Trends shown in the time-averaged axial velocity profiles have been previously discussed in Section 3.4.2. At Position D, the velocity profile is flat, corresponding to the region upstream of the discharge electrodes and wall strengtheners. At Position F the velocity profile is influenced by the presence of the strengtheners. The values close to the strengthener are retarded, whilst the values between the facing strengtheners are increased. Up to this point, no particular trends are evident in the fluctuating velocity components of Figure 4.17. The profiles at Positions D and F remain flat at a value of 0.3 - 0.4 ms^{-1}. This corresponds to a turbulence intensity of 15 - 25%.

At Position G the effect of strengtheners is most marked, with the time-averaged velocity falling to zero inside the vortex downstream of the strengthener. As before, the velocity in the region between facing strengtheners compensates by increasing to maintain the volumetric throughput. At this point, a significant change occurs in the fluctuating components. Behind the strengthener, v' decreases to a value of 0.25 - 0.3 ms^{-1}. Moving towards the centre of the duct, the fluctuating

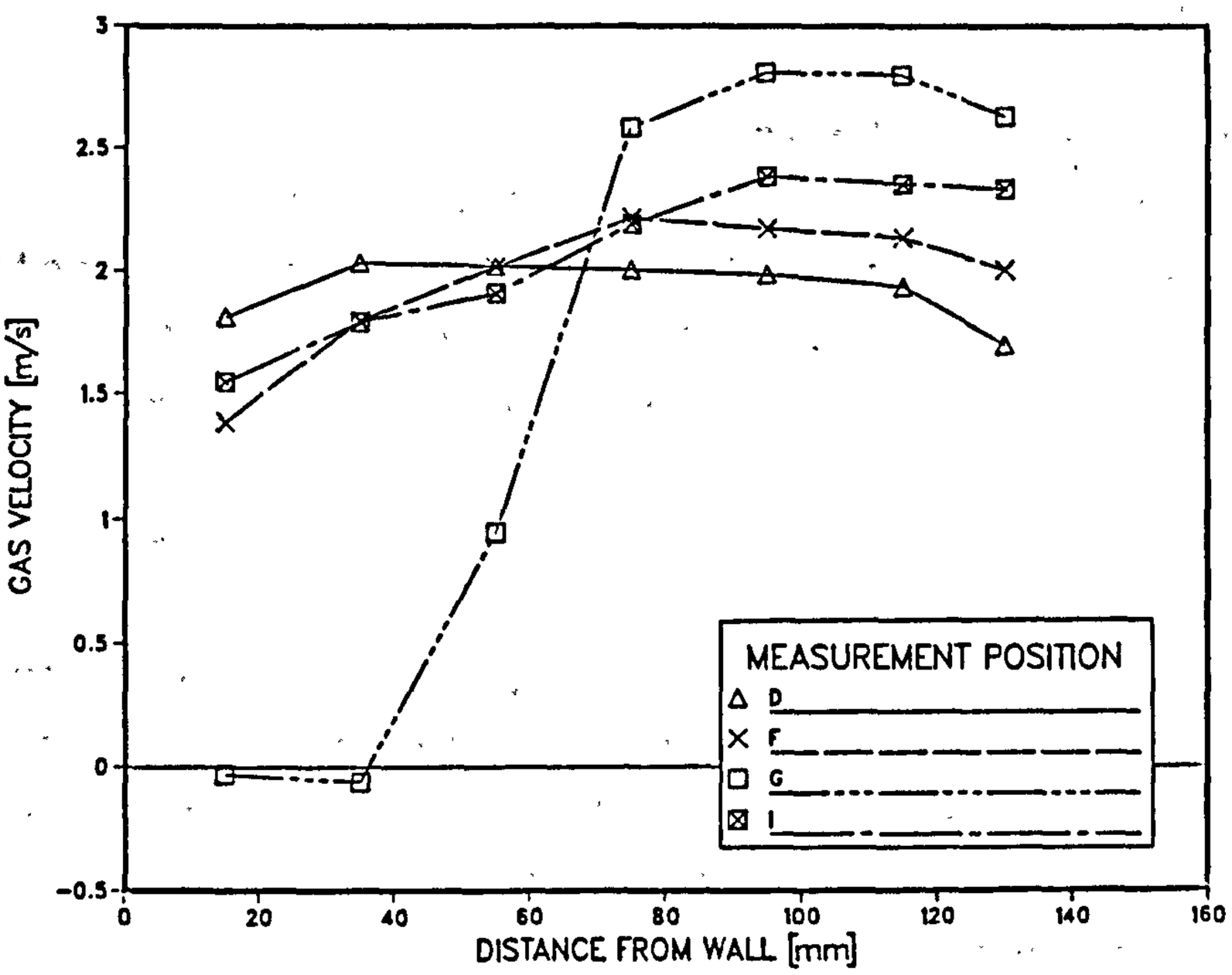

Fig. 4.16 Time-averaged axial velocity component

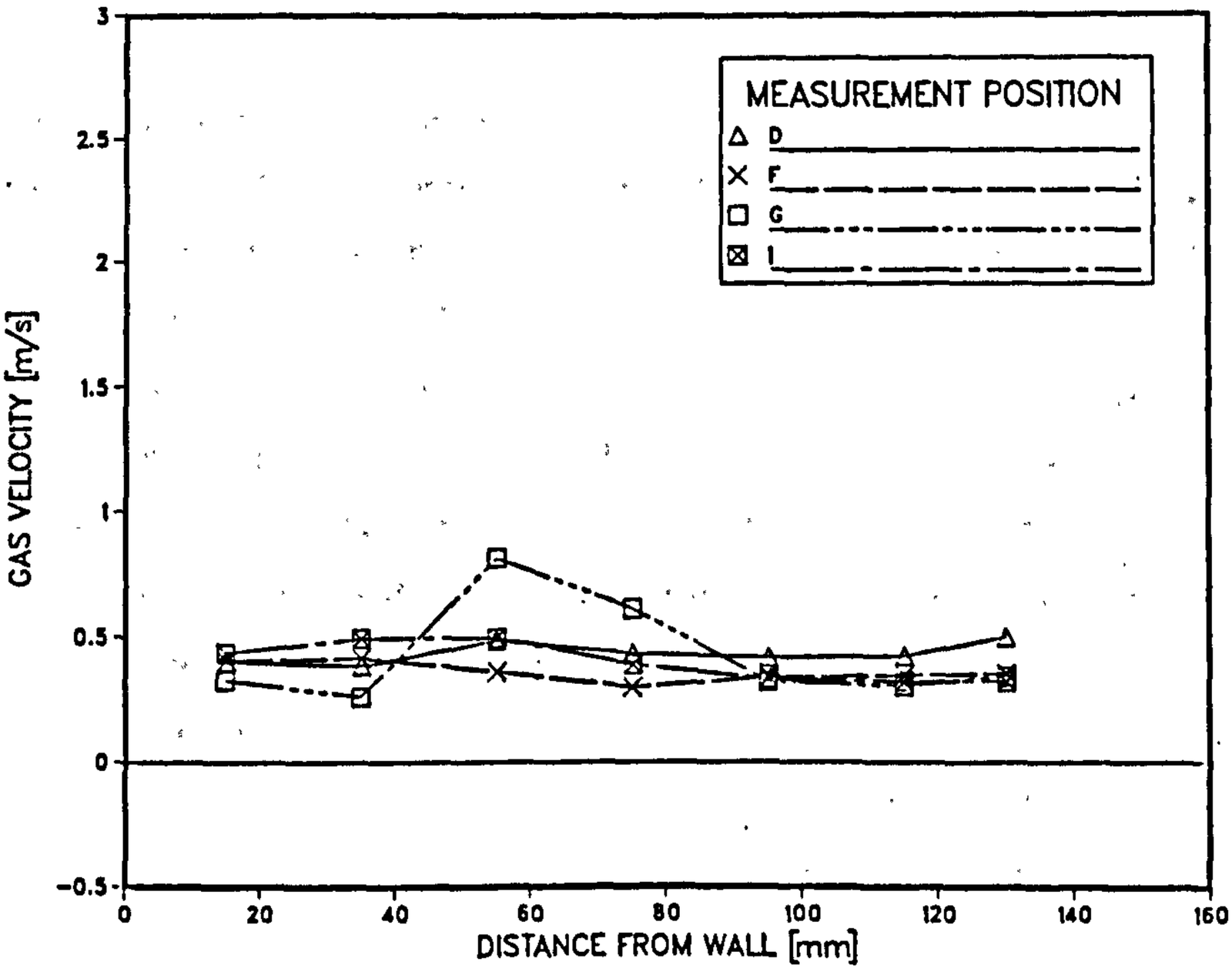

Fig. 4.17 Fluctuating axial velocity component

velocity increases rapidly at the location corresponding to the edge of the strengthener, and then falls gradually, attaining similar values to those at Position F.

At Position I, the time-averaged gradient across the duct is still present, although less pronounced than at Position G. The fluctuating velocity values have returned to an almost flat profile, but with slightly higher values occurring near the collection wall.

(ii) Transverse

Figures 4.18 and 4.19 show time-averaged and r.m.s. fluctuating transverse velocity components across the precipitator duct at Positions D, F, G and I. Again the results at Position J have been omitted. Positive values represent velocities towards the collection wall.

At Position D the time-averaged velocity components show no particular trend. The fluctuating velocity profile is fairly flat except for a gentle decrease in value from 0.4 ms^{-1} at 60 mm from the wall to 0.25 ms^{-1} at 15 mm from the wall.

Indicated in Figure 4.20 is the direction of the time-averaged velocity components at Position F and G. Note that the length of the arrows is not representative of the speed of the gas flow. At Position F the time-averaged velocity value close to the wall is directed towards the wall, whereas that close to the strengthener arm acts towards the centre of the duct. Inside the strengthener, the directions of the time-averaged components indicate the presence of a vortex. The three values just outside the strengthener are directed towards the centre of the duct, due to the diversion of streamlines around the strengthener. The change in direction of the three values closest to the

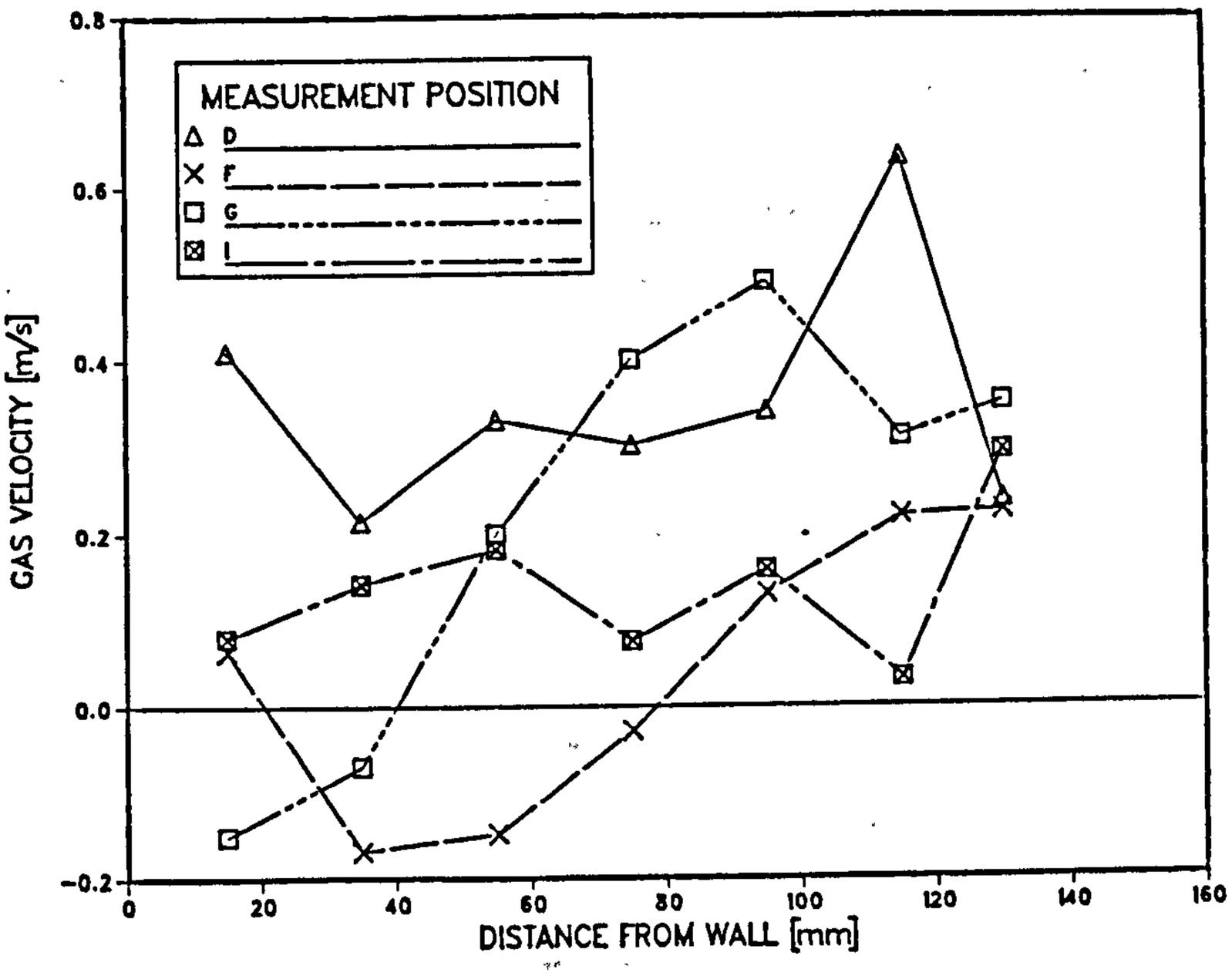

Fig. 4.18 Time-averaged transverse velocity component

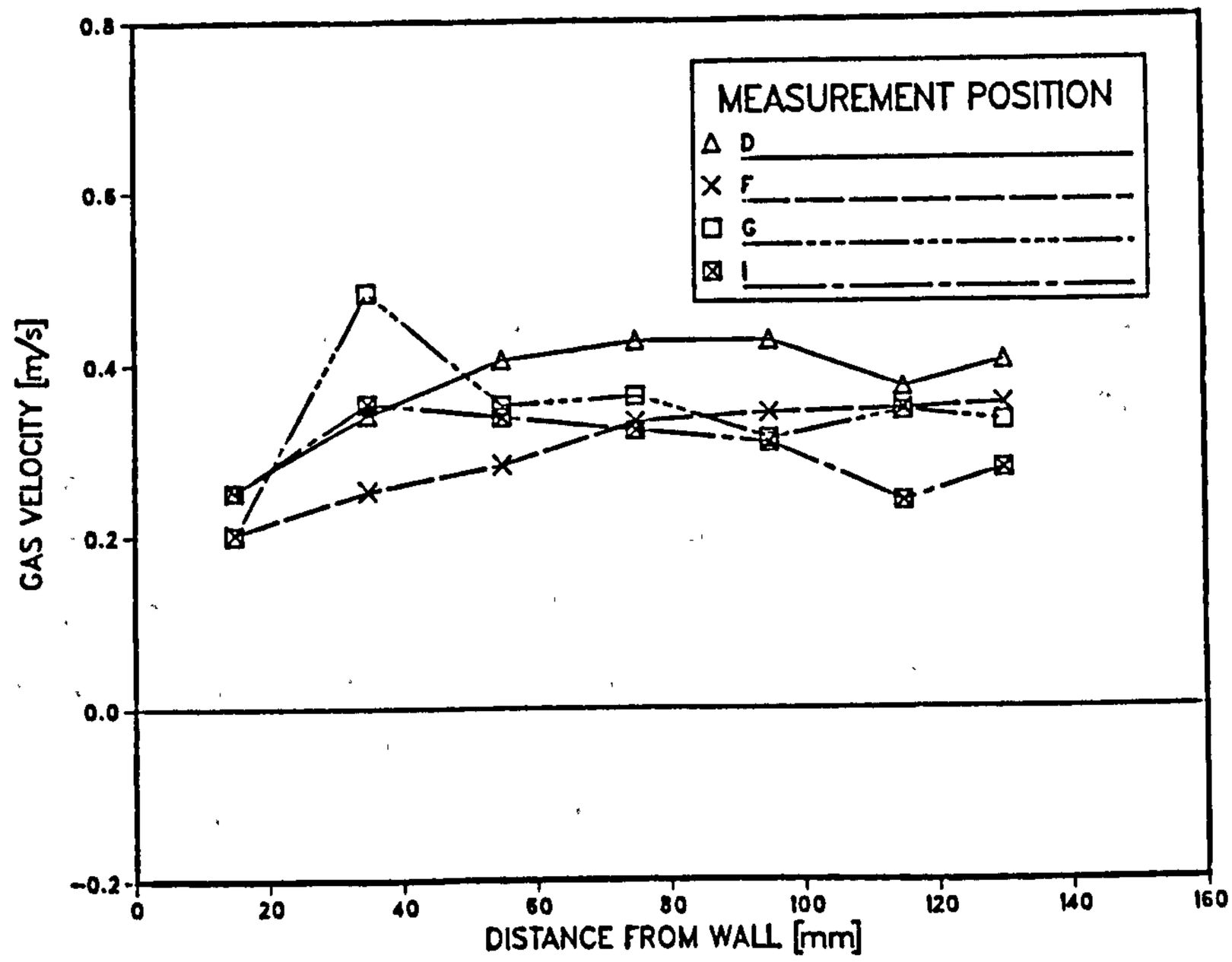

Fig. 4.19 Fluctuating transverse velocity component

centre of the duct is probably due to the diversion of the flow field around the second discharge electrode. At Position G, the two velocity values closest to the wall are directed towards the centre of the duct, again indicating the presence of a vortex. The remaining values are directed towards the collection walls indicating the return of the streamlines to the wall around the vortex.

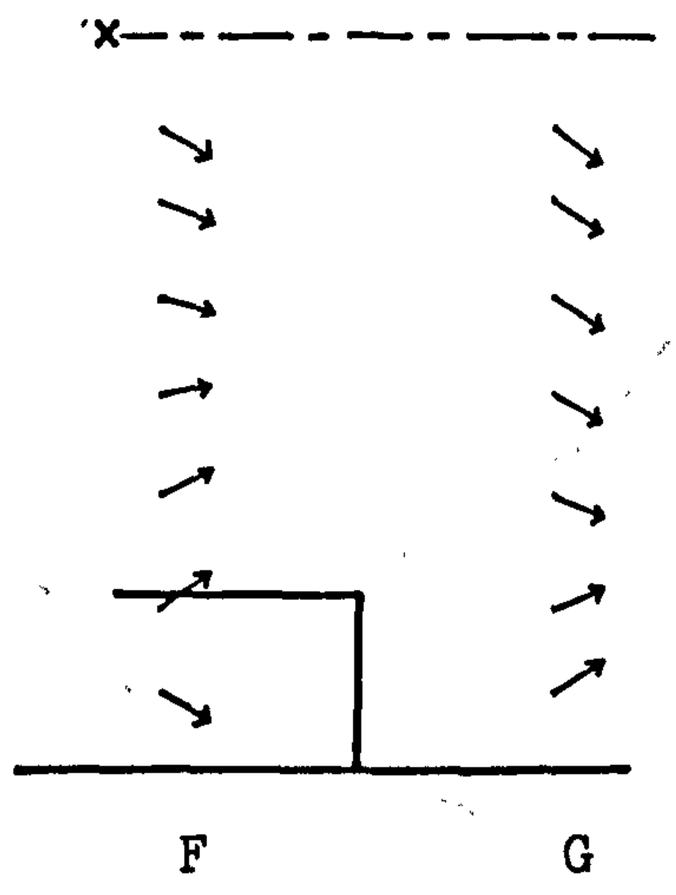

Fig. 4.20 Direction of time-averaged velocity components at positions F and G

Figure 4.19 shows the fluctuating transverse velocity profile at Position F to be significantly lower than that at Position D, although the values follow a similar trend - decreasing gradually from the centre of the duct to the wall. At Position G the fluctuating component increases markedly to a peak value, just inside the wall strengthener. At Position I, neither the time-averaged nor the fluctuating values show any particular trends.

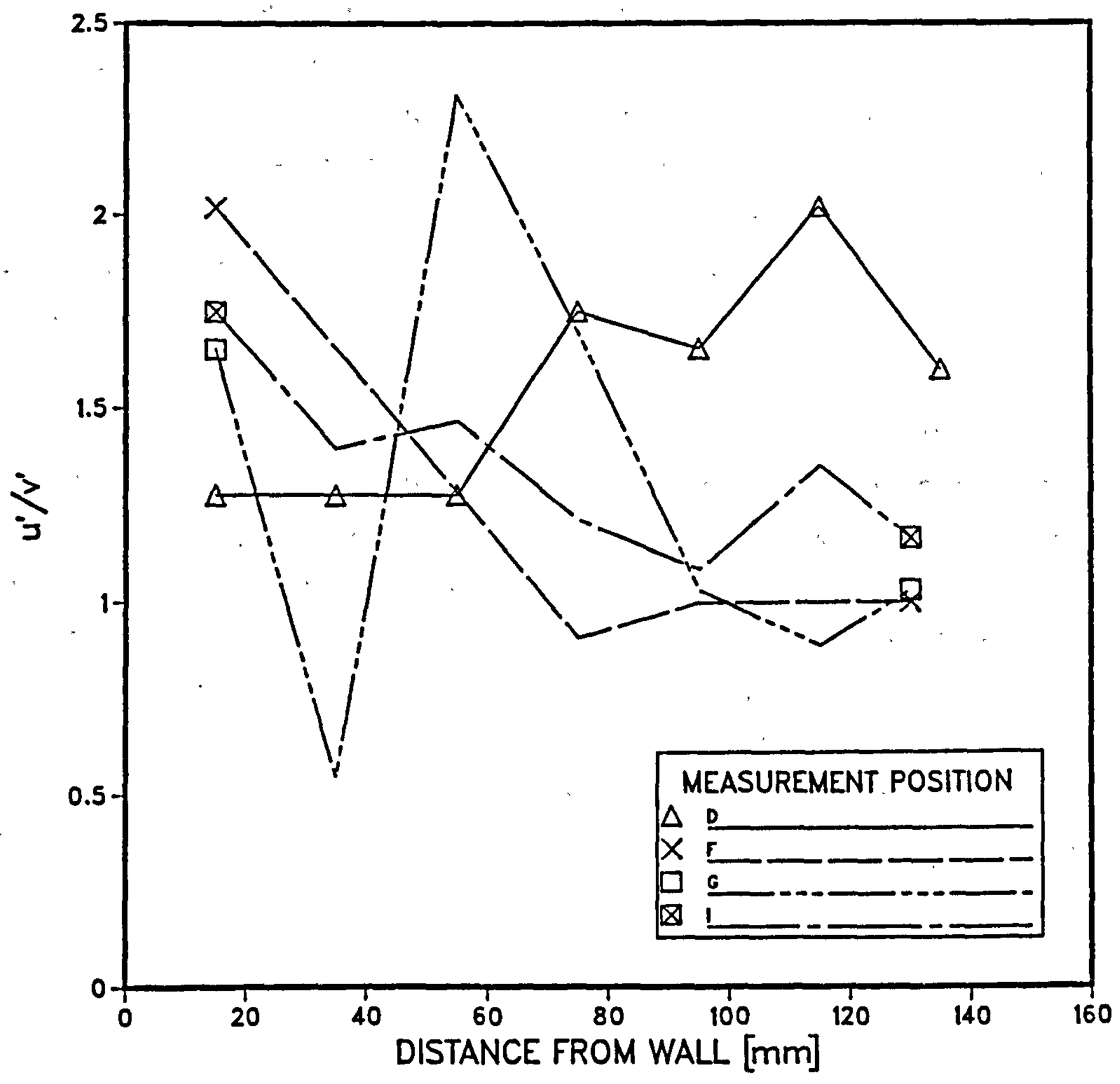

Fig. 4.21 Ratio of axial to transverse fluctuating velocity components

4.2.3.2 Ratio of axial to transverse fluctuating velocity

Shown in Figure 4.21 are values of the ratio of axial to transverse fluctuating velocity components, u'/v', measured across the precipitator duct at Stations D, F, G, I and J. For isotropic turbulence, this ratio will be 1. As can be seen from the graphs, this condition is rarely attained. In most cases, u' is greater than v' and the ratio increases towards the wall. At Station D the reverse trend may be observed, with almost isotropic conditions extending approximately 60 mm into the duct from the wall. At Station F a linear decay of u'/v' occurs from the wall to a distance halfway between the wall and the duct centreline. Isotropic conditions then prevail to the centre of the duct.

At Station G, u'/v' fluctuates markedly from point-to-point due to the close proximity of the wall strengthener. The values measured at distances of 15, 35 and 55 mm from the wall correspond well with those that would be expected at positions a, b and c of a vortex as shown in Figure 4.22. At position a and c, the gas velocity is in the axial direction and hence u'/v' > 1. At position b, the gas velocity is directed towards the wall resulting in u'/v' < 1. Further evidence in support of the vortex is obtained from the time-averaged axial velocity components displayed in Figure 4.16.

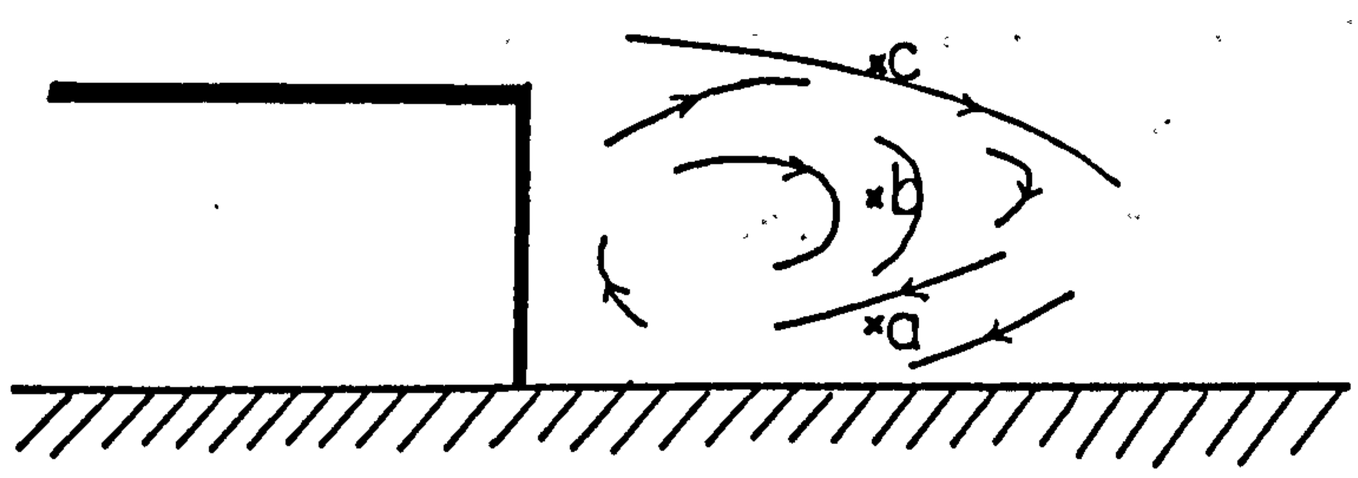

Fig. 4.22 Location of measurement positions a, b, and c behind strengthener

The values of u'/v' at Stations I and J are similar, which is to be expected because of their similar surroundings.

4.2.3.3 Relationship between r.m.s. fluctuating velocity and dispersion coefficient

As discussed in Section 4.1.1, dispersion coefficient values close to the injection point may be expressed in terms of the r.m.s. transverse fluctuating velocity component, v'. To test this theoretical relationship, values of v' were measured at Stations H and N with flow modulation pipes installed. The discharge electrodes were removed and measurements were made on the duct centreline, so that conditions were similar to those used in obtaining the results of Figures 4.7. The measured values of v' are shown in Table 4.4.

Position H	Position N
0.252	0.163

Table 4.4 R.m.s. transverse fluctuating velocities at Positions H and N.

Substituting the above values of v' into equation 4.3 enabled dispersion coefficient values to be calculated at distances of 0.1 and 0.2 m downstream from the aerosol source. The predicted results are as shown in Figure 4.7. The agreement between predicted and experimental values is satisfactory, thus validating the relationship between dispersion coefficient and r.m.s. transverse fluctuating velocity.

CHAPTER 5

MEASUREMENT OF DUST CONCENTRATION PROFILES

5.1 Introduction

A particle sampling method has been developed for extracting dust from the precipitator duct. This has provided an opportunity for assessing the effect of gas velocity, flow modulation pipes, wall strengtheners, applied voltage and electrode geometry on particle concentration and size distribution. The results have also provided data for comparison with theoretical predictions from the numerical models presented in Chapter 6.

An ideal method for measuring particle concentration would involve a non-intrusive technique, such as light scattering or extinction. Although such methods now exist for simultaneous measurement of particle size distribution and concentration, the technique is indirect and prone to resolution problems for small particles. This chapter describes the development and use of a sampling device which causes sufficiently small flow disturbance for the results to remain unaffected by its presence.

The particle size range of primary interest is 1-10 μm since it is within this range that precipitator efficiency falls to a minimum. The dust chosen for the majority of experimental work was alumina, which is easily dispersed and has no known health hazards. It is commercially available in a range of size fractions, and size analyses of different fractions showed alumina P15 to be most suitable. Figure 5.1 shows a comparison of the size distribution of alumina P15 analysed using the Coulter Counter and Sedigraph techniques. The Coulter Counter measures particle volume, and particle size is output as the diameter of the

equivalent sphere. The Sedigraph measures the settling speed of a particle, and a Stokes' diameter is returned. The close agreement between the curves in Figure 5.1 confirms microscope observation of the particles showing that the sphericity of the dust is close to unity. Also, for particle sizes of interest in this work (i.e. < 12 μm) the density of the dust is uniform.

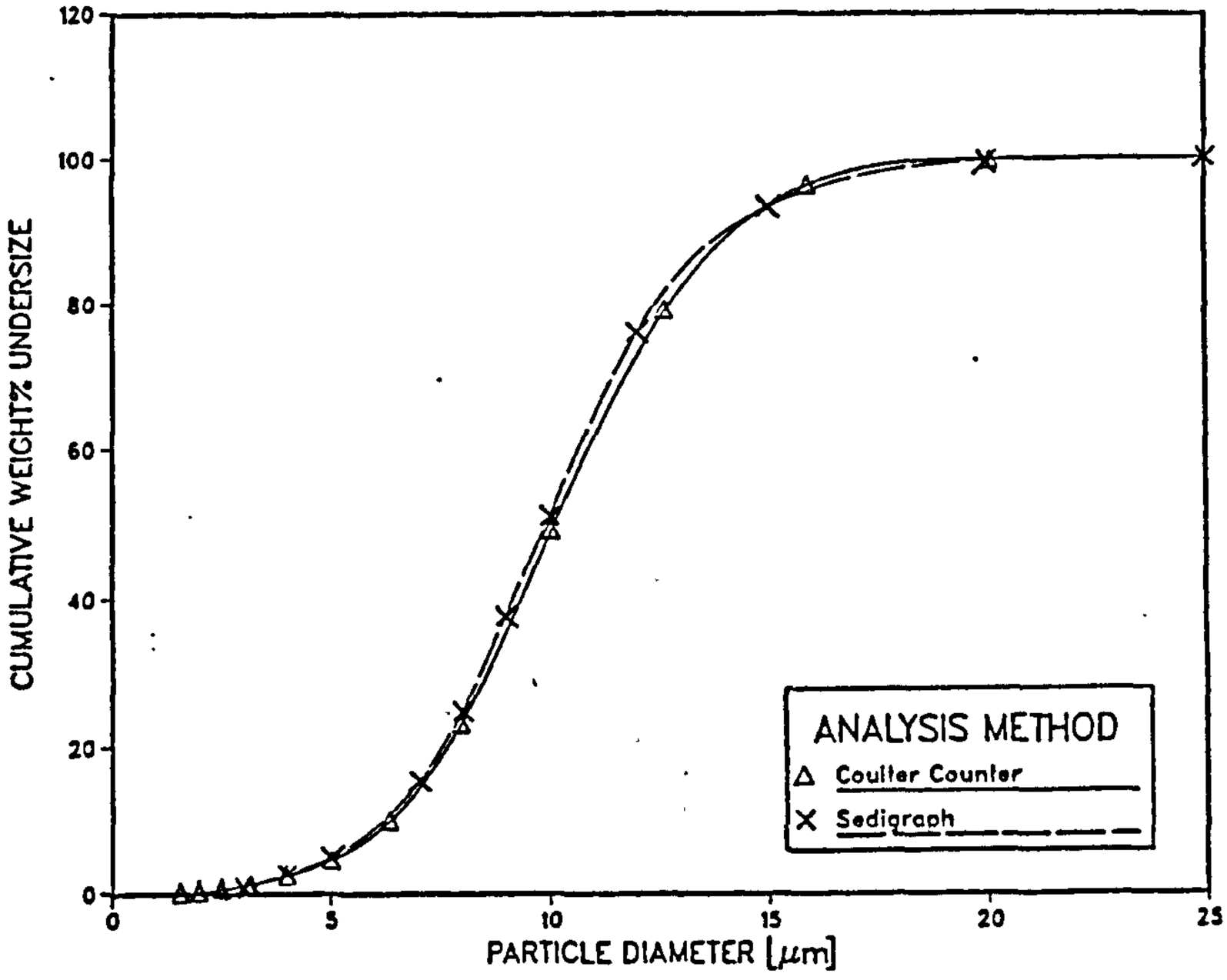

Fig. 5.1 Size analysis of alumina P15 test dust

5.2 Experimental procedure for simultaneous measurement of dust concentration and size distribution

5.2.1 Sampling device

The sampling device consisted of seven 5 μm pore-size, cellulose acetate/nitrate Millipore filters, mounted at the end of individual L-shaped glass pipes (see Figure 5.2).

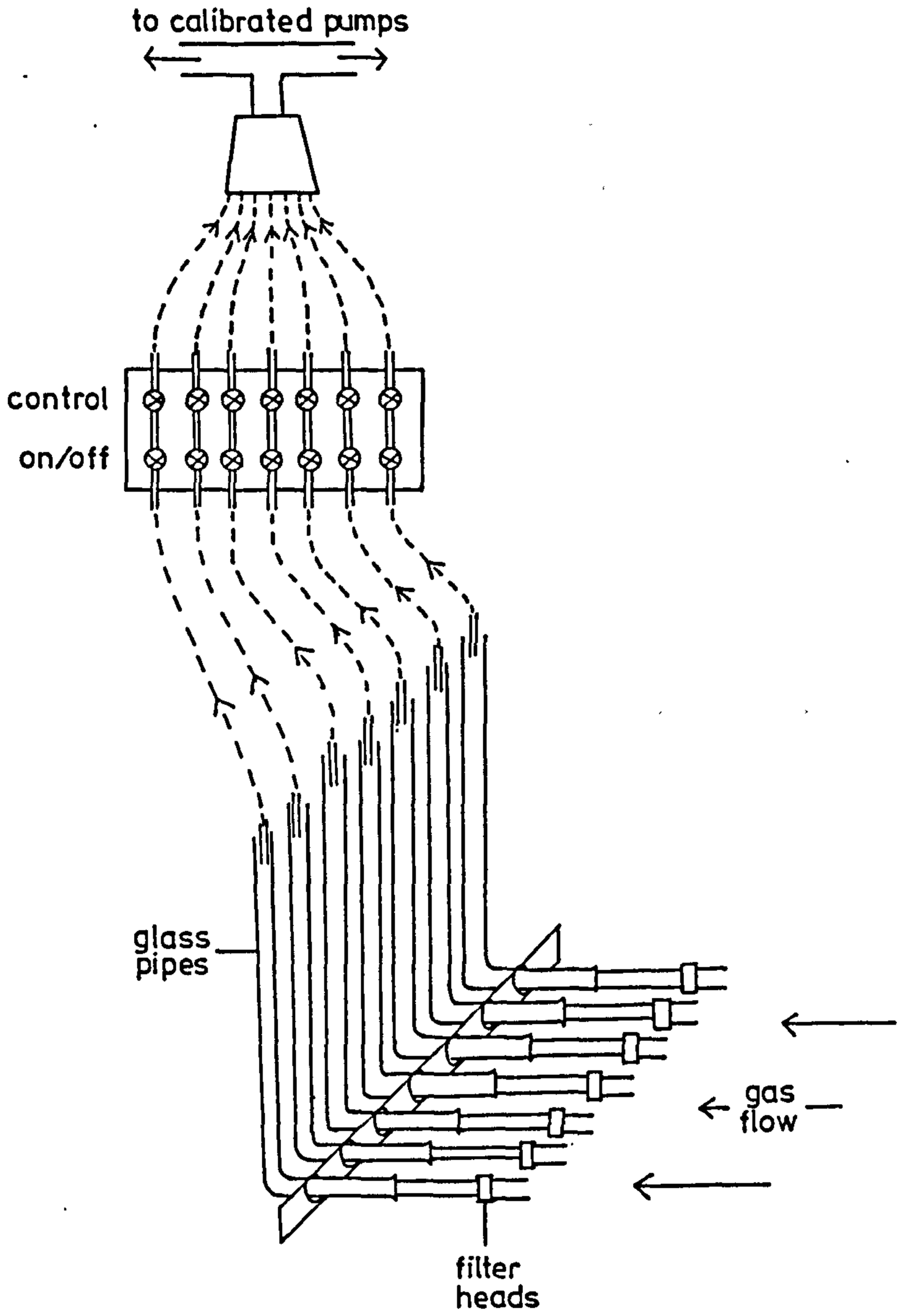

Fig. 5.2 Schematic diagram of particle sampling device

The array of pipes was supported by a perspex clamp to maintain the filter heads at a fixed distance apart. Cone and socket joints were incorporated along the horizontal sections of the glass pipes, allowing easy removal of the sampling heads without disturbing the whole system. Air-leaks at the cone/socket joint were eliminated by greasing the cones prior to each experiment, and attaching elastic bands across the joint. One end of the elastic band was

fastened around a glass hook, mounted between the filter head and the cone/socket joint, and the other was secured around the vertical section of the sampling line. Figure 5.3 shows an exploded view of the sampling heads. The front face of each filter cassette was cut back to allow for the insertion of the cassette head extension (see Section 5.2.4.1), without loss of exposed filter area.

Flow through the filter heads was maintained by two vacuum pumps attached in parallel to a glass manifold, as shown in Figure 5.2. Seven holes were drilled into the manifold bung, and a nylon pipe was passed through each hole, via two valves, to the sampling head. The first valve was used as an on/off switch for the gas flow, and the second controlled the face velocity of the filter.

The filter cassettes were glued into the ends of the glass pipes, ensuring alignment of the cassette head extensions in the vertical plane. Removal of the filter head array was most easily achieved by releasing the cone and socket joints and removing all seven filter heads together. Individual cassettes could then be carefully unscrewed, and the filter media removed with tweezers to avoid loss of dust. Concentration and size analyses of the dust samples were obtained using a Coulter Counter. Transfer of the dust from the filter medium to the electrolytic solution was performed with the aid of an ultra-sonic bath. To ensure complete removal of all the particles from the filter media, progressively longer periods of sonification were applied. Coulter Counter analysis of the solution showed that a sonification period of 90 seconds was sufficient to remove all the particles. Microscopic observation of the cleaned filter, submerged in immersion fluid, confirmed that no particles remained embedded in the complex internal structure of the filter media.

CONTAINS CLEAR OVERLAYS

OVERLAYS SCANNED SEPERATELY AND OVER THE RELEVANT PAGE.

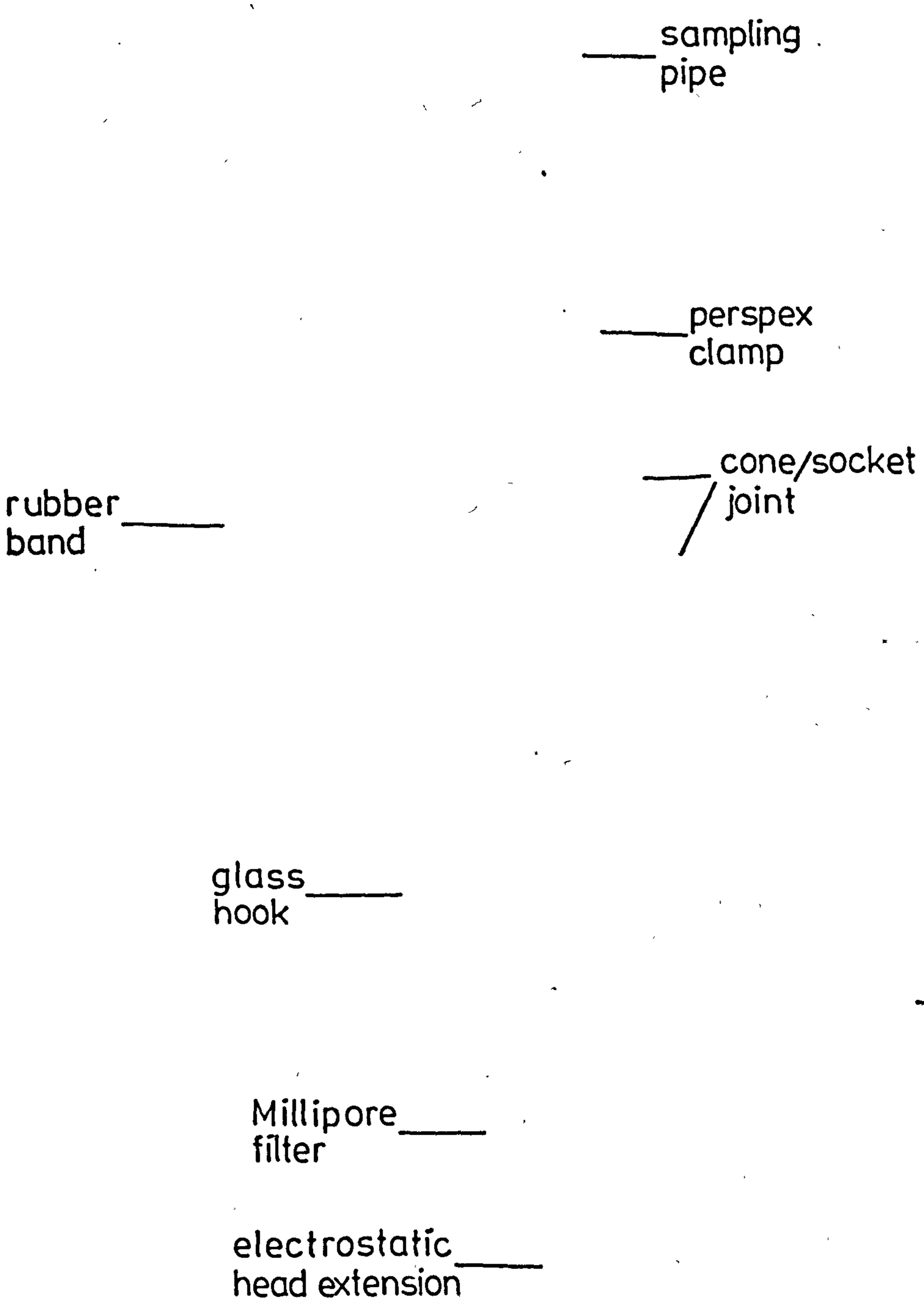

Fig. 5.3 Exploded view of sampling heads

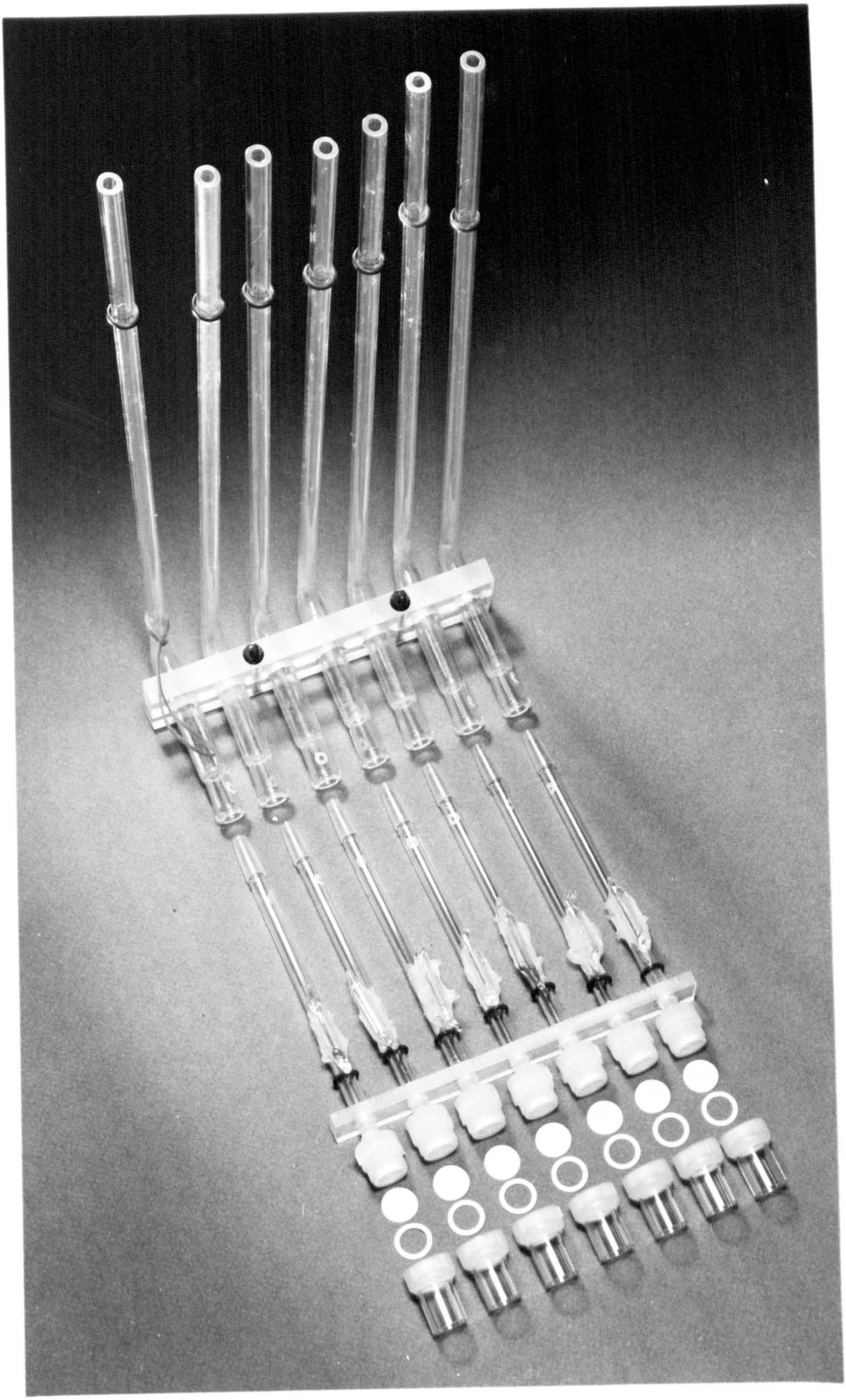

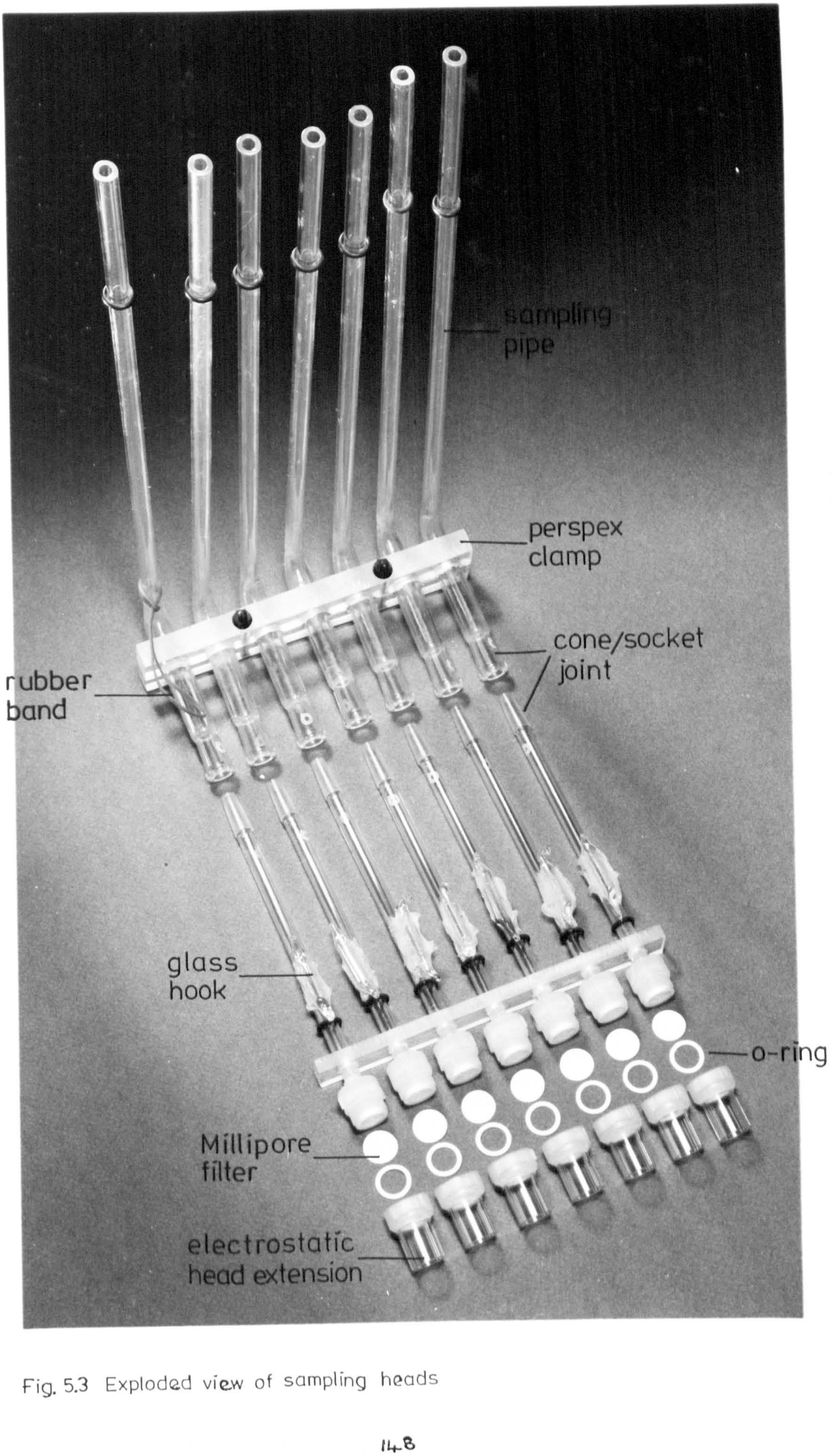

Fig. 5.3 Exploded view of sampling heads

Although sampling of particles with size down to 1 μm diameter was required, a pore-size of 5 μm was necessary so that a sufficiently high filter face velocity could be maintained. Liu et al. (1983) have measured the collection efficiency for different air sampling filter media as a function of particle size and filter pressure drop. The results show that for a 5 μm pore-size filter with a face velocity of 0.98 ms^{-1}, the collection efficiency of a 1 μm particle is greater than 99.99%. A velocity of 2 ms^{-1} will enhance collection still further.

At high dust loadings, the increased resistance will cause a reduction in the flow rate through the filter medium. The effect was checked by inserting a rotameter along the sampling line and measuring the velocity as a function of dust deposit level. The effect was found to be insignificant for dust loadings experienced during this work.

5.2.2 Dust feeder

A Venturi dust dispersion device (see Figure 5.4) was used to inject dust at a constant rate into the precipitator. The stationary feed-hopper emptied onto the rotating platform into which a series of circular grooves were cut. The platform then passed under a knife-edge scraper which removed the excess dust, leaving the grooves filled. The dimensions of a particular groove along with the rotation speed of the table defined the mass flow rate of the injected dust. Flow of the compressed air through a sonic nozzle provided sufficient pressure drop to lift the dust from the groove and through the suction pipe, by means of the Venturi effect. It also produced a high shear field, capable of breaking up dust agglomerates. The head of the suction pipe was profiled to encourage total removal of the dust from the groove. The dust was finally passed through

CLEAR OVERLAYS

OVERLAYS SCANNED SEPERATELY AND OVER THE RELEVANT PAGE.

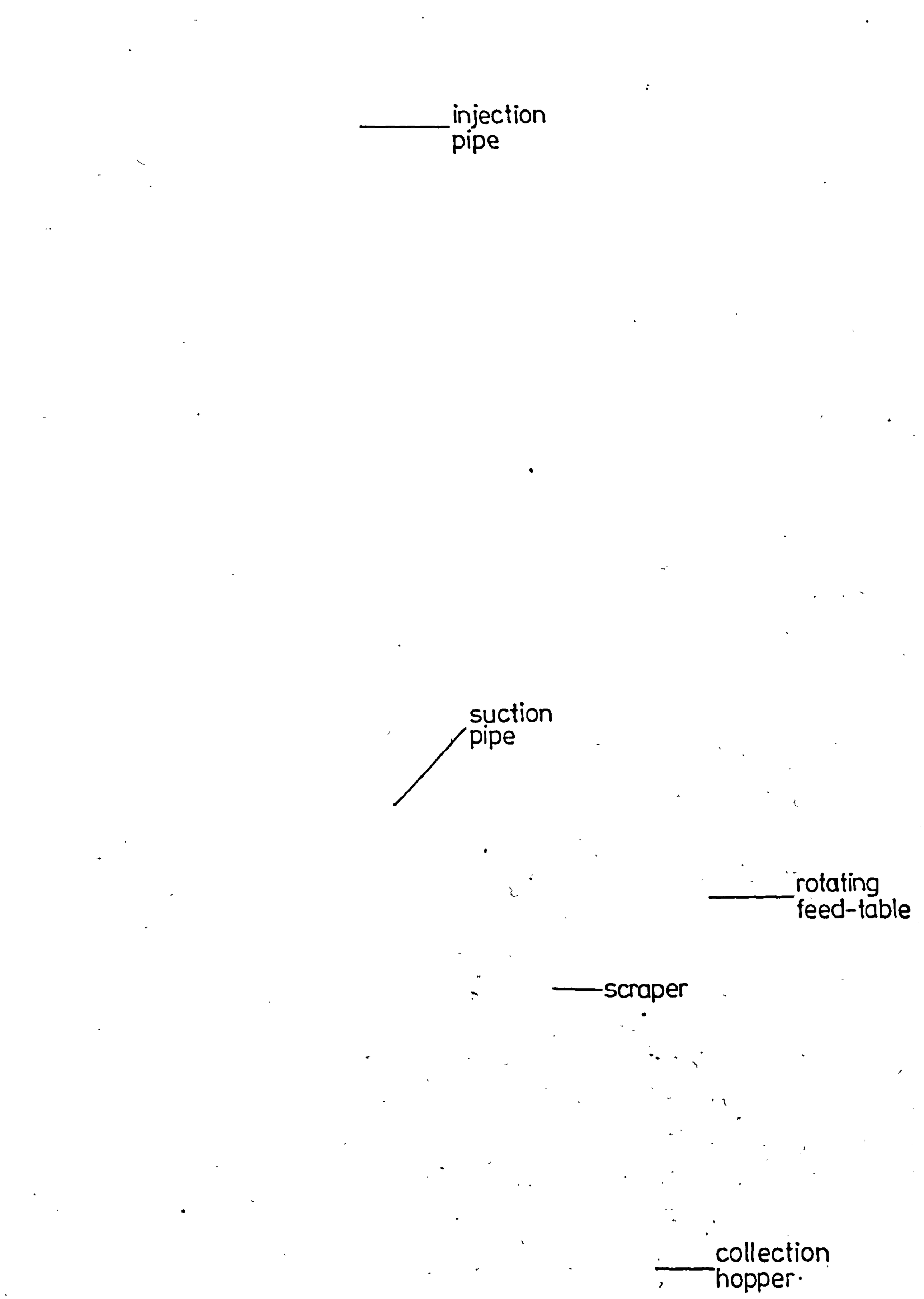

Fig. 5.4 Dust dispersion and feed device

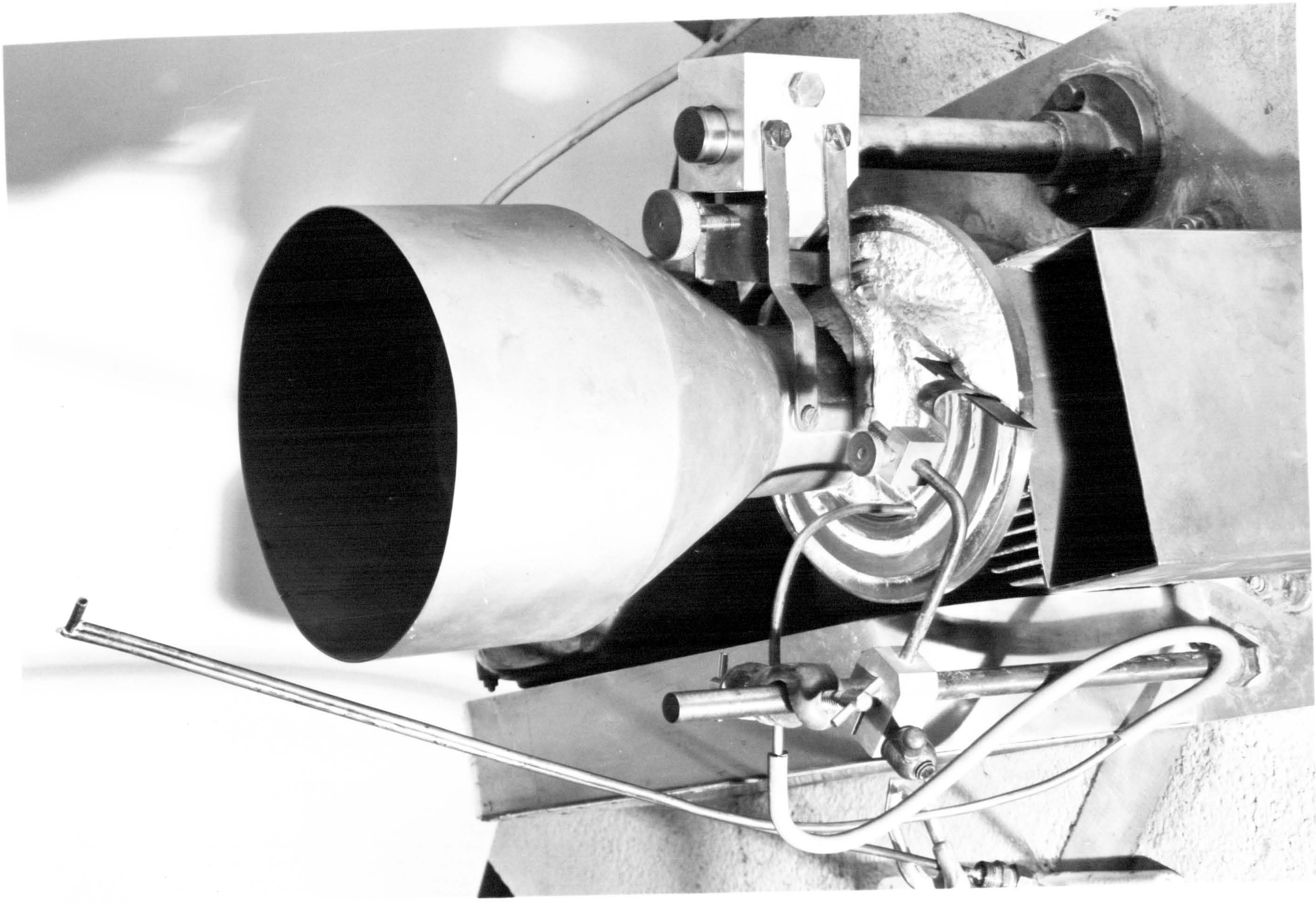

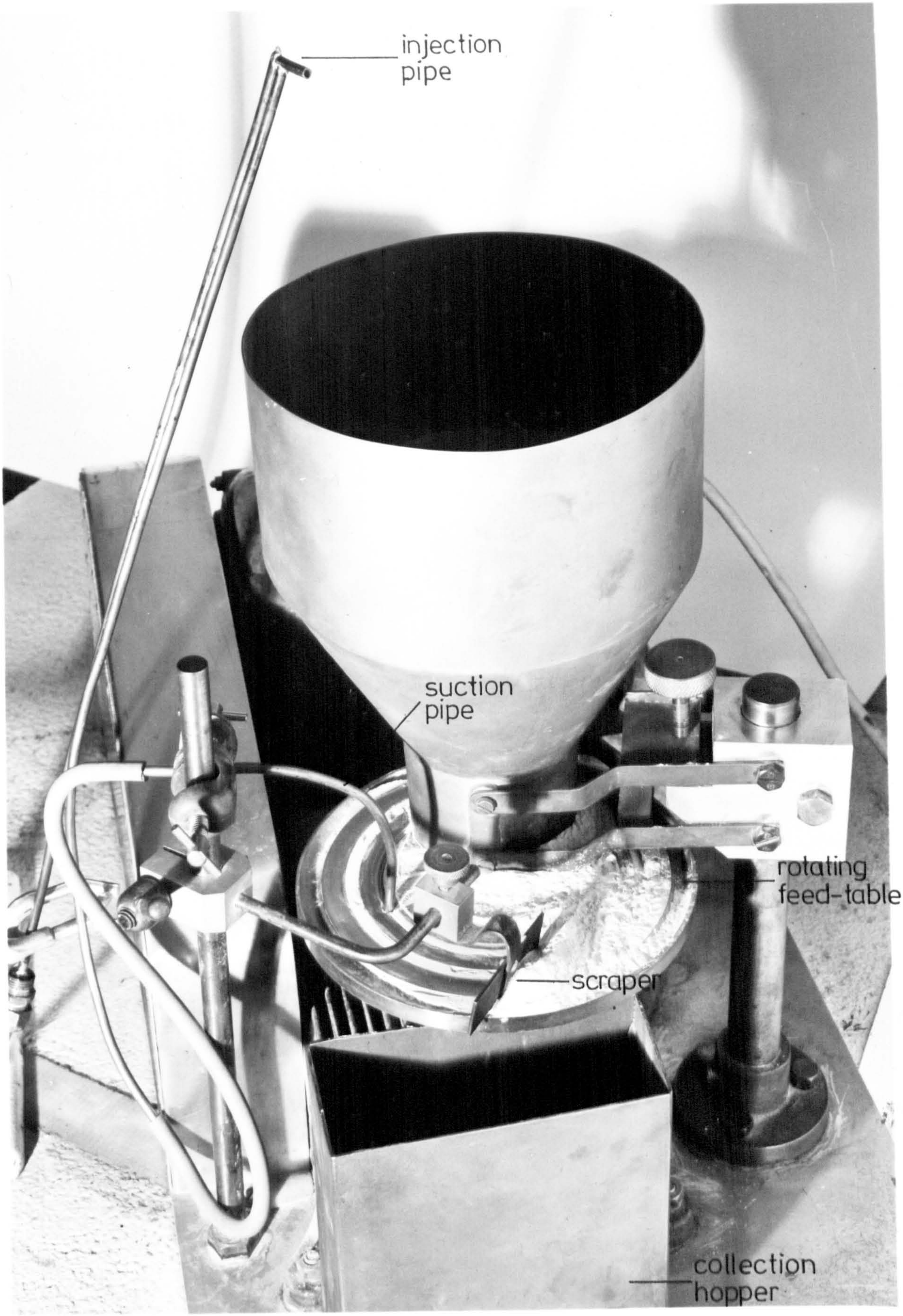

Fig. 5.4 Dust dispersion and feed device

the injection pipe with internal diameter of 2 mm, and into the duct.

The feeder system was mounted on a rigid support frame, independent of the precipitator duct, to avoid transmitting the mechanical vibrations of the feeder to the duct inlet. To minimise transport losses, vibrators were fitted to the suction and injection pipes, and the feeder was positioned as close as possible to the duct inlet to reduce the necessary pipe length. A vibrator was also fitted to the feed hopper to encourage even flow of dust onto the platform.

Complete dispersion of the dust from the feeder was necessary to ensure that Coulter analyses of the Millipore filter samples were representative of the concentration inside the duct. If insufficient shear force was applied to the dust before injection, the fines would remain attached to the larger particles. The fines would then migrate in the precipitator with the same velocity as the large particles. During Coulter analysis of the sample, the high energy involved in ultrasonic dispersion would cause disassociation of fines, resulting in a misleading concentration value for small particles. To test the dispersion of the dust injected into the duct by the dust feeder, a Royco Particle Size Analyser was placed inside the precipitator, near to the inlet. The high percentage of fines present in the measured sample gave confidence in the degree of dispersion produced by the dust feeder. Further evidence was provided by microscope observation of a dispersed dust sample, deposited on a small metallic plate.

Reentrainment of the dust deposited on the walls of the duct and in the honeycomb mesh in previous runs provided a possible source of error. To eliminate this unpredictable source of contamination, the premixing stage, honeycomb mesh

and precipitator walls were thoroughly rapped between successive runs.

5.2.3 Premixing stage

To make the concentration measurements realistic, a uniform dust concentration in both vertical and horizontal directions was required at the duct inlet. To measure the concentration profiles, a non-intrusive method of light scattering was employed. A 40mW Helium-Cadmium laser beam was passed through a vertical glass-covered slit in the wall of the precipitator. The light scattered vertically from the dispersed dust was reflected by a mirror angled at 45° to the horizontal, and into the P.M.T. orientated above the position of measurement. The optics of the P.M.T. were arranged as in Chapter 4, so that a 1 mm slice of the laser beam was observed at each measurement position.

Initially, tests were performed to evaluate the turbulent mixing induced by the 0.1 m flow modulation pipes at the duct inlet. The dust was injected into the mainstream gas flow through a 5 mm diameter hole cut halfway down the downstream side of the central flow modulation pipe. The laser beam was positioned about 50 mm upstream of the first discharge electrode and a concentration profile was measured as described above. The results shown in Figure 5.5 indicate the presence of a significant concentration profile suggesting insufficient mixing by the flow modulation pipes alone. In an attempt to improve the uniformity of the dust concentration at the duct inlet, the injection pipe was removed from the central pipe and positioned approximately 0.5 m upstream of the honeycomb mesh flow straighteners. Although much improved, a concentration profile across the duct was still apparent.

Eventually, the problem was solved by the installation

of a premixing stage at the entrance to the duct. This consisted of a 0.7 x 0.7 x 1.0 m chipboard box containing four facing fans, attached to the centre of the walls. The dust was injected through a 0.3 m diameter circular hole, cut in the front end of the stage, and the action of the fans provided violent mixing conditions for the dust. Subsequent concentration measurements (see Figure 5.5) showed the effect of the additional turbulence, produced by the premixing stage, to be sufficient to maintain a uniform dust profile at the inlet. Due to the axi-symmetric geometry of the premixing stage, the dust was assumed to be mixed equally well in the vertical plane.

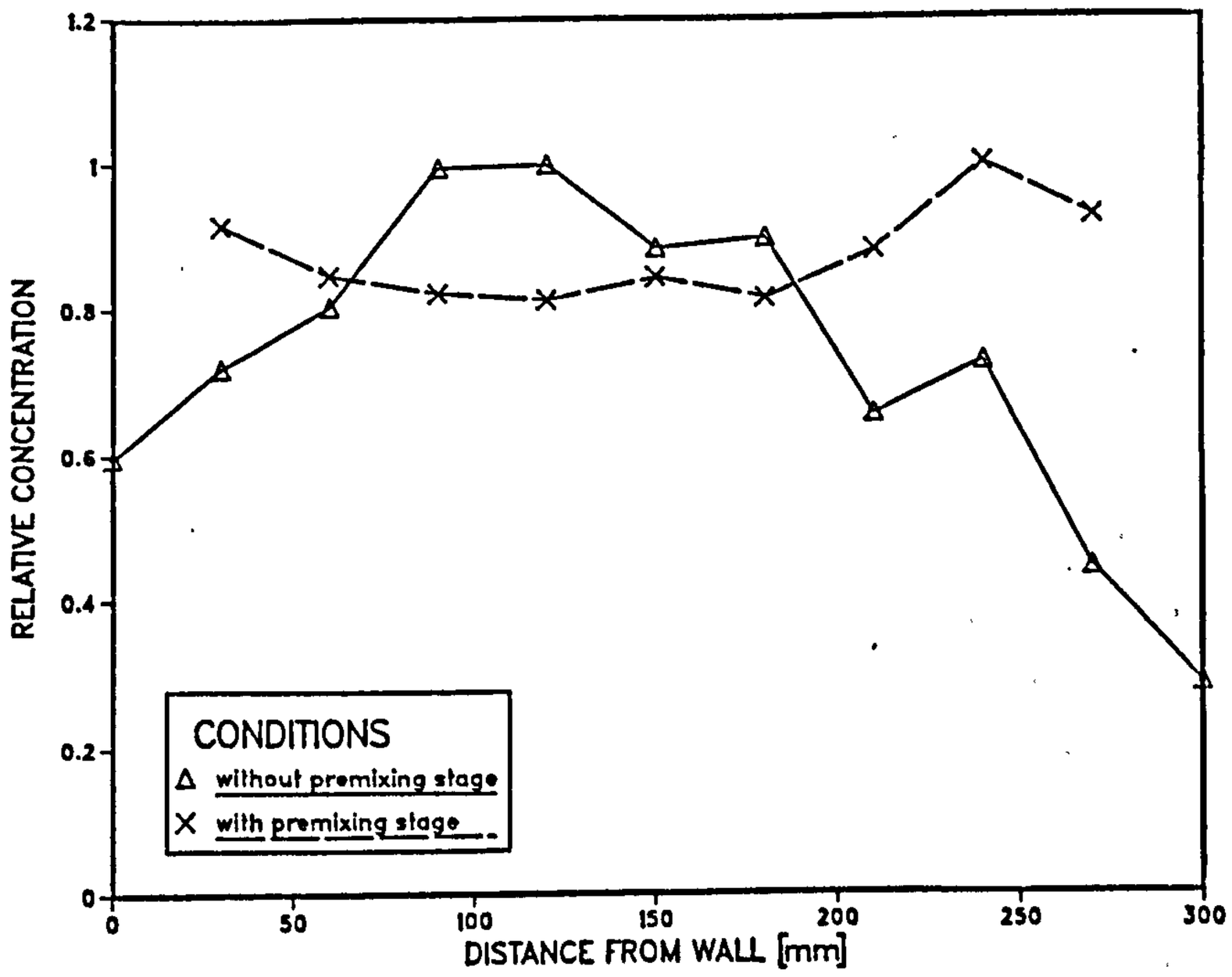

Fig. 5.5 Dust concentration profiles across precipitator inlet, with and without premixing stage

The effect of the premixing stage on the velocity profile downstream of the 0.1 m flow modulation pipes tested by measuring the gas velocity in the precipitator duct with and without the fans turned on. No change in velocity was observed.

5.2.4 Representative sampling

5.2.4.1 Electrostatic deflection

Deposition of a high resistivity dust on the sampling filters results in a gradual increase in the repulsive electrostatic force acting on further incoming particles. If significant, this force will decelerate an approaching particle. If the particle is not travelling along the central axis of the filter, the unbalanced radial electrostatic forces may be sufficient to push the particle around the filter head. The effect of this would be a reduction in capture efficiency of the sampling system. The likelihood of reduced efficiency due to this mechanism has been investigated in Appendix B, by mathematically balancing the electrostatic force on a charged particle approaching a filter with the drag force exerted by the surrounding gas. The differential equation describing the motion of a particle approaching a circular filter covered with n similarly charged, evenly spaced particles was solved using the 4^{th} order Runge-Kutta method. The distance L_c from the filter face was then calculated, at which the effect of the repulsive force on particle trajectories was negligible.

The calculations resulted in modified sampling heads incorporating glass testtube sections, of length greater than L_c, onto the front of the sampling heads. By assuming that all particles entering the front of the head extension were captured, the effect of electrostatic repulsion could be ignored. A value of L_c = 10 mm was found to be

sufficient for this purpose.

5.2.4.2 Anisokinetic sampling

Calculation of the efficiency of a sampling probe is complicated and depends on particle size, probe dimensions and geometry, air velocities surrounding the probe, (u), and inside the probe, (w). The deviation of larger particles from tortuous flow lines, due to their inertia, causes the dust concentration entering the probe head to vary, depending on the ratio of u to w.

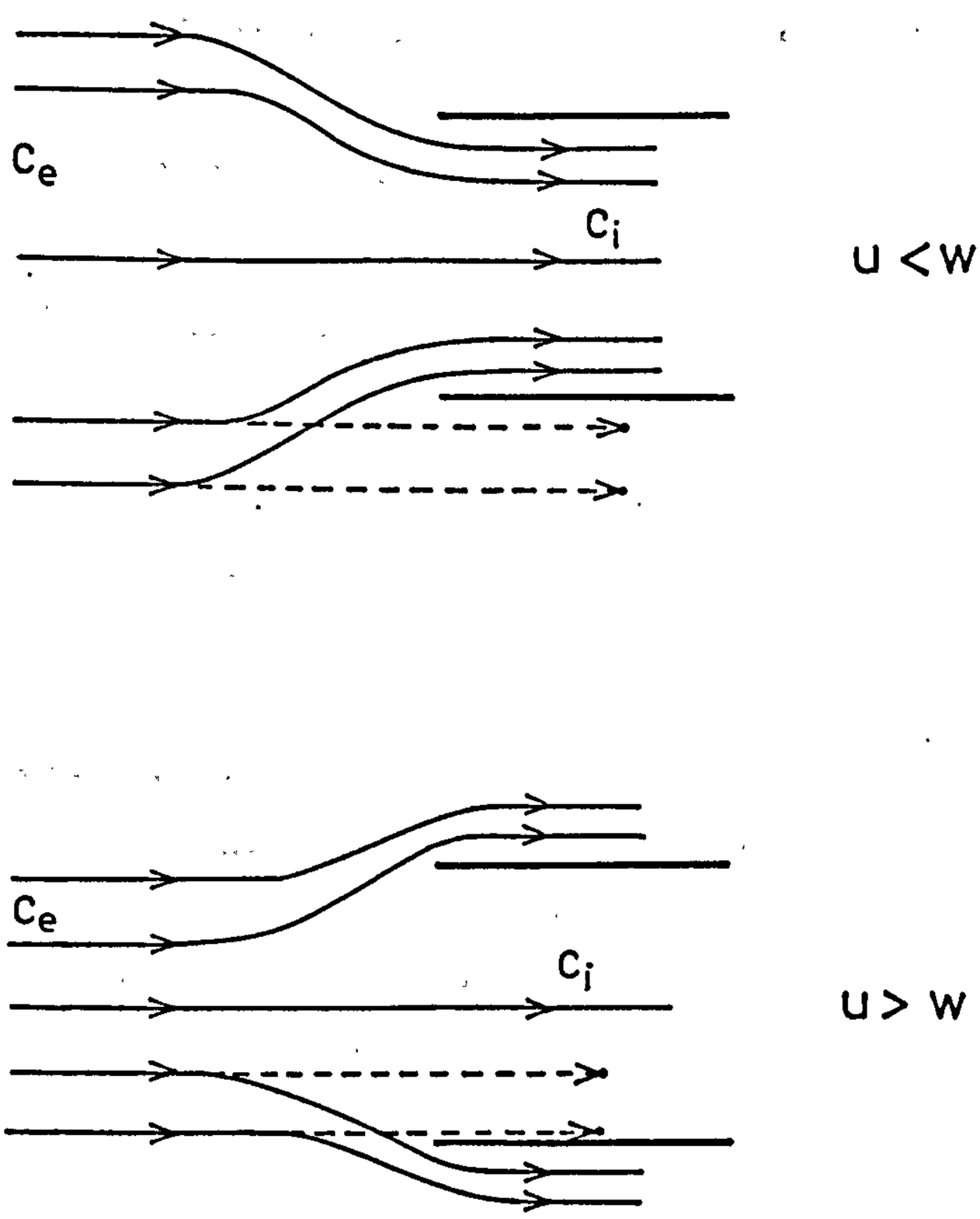

Fig. 5.6 Effect of anisokinetic sampling on particle collection

If u<w, the gas flow lines are drawn into the probe head (see Figure 5.6), and particles close to the edge of the probe pass along the outside of the sampling head. This causes a deficiency in the number of particles entering the probe head. If u>w, the gas flow lines are diverted around the probe head, and particles close to the edge of the probe that fail to follow the gas flow lines carry straight on into the sampling head. This causes an increase in the number of particles entering the probe head.

The extent to which these phenomema affect the sampling efficiency of the probe, e, depends on the particle relaxation time, T_p, which describes how quickly a particle will respond to fluctuations in gas velocity. Belyaev and Levin (1974) evaluated an expression incorporating the corresponding Stokes' Number Stk_w, from which values of sampling efficiency may be calculated.

$$e = 1 + (u/w - 1)\left[\frac{2(u/w) + 0.62}{(Stk_w)^{-1} + 2(u/w) + 0.62}\right] \qquad (5.1)$$

where $Stk_w = wT_p/D$,

D = probe diameter (m),

$T_p = d_p^2 \rho_p C/18\mu$

The relaxation time for a 10 μm particle of alumina is approximately 12×10^{-4} seconds. For a 10 mm diameter sampling head and surrounding gas velocity of 2.0 ms^{-1}, the corresponding Stk_w is 0.24. Equation 5.1 shows that for

$u/w = 0.75$ - $e_{error} = 8.4\%$,

and

$u/w = 1.25$ - $e_{error} = 10.7\%$.

For smaller particles, the errors will be less. The above calculations show that the error is most significant if the

sampling velocity is less than that surrounding the probe. In the case of steady flow, the problem can be obviated by sampling isokinetically. However, in turbulent flow the velocity fluctuates about the mean. Suppose that u/w fluctuates between 0.75 to 1.25, then the instantaneous error will vary between 8.4 and 10.7%. However, the errors over an extended period of time will tend to cancel out.

Experiments were performed to assess the magnitude of the anisokinetic errors incurred during a typical sample test. A single filter head was positioned approximately 70 mm from the precipitator wall in a gas flow with a time-averaged velocity of $2ms^{-1}$. Three 10-minute runs were performed using probe velocities of 1.7, 2.0 and 2.25 ms^{-1}, and the amount of dust collected in each anisokinetic run was compared with that collected isokinetically.

Figure 5.7(i) shows the raw data prior to the application of any corrections. Figure 5.7(ii) shows the same data corrected for volumetric throughput of gas, thereby increasing the concentration values by a factor of w/u. Figure 5.7(iii) shows the effect of the corrections predicted by the theory of Belyaev and Levin. Comparison of Figures 5.7(i)-5.7(iii) shows the most important correction to be the volumetric throughput for different probe velocities. Consequently, anisokinetic corrections were omitted except in the region directly behind the wall strengtheners, where velocity values are close to zero. The increase in fines, experienced for all anisokinetic velocities, is probably due to an error in the isokinetic result. Division by values that are too low will produce relative values too high.

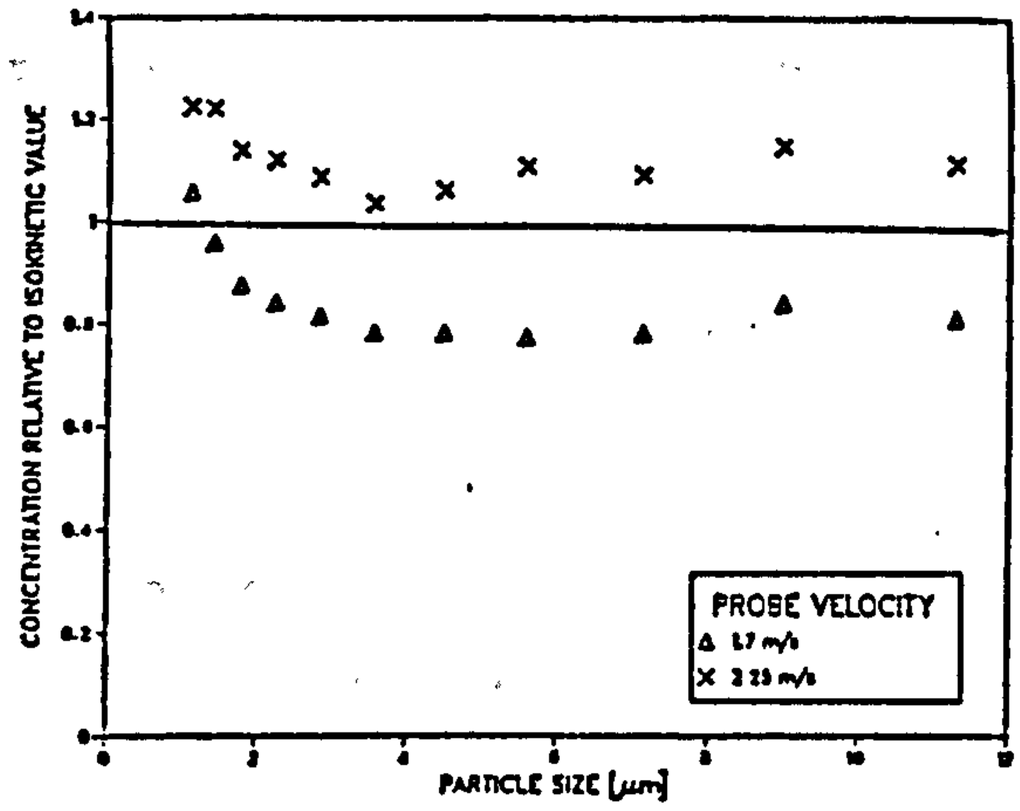

i) Raw data – gas velocity 2 m/s

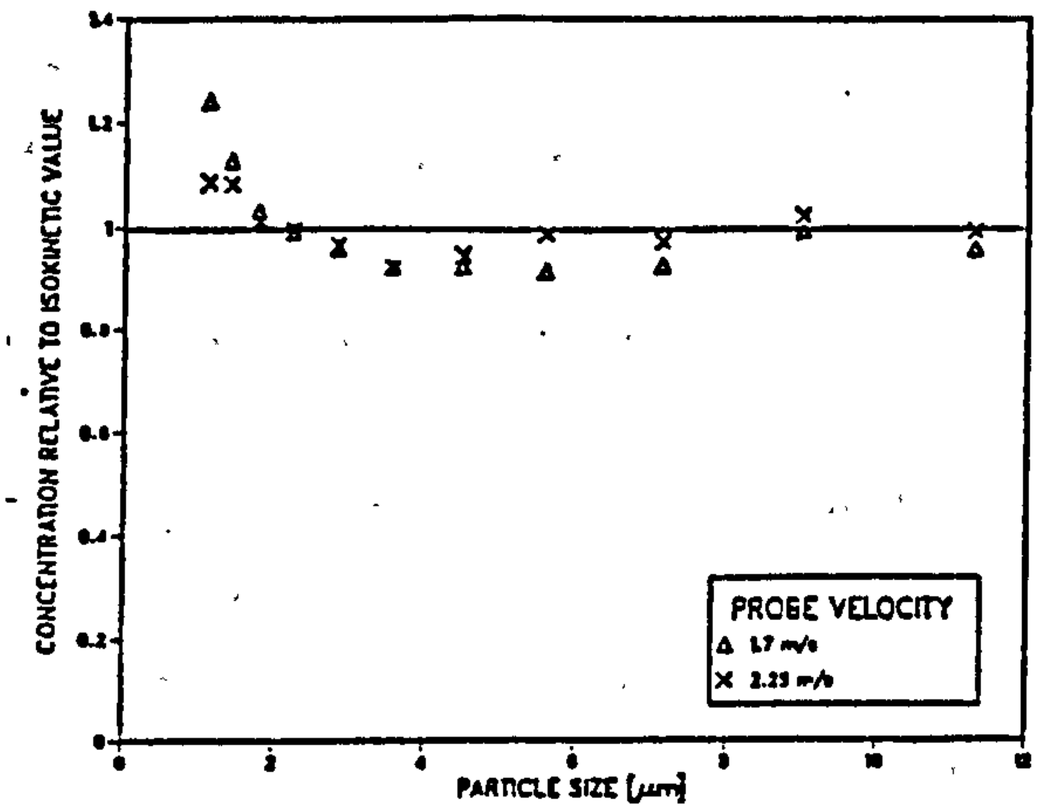

ii) Data corrected for volumetric throughput

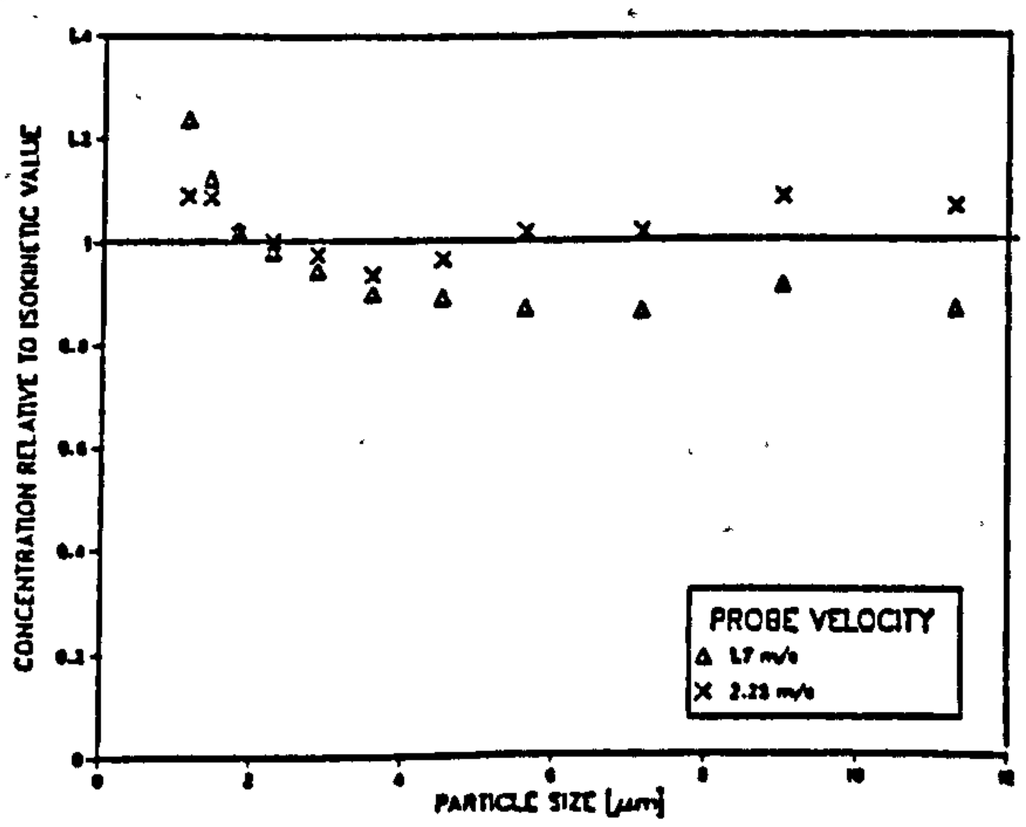

iii) Data corrected for anisokinetic sampling

Fig. 5.7 Effect of anisokinetic sampling on measured collection efficiency

5.2.5 Control of sampling velocity

In the previous section, the importance of isokinetic sampling was emphasised. The seven sampling heads were attached to the same manifold, so that the velocity through each filter could be individually controlled by the on/off and control valves along each sampling line.

The gauge on the vacuum pump was calibrated against velocity in the following manner:

a) Sampling line 1 was opened, and a rotameter was attached to the front of the sampling head.
b) With sampling lines 2-7 closed, the first point of the pressure gauge versus filter velocity calibration curve was calculated.
c) Further points on the calibration curve were determined by gradually opening sampling lines 2-7 and noting the corresponding rotameter and vacuum gauge readings.

Once calibrated, the velocity through each filter head could be individually set, by closing all other sampling lines and adjusting the control valve until the gauge read a value corresponding to the required velocity.

The effect of the sampling device on the flow field was investigated using the laser-Doppler photon correlation system, as described in Section 3.2.2. Velocity measurements were made at a series of locations across the front of the sampling device, at a distance of 3 mm upstream from the cassette head extensions. The sampling device was then removed from the duct and the measurements repeated. Comparison of velocity profiles showed negligible distortion of the flow field upstream of the sampling device.

5.2.6 Analysis of samples

The concentration and size distribution of particles captured by the filter media were measured using a Model TAII Coulter Counter. The dust from each filter was transferred to 200 ml of an electrically conductive liquid (Isoton) as described in Section 5.2.1. The Coulter Counter technique relies on the flow of an electrically conductive suspension through a small aperture, with an electrode immersed on either side (see Figure 5.8). The main contribution to electrical resistance between the electrodes is provided by this aperture. As particles are swept along with the electrolyte through the aperture, the resistance between the electrodes increases. This produces a voltage pulse, of short duration, with magnitude proportional to particle volume. The voltage pulses are amplified and fed to a threshold circuit, with an adjustable threshold level. If this level is reached or exceeded, the pulse is counted. By taking a series of counts at selected threshold levels, data is directly obtained for plotting cumulative frequency versus particle size.

The threshold level assigned to a particular channel defines the size range measured. Each of the 16 channels available in the Model TAII have threshold levels which are set to measure particles with volume twice that in the previous channel (i.e. $2^{3/2} \times d_p$). The minimum threshold level is limited by the signal-to-noise ratio and coincidence, and the blockage of the aperture by large particles determines the maximum level. The size distribution in the sample solution needs to be carefully controlled to avoid these extremes.

Ten replicate Coulter analyses were performed on each sample. The output data was transferred via an interface to a Commodore 4032 PET, where it was stored and manipulated to

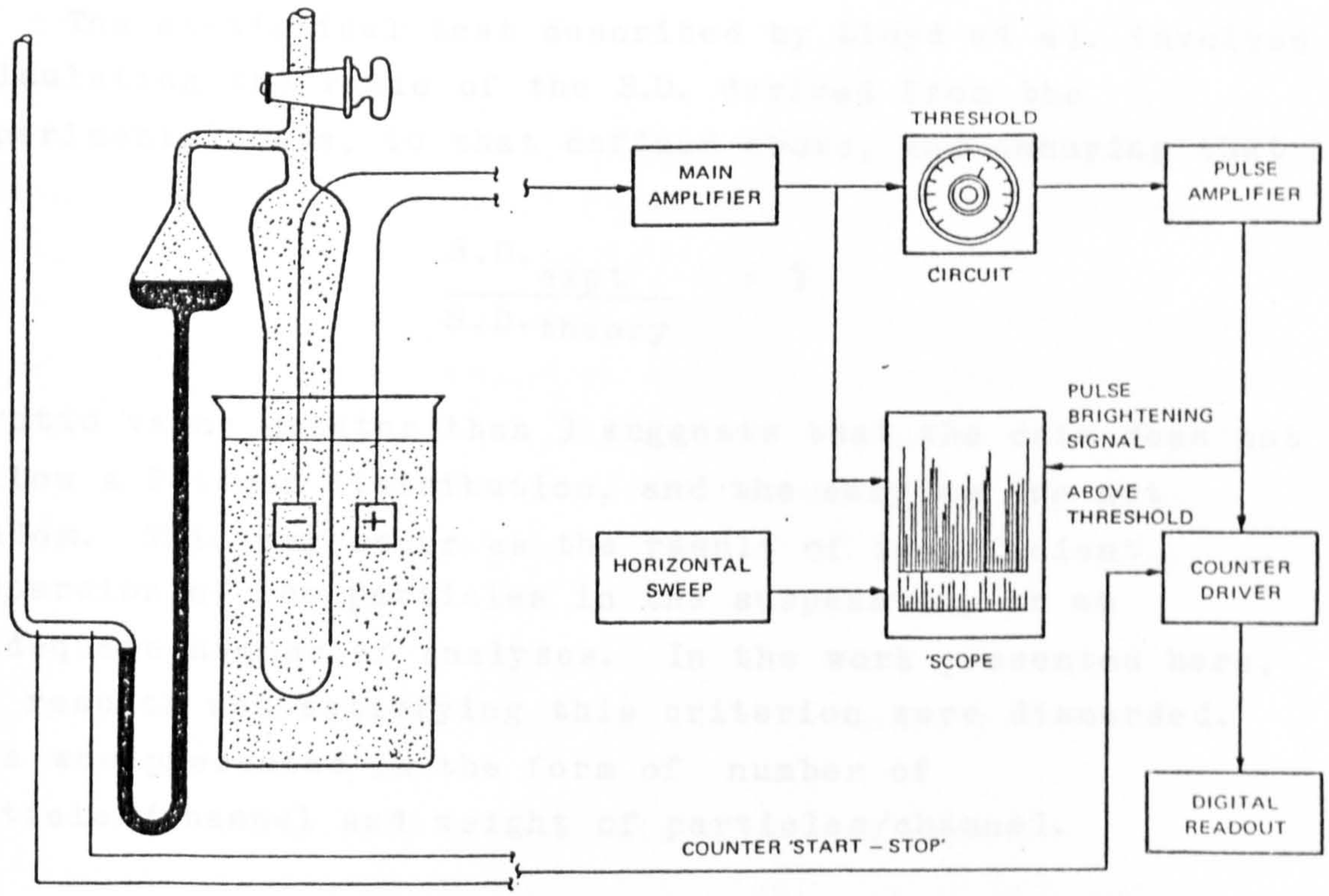

Fig. 5.8 Schematic diagram of Coulter Counter principle

obtain the required information. Lloyd et al. (1977) have defined a statistical test which has been used as the criterion for acceptability of the data. BS3406 states that the number of particles in the j^{th} channel n_j, should be distributed according to a Poisson distribution. The theoretical standard deviation, S.D., for such a distribution is defined by

$$S.D._{theory} = (n_j)^{1/2}$$

The statistical test described by Lloyd et al. involved calculating the ratio of the S.D. derived from the experimental data, to that defined above, and ensuring that

$$\frac{S.D._{expt}}{S.D._{theory}} < 3$$

A ratio value greater than 3 suggests that the data does not follow a Poisson distribution, and the samples are not random. This may occur as the result of insufficient dispersion of the particles in the suspension, or an inadequate number of analyses. In the work presented here, any results not satisfying this criterion were discarded. Data was presented in the form of number of particles/channel and weight of particles/channel.

5.2.7 Results and discussion

The following results represent a concise description of the extensive concentration data, obtained from numerous Coulter Counter analyses of dust samples. For each experimental run (usually 10 minutes sampling time), 7 particle size distributions were obtained, corresponding to the seven filter positions across half the precipitator duct. It was necessary to reduce this data to a less complex form, so that trends could be deduced without loss of detail.

The inlet concentration was measured repeatedly throughout the experimental programme. Since the dust concentration profile across the entrance to the precipitator was uniform (see section 5.2.3), an average of the 7 adjacent values could be used to represent the inlet concentration. Downstream results were then divided by this value to give relative concentration results. The data could be represented graphically in either of the following ways:

a) Distance from wall versus relative concentration

This method produces 7 points of a concentration profile, for a given particle size. It is the most useful way of displaying data to show concentration profile development, and for comparison with the theoretical predictions of numerical models.

b) Particle size versus relative concentration

This method produces up to 16 points on seven relative concentration graphs, corresponding to each of the filter head positions across the duct. To reduce the volume of data, an average of these 7 curves are

generally presented in the form of an average relative concentration.

5.2.7.1 Reproducibility

Reproducibility tests were made on the concentration at the inlet to the precipitator duct. Figure 5.9 shows that the results for three tests performed consecutively are within 10%, confirming an acceptable degree of reproducibility.

Comparison of inlet concentration values measured periodically over the entire duration of the experimental programme, reveals a variation in the size distribution of the input dust with time (see Figure 5.10). The effect is due to the abrasive nature of the alumina P15, causing gradual wear of the injection pipe. Attrition of the large particles may then occur on sharp edges so that the number of fines is markedly increased. Important in this argument is the fact that a 10 μm particle could theoretically be ground into approximately 1000 x 1 μm particles. Therefore, a significant increase in fines does not necessarily produce a corresponding decrease in the number of large particles. For most particle sizes, the increase with time is not great and interpolation may be carried out with confidence. For particles < 2 μm, similar interpolation may lead to more significant errors, and although these results have been included for completeness they should be viewed with a certain amount of scepticism.

The number of particles in the Coulter channel corresponding to d_p > 12.0 μm is often fewer than 20. The statistical analysis of samples containing such a small number of particles is likely to introduce large errors, and the results have consequently been omitted.

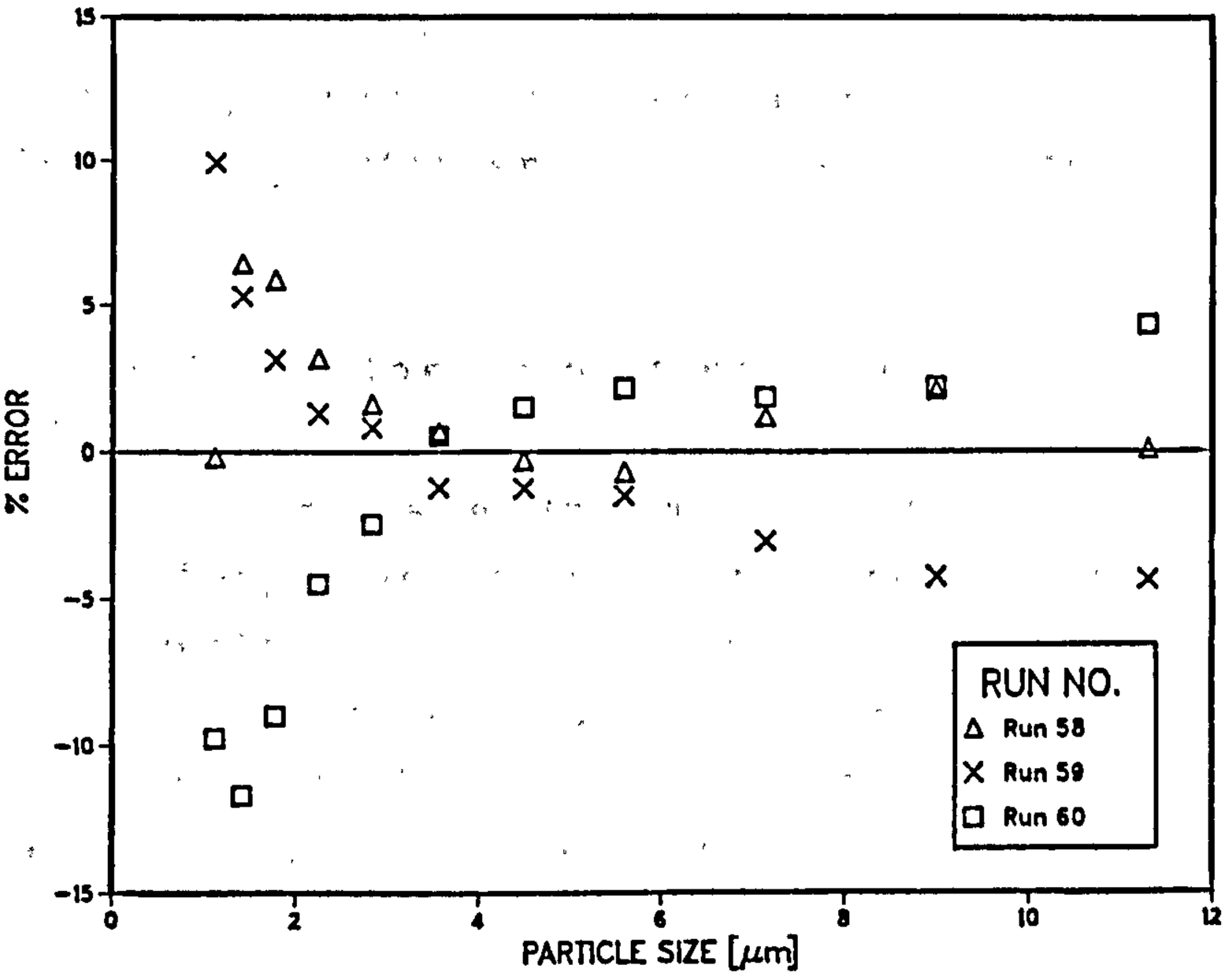

Fig. 5.9 Reproducibility test of consecutive samples

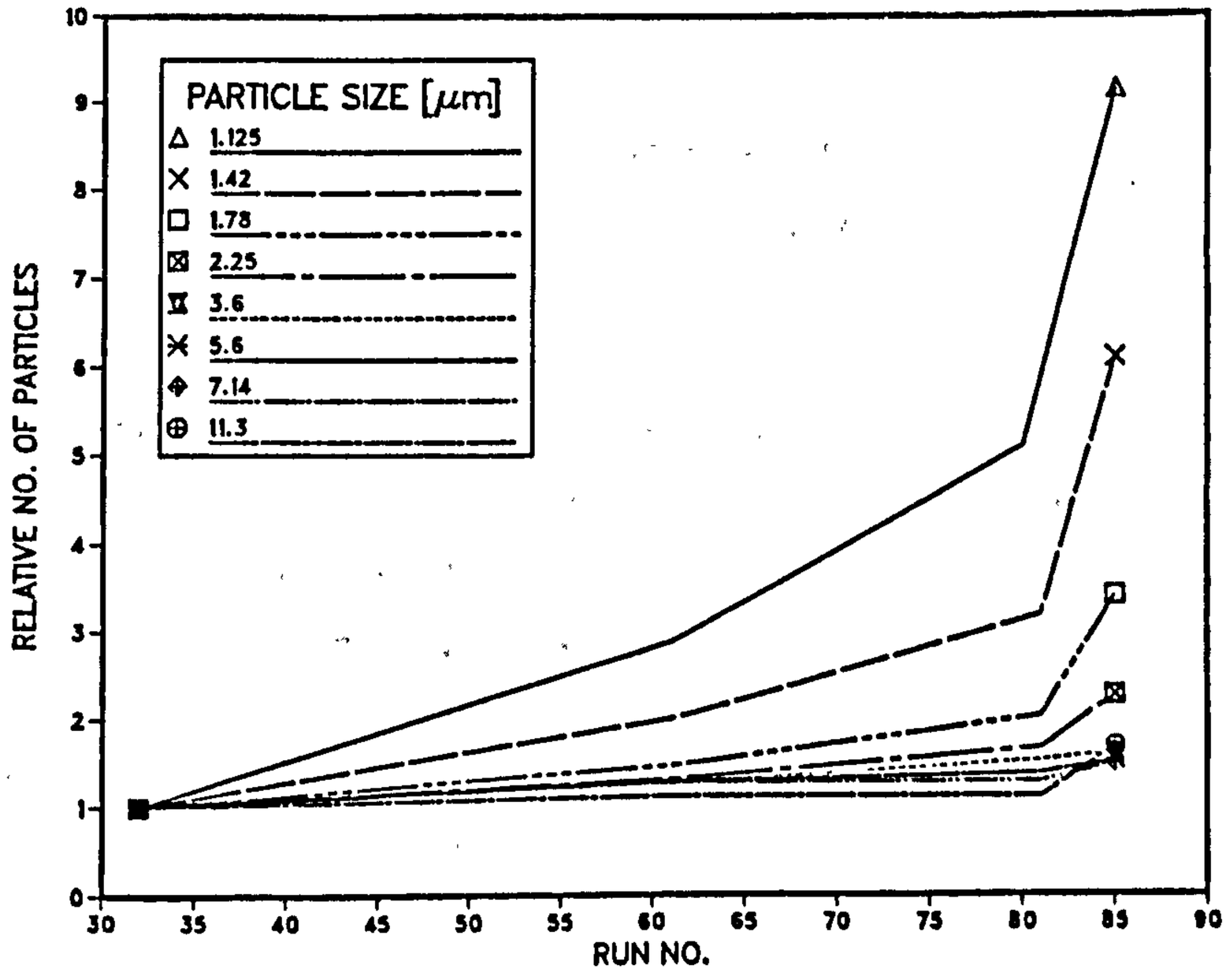

Fig. 5.10 Change of inlet concentration

The standard configuration used for experimental tests was that found in an industrial precipitator, i.e. applied voltage of -65KV, with 0.1 m diameter flow modulation pipes and wall strengtheners installed, at a gas velocity of $2ms^{-1}$. Any deviation from standard conditions is noted in the results.

5.2.7.2 Effect of flow modulation pipes

Pipes of 0.1 m diameter were spaced across the inlet to the precipitator, downstream of the honeycomb mesh, as in industrial precipitators. The function of the pipes is to provide a back-pressure so that uniform gas flow distribution across the inlet may be maintained. Their presence may affect dust collection in some or all of the following ways:

a) Inertial collection of dust on the upstream sides of the pipes may cause a temporary reduction in the number of particles entering the precipitator. Periodic rapping of the walls may cause this layer to dislodge, producing particle shedding. Visual observation of the pipes showed collection by this mechanism to be negligible.

b) The time-averaged flow field will be affected as described in Chapter 3. This must influence particle migration.

c) Increasing the gas turbulence at the inlet may be advantageous in ensuring that all particles are carried into the region of high ion density surrounding the discharge electrode. Maximum charging of the dust will then occur at the inlet, and the possibility of a particle entering the duct and remaining close to the collection wall, thereby acquiring a low electric charge, is reduced. Alternatively, an increase in

turbulence may be detrimental to collection because of the increased back-mixing.

d) Increased turbulence may enhance mechanical deposition, particularly for large particles.

Experimental tests were carried out to assess the effect of the pipes on the dust concentration within the precipitator. A log-linear plot of the concentration measurements made at two downstream locations are shown in Figure 5.11. Position G is downstream of the first strengthener, and consequently the results reflect the behaviour in the inlet section where the effect of the pipes should be dominant. Collection of large particles is increased by the presence of the pipes, but the concentration of small particles is relatively unaffected. This is consistent with the theory of turbulent deposition where large particles are deposited more readily as turbulence is increased. The influence of mechanical deposition has been studied separately and is discussed in Section 5.3. The individual mechanisms mentioned in c) are important but tend to cancel each other out.

The results for Position J are also presented in Figure 5.11, and reflect the performance of both the inlet section and the region between wall strengtheners. The overall influence of the pipes is less severe and appears to be detrimental to collection in the zone behind the first strengthener. This may be explained by the increased transverse back-mixing of charged particles which may decrease electrical collection. For small particle sizes, consistently anomalous results were obtained.

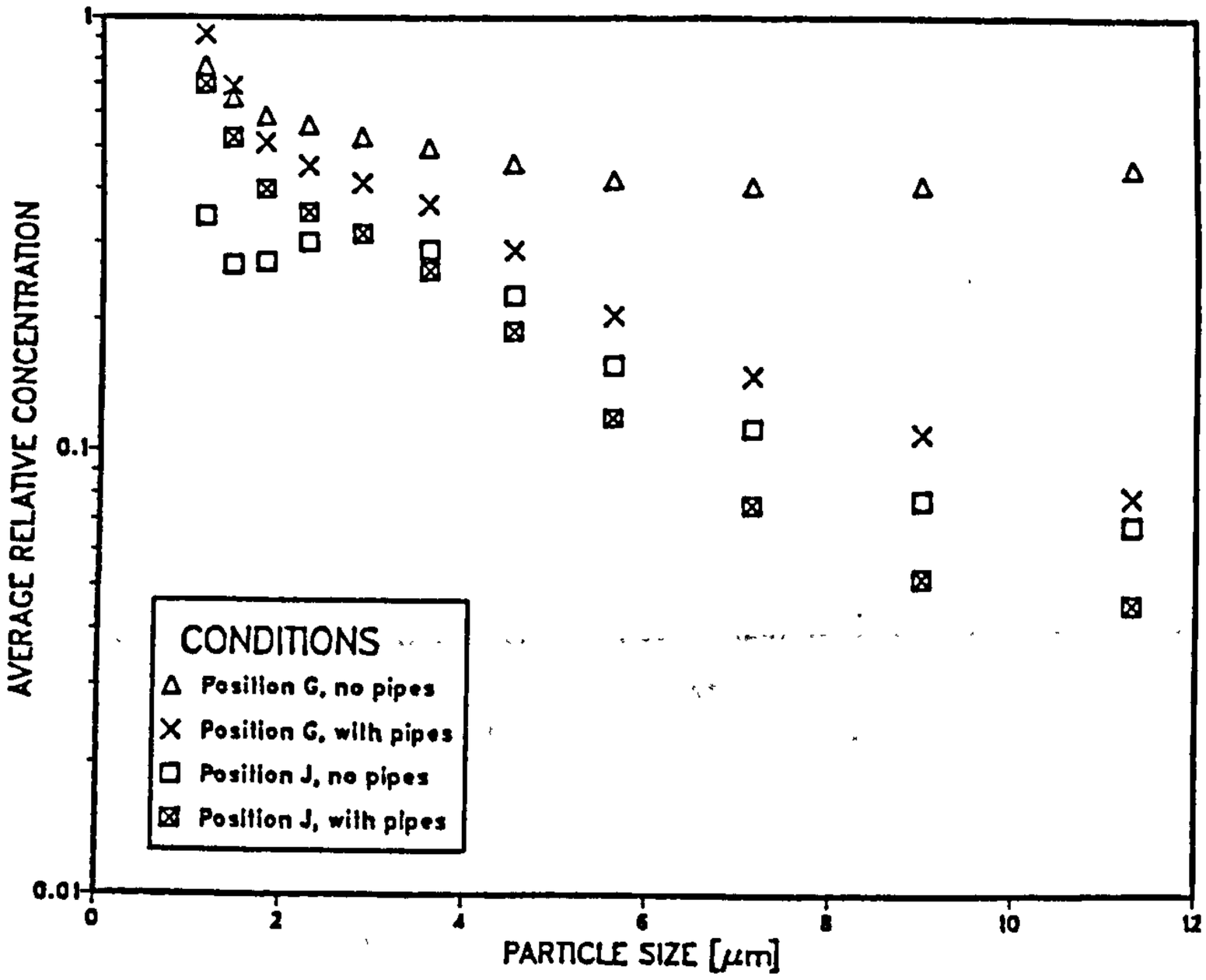

Fig. 5.11 Effect of flow modulation pipes on dust concentration

5.2.7.3 Effect of applied voltage

Concentration measurements made at Position G for applied electrode voltages of -65, -50, -30 and 0 KV are presented in Figure 5.12. To emphasise the effect, the wall strengtheners were removed from the precipitator. The concentration falls rapidly with increasing voltage, except for the fines which are relatively unaffected. Collection increases with voltage for all particle sizes greater than 2 μm.

Figure 5.13 shows the concentration profiles across the duct for 2.25, 3.6, 7.14 and 11.3 μm particles. For the 0 KV case the results show a concentration profile which falls off rapidly as the wall is approached. This is consistent with the mechanism of turbulent deposition. When voltage is applied, the curves clearly indicate concentration gradients

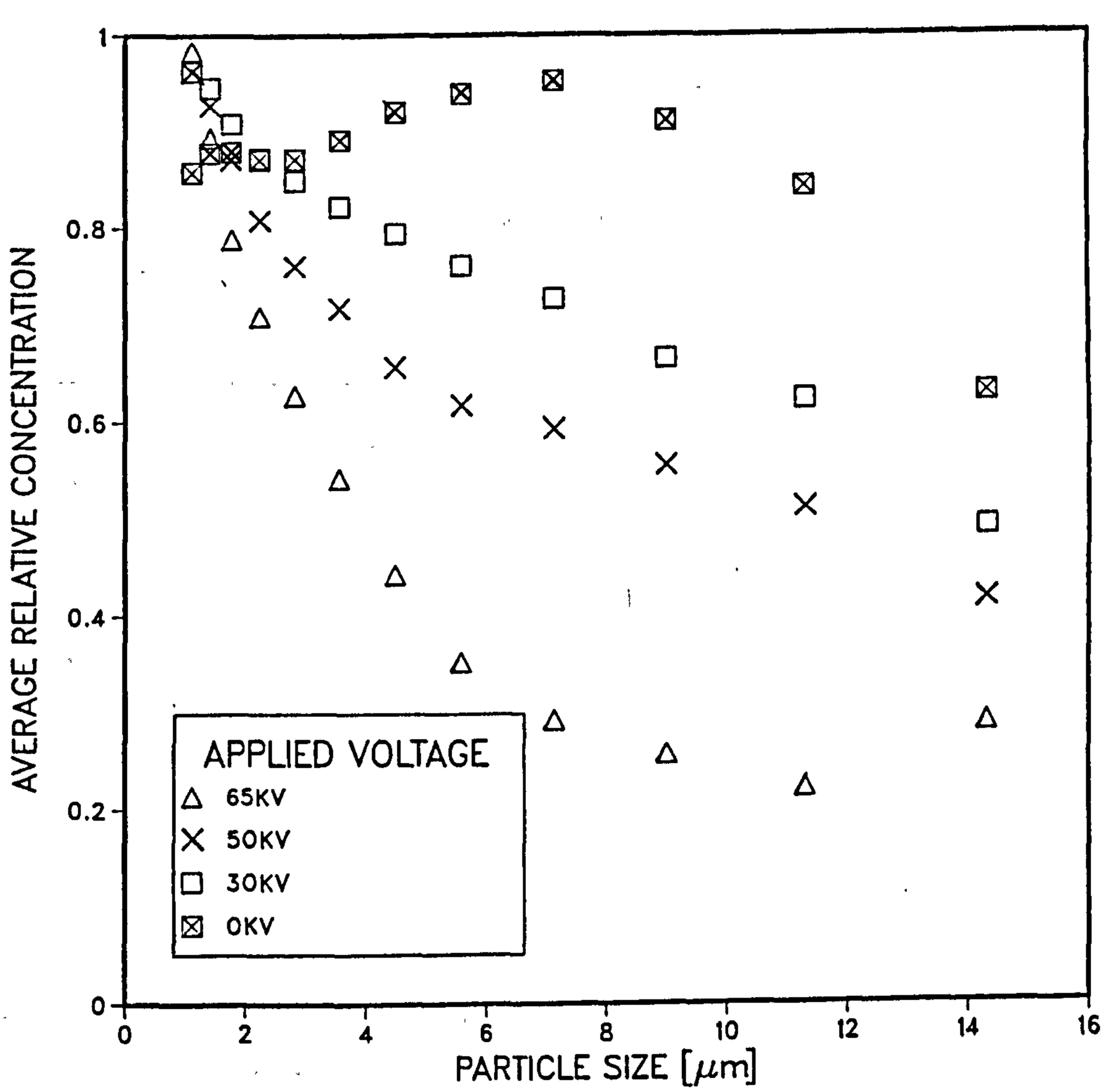

Fig. 5.12 Effect of applied voltage on dust concentration

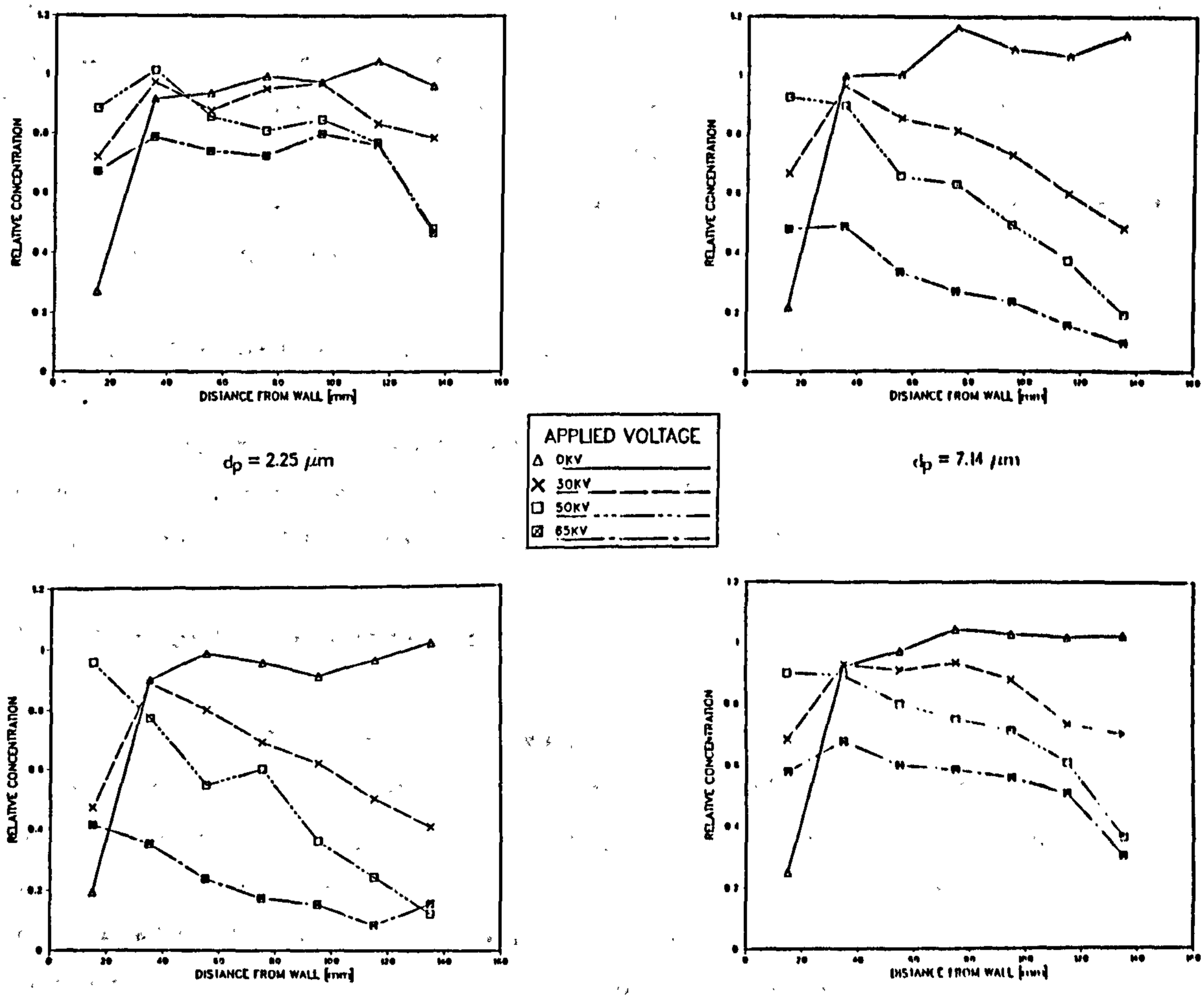

Fig. 5.13 Effect of applied voltage on dust concentration profiles

across the duct, which become more pronounced for large particles. The migration of particles from the centre of the duct results in a build-up of dust near the collection wall. This is contrary to the assumption of a flat concentration profile as used in the derivation of the Deutsch-Anderson equation, and supports the use of the convective-diffusion approach. Uniform concentration profiles occur only for $d_p < 3\mu m$, due to the combination of low electrical mobility and turbulent back-mixing.

5.2.7.4 Concentration versus distance downstream

Concentration measurements were made at different locations downstream in the precipitator duct, both with and without the wall strengtheners installed.

(i) Without strengtheners

Figure 5.14 shows the way in which particle concentration falls with distance downstream. As expected, the collection efficiency at all locations increases with particle size. The reduced collection of smaller particles may be attributed to a lower electrical mobility and increased back-mixing, together with a lower mechanical efficiency. The significant fall in concentration of fines after position G may be due to the decay of the high turbulence produced by the flow modulation pipes, resulting in reduced back-mixing. The concentration at position C shows that the electrified region surrounding the discharge electrode extends sufficiently far upstream to produce 15% collection of the large particles prior to the first electrode.

It is appropriate to examine the decay of concentration with distance downstream in relation to the Deutsch-Anderson equation (1.1). For the case without wall strengtheners, a

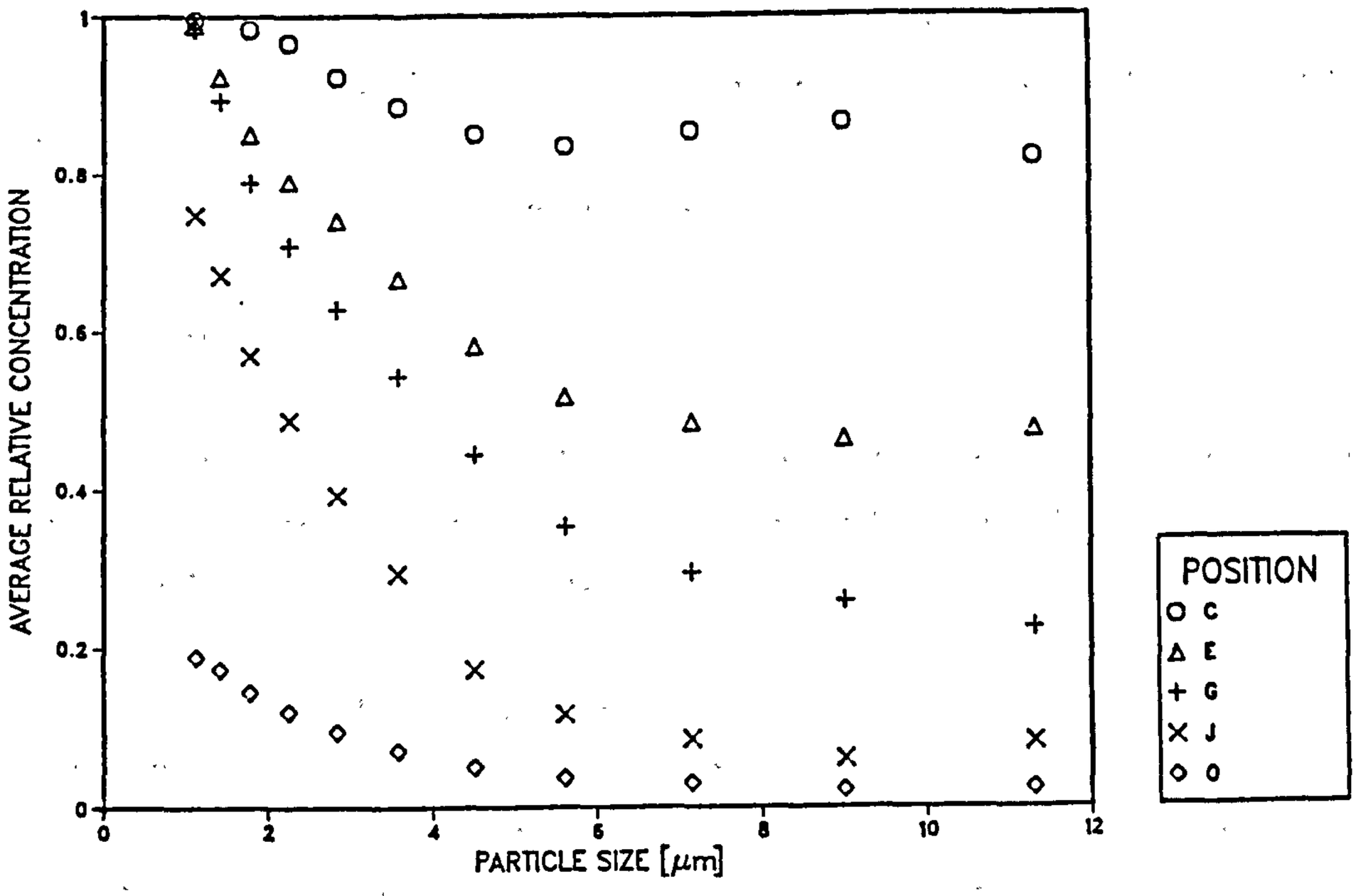

Fig. 5.14 Dust concentration at different downstream locations (no wall strengtheners)

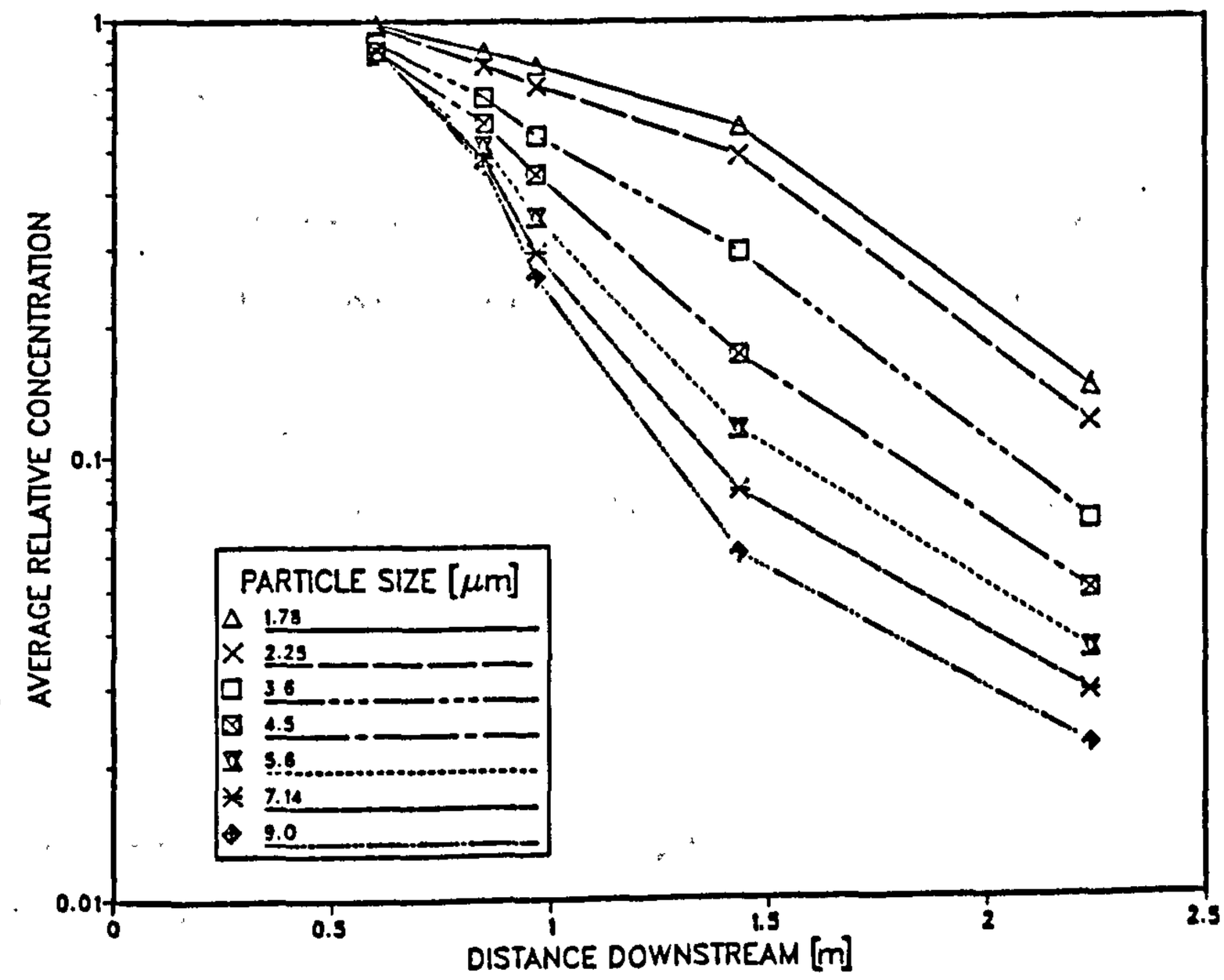

Fig. 5.15 Log-linear plot of dust concentration versus distance downstream (no wall strengtheners)

log-linear plot of average relative concentration for a range of particle sizes is presented in Figure 5.15. All the curves are close to linear, confirming both the importance of transverse back-mixing and the validity of the expression:

$$\ln(c/c_o) = -KL$$

where K = constant (m^{-1}).

L is the effective length of the precipitator which is shown to extend from approximately 0.5 m downstream of the flow modulation pipes in this case.

The development of concentration profiles down the precipitator duct for particle sizes of 2.25, 5.6 and 11.3 μm is demonstrated in Figure 5.16. The importance of turbulent mixing in maintaining a flat concentration profile for small particles is evident. In this case, the back-mixing assumption associated with the Deutsch equation is valid. For larger particles, the electrical mobility is much higher and concentration profiles build up rapidly as the particles migrate towards the wall. Consequently, any agreement of the results with the Deutsch-Anderson expression is fortuitous.

In an industrial precipitator where high dust loadings are involved, the enhancement of electric field by particle space charge density will diminish downstream where there are fewer particles available to supply the space charge. This will cause the collection to fall off with distance downstream.

(ii) With strengtheners

The effect of wall strengtheners on the average relative concentration is shown in Figure 5.17 for Positions

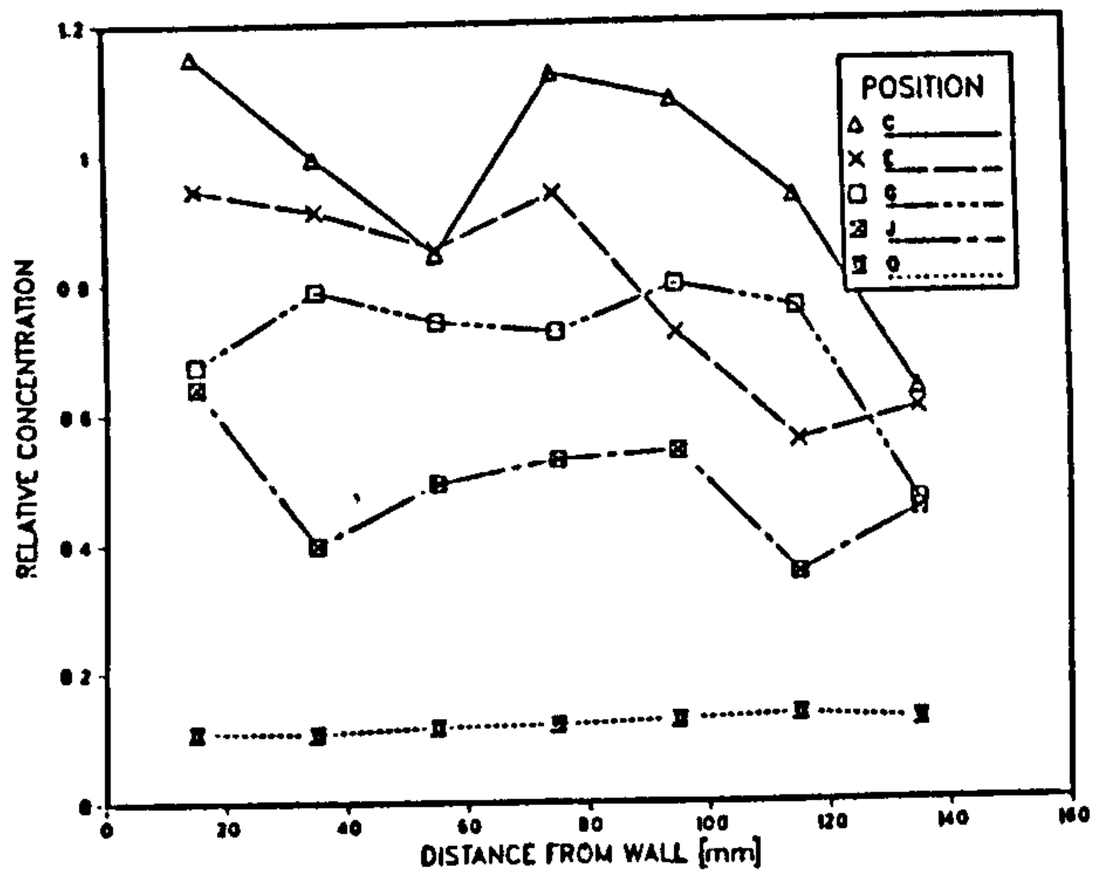

$d_p = 2.25\ \mu m$

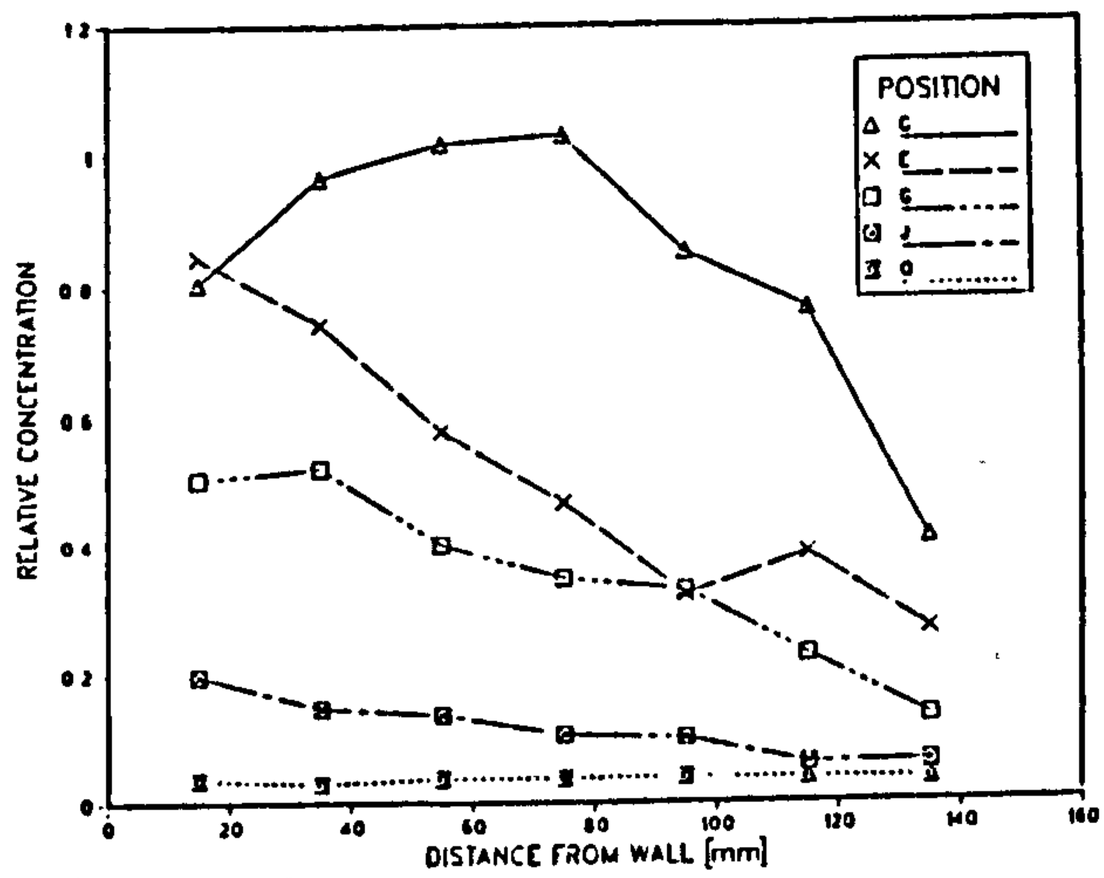

$d_p = 5.6\ \mu m$

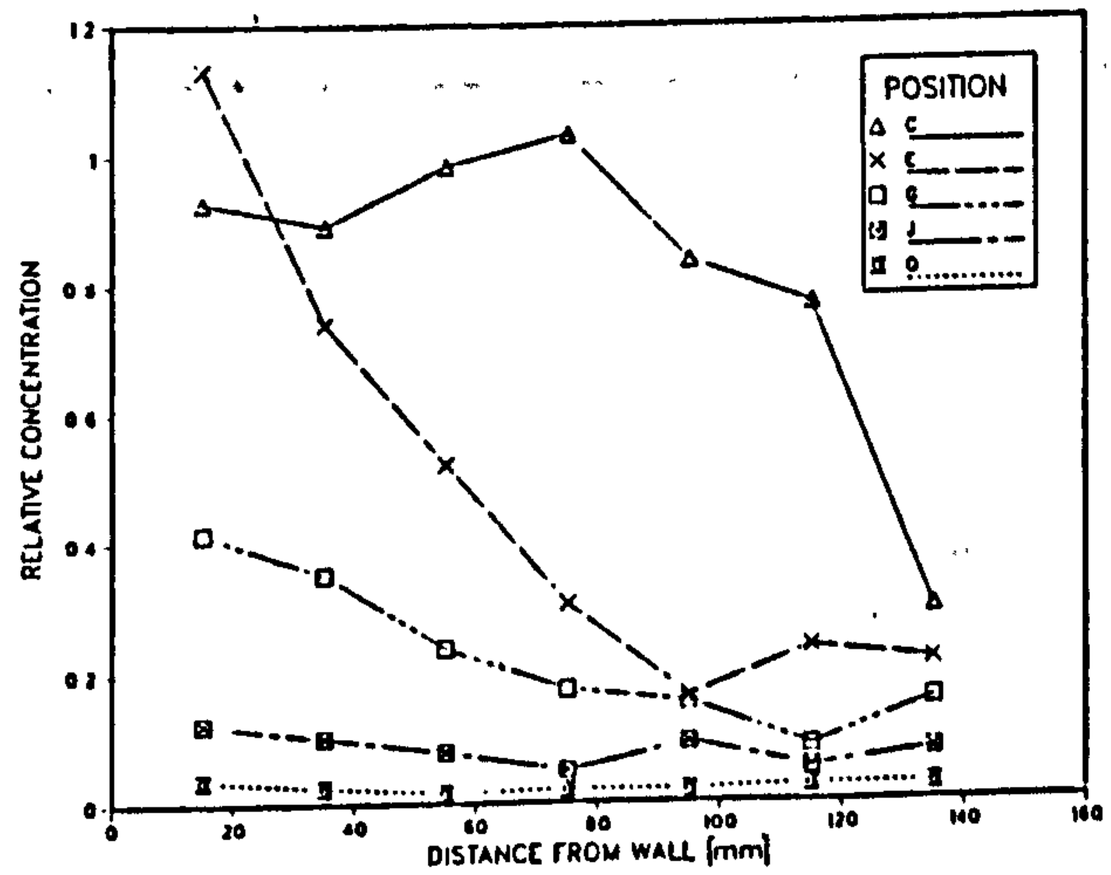

$d_p = 11.3\ \mu m$

Fig. 5.16 Development of dust concentration profiles (no wall strengtheners)

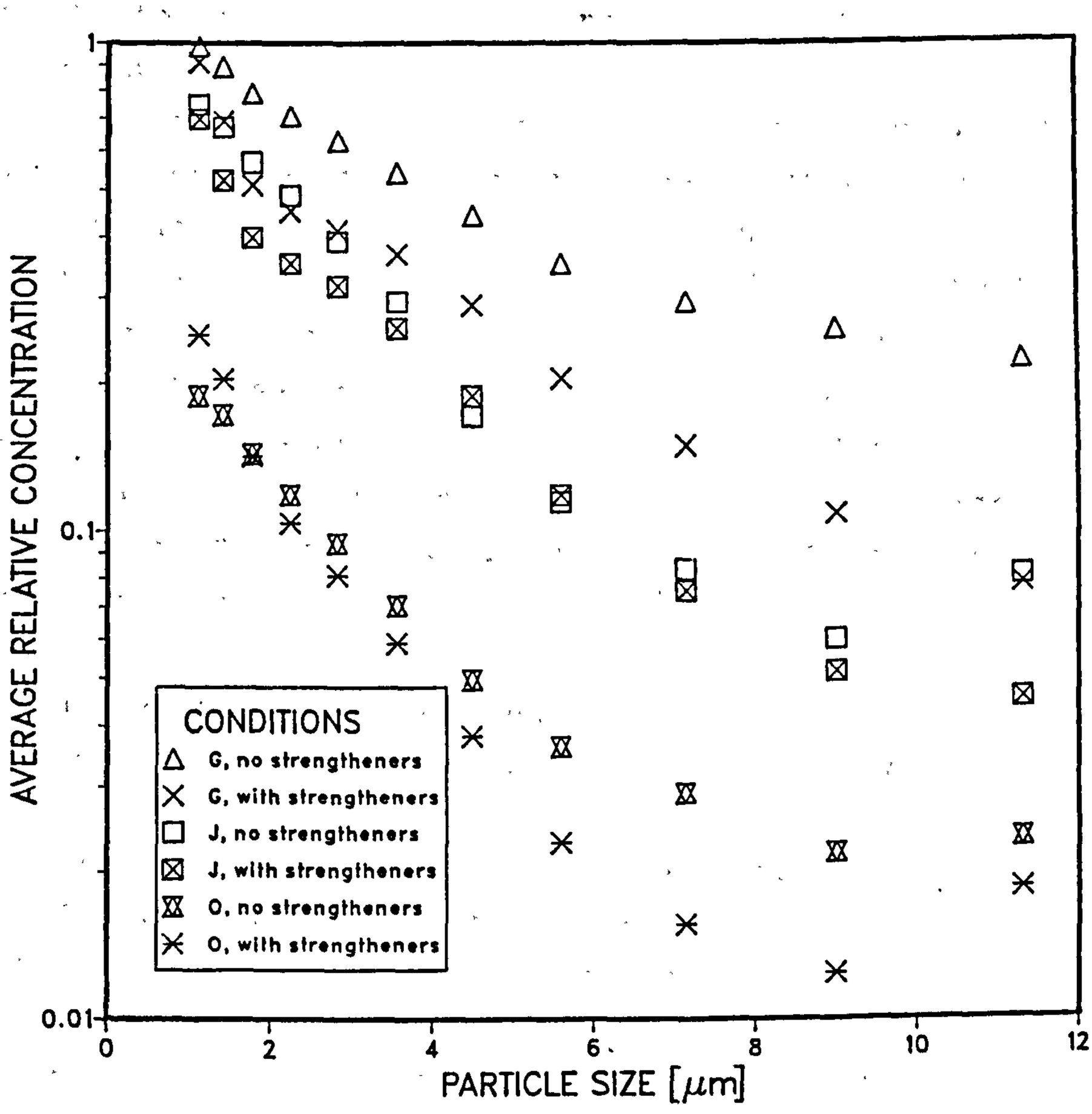

Fig. 5.17 Effect of wall strengtheners on dust concentration

G, J and O. Particle collection is considerably enhanced in the region surrounding the wall strengtheners. The mechanisms responsible for this are associated with the inertial transport of particles into the front of the strengthener, enhanced wake capture, and an increase in collection area. The undulating behaviour of relative concentration with distance downstream emphasises the importance of strengtheners in influencing particle capture. Attempts to use a Deutsch-Anderson type model to describe the concentration decay should be confined to long ducts in which this undulating effect can be averaged out. From the results it appears that the presence of strengtheners slightly increases the collection of dust. It must be noted that the enhanced collection into the front of the first strengthener may be higher than for subsequent strengtheners due to the increased tortuosity of particle trajectories caused by the presence of the flow modulation pipes. Supporting evidence of this mechanism can be inferred from the results of Figure 5.18, particularly in the case of large particles.

One would intuitively expect the collection of large particles to be increased in the presence of wall strengtheners. Their high inertia would carry them into the stationary zone within the strengtheners, whilst the fines would follow the streamlines directed around them. Examination of Helium bubble trajectories (see Figure 3.16), shows the streamline path to move away from the wall upstream of the strengthener, in a very gradual way. Thus, most of the particles would be capable of following the streamlines, and not thrown into the stationary zone. Downstream of the strengtheners, the streamlines are contorted more rapidly due to the production of vortices. It is here that the fines are carried into close proximity with the collection walls, whereas the larger particles follow a less tortuous path.

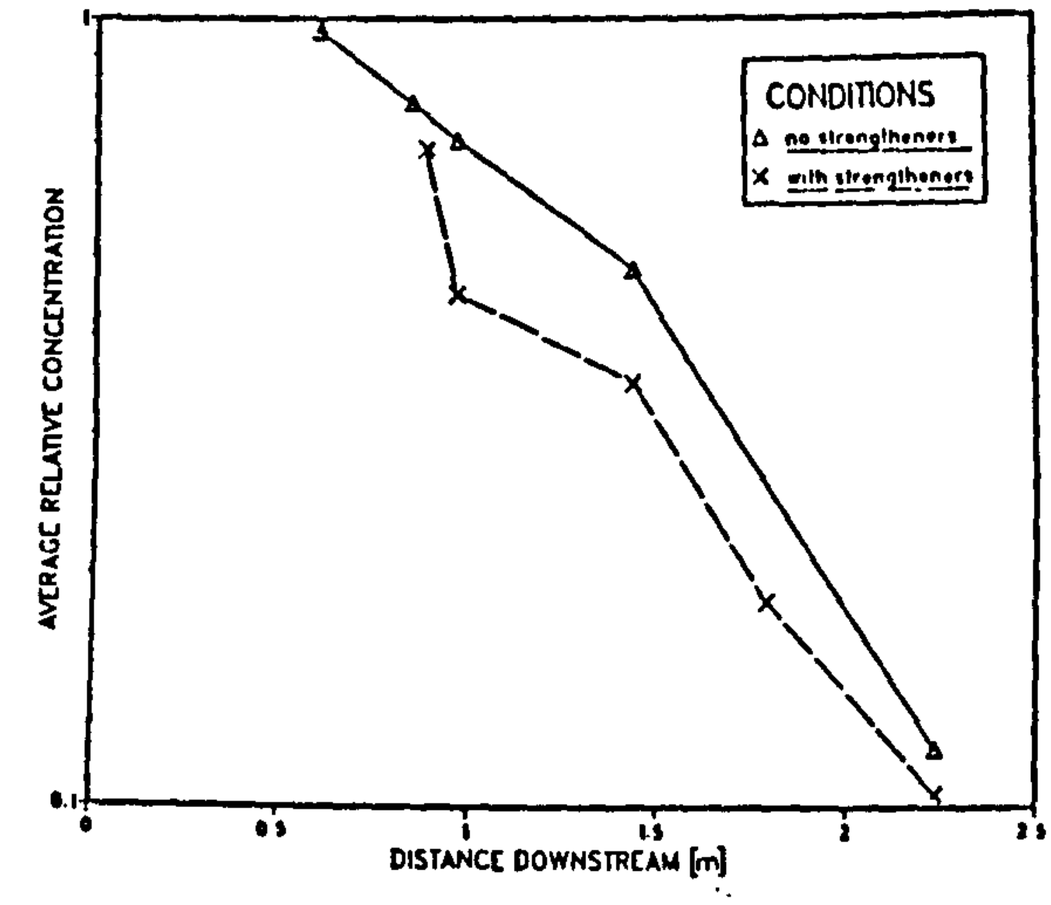

$d_p = 2.25\ \mu m$

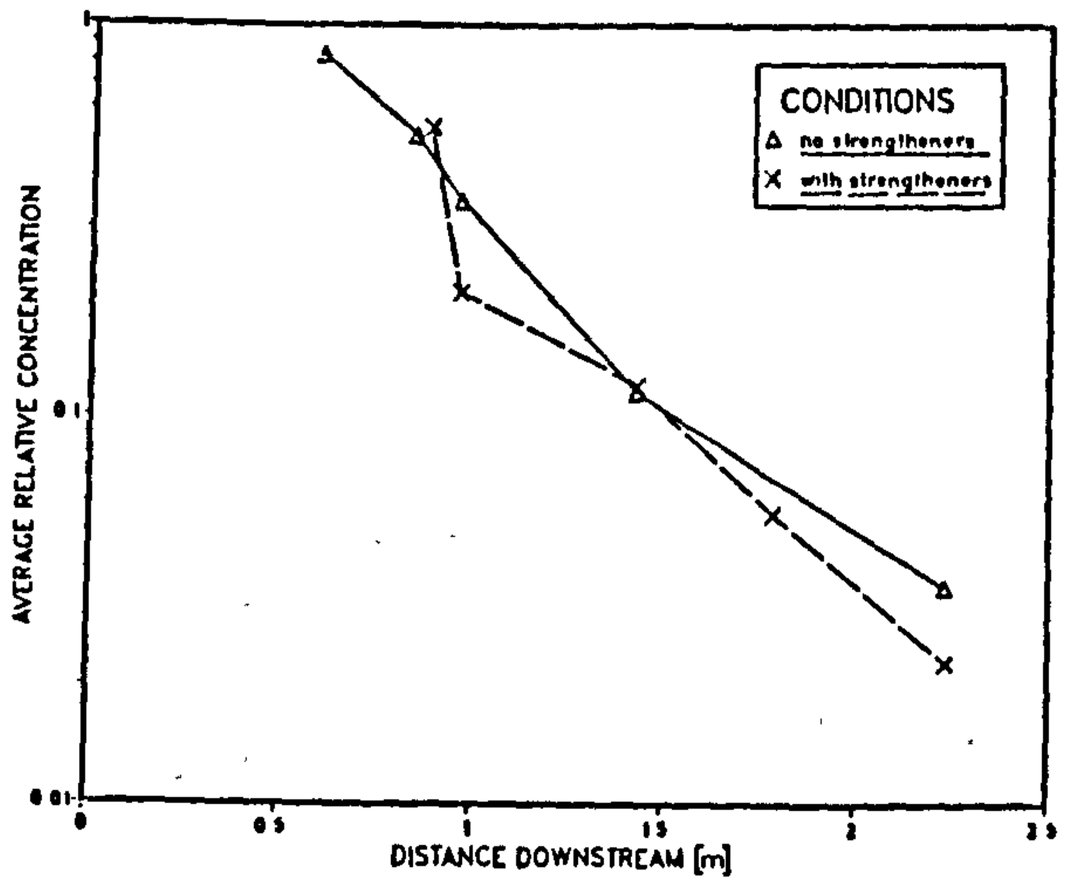

$d_p = 5.6\ \mu m$

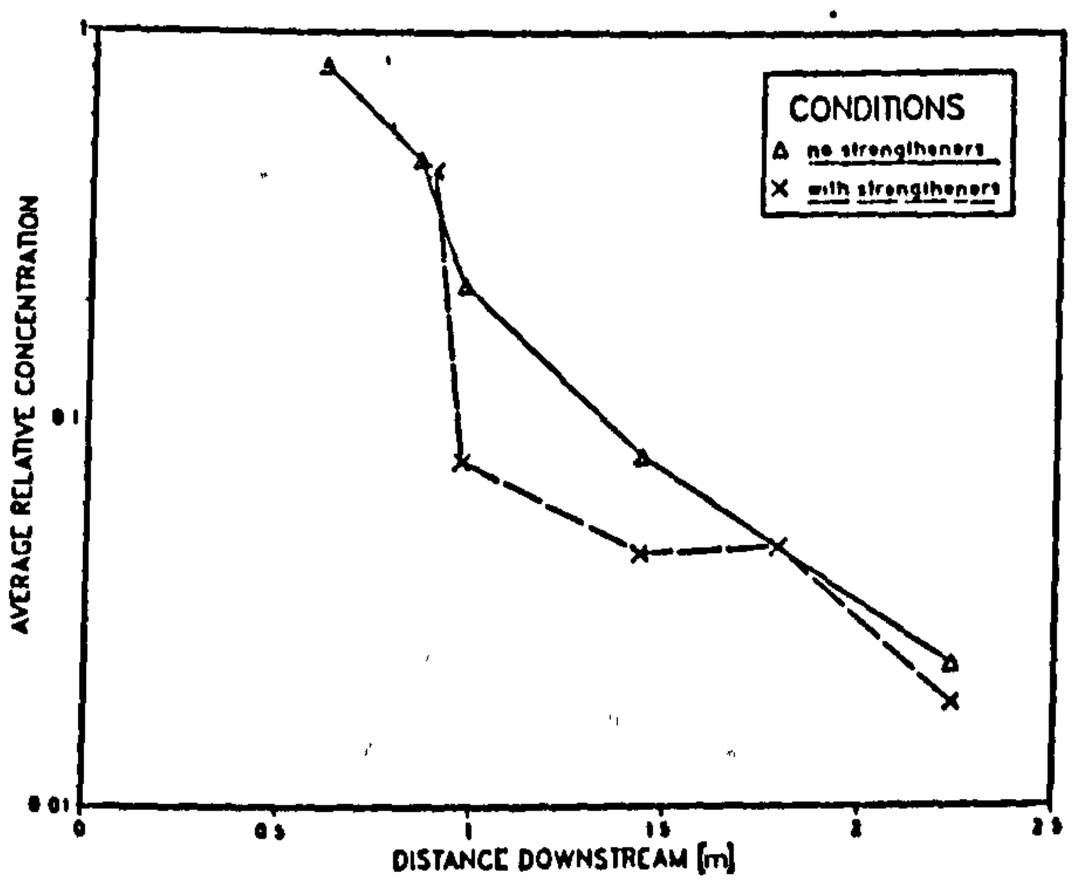

$d_p = 11.3\ \mu m$

Fig. 5.18 Effect of wall strengtheners on decay of dust concentration

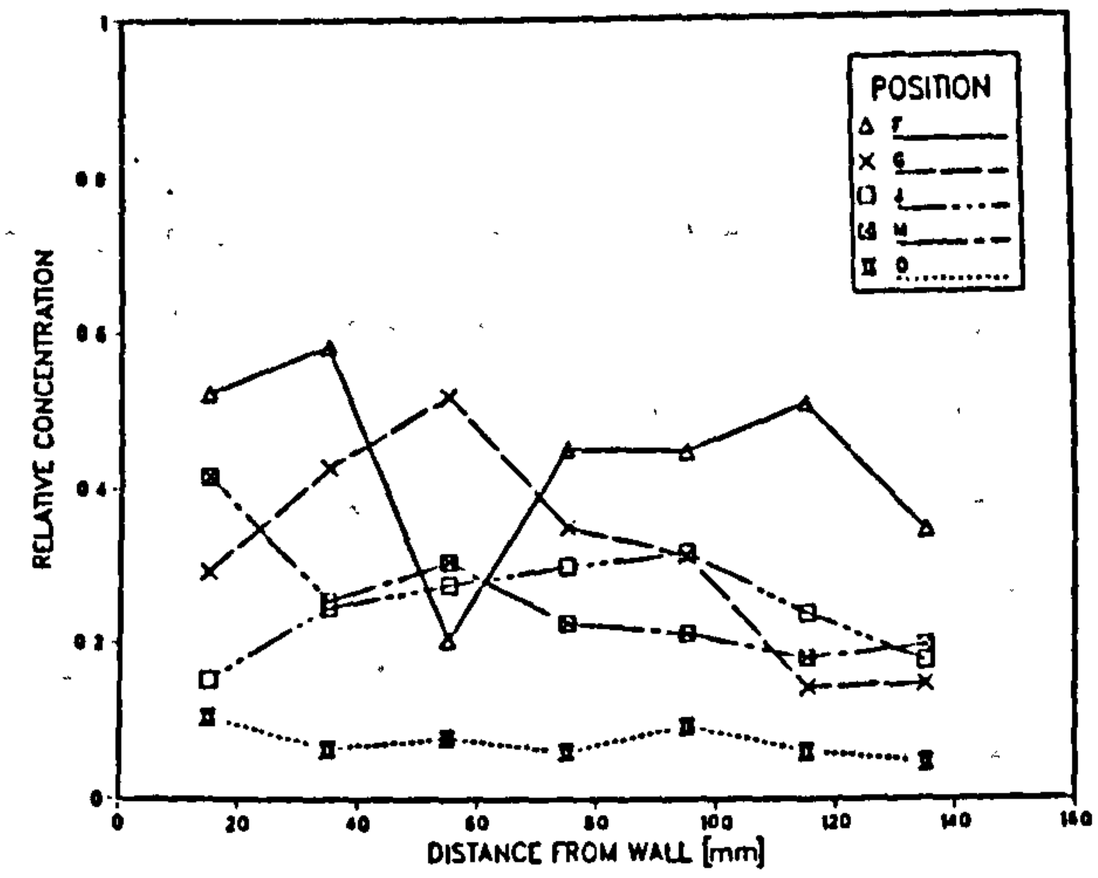

$d_p = 2.25\ \mu m$

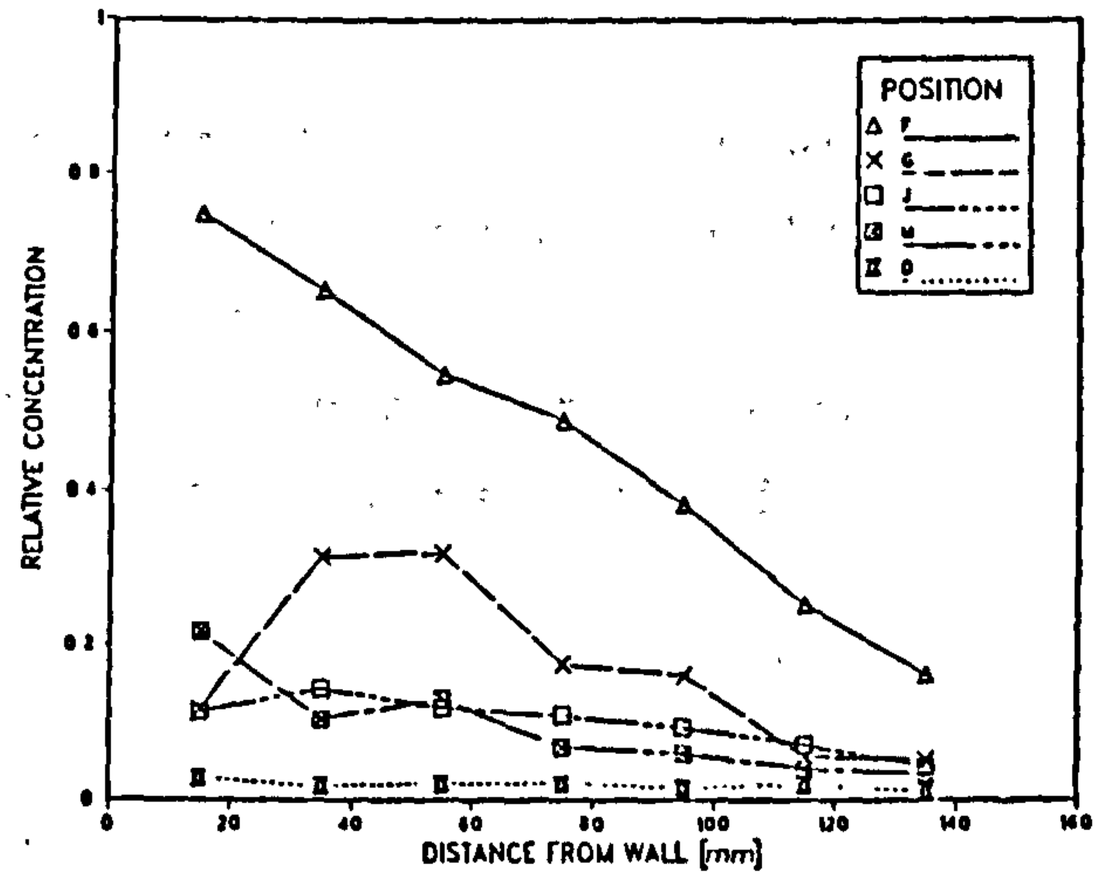

$d_p = 5.6\ \mu m$

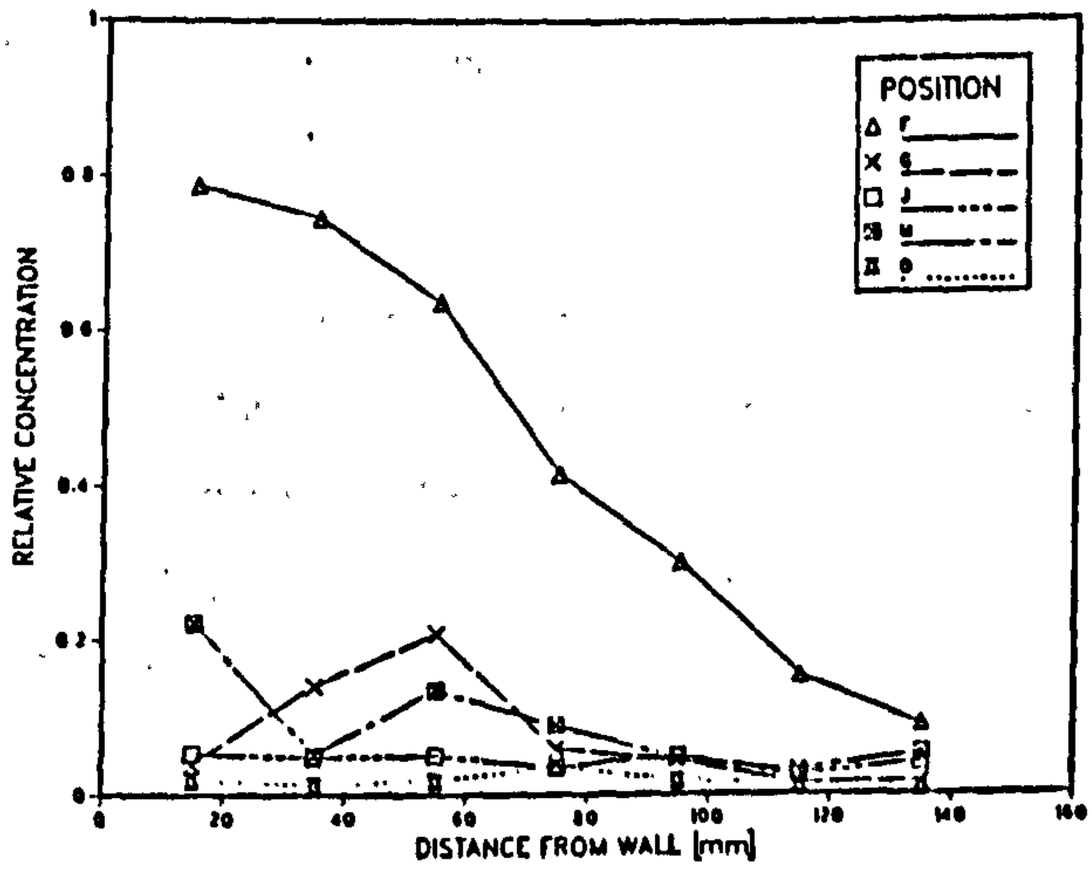

$d_p = 11.3\ \mu m$

Fig. 5.19 Development of dust concentration profiles (with wall strengtheners)

The development of concentration profiles down the duct with the strengtheners installed is shown in Figure 5.19. The sudden fall in concentration in the short section between Positions F and G is most apparent. This section is immediately downstream of the second electrode and coincides with the location of the first strengthener. At Position F the concentration profile is fairly flat for small particles, but a significant build-up of particles towards the wall becomes evident as electrical mobility increases. At Position G, which is 40 mm downstream from the strengthener, the concentration profile appears to be shifted towards the wall. However, the two sampling points closest to the wall are in the shadow of the strengthener, and show significantly lower concentrations. Such results cannot be explained by anisokinetic errors, since the effect is experienced equally for the full range of particle sizes. These results support the mechanism of electrically-enhanced wake capture, as shown in Figure 5.20.

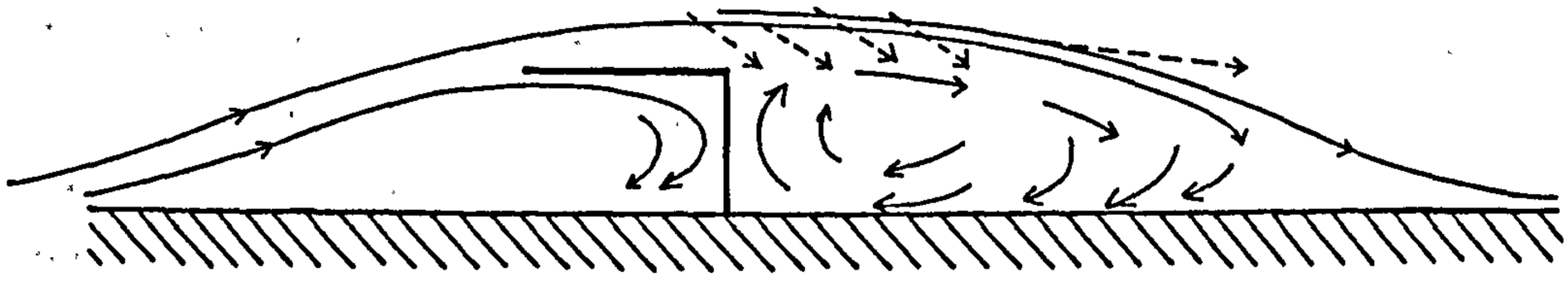

Fig. 5.20 Electrostatically-enhanced capture of particles into wake formed downstream of wall strengthener

Particles are transported by electrical migration and turbulent motion from the mainstream flow into outer edge of the wake. The circulating motion of the fluid in this region conveys the particles in to close proximity with the wall where there is a high chance of capture. The mechanism transporting the large particles into the wake will be electric migration, whereas for small particles turbulent

motion will dominate.

5.2.7.5 Effect of gas velocity

The concentration of dust in the precipitator duct has been measured at Position G for gas velocities of 1, 2 and 3 ms^{-1}. Due to the drastic drop in gas velocity in the region behind the wall strengtheners (down to approximately 0.1 ms^{-1}), anisokinetic sampling errors were accounted for as well as volumetric throughput corrections. The corrected results are shown in Figure 5.21. For particles > 3 μm, minimum concentration appears to coincide with a gas velocity of 1 ms^{-1}.

Conventional design procedures require effective migration velocities, w_e, to be back-calculated from concentration measurements, using the Deutsch equation. These values of w_e are then used to optimise on operating conditions. Care must be taken in the interpretation of these results, since the migration velocity for a gas velocity of 3 ms^{-1} needs to be three times that for a gas velocity of 1 ms^{-1} if equivalent-length precipitators are to produce the same collection, i.e. residence time in the precipitator must be the same if results are to be comparable.

The value of w_e obtained as above is a fitting parameter, and consequently takes into account the effect of turbulence, electric wind, reentrainment and other non-ideal phenomena. Additionally, for a non-uniform electric field such as that found in a wire-plate precipitator, the value of w_e represents an average of the field-dependent mechanisms such as particle charging and migration. Consequently, the effective migration velocity can deviate greatly (often by orders of magnitude) from the theoretical migration velocity, w.

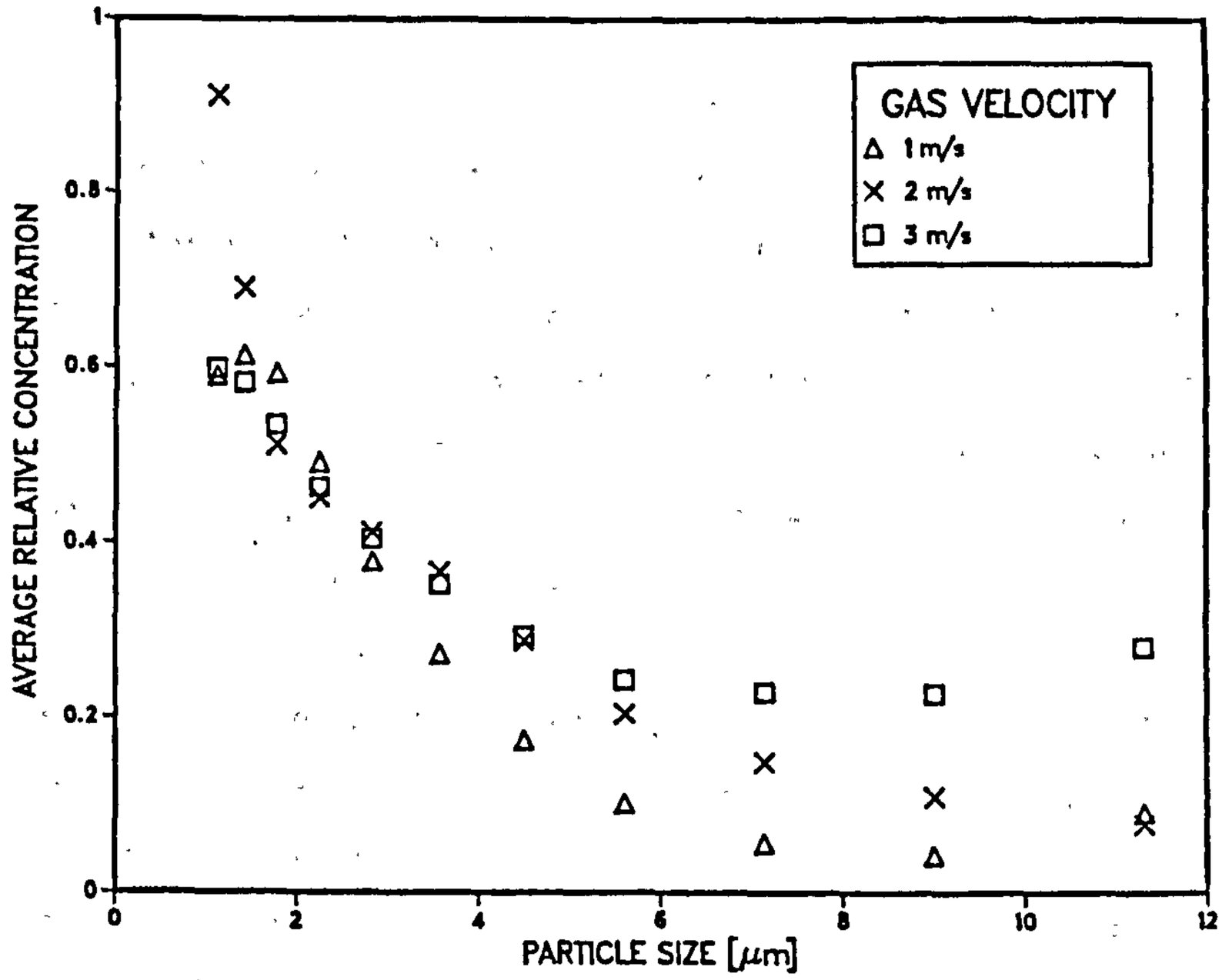

Fig. 5.21 Effect of gas velocity on dust concentration

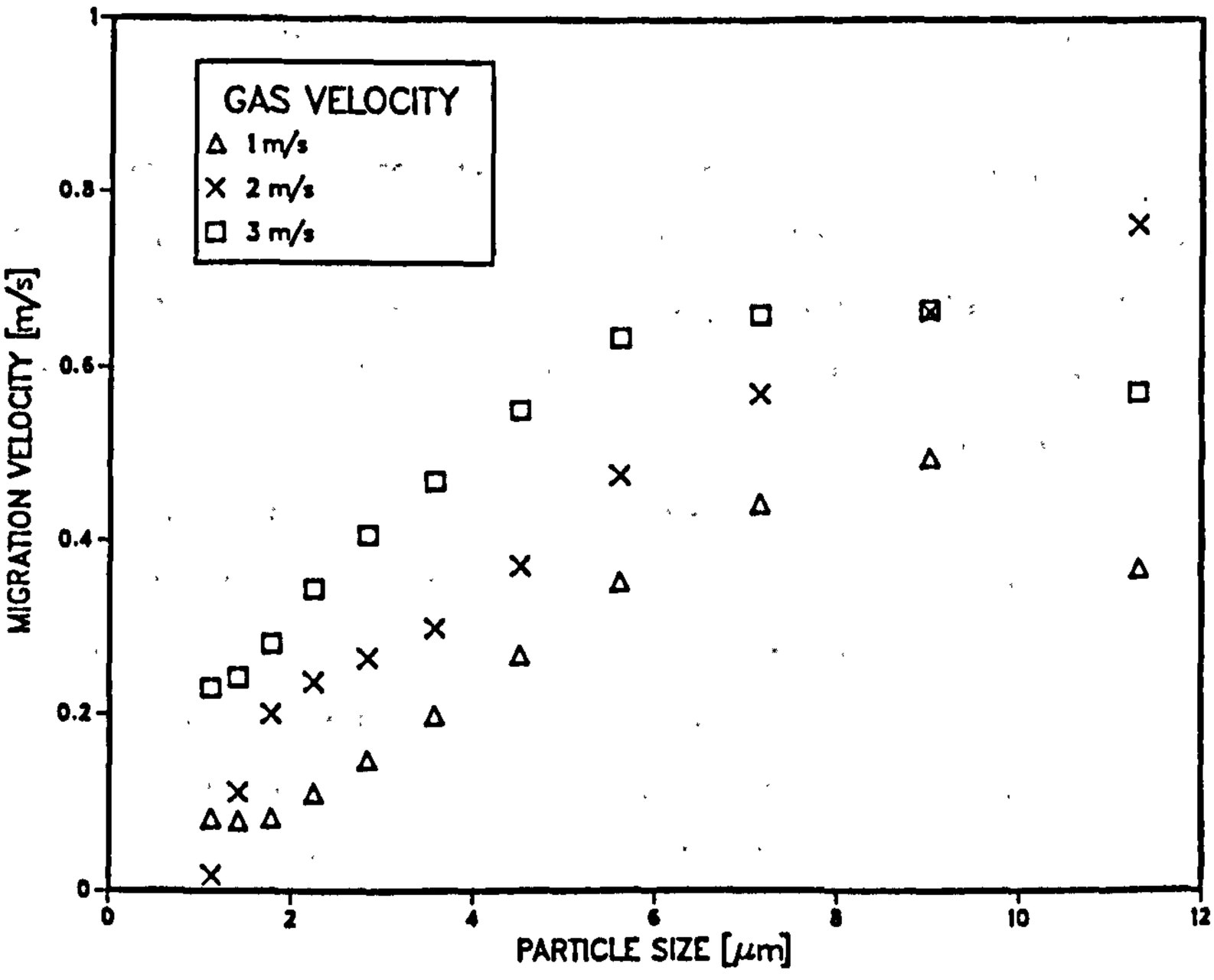

Fig. 5.22 Effect of gas velocity on effective migration velocity

Figure 5.22 shows the effective migration velocity values, back-calculated from the concentration data, for 1, 2 and 3 ms^{-1}. Although low velocities produce preferred turbulence conditions for the collection of particles, electric wind may prove to be a significant factor. The effect of the electric wind may be sufficient to increase turbulence and cause recirculation currents to be set up, possibly even leading to reentrainment. This explains the reduced collection at 1 ms^{-1} for all particle sizes, an effect which is more pronounced for smaller particles with lower electrical mobility.

Field trials performed by Parker (1980) have suggested an optimum gas velocity in the range 1.5 - 2.0 ms^{-1}. The data presented in Figure 5.22 corresponds to a distance of only 1 m downstream, and is insufficient to confirm or refute this. The validity of this method of comparison is doubtful, particularly for systems with wall strengtheners, and may only be useful for a qualitative ranking of different designs.

5.2.7.6 Comparison of collection by twisted square, axial and transverse orientated sawtooth electrodes

Concentration values were measured across the duct at Position J with an applied electrode voltage of -65KV. Two different orientations of the sawtooth electrodes were investigated. Initially the electrodes were positioned with their points aligned with the axis of the duct (axial orientation). Measurements were then made with each electrode turned through 90° so that the points faced the walls (transverse orientation). From the results in Figure 5.23, it appears that axial sawtooth and twisted square electrodes produce similar amounts of collection. Transverse sawtooth electrodes produce inferior collection. The reduced collection of fines may be caused by the increase in

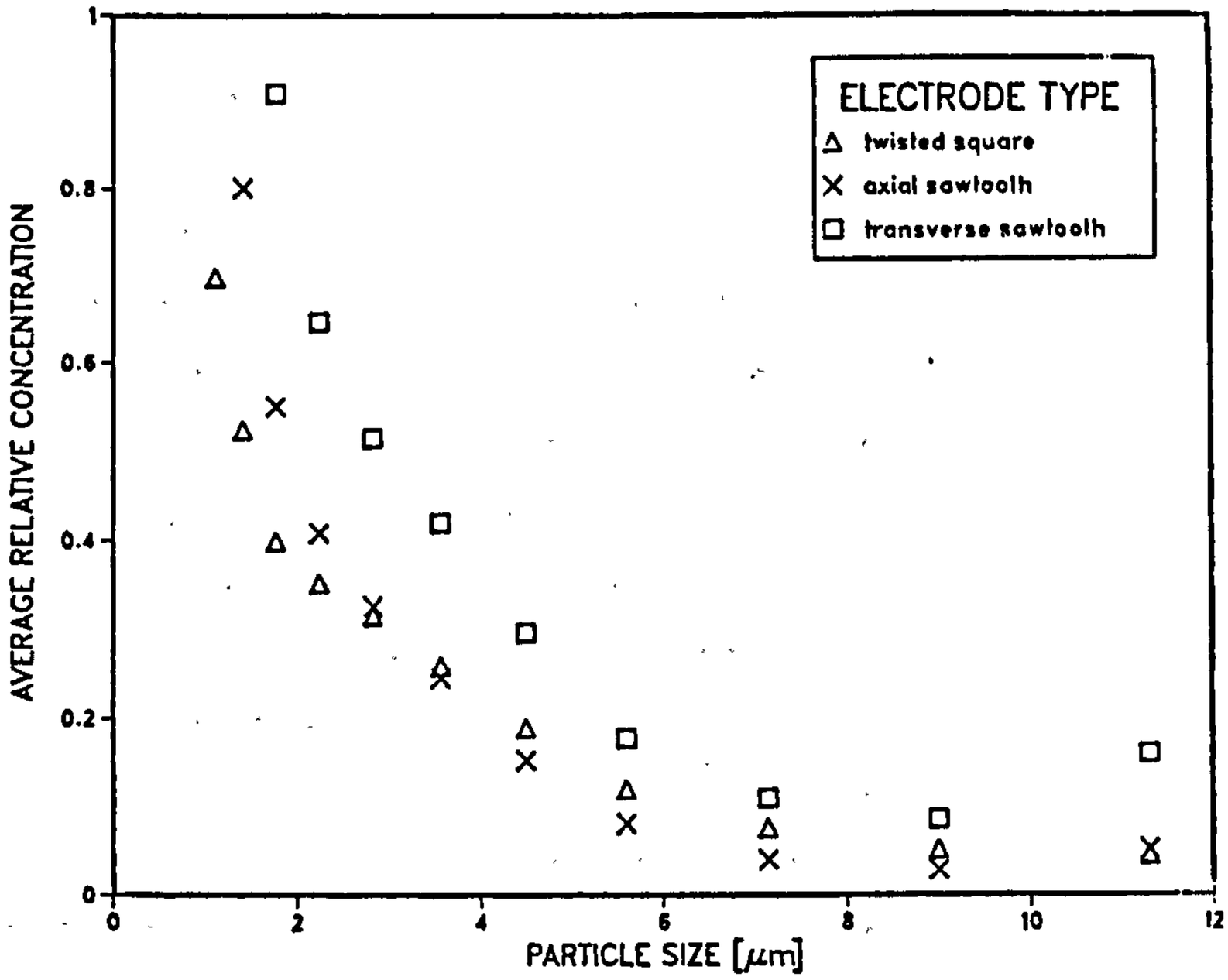

Fig. 5.23 Effect of discharge electrode on dust concentration

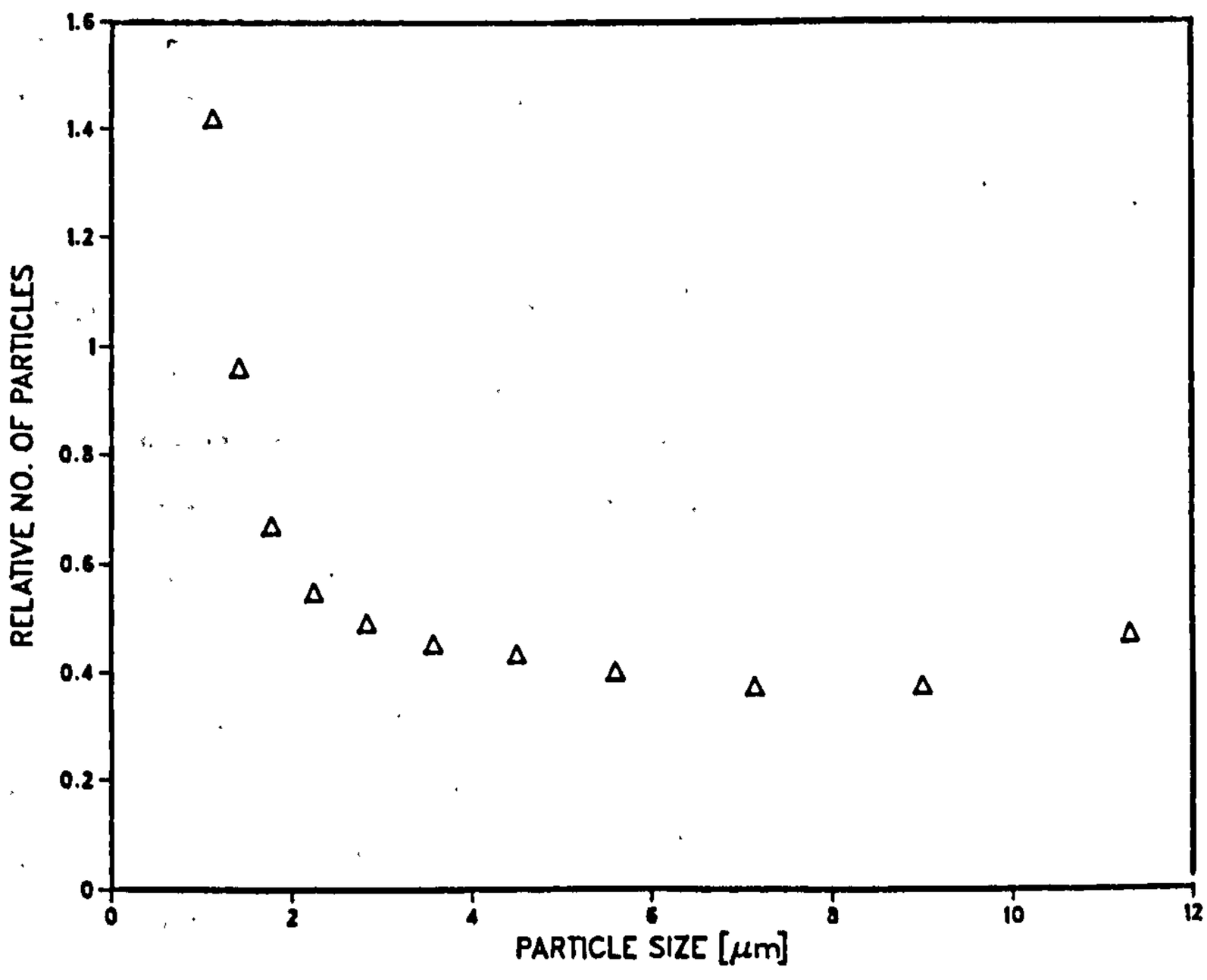

Fig. 5.24 Amount of dust collected in shadow region

turbulence produced by the transverse orientation of the electrodes.

A detailed examination of the measurement position, with respect to the ion density distribution in the duct, aids further explanation of the results. The corona discharge is emitted from the sharp points spaced evenly along the length of the electrodes. The current produced by these electrodes is approximately 3 mA, which is almost twice that emitted by the twisted square electrodes. For transverse sawtooth electrodes, the ions are ejected directly towards the walls, leaving large areas of dead space between the electrodes, as described by Coventry (1985). Axially orientated electrodes produce an ion density that is distributed more evenly throughout the duct, although dead space still occurs in regions adjacent to the electrodes.

Photographic evidence of this dead space is displayed in Figure 5.25, where an outline of the first axially orientated sawtooth electrode is clearly imprinted onto the collected dust layer. The region of wall opposite the electrode is almost devoid of particles, due to the lack of ions and also the low electric field value. Quantitatve analysis of the number of particles landing in this shadow region was determind by attaching a strip of aluminium foil across the area of interest. Dust was then injected into the duct for 10 minutes, with an applied voltage of -65KV. Samples measuring 25 x 25 mm were cut from the aluminium foil, in both the shadow and dusty regions, and Coultered to enable comparison between concentration of particles.

Figure 5.24 shows the number of particles landing in the shadow region as a fraction of those in the dusty region. For particle sizes > 3 μm the collection in the shadow region is only approximately 40% of that in the

CLEAR OVERLAYS

OVERLAYS SCANNED SEPERATELY AND OVER THE RELEVANT PAGE.

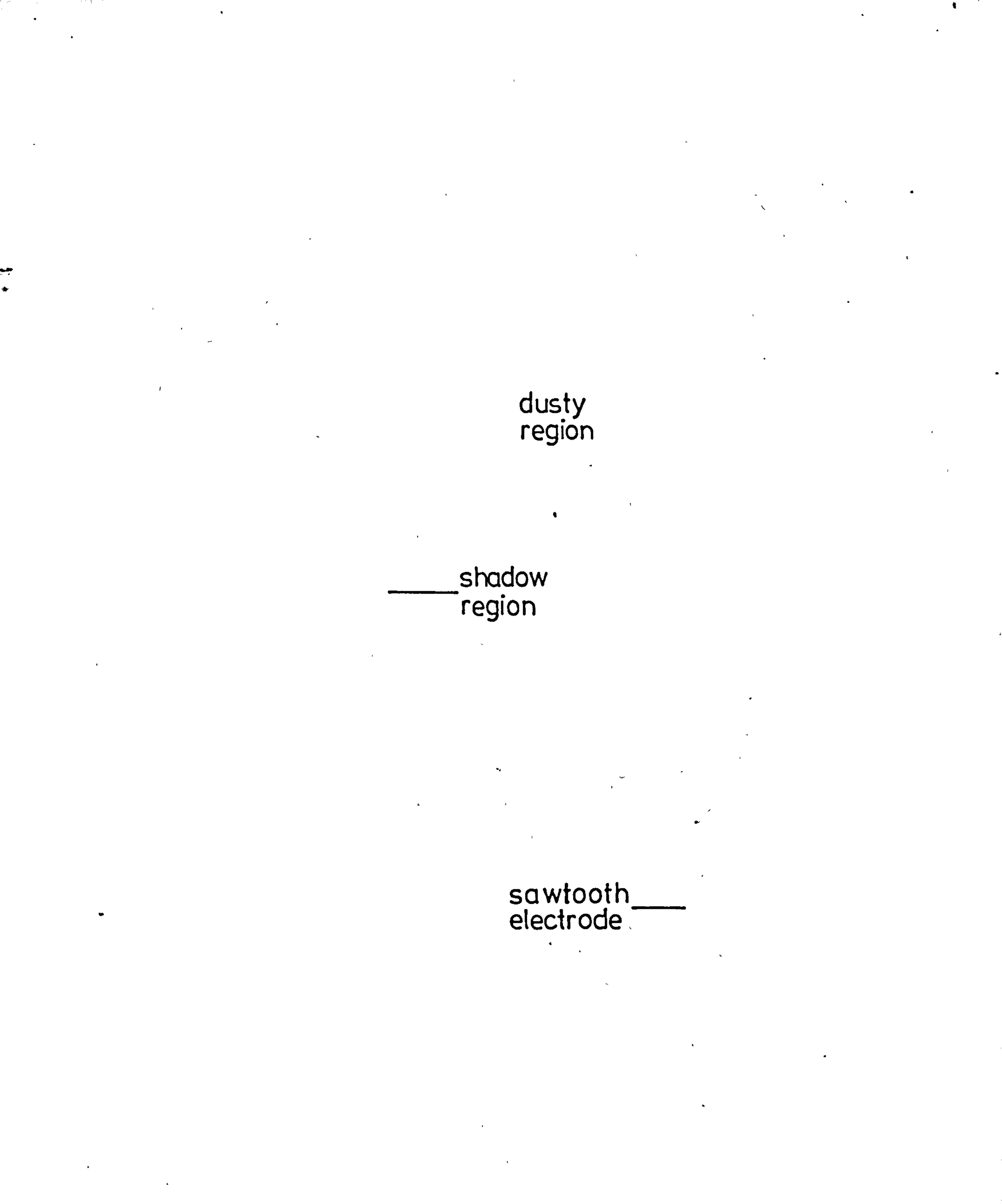

Fig. 5.25 Shadow region on wall opposite electrode

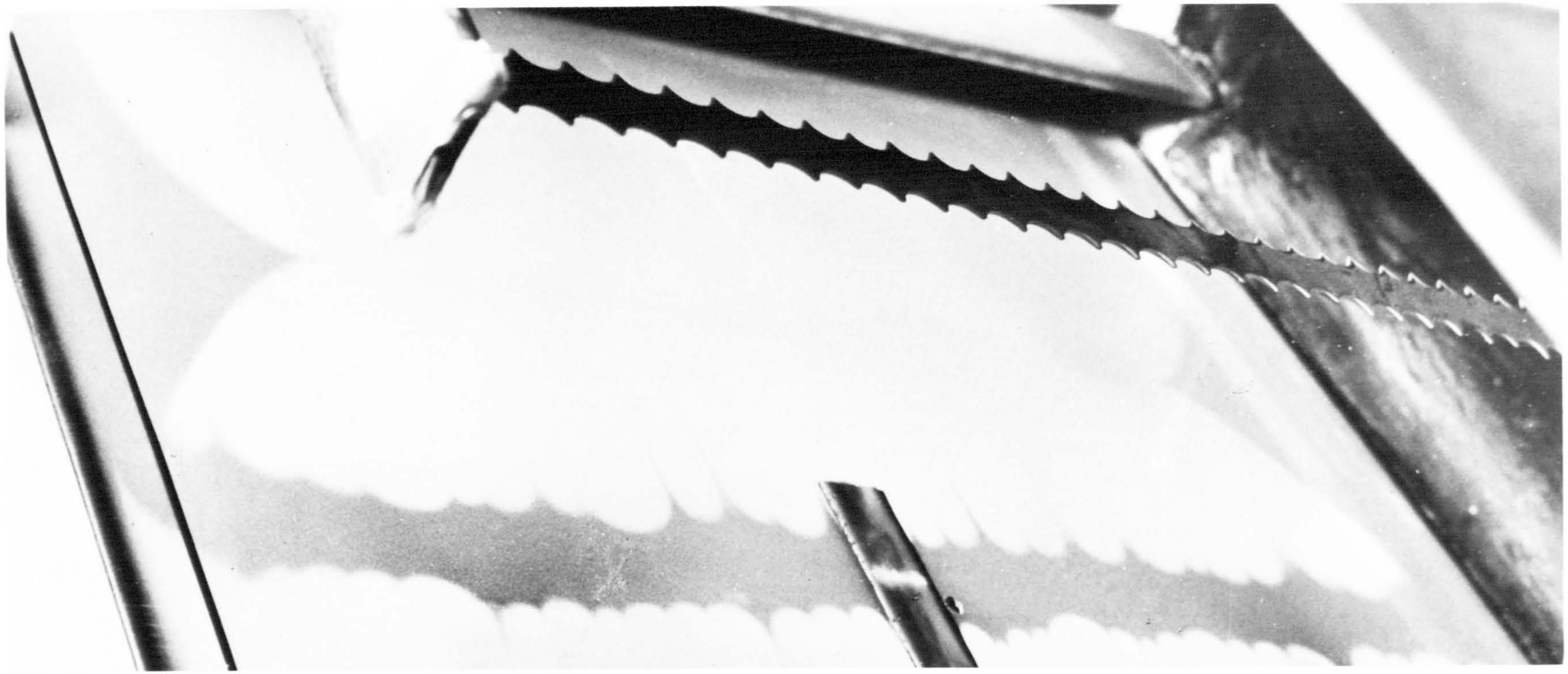

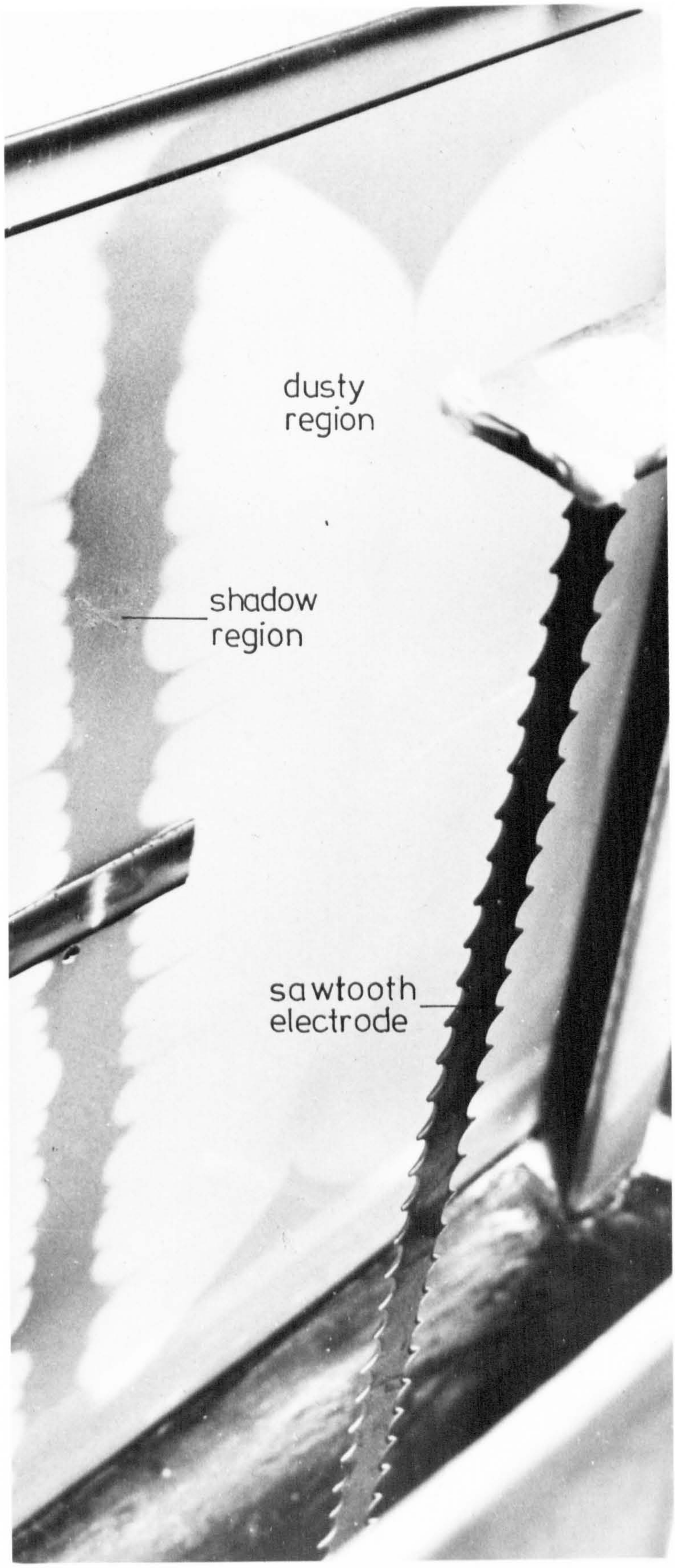

Fig. 5.25 Shadow region on wall opposite electrode

adjacent dusty region. As expected, smaller particles are affected less since electrostatic collection is low anyway.

5.3 Mechanical deposition on collection walls

Information on the amount of dust deposited on the walls of the precipitator was required in order to assess the extent of turbulent deposition in the absence of applied electrode voltage. The collection due to this mechanism is expected to be of the order of a few percent, and is more accurately determined by a direct analysis of wall deposits rather than attempting to deduce values from small fractional changes of the bulk flow.

5.3.1 Method

A method of collecting and removing samples from the walls was developed, which also allowed investigation into localised fluctuations of mechanical collection due to the presence of wall strengtheners and flow modulation pipes. Strips of aluminium foil, coated with Nonidet P40 to retain the collected particles, were stuck along the walls of the precipitator. After 30 minutes of dust deposition the strips were carefully removed from the wall and cut into 50x50 mm sections. Each section was then analysed using the Coulter Counter as described in Section 5.2.6.

5.3.2 Results and discussion

The amount of dust collected on the aluminium foil samples attached to the precipitator wall was analysed with the Coulter Counter. The number of particles collected mechanically was measured both with and without wall strengtheners, and included samples taken from the surfaces of the strengtheners.

5.3.2.1 Relative concentration

Mechanical deposition results may be displayed in a most informative manner by plotting the no. of particles/m^2 collected on the wall, n_s, as a fraction of the no. of particles/m^2 at the inlet, n_i. The amount of dust deposited at various distances downstream can than be examined, to give direct information on the localised effect of wall strengtheners and the flow modulation pipes. Dust samples taken from the wall strengtheners were treated in a similar manner.

(i) Without strengtheners

Figure 5.26 displays the trend of increasing mechanical deposition for larger particles. The effect of the 0.1 m diameter flow modulation pipes at the inlet is to encourage deposition, particularly for large particles. The deposition of fines is hardly affected by their presence. The deposition appears to level off between 0.9 - 1.0 m downstream from the pipes.

(ii) With strengtheners

The results of wall deposition measurements made with strengtheners installed are shown in Figure 5.27. In general, deposition increases with particle size. Interesting is the increase in deposition by a factor of approximately 3 for the 2.25 μm particles at a position midway between the wall strengtheners. This effect is not apparent for the larger particles, and may be explained by examination of Helium bubble traces (see Figure 3.16). Midway between the strengtheners corresponds to the position where the streamlines are pushed back to the wall following the wake region downstream of the wall strengthener. The small particles are able to follow the path of the

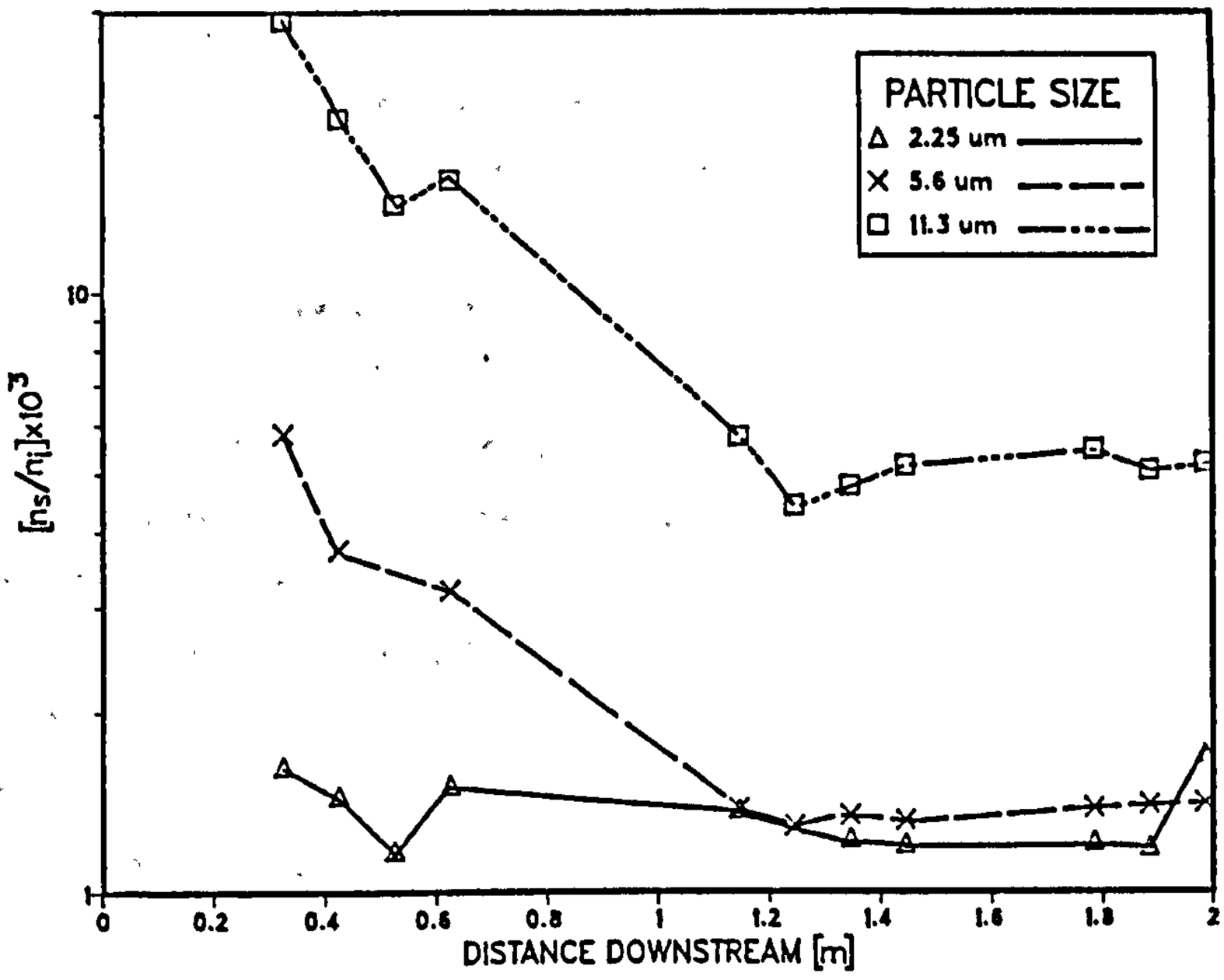

Fig. 5.26 Mechanical deposition versus distance downstream (no wall strengtheners)

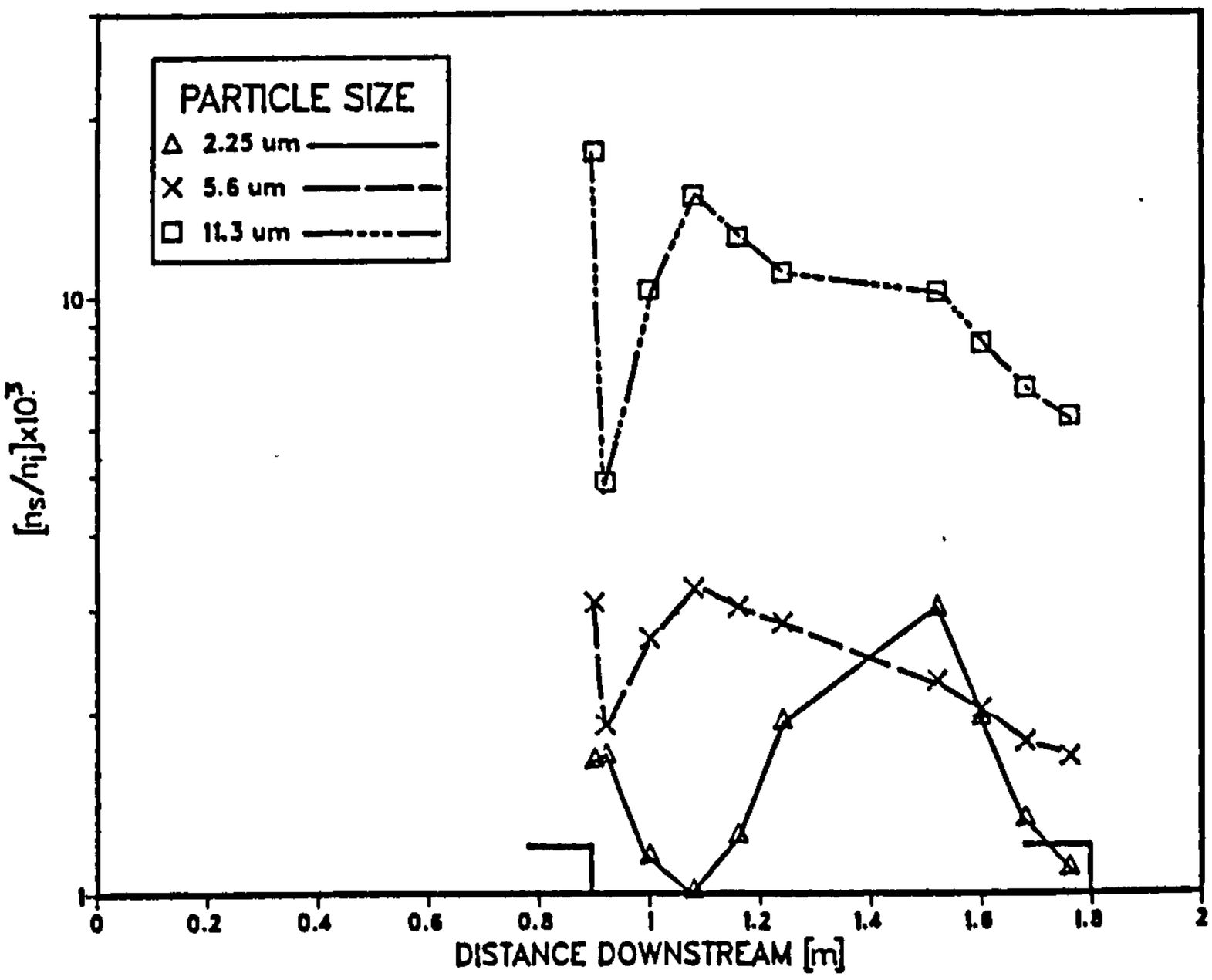

Fig. 5.27 Mechanical deposition versus distance downstream (with wall strengtheners)

streamlines and are brought into close contact with the wall, thereby enhancing their collection. The larger particles, however, follow a less tortuous path due to their high inertia, and are detoured around the next strengthener without approaching close to the wall.

Table 5.1 shows the relative number of particles for positions A, B and C on the wall strengtheners for 2.25, 5.6 and 11.3 μm particle sizes. The location of positions A, B and C are shown in Figure 5.28. It appears that the deposition of large particles onto region A is lower by a factor of 4 than on regions B and C. This may again be explained by the high inertia of the large particles, causing them to deviate from the streamlines and hence resist collection.

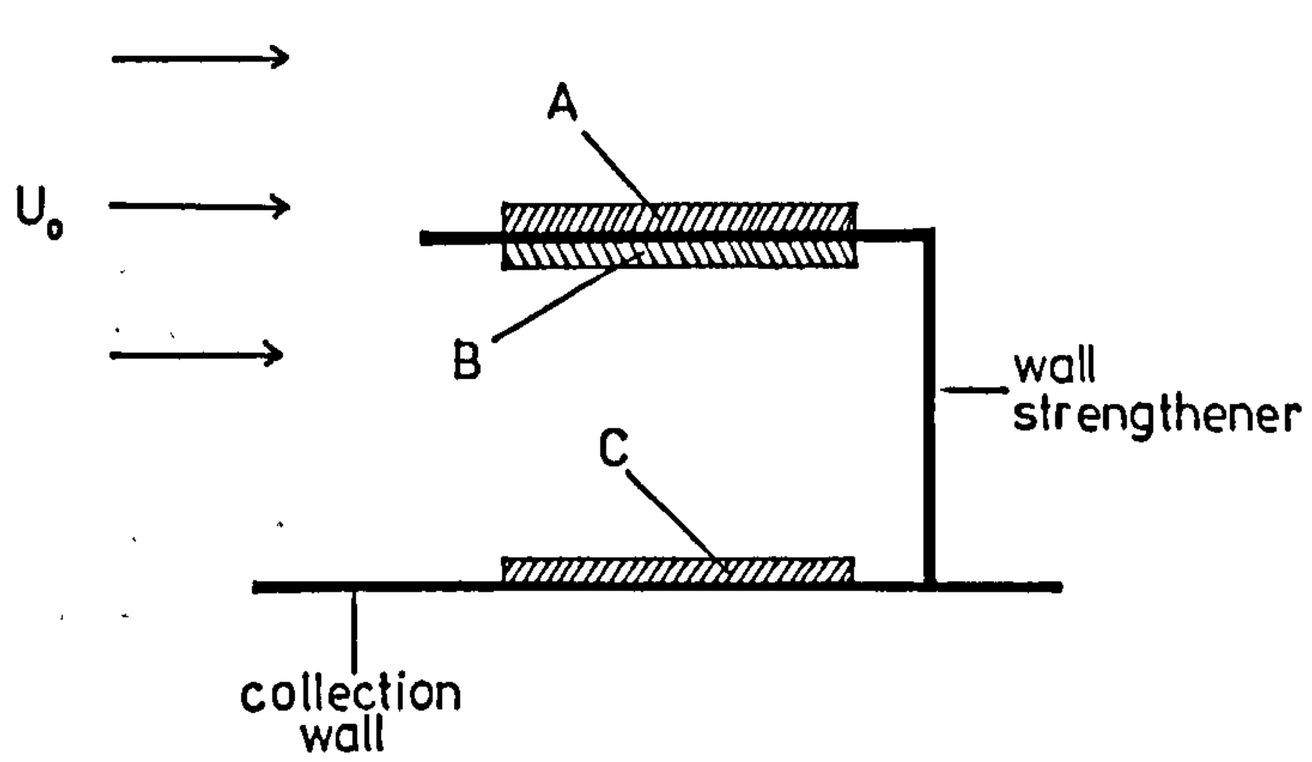

Fig. 5.28 Location of samples A, B and C on wall strengthener

Particle size (μm)	$(n_s/n_i)x10^3$ A	B	C
2.25	1.7	1.5	1.7
5.6	4.5	3.4	3.1
11.3	4.1	15.5	17.5

Table 5.1 Mechanical deposition on wall strengtheners

Approximately equal covering of surfaces A, B and C occurs for fines, but more 5.6 μm particles are deposited on surface A than surfaces B or C. This is possibly because the inertia of 5.6 μm particles is low enough for them to remain near to surface A, but high enough for turbulent deposition to be significant.

5.3.2.2 Deposition velocity

It is informative to compare the degree of mechanical deposition with that predicted theoretically, as discussed in Section 1.5. Dimensionless deposition velocity values, V_d^+, and dimensionless relaxation times, T_p^+, were calculated for each particle size range, to allow comparison with the experimental data of others. The results shown in Figure 5.29 were measured at a distance far enough downstream for the effect of the flow modulation pipes to be negligible, and correspond to values of v^*=0.1 and 0.5 ms^{-1}.

Agreement with the theoretical curve predicted by the models discussed in Section 1.6 is best for large particles when v^*=0.1 ms^{-1}. The deposition velocity for T_p^+<1 is much higher than the predicted values for both values of v^*. This is probably caused by electrostatic attraction of the fines to the collection walls by image forces. The residual particle charge occurs as a result of tribo-electric charging in the dust dispersion process. This cannot be

easily eliminated, and provides further support for discarding concentration results in the lower channels of the Coulter Counter analysis. Also, the theoretical values are for the case of fully developed channel flow, which is a condition probably never attained in a precipitator, particularly with wall strengtheners present.

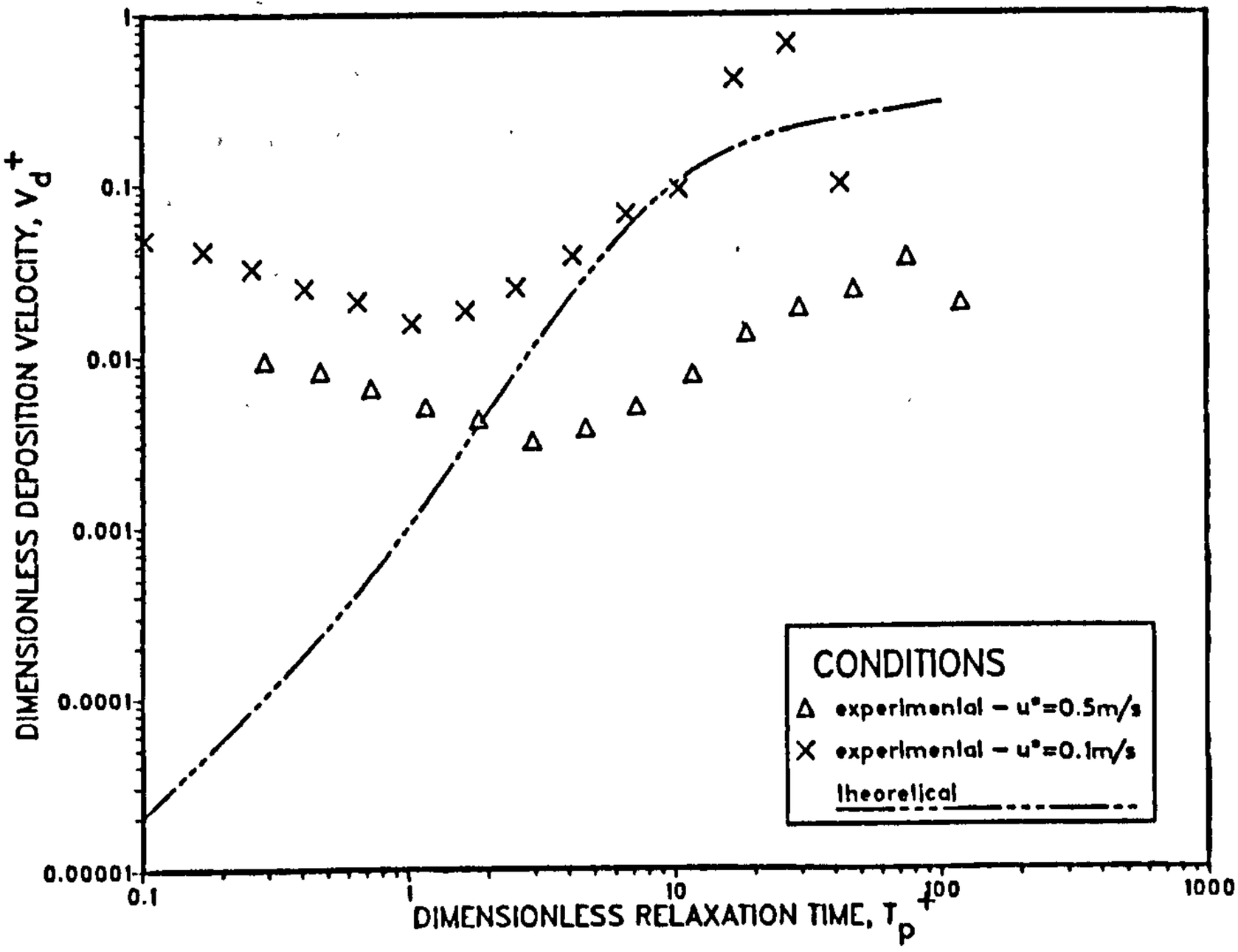

Fig. 5.29 Comparison of experimental and theoretical V_d versus T_p curves

This method of representing data may be severely misleading, particularly for the measurements in the stationary zones within wall strengtheners. The concentration values here are likely to be significantly lower than in the central core of the duct, thus leading to deposition velocity values that indicate lower collection than expected.

5.3.2.3 Mechanical efficiency

Mechanical efficiency values were calculated by dividing the total amount of dust collected on the walls by the total amount of dust injected into the precipitator during the 30 minute run time. This was determined from simultaneous inlet concentration measurements using the sampling probe as described in Section 5.2. The efficiency values for particle sizes 2.25 and 11.3 μm are shown in Table 5.2, and correspond to a duct length of 1.8 m (i.e. up to the second set of wall strengtheners). Since deposition samples were only analysed at specific locations along the wall, intermediate values were interpolated.

Particle size (μm)	Efficiency (%)	
	Without strengtheners	With strengtheners
2.25	1.74	2.19
11.3	16.6	21.04

Table 5.2 Effect of wall strengtheners on mechanical efficiency

The results in Table 5.2 show that although the mechanical efficiency of the 11.3 μm particles is almost ten times that of the 2.25 μm particles, the presence of the wall strengtheners increases the value by approximately 23% in both cases.

CHAPTER 6

NUMERICAL MODELLING

6.1 Introduction

Experimental procedures for assessing electrostatic precipitator designs are costly and time consuming, and nowadays the analyses can be performed more easily using reliable mathematical models. The availability of powerful computing facilities has encouraged the development of improved numerical techniques for modelling precipitator performance. One simple analytical solution, the Deutsch-Anderson expression, requires that all the complex phenomena involved in the process of particle migration and capture are represented by a single parameter - the effective migration velocity, w_e. However, such a simple model would appear to be of assistance only when considering scale-up or minor alterations to an established design. Ideally, each mechanism contributing to precipitator performance would be incorporated explicitly into a model so that its individual effect could be controlled and assessed. Unfortunately, the mathematical description of effects such as particle space charge density are complicated, and often information must be obtained experimentally. Alternatively, mathematical assumptions and simplifications can be applied.

Clearly it is necessary to estimate the relative importance of a particular mechanism before attempting a detailed mathematical description. The work described in this thesis concentrates on the factors affecting particle motion in a working precipitator, and some of the contributing mechanisms have been studied to gain insight into their relative importance. A popular method for describing particle motion in a precipitator adopts the convective-diffusion approach (ref. Williams and Jackson

(1962), Leonard et al. (1983)). This involves the analytical or numerical solution of a differential equation incorporating terms describing the diffusion and electrical migration of particles. Analytical methods of solution tend to be cumbersome, and point-to-point changes in parameters such as gas velocity and diffusion coefficient cannot easily be accommodated. Numerical solution of the differential equation using finite difference techniques is more amenable to the inclusion of locally varying parameters. A model of this type is developed in this chapter, employing a Crank-Nicholson solution scheme (ref. Smith (1978)).

The main difficulty in the application of the convective-diffusion equation lies in the choice of boundary conditions. Much discussion on the subject has already been published, and it appears that a simple equation is inadequate in representing the complex mechanisms that affect particle transport and capture on the wall. These mechanisms include particle-particle cohesion, particle-wall adhesion, reentrainment, turbulent deposition and electrical migration across the fluid boundary layer.

Alternative methods of solving the convective-diffusion equation have also been considered (reference Samuel (1981) and Lawless, Dunn and Sparks (1981)). The model of Lawless et al. is of particular interest, and in this chapter a second numerical model is developed which adopts their approach. The method assumes that the transport of dust down the precipitator can be represented mathematically by the step-wise progression of vertical line-sources of dust. The motion of these sources is governed by electrical migration and lateral diffusive spread. The concentration values yielded by the model are located at the nodes of a grid superimposed on the duct geometry. This type of model allows a more realistic description of the mechanisms affecting particle collection, although new problems arise,

such as the relevant choice of diffusion coefficient values (see Section 6.6.3).

Both of the above methods for obtaining dust concentration profiles rely on the accuracy of the electric field calculations. Previous solutions of the convective-diffusion equation have in general been confined to situations involving a uniform electric field, such as that found between two parallel plates (reference Leonard et al. (1983)). Although the results from such models are useful in assessing the dominant mechanisms in the collection zone of a two-stage precipitator, more realistic electric field values are required if comparisons with results from wire-plate systems are to be made.

The main aims of the work described here are;

a) to develop models capable of incorporating spatial-dependent parameters such as gas velocity and diffusion coefficient,
b) to use the models to identify the important mechanisms affecting particle migration and collection,
c) to test the models by comparing theoretical and experimental results,
d) to compare the two different approaches, noting the advantages and disadvantages of each.

6.2 Schematic representation of modelling strategy

The flow chart below shows the procedures employed in the computer program to calculate dust concentration using either finite difference or line-source methods. Calculation of the electrical conditions in each case is the same. Figure 6.1 shows the computational grid superimposed onto the precipitator duct. The geometry of the wire-plate

FLOW CHART OF COMPUTER MODEL

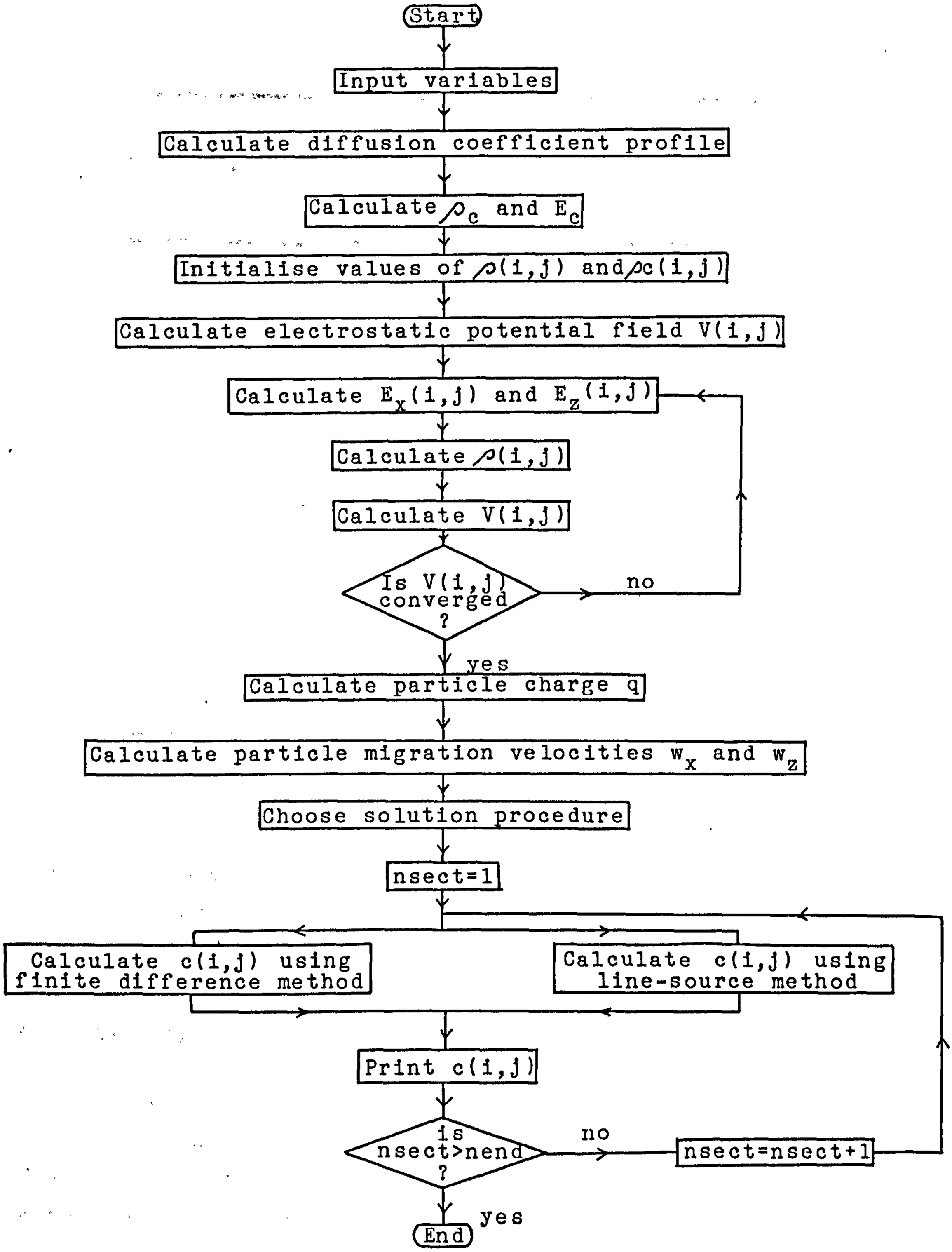

design is such that the electric field in the rest of the duct can be deduced via symmetry considerations.

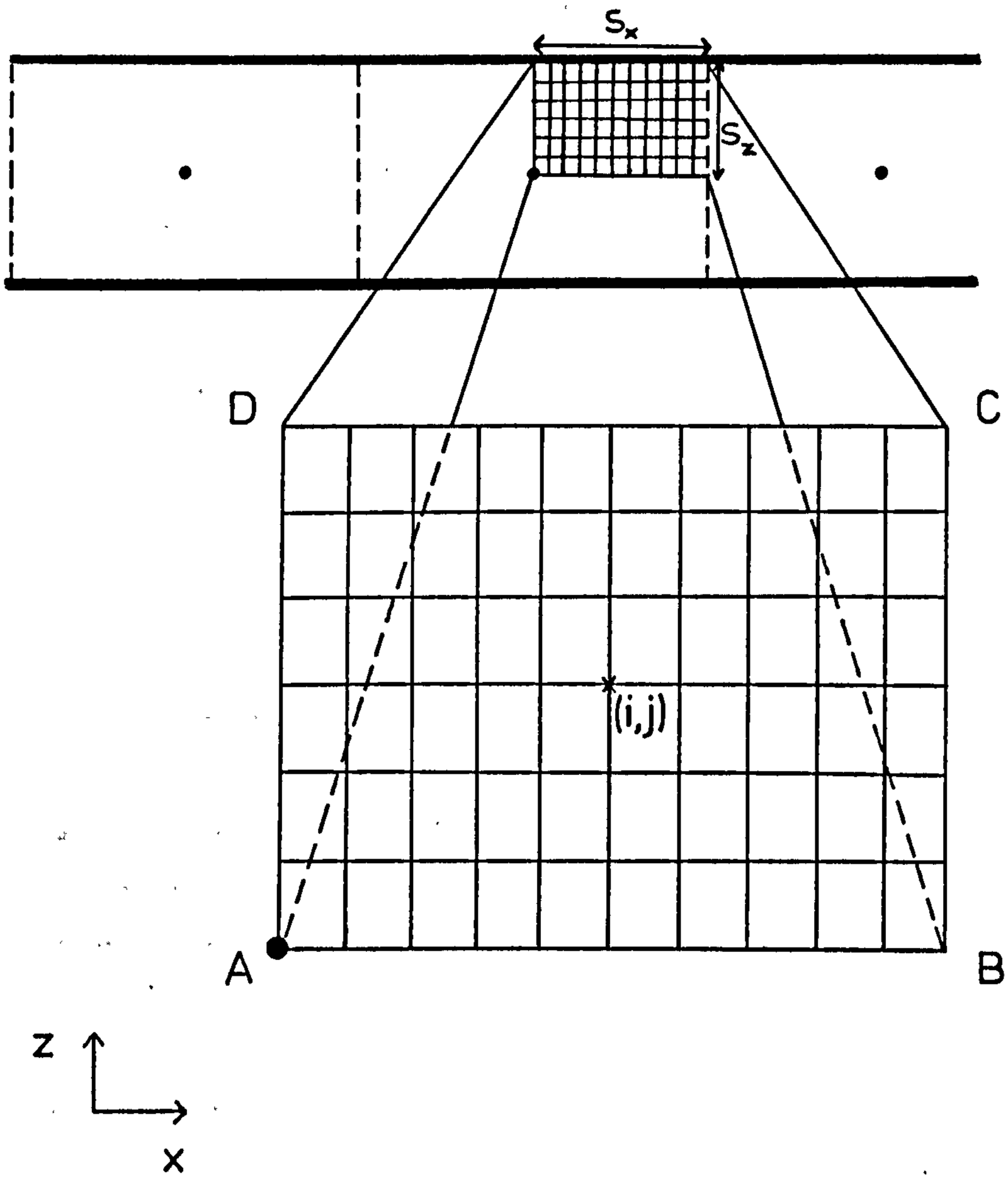

Fig. 6.1 Computational grid used to simulate electrostatic precipitator duct

6.3 Calculation of electrical conditions

A detailed explanation of the method described here for calculating electric field values can be found in Leutert and Bohlen (1972). More rigorous methods, which include the effect of space charge density, have since been developed

(see Section 1.2.1), but such extensive analysis of the electric field does not fall within the scope of this work. In Chapter 5 low dust loadings have been used extensively and consequently particle space charge effects are minimised.

For steady state conditions, and assuming magnetic effects to be negligible, the electric field may be described by the following equations:

$$\nabla^2 V = -\rho/\varepsilon_o \qquad \text{- Poisson's equation}$$

$$\underline{E} = -\nabla V$$

$$\underline{J} = \rho b \underline{E}$$

$$\nabla . \underline{J} = 0 \qquad \text{- Current continuity equation}$$

where $\underline{E}$ = electric field (Vm^{-1}),
ρ = space charge density (Cm^{-3}),
$\underline{J}$ = current density (Am^{-2}),
b = electrical mobility of charge carriers ($m^2V^{-1}s^{-1}$)

Finite difference replacements in these equations allow values of V and ρ to be calculated iteratively throughout the grid, as outlined in Section 6.2.

6.3.1 Electrostatic potential

An approximation to the potential field is required to initiate the iterative procedure described in Section 6.2. This is obtained from the expression previously defined in Section 1.2.1., but omitting the second term which estimates space charge effects. Tests show that sufficient accuracy is obtained by using $-3<m<3$ in the summation terms. This expression is only valid for applied voltage values less

than the critical voltage (which signifies the onset of corona discharge), but is a useful first approximation for the iterative procedure.

6.3.2 Electric field

To calculate the electric field values $E_x(i,j)$ and $E_z(i,j)$ throughout the grid, current values of the potential field V(i,j) are substituted into a finite difference form of $\underline{E} = -\nabla V$, viz

$$E_x(i,j) = -\frac{(V(i,j)-V(i-1,j))}{h}$$

and

$$E_z(i,j) = -\frac{(V(i,j)-V(i,j-1))}{k}$$

Calculations are simplified by zero values on the boundary conditions, which are as follows:-

$$AB - E_x = 0$$
$$BC - E_x = 0$$
$$CD - E_x = 0$$
$$DA - E_z = 0$$

These boundary conditions are later shown to be essential in the solution of the space charge density equations.

The electric field E_c acting at the surface of the discharge electrode is calculated from an empirical expression derived by Peek (1929)

$$E_c = f(30\delta + 9(\delta/r)^{1/2}) \times 10^5$$

where f = wire roughness (f=1 for a smooth wire),
δ = relative density of the air,
r = radius of discharge electrode (cm)

6.3.3 Space charge density

Space charge density $\rho(i,j)$ is determined by expressing the current continuity equation in the form

$$\nabla.\underline{J} = \nabla.(\rho b\underline{E}) = 0$$

giving

$$b(\rho \nabla.\underline{E} + \underline{E}.\nabla\rho) = 0$$

Assuming constant mobility and applying Poisson's equation, this expression reduces to

$$\rho^2/\varepsilon_o = -\underline{E}.\nabla\rho \qquad (6.1)$$

Substituting the backward difference replacement terms

$$\frac{\partial\rho(i,j)}{\partial x} = \frac{\rho(i,j) - \rho(i-1,j)}{h}$$

$$\frac{\partial\rho(i,j)}{\partial z} = \frac{\rho(i,j) - \rho(i,j-1)}{k}$$

into equation 6.1 yields

$$\rho(i,j)^2 + \frac{\varepsilon_o(E_x k + E_z h)}{hk}\rho(i,j) - \frac{\varepsilon_o}{hk}(E_x k\rho(i-1,j) + E_z h\rho(i,j-1)) = 0$$

This is a quadratic which can be solved to yield a value for $\rho(i,j)$. The initial values of space charge density are

$$\rho(i,j)=0$$

$$\rho(1,1)=\rho_c$$

where ρ_c is the approximate space charge density at the discharge electrode, defined by McDonald et al. (1977) as

$$\rho_c = \frac{2s_x J}{100bfr(30\delta + 9(\delta/r)^{1/2})} \times 10^{-3}$$

6.3.4 Potential field

The potential field V(i,j) is calculated by expressing Poisson's equation in the form

$$\frac{\partial^2 V}{\partial z^2} + \frac{\partial^2 V}{\partial x^2} = -\rho/\varepsilon_o \qquad (6.2)$$

Substituting the central difference replacements

$$\frac{\partial^2 V(i,j)}{\partial x^2} = \frac{V(i+1,j)-2V(i,j)+V(i-1,j)}{h^2}$$

$$\frac{\partial^2 V(i,j)}{\partial z^2} = \frac{V(i,j+1)-2V(i,j)+V(i,j-1)}{k^2}$$

into equation 6.2 and rearranging gives

$$V(i,j) = \frac{1}{2(h^2+k^2)} \Big[h^2(V(i,j+1)+V(i,j-1)) + k^2(V(i+1,j)+V(i-1,j)) + h^2k^2\rho(i,j) \Big]$$

This expression allows new values of V(i,j) to be calculated from surrounding old values of potential field and space charge density. Initial potential field values are obtained from Cooperman's electrostatic solution.

6.4 Calculation of particle migration

6.4.1 Particle charge

Once sufficient iterations have been performed for the potential field values to converge, the corresponding electric field components E_x and E_z are used to determine the electric charge, q, acquired by the particles. For

simplicity it is assumed that each particle attains its limiting charge q_s, as defined by equation 1.2, on entering the precipitator. In reality, this value reflects the optimum charging conditions experienced by the particle, since the loss of charge from a particle is relatively slow. This could only be accounted for in the model if particle trajectory calculations were performed and the information concerning the history of the particle motion was stored. This type of calculation requires vast amounts of memory, and cannot be incorporated into the convective-diffusion approach since individual particles are not 'tagged'. The error introduced by assuming that all particles acquire the same charge, regardless of their history, is most significant in the first grid section, where some particles entering the duct close to the walls may not have acquired much charge.

This approximation invalidates the use of a sophisticated model for calculating particle charge. Consequently, the simple field charging equation derived by Pauthenier (1932) was used, where

$$q = 12\varepsilon_o \pi (d_p/2)^2 E_{av}$$
$$= 3\varepsilon_o \pi d_p^2 E_{av} \qquad (6.3)$$

where $E_{av} = ((E_x)_{av}^2 + (E_z)_{av}^2)^{1/2}$

As discussed in Section 1.2, this limiting charge value is attained in a sufficiently short period of time as to be regarded as instantaneous for the purpose of electrostatic precipitator calculations.

6.4.2 Migration velocity

The migration velocity of a particle has components in both x- and z- directions i.e. axial and lateral components.

The axial values have been ignored by previous workers, but their effect on concentration profiles may be significant. Equating the electric force with Stokes' drag force yields

$$w_x = \frac{E_x(i,j)q}{3\pi\varepsilon_o d_p} \qquad \text{and} \qquad w_z = \frac{E_z(i,j)q}{3\pi\varepsilon_o d_p}$$

Local variations in migration velocities are accounted for by the values of $E_x(i,j)$ and $E_z(i,j)$. Since E_z is zero on the centreline of the duct, the theoretical lateral migration velocity w_z on the centreline is also zero. This would result in the particles which are not removed by diffusion remaining on the centreline indefinitely. In reality, however, particles quickly clear from the centre because w_z is non-zero everywhere except on the exact centreline. To overcome this problem in the model, the centreline values of w_z are set equal to those on the adjacent grid line (i.e. j=2).

6.5 Calculation of concentration profiles

6.5.1 Finite difference method

Numerical solution of the convective-diffusion equation using finite difference techniques has been discussed in Section 1.6.2. Conflicting views arise in the literature concerning the form of the governing differential equation and its related boundary conditions. It is acknowledged that the general equation consists of electrical migration and diffusional flux terms as follows:

$$D_x\frac{\partial^2 c}{\partial x^2} + D_z\frac{\partial^2 c}{\partial z^2} - w_z\frac{\partial c}{\partial z} - (U_o+w_x)\frac{\partial c}{\partial x} = 0 \qquad (6.4)$$

where D_x = diffusion coefficient in x-direction (m^2s^{-1}),
D_z = diffusion coefficient in z-direction (m^2s^{-1}),

w_x = migration velocity in x-direction (ms^{-1}),
w_z = migration velocity in z-direction (ms^{-1}),
U_o = gas velocity (ms^{-1}).

To simplify the solution many investigators have eliminated the terms involving D_x and w_x, assuming them to be negligible compared to the convective flux, $U_o \partial c/\partial x$. From the experimental measurements of fluctuating velocity components described in Chapter 4, it appears that the flow field in the precipitator is almost isotropic. This implies that D_x is of the same order of magnitude as D_z, so that for conditions pertaining to those in a real precipitator, the axial diffusive flux $D_x \partial^2 c/\partial x^2$ is negligible compared to the convective flux $U_o \partial c/\partial x$. This assumption has been incorporated into the model described here.

Theoretical calculation of the relative magnitude of U_o and w_x have shown that the values may be of comparable size at locations in the vicinity of the discharge electrodes. Also, frame-by-frame analysis of cine films showing helium bubble trajectories in a precipitator indicates a reduction in axial velocity as the bubbles approach the discharge electrodes. This evidence suggests that w_x influences particle motion to the extent that the corresponding term in equation 6.4 should not be omitted. Downstream of the discharge electrode w_x acts in the same direction as the mean gas flow, and the effect will be to clear particles rapidly from this region. Consequently, detailed modelling of the wakes caused by the discharge electrodes is not essential since the regions are largely devoid of particles.

The modified form of the governing equation used in the model described here is

$$D_z \frac{\partial^2 c}{\partial z^2} - w_z \frac{\partial c}{\partial z} - (U_o + w_x) \frac{\partial c}{\partial z} = 0 \qquad (6.5)$$

The Crank-Nicholson finite difference scheme was used to solve equation 6.5. This method effectively applies the differential equation to the point (i+1/2,j) as shown in Figure 6.2, which enables the concentration values on row i+1 to be expressed in terms of those on row i.

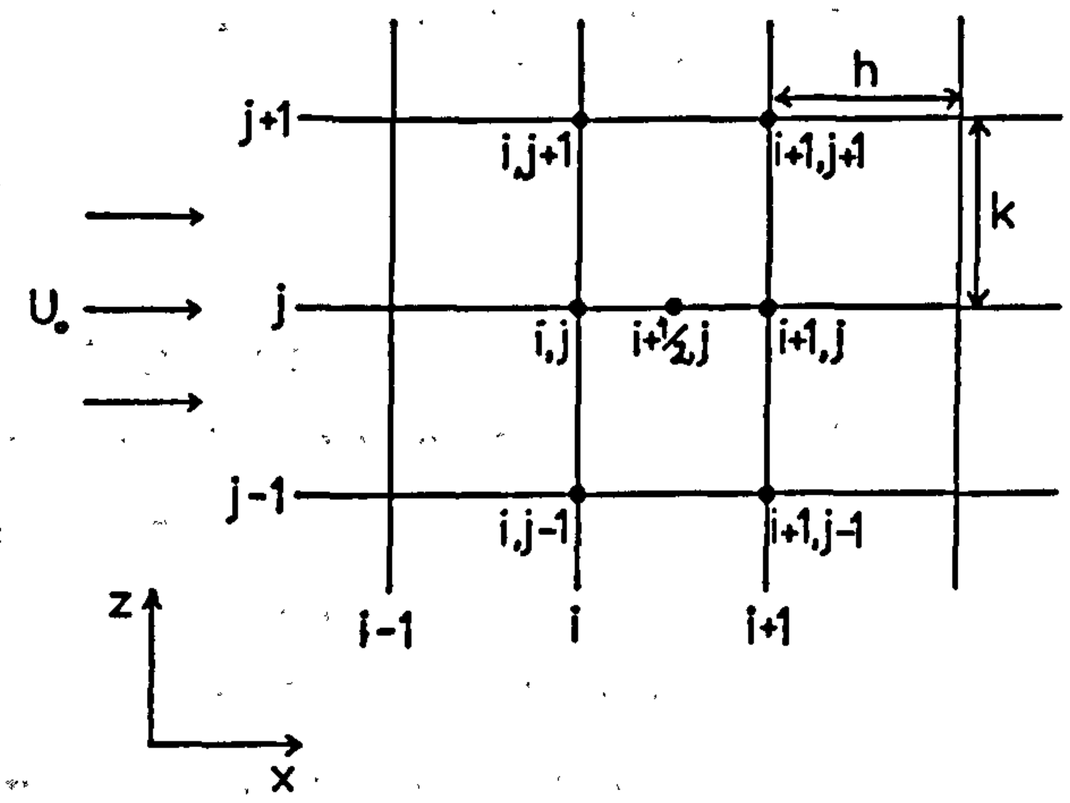

Fig. 6.2 Application of Crank-Nicholson finite difference scheme

Thus the solution progresses down the duct in a step-wise fashion using concentration values on the previous row to calculate new values. To initiate the procedure, a uniform concentration profile of unit magnitude was assumed to exist across the precipitator inlet. The computed concentration values on downstream rows therefore represent relative concentration profiles.

The derivative terms in equation 6.5 are replaced by the following central difference approximations,

$$\frac{\partial c}{\partial x} = \frac{c(i+1,j)-c(i,j)}{h}$$

$$\frac{\partial c}{\partial z} = (1-\theta)\frac{[c(i,j+1)-c(i,j-1)]}{2k} + \theta\frac{[c(i+1,j+1)-c(i+1,j-1)]}{2k}$$

$$\frac{\partial^2 c}{\partial z^2} = (1-\theta)\frac{[c(i,j+1)-2c(i,j)+c(i,j-1)]}{k^2} + \theta\frac{[c(i+1,j+1)-2c(i+1,j)+c(i+1,j-1)]}{k^2}$$

where $0<\theta<1$.

The z-direction derivatives at the point (i+1/2,j) are represented by the average of the finite difference replacement terms on rows i and i+1. A weighting factor θ is incorporated which improves the stability of the solution procedure, especially in the non-linear region surrounding the discharge electrode. The method is only truly Crank-Nicholson when $\theta=0.5$. Replacing the derivative terms of equation 6.5 and substituting

$$K_1 = w_z/2k,$$
$$K_2 = D_z/k^2,$$
$$K_3 = (U_o+w_x)/h,$$
$$K_4 = w_z^2/D_z,$$

yields:

$$\begin{aligned} c(i+1,j+1)\theta(K_1-K_2) + c(i+1,j)(K_3+2\theta K_2) - c(i+1,j-1)\theta(K_1+K_2) \\ = c(i,j+1)(1-\theta)(K_2-K_1) + c(i,j)(K_3-2(1-\theta)K_2) \\ + c(i,j-1)(1-\theta)(K_1+K_2) \end{aligned} \qquad (6.6)$$

The boundary condition assumed at j=1 corresponds to zero net concentration flux across the centreline, which is described by

$$D_z \frac{\partial c}{\partial z} = w_z c \qquad (6.7)$$

Representing the concentration at the point (i+1/2,1) by

$$c(i+1/2,1) = \frac{[\theta c(i+1,1)+(1-\theta)c(i,1)]}{2}$$

and the derivative terms as before, equation 6.7 may be written in the form

$$(1-\theta)c(i,j-1) + \theta c(i+1,j-1) = (1-\theta)c(i,j+1) + \theta c(i+1,j+1) - K_4[\theta c(i+1,j)+(1-\theta)c(i,j)]$$

This equation is used to eliminate the terms containing c(i,j-1) and c(i+1,j-1) from the general equation 6.6, yielding

$$c(i+1,1)[\theta(4K_1+2K_2+K_4)+K_3] - 2c(i+1,2)K_2 = c(i,1)[K_3-(1-\theta)(4K_1+2K_2+K_4)] + 2c(i,2)(1-\theta)K_2 \qquad (6.8)$$

The form taken by the boundary condition at the collection wall has been the subject of much debate. The boundary is complicated by the presence of a fluid sublayer adjacent to the wall, across which the particles can only traverse by electrical migration. Whilst some authors have used the infinite sink assumption so that c=0 on the walls, Leonard et al. (1980) have mathematically justified the use of the derivative condition $\partial c/\partial z=0$. To retain full generality, a combination of these boundary conditions has been employed in the work described here, giving

$$\propto \frac{\partial c}{\partial z} + (1-\propto)c = 0 \qquad (6.9)$$

where α is a constant in the range $0<\alpha<1$. In finite difference form, equation 6.9 becomes

$$(1-\theta)c(i,j+1) + \theta c(i+1,j+1) = (1-\theta)c(i,j-1) + \theta c(i+1,j-1) - k\frac{(1-\alpha)}{\alpha}[(1-\theta)c(i,j)+\theta c(i+1,j)]$$

Substituting this equation into the general equation 6.6 allows terms involving c(i+1,j+1) and c(i,j+1) to be eliminated, yielding

$$2c(i+1,n-1)\theta K_2 - c(i+1,n)[K_3+\theta K_2(K_5+2)-\theta K_1 K_5] = c(i,n)[(1-\theta)K_2(K_5+2)-(1-\theta)K_1K_5-K_3] - 2c(i,n-1)(1-\theta)K_2 \quad (6.10)$$

where $K_5 = k(1-\alpha)/\alpha$.

Equations 6.6, 6.8 and 6.10 together constitute a system of simultaneous linear equations relating concentration values on row i+1 to those on the preceding row i. The system can be written in the form

$$[A][C]_{i+1} = [B][C]_i \quad (6.11)$$

where $[A]$ and $[B]$ are tridiagonal matrices and $[C]_{i+1}$ and $[C]_i$ are the concentration profiles on rows i+1 and i respectively. Equation 6.11 reduces to the simpler form

$$[A][C]_{i+1} = [b] \quad (6.12)$$

once the values $[C]_i$ are known. The tridiagonal form of $[A]$ is amenable to reduction to upper bi-diagonal form using Gaussian elimination (with partial pivoting), and the $[C]_{i+1}$ values are then computed using back-substitution.

As described above, the solution procedure is initiated by assuming a constant unit concentration on row i=1. The

concentration values on row 2 are then found by solving equation 6.12, and these values themselves form the input for matrix [b].

6.5.2 Line-source method

As described previously, this approach is based on the assumption that the transport of dust along the precipitator can be simulated by the step-wise progression of a series of adjacent, vertical line-sources. The sources are located at the nodes of a grid as shown in Figure 6.3. The sources travel down the duct with velocity U_o, and the emitted dust moves towards the collection walls by electrical migration and spreads due to lateral diffusion.

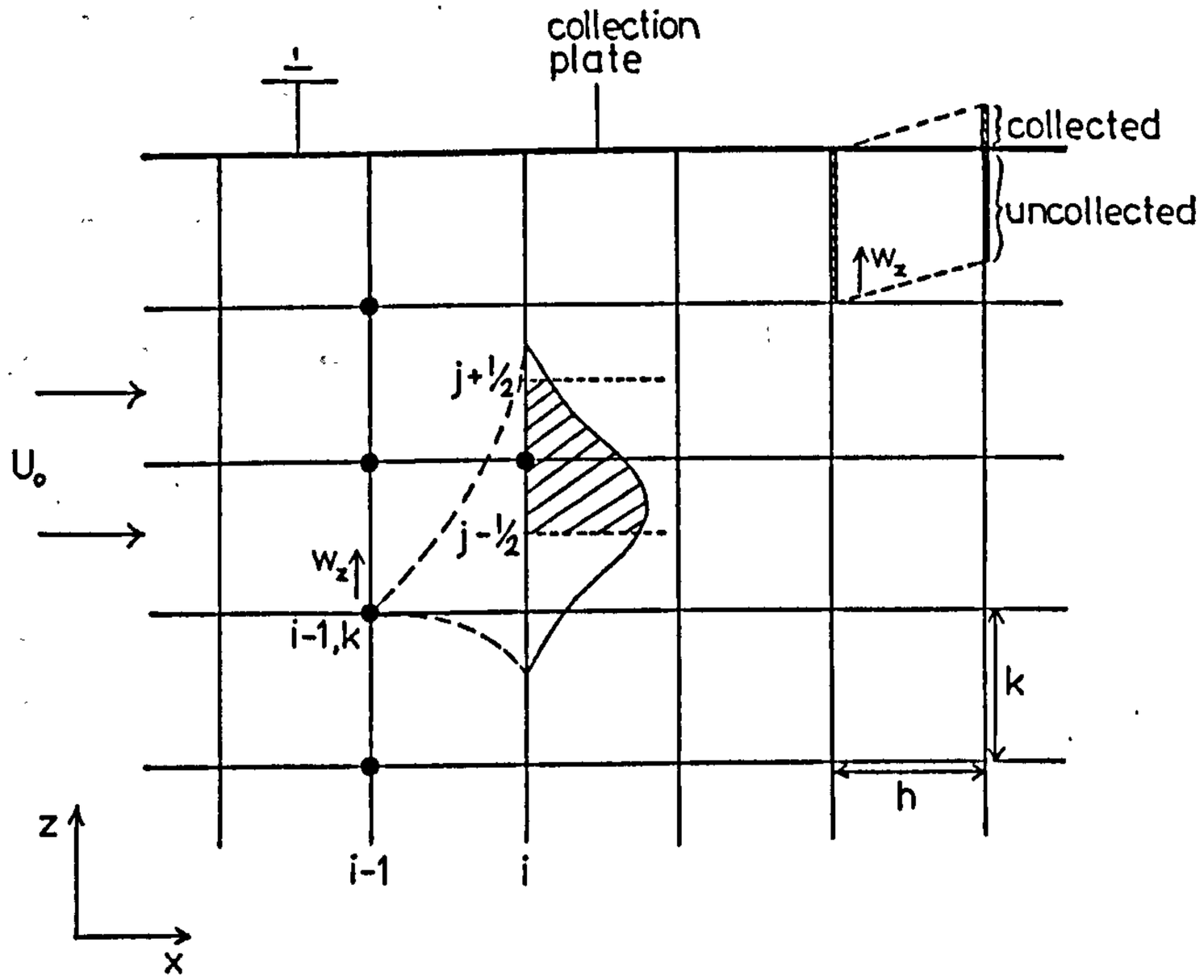

Fig. 6.3 Progression of dust down precipitator duct due to electrical migration and lateral diffusion of line sources

To illustrate the calculation procedure, consider the concentration c(i,j) in Figure 6.3. The amount of dust from the kth source node on row (i-1), falling in the region (j-1/2) and (j+1/2) surrounding the jth receiving point on

row i, is attributed to node (i,j). The total concentration c(i,j) at that point is determined by summing the contributions from all of the sources on row (i-1). Performing this calculation for each of the n receiving points on the ith row yields a concentration profile. These values subsequently act as the sources for the following (i+1)th row.

The expression used to describe the one-dimensional spread of a line-source is

$$c = \frac{W}{\sqrt{4\pi Dt}} \exp[-(z-w_z t)^2/4Dt]$$

where w_z = migration velocity (ms^{-1}),
z = distance from line through axis of source in direction of spread (m),
t = time allowed for sources to diffuse (s).

Integration of this equation to calculate the amount of dust falling within the region (j-1/2) and (j+1/2) is performed numerically using the trapezoidal rule. Tests showed sufficient accuracy to be obtained by dividing the region into 10 sections of width k'. The area under the curve was then given by

$$\text{Area} = (k'/2)[c_o+(2c_1 \ldots. +2c_{10}) + c_{11}]$$

Boundary conditions are simulated by assuming negligible diffusive spread of the sources across the grid space closest to the wall. Thus, particles can only reach the wall by electrical migration across the final stage. This is an attempt to model physically the boundary layer, where the diffusion coefficient falls to zero. For the purpose of calculation, particles at the (n-1)th source node are assumed to be distributed uniformly across the grid

space as shown in Figure 6.3. Time t is allowed for the line source to migrate towards the wall with velocity w_z. The fraction of the line crossing the wall boundary in this time interval is captured. The uncaptured fraction remaining in the duct contributes to the source node (n-1,i+1) on the following row.

Due to the axial symmetry of the precipitator, only one side of the duct is considered. For a receiving node on the centreline (j=1), contributions from all sources on the previous row (except that on the centreline) are doubled to account for the source nodes on the other side of the duct. Contributions to receiving points not on the centreline, from sources on the other side of the duct, are assumed to be negligible due to the high migration velocity of the point sources away from the centreline.

To simulate a uniform dust concentration profile at the duct inlet, the point sources on the first grid-line (k=1) are all assumed to be of unit magnitude. Depending on the relative strength of the diffusive and electrostatic forces, the particles will gradually be captured and the total mass of dust in the duct will decay.

6.6 Results and discussion

6.6.1 Effect of spatially-dependent parameters

A number of simulations were carried out for each model to ascertain the importance of different parameters affecting particle collection in the precipitator. Figures 6.4 and 6.5 show the predicited concentration profiles across the duct for the finite difference and line source models respectively. The simulations were performed for 11.3 μm particles in a straight duct system (no wall strengtheners). The peak value of the dispersion

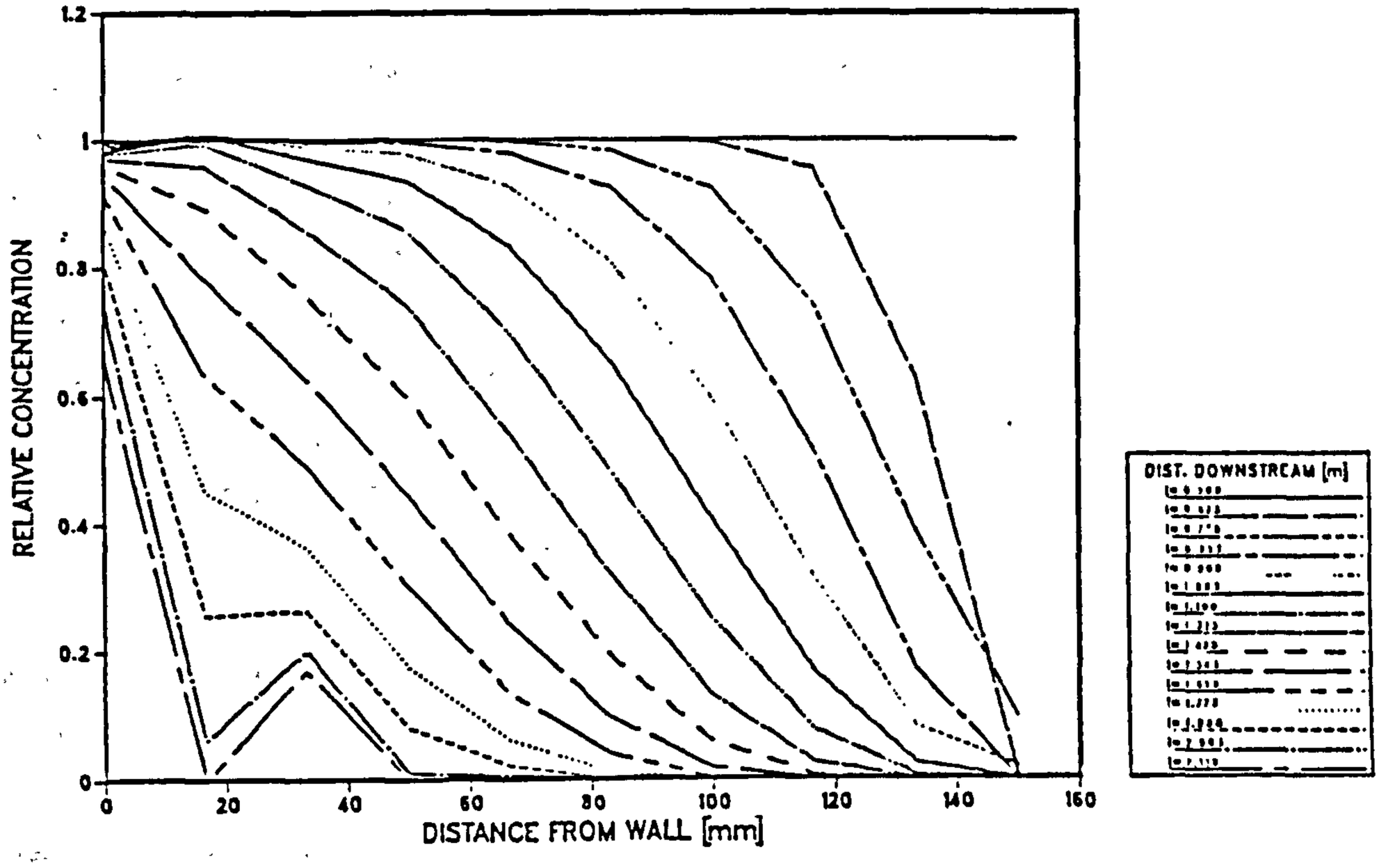

Fig. 6.4 Concentration profiles across precipitator duct predicted by finite difference method

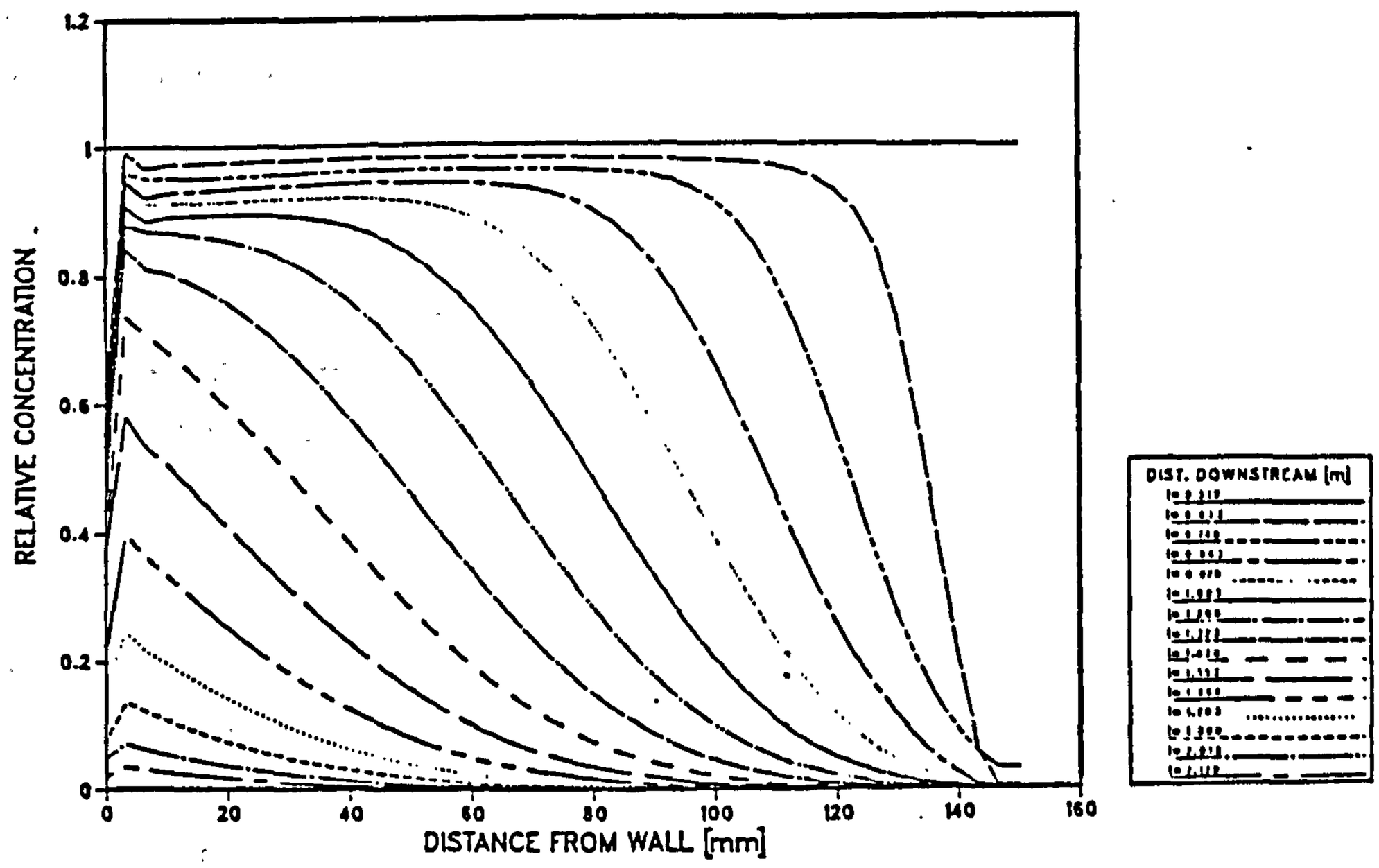

Fig. 6.5 Concentration profiles across precipitator duct predicted by line-source method

coefficient profile was chosen as $0.001 m^2 s^{-1}$, and the discharge electrode voltage was set to 65KV.

Alternate curves on the figures represent the concentration adjacent to, and in between successive discharge electrodes as the dust progresses down the precipitator duct. The models predict similar concentration profiles except in the region close to the wall. In the case of the finite difference model, the concentration values at the wall remain high and the concentration falls almost linearly towards the centre of the duct. This suggests that the boundary condition $\partial c/\partial z=0$ still allows much of the dust to migrate to the wall. In fact, the concentration at the wall becomes a dominant feature further down the duct where most of the dust has been collected. In contrast to these results are the predicted concentration values at the wall for the line source method. In this case the dust appears to build up at the node adjacent to the wall whilst the value on the wall remains low. The way in which the collection mechanism is modelled in the line source method may be significantly affected by the grid density, as mentioned previously. A smaller cell width may cause increased collection since a larger fraction of the source located adjacent to the wall will arrive at the wall in a given time interval. Due to the difficulties experienced in the mathematical representation of particle collection, subsequent efficiency values are calculated based on the amount of dust remaining in the precipitator duct, rather than the amount collected on the walls.

Figure 6.6 and 6.7 show the fall in penetration of dust down the precipitator duct for particle sizes of 2.25, 5.6 and 11.3 μm. These particle sizes were chosen to correspond with the experimental results obtained using the Coulter Counter, as described in Section 5.2.6. The predicted penetration values show similar trends for both models, and

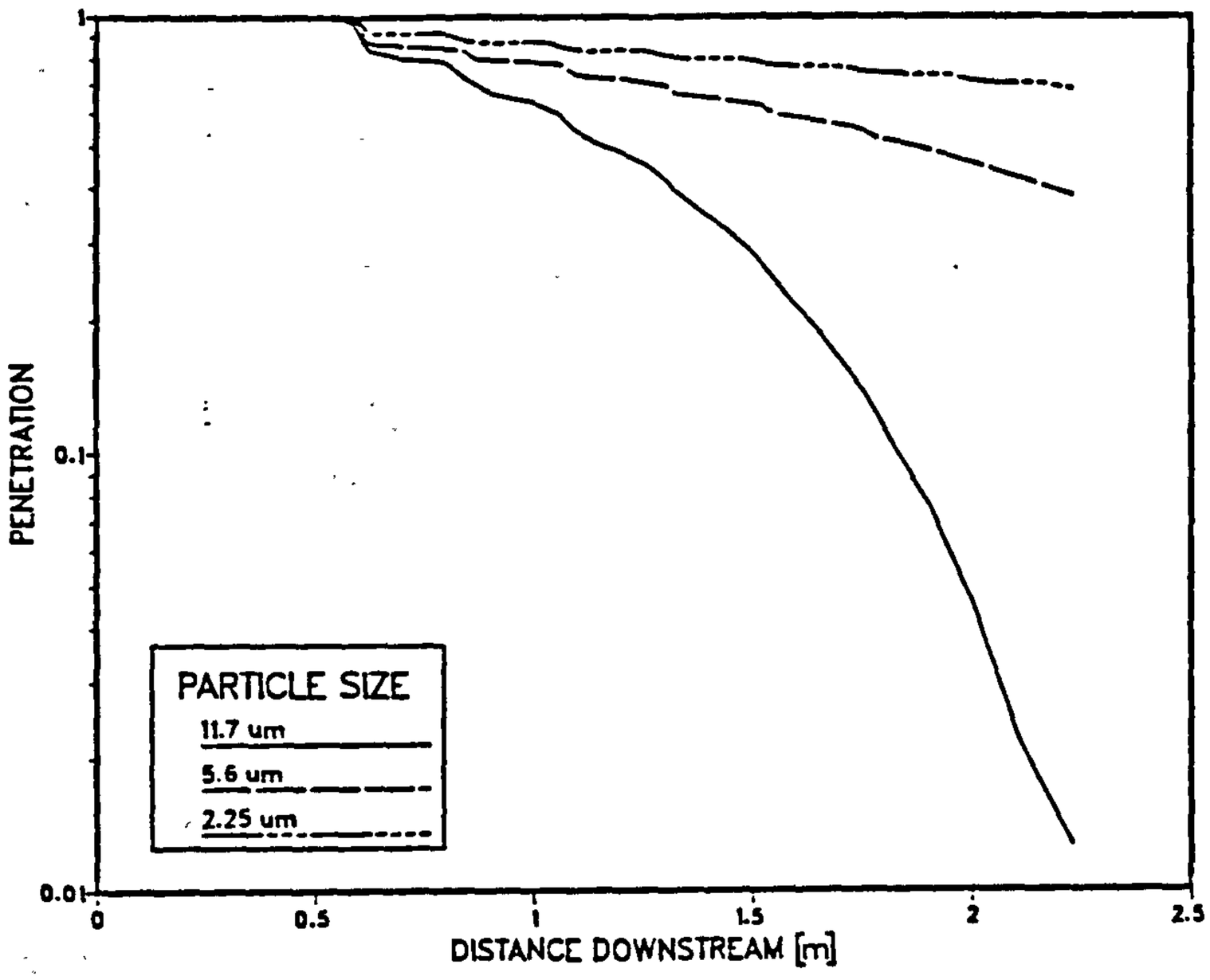

Fig. 6.6 Fall in dust penetration with distance downstream predicted by finite difference method

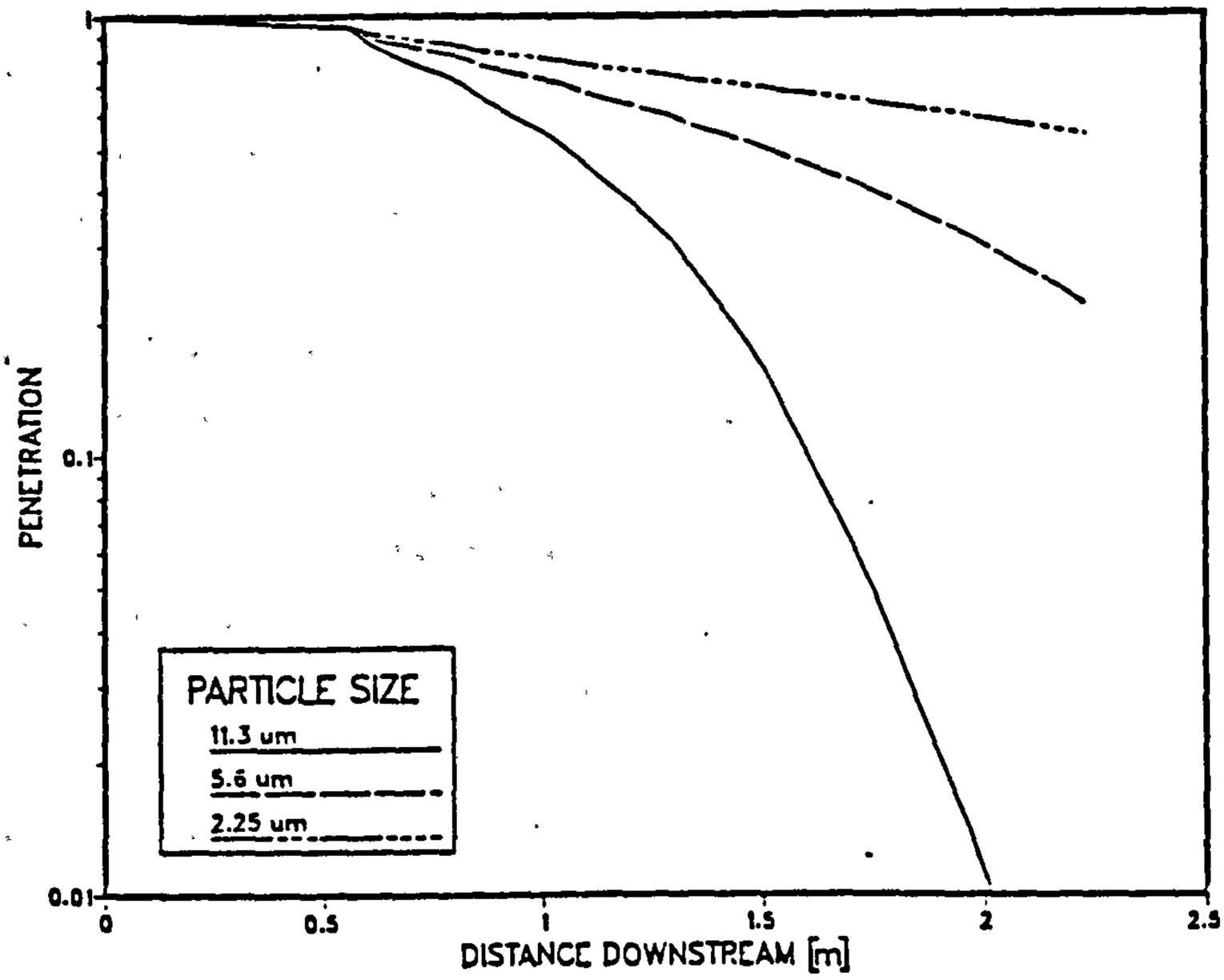

Fig. 6.7 Fall in dust penetration with distance downstream predicted by line-source method

show the penetration to markedly increase for smaller particles. For Deutschian-type collection, such a plot of log(penetration) versus distance downstream would be expected to fall on a straight line. In Figures 6.6 and 6.7 this behaviour is only observed for small particles where the electrical migration velocity values are low, and hence turbulent diffusion mechanisms dominate. This corresponds to the Deutsch assumption of infinite back-mixing across the precipitator duct. The "wiggles" in the curves are caused by periodic increases in collection as the particles pass the high electric field region surrounding the discharge electrodes. These "wiggles" are more apparent in the case of the finite difference model.

Figure 6.8 and 6.9 show the effect in both models of varying the dispersion coefficient value. The predictions have been made for small particles at low voltages to emphasise the effect of dispersion. The models predict markedly different trends when the dispersion coefficient is decreased from 0.01 to 0.0001 m^2s^{-1} for 2.25μm particles. The finite difference model shows an increased penetration value for the high dispersion coefficient value. Although the "wiggles" in the curve are prominent, an average of the values would produce almost a straight line, as predicted by the Deutsch theory. The slight increase in penetration values predicted by the finite difference model is probably due to the onset of numerical instabilities. In contrast to the finite difference model, the line source model predicts an exponential fall of penetration with distance downstream for both values of dispersion coefficient. The penetration values are higher for the low dispersion coefficient case. The effect of varying the dispersion coefficient on the magnitude of the predicted penetration is much greater for the line source model. Also, the "wiggles" are no longer present in the curves.

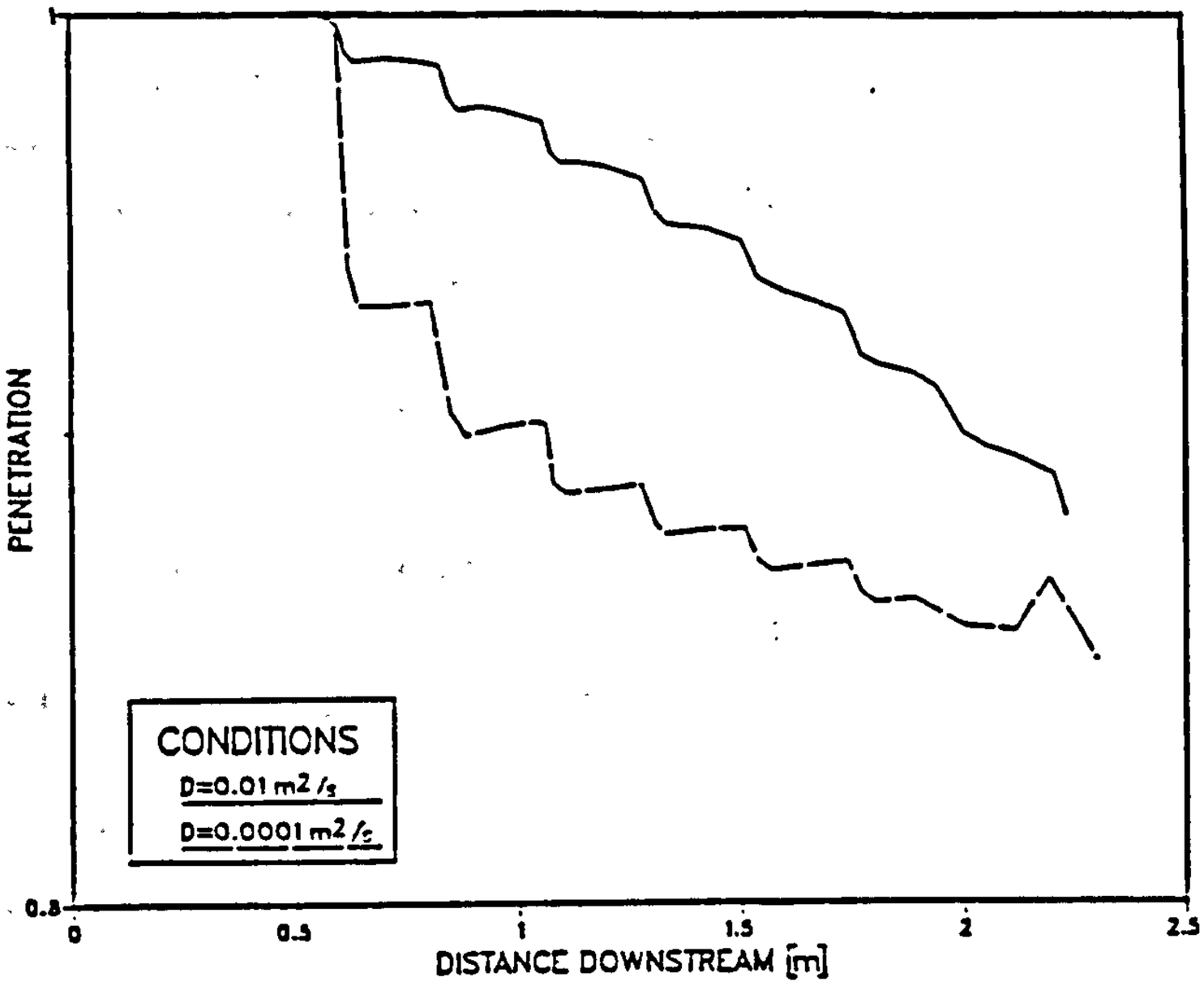

Fig. 6.8 Effect of varying dispersion coefficient on penetration for finite difference method

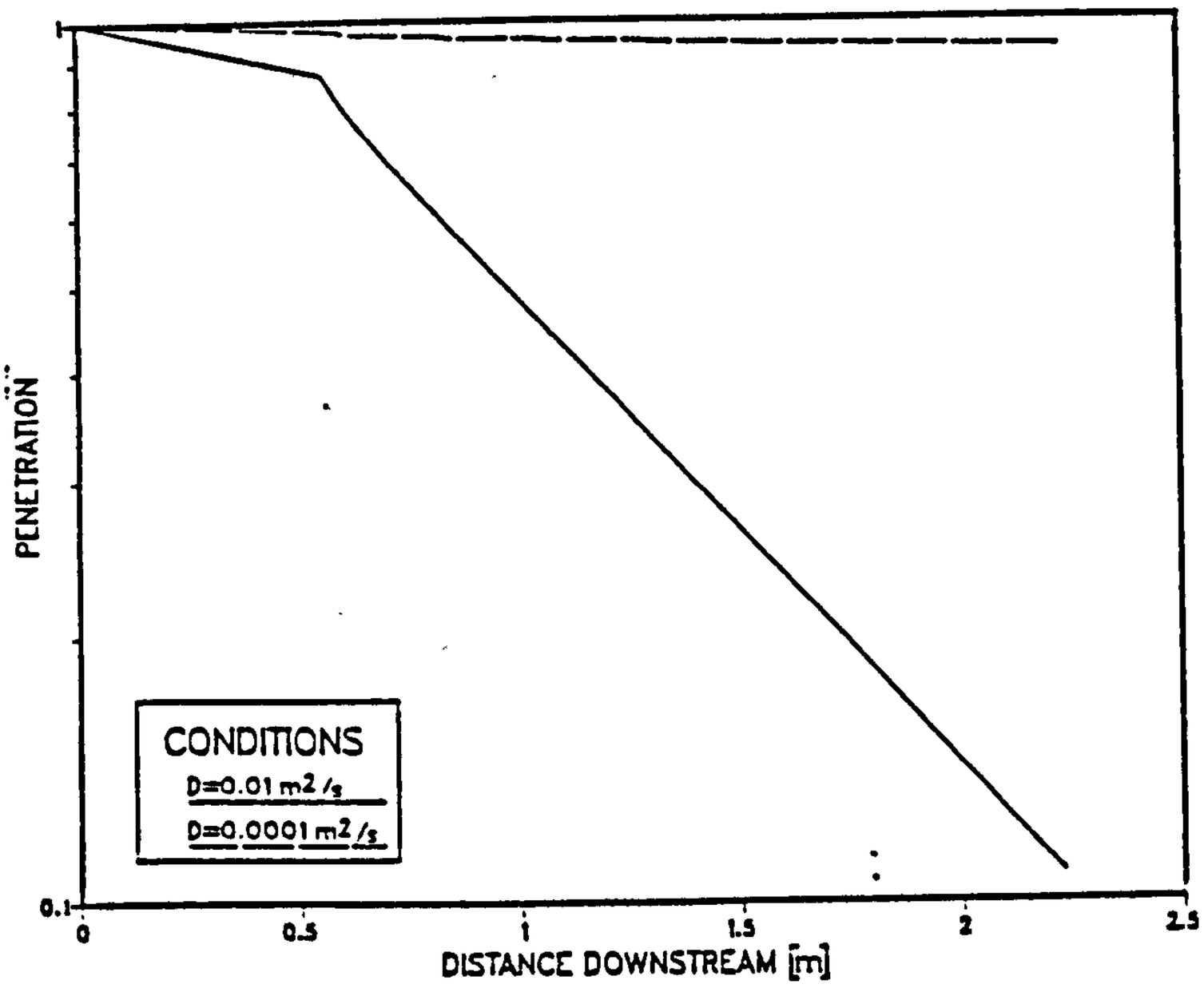

Fig. 6.9 Effect of varying dispersion coefficient on penetration for line-source method

The experimentally measured variation of dispersion coefficient across the precipitator duct was incorporated into both mathematical models. The dispersion coefficient profile was approximated mathematically by the following,

$$D(j)=0.0339 \times disp \times (z^{0.675})$$

where disp = peak value of dispersion coefficient (m^2s^{-1}).
z = (mm)

This expression was used to calculate values of D(j) at different positions across the precipitator duct, given an initial peak central value. To examine the effect of incorporating profiled dispersion coefficient values, profiled (varying D) and non-profiled (constant D) simulations were performed using both models. In these simulations the non-profiled value of D was set equal to the peak central value in the profiled case. Typical results are shown in Figure 6.10 for 5.6 μm particles at 65KV.

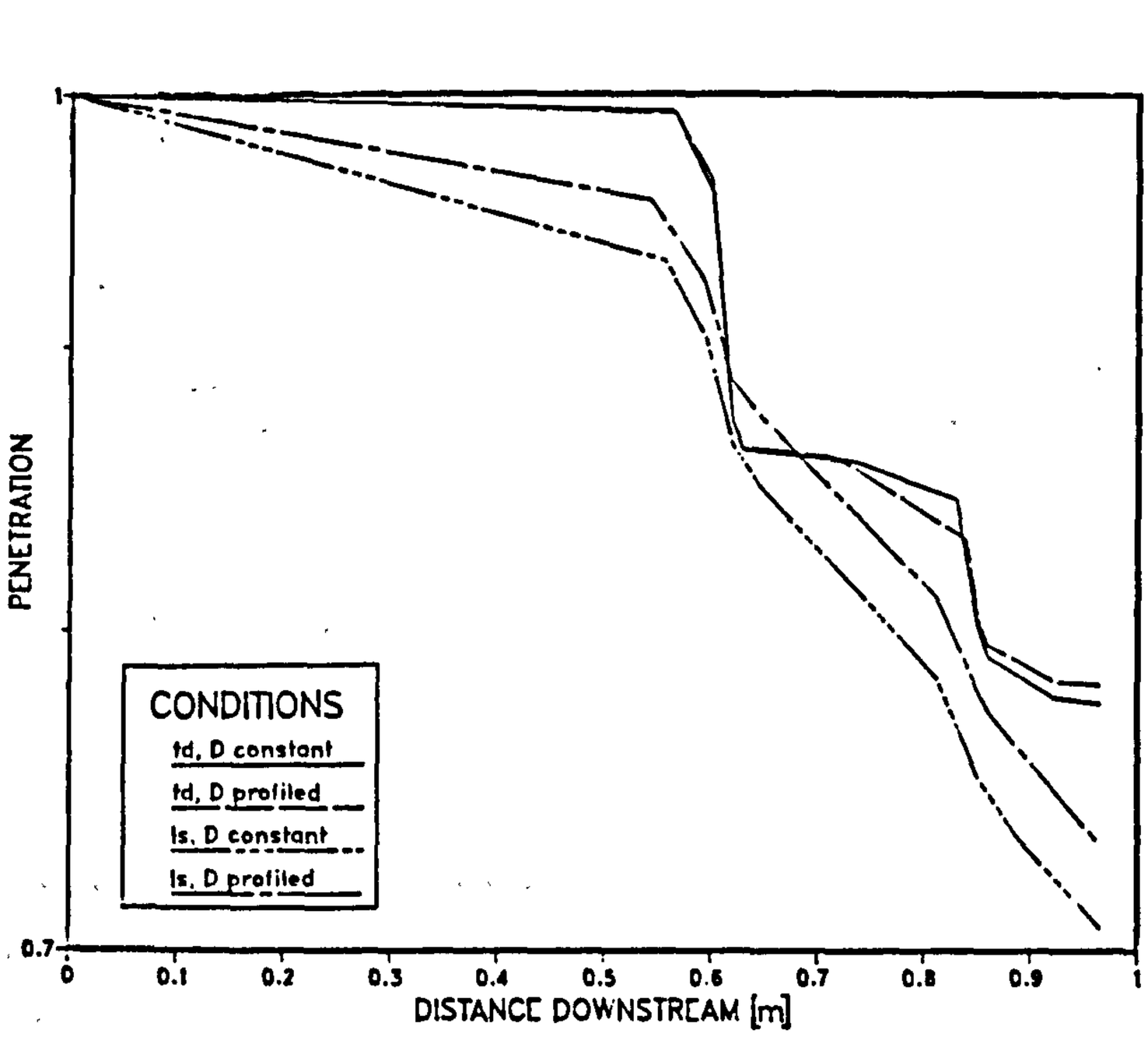

Fig. 6.10 Effect of incorporating dispersion coefficient profile across duct

The value of disp was taken as $0.001 m^2 s^{-1}$. The finite difference model is virtually unaffected by the substitution of a profiled dispersion coefficient. However, the line source model predicts lower penetration values for the case of a constant dispersion coefficient. The likely cause of this increased collection is highlighted in Figure 6.11 which shows the dust concentration profiles across the precipitator duct for both models with D(j) profiled and constant. All curves are in close agreement except for that predicted by the line source method with constant D(j). These results are discussed further in Section 6.6.3.

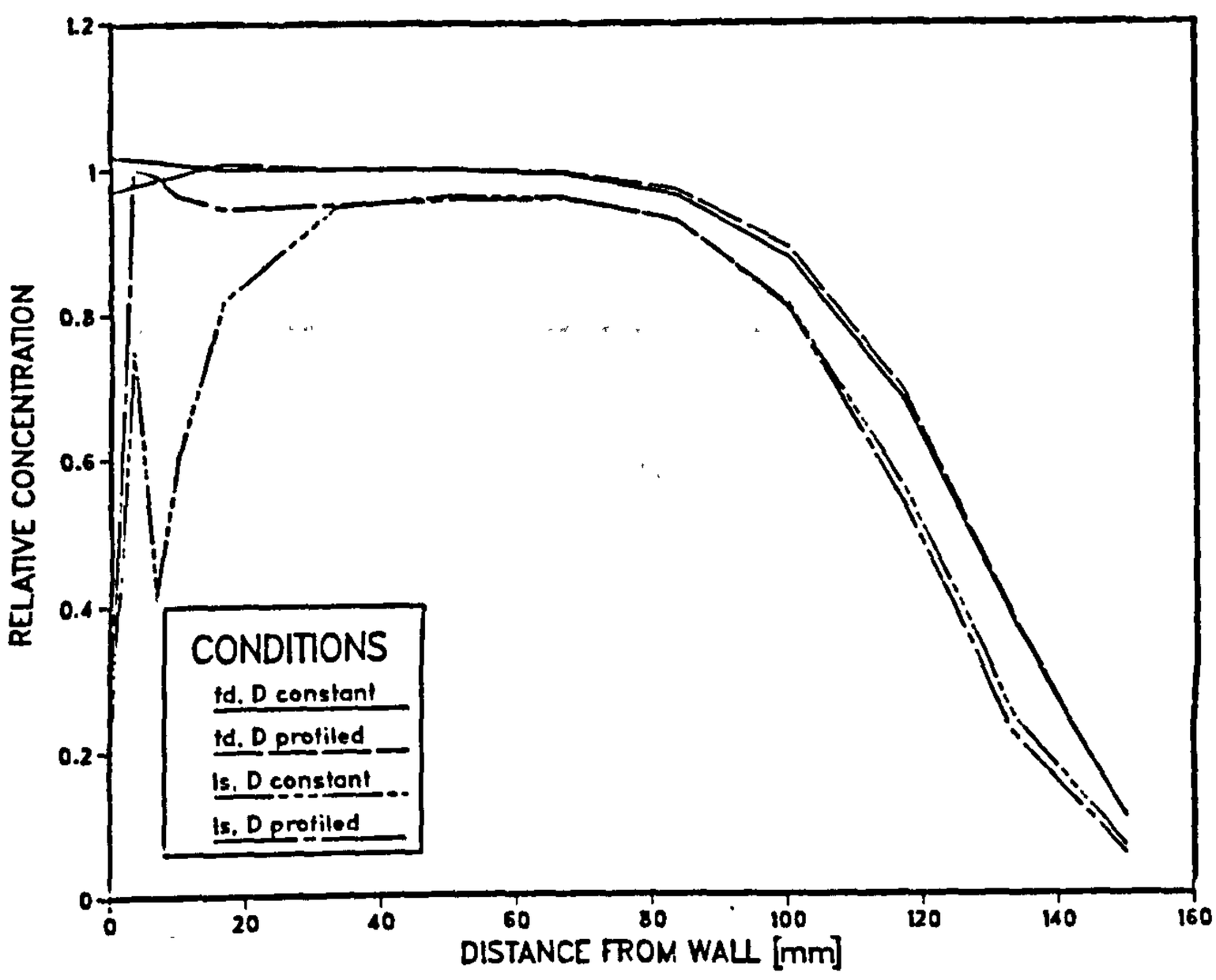

Fig. 6.11 Effect of dispersion coefficient profile on concentration profile across duct

The concentration profiles produced by both models were used to calculate the simulated penetration values along the precipitator duct with and without wall strengtheners. The effect of strengtheners was modelled by setting the fluid

velocity to zero in the regions immediately upstream and downstream of each strengthener, as described in Section 3.4.3. Figure 6.12 shows the prediction of both models for a particle size of 5.6 μm. The value of disp was set to 0.001 $m^2 s^{-1}$, and the discharge electrodes were set at 65KV. The predictions by the finite difference model are virtually unchanged by the presence of the wall strengtheners. However, the line source model predicts a significant increase in particle collection in the region surrounding the wall strengthener, although in the region between strengtheners the particle collection rate is reduced. The net effect is that the overall collection efficiency is approximately the same with or without strengtheners.

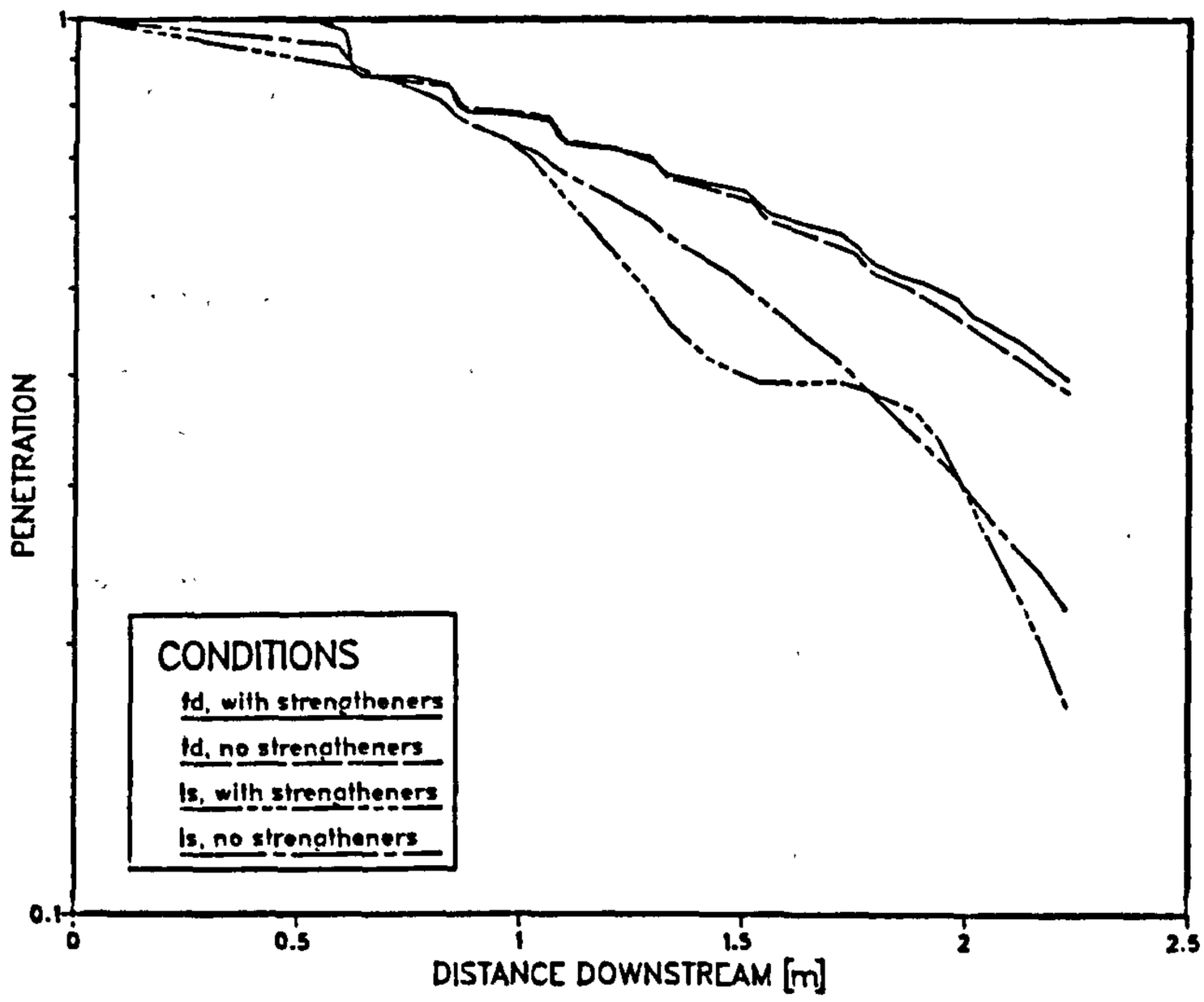

Fig. 6.12 Effect of wall strengtheners on predictions of both models

The main effect of strengtheners as modelled in this way is to increase the average mainstream velocity of the fluid. This will reduce the residence times of the particles in the duct, thereby leading to reduced collection. This is then offset by the enhanced collection of particles in the stationary zones surrounding each strengthener.

6.6.2 Comparison of theoretical predictions and experimental results

Some of the theoretical predictions presented in Section 6.6.1 have been compared to the experimental results described in Chapter 5. Whilst quantitative differences occur, the general trends demonstrated by the experimental results are reflected by both models.

Comparison of Figures 6.6 and 6.7 with the curves in Figure 5.18 corresponding to no strengtheners shows a similar fall in dust penetration with distance downstream for particles of sizes 2.25, 5.6 and 11.3 μm. (Note the different ordinate scales for the 2.25 μm particle). In each case, the small particles behave as predicted by the Deutsch equation, suggesting infinite back-mixing across the duct. Quantitative agreement between the theoretical and experimental results is only achieved for the 11.3 μm particles. For smaller particle sizes the experimental penetration values are much lower (less than 10% in some cases) than the predicted results. The cause of this discrepancy probably lies in the method used by the models to calculate the electric charge acquired by the particles. The experimental results were measured with negative voltage applied to the discharge electrodes, which provides free electrons for additional charging of the particles. No provision was made in the models to account for this excess charge. Also, any error in the choice of dispersion

coefficient value for the models would be accentuated in the small particle calculations where dispersion phenomena dominate.

Further evidence of the agreement between experimental results and theoretical predictions is provided by comparing Figure 6.12 with the curve in Figure 5.18 corresponding to 5.6 μm particles. None of the results suggest that the presence of the wall strengtheners significantly affects the overall collection efficiency of the precipitator. The enhanced collection predicted by the line source method in the region surrounding the strengthener closely resembles the experimental results. The actual penetration values obtained experimentally are lower than those predicted by either model.

6.6.3 Assessment of computational methods

Both the line source and finite difference models incorporate several spatially-dependent parameters - gas velocity, electrical migration velocity and dispersion coefficient. Inevitably, there is a price to be paid for the improved realism that these models intend to achieve. For example, the rapid increase in electrical migration velocity near the discharge electrode is a source of instability, particularly for the finite difference model. Indeed, when the coefficients in the finite difference scheme contain as many as three independent, locally-varying parameters, it is to be expected that the system of equations is more prone to instabilities. The limits of stability need to be further examined so that the range of conditions may be determined over which the model can be successfully applied.

The line source method appears to overreact to changes in the value of dispersion coefficient, particularly when a

constant value is assumed across the precipitator duct (i.e. no dispersion coefficient profile). This results from misrepresentation of the collection mechanism, caused by a grid that is too coarse for the chosen value of dispersion coefficient. In a given timestep, some of the dust that is close to the collection wall is diffused "through" the wall and does not experience the additional resistance to collection provided by the boundary layer. The absence of the boundary layer effect in these cases causes the low concentration values shown in Figure 6.11, in the region close to the wall. Dust which arrives at the node adjacent to the wall is collected less easily since the dispersion coefficient is set to zero at this point.

Ideally this problem could be eliminated by incorporating a dispersion coefficient which varies throughout the calculation depending on the position of the dust. However, this would require the use of a very dense computational grid, which is impractical for most calculations. In the models described here, a compromise has been achieved by using a profiled dispersion coefficient which limits the dispersion mechanism as the particles approach the wall. This method still requires a sufficiently dense grid so that particles close to the centre of the duct are not dispersed "through" the wall in a single timestep. This criterion is easily satisfied for all but the coarsest of grids.

The results of the line source model could also be improved by increasing the length-to-width ratio of the computational cells, h/k. Conversely, the finite difference method achieves greater accuracy for decreased values of h/k, especially in the region surrounding the discharge electrodes where rapid changes in the electric field values occur.

Measurement of local dispersion coefficient values, as described in Chapter 4, calls into question the way in which dispersion effects are incorporated in the computational simulation of electrostatic precipitators. If the numerical model incorporates a step-wise solution technique, where the dust concentration on the (i+1)th gridline is calculated from that on the (i)th gridline, confusion arises in the choice of the most relevant dispersion coefficient value. Intuitively, one might expect that the most appropriate value would be that corresponding to the computational grid spacing. This implies that the turbulent mixing is a function of the mathematical procedure used to solve the problem. Also, the predicted outlet concentration of a point source located at the duct inlet would be much less than expected, due to the artificially low turbulent mixing.

Alternatively, one might choose to implement the large-scale diffusion coefficient, regardless of grid spacing. This would undermine the advantages of a step-wise solution procedure, since the spread of material would be overestimated unless the grid spacing was sufficient for the full range of eddies to be effective, i.e. grid spacing > $2x_o$. In this case, local fluctuations in dispersion coefficient, as measured in Section 4.1, could not be included.

A property not included in either of the numerical models is the inertia of large particles. In reality, the effect of inertia would be to increase mechanical deposition and inertial impaction onto the wall strengtheners. Both of these collection mechanisms have been investigated experimentally in Section 5.3 and could, if required, be included in the models empirically. Also, in applying these models to the full range of particle sizes present in an industrial precipitator, the reduction in effective dispersion coefficient with particle size is another factor

which becomes relevant. This could be incorporated in the models simply using the relationship between particle and fluid diffusivities for a given particle size, as discussed in Section 1.4.3.

A major simplification in the models is the assumption that all particles acquire the same limiting charge value - based on the average electric field in the precipitator. As discussed in Section 1.1, the assumption that particles immediately acquire their limiting charge on entering the precipitator is, in general, acceptable. However, inaccuracies can occur since it is assumed, for example, that a particle entering the precipitator close to the collection walls will acquire the same charge as a particle passing close to a discharge electrode where the electric field is much stronger. This is most relevant in the initial stages of the precipitator duct. Further downstream, the particles are more likely to have passed through regions of both high and low electric field, so the distribution of particle charge values will be narrower. To model charging conditions more realistically, a record of maximum electric field value experienced by each particle would need to be kept, and the corresponding value of charge attributed to the particle.

One further effect not accounted for in either of the numerical models is particle space charge density. This phenomenon is difficult to incorporate since it requires knowledge of the dust concentration before it can be calculated. The space charge then itself affects dust migration through the electric field values. Thus it is best modelled by iterating successively over the entire duct calculation scheme until changes in particle space charge density produce no significant modification to the dust concentration. Otherwise, prior assumptions about the dust concentration distribution must be made.

CHAPTER 7

CONCLUSIONS

The purpose of the work presented in this thesis has been to provide information on some of the mechanisms affecting particle migration in an electrostatic precipitator. This has been done through both experimental and theoretical investigation. The experimental work was performed on a pilot-scale test rig of a wire-plate precipitator, designed to provide maximum visual access to the inner workings of the precipitator duct.

Analysis of the steady-state flow field was undertaken using hot-wire anemometry, laser-Doppler photon correlation and flow visualisation techniques. The results showed that the velocity profile across the precipitator duct was only slightly disturbed by the presence of the twisted square discharge electrodes. Two flat plate configurations were considered;

a) without wall strengtheners - plug flow was found to give a sufficiently accurate representation of the velocity field for most purposes. The velocity deviations caused by the presence of the discharge electrodes occurred in a region devoid of particles, and therefore accurate mathematic modelling of the velocity field in this region was unnecessary.
b) with wall strengtheners - the velocity field was simulated by imposing a theoretical sinusoidal boundary along both walls, with peak amplitude of the curves corresponding to the location of the strengtheners. The velocity outside the boundary was set to zero to represent the stationary zones upstream and downstream of the strengtheners. The velocity profile inside the boundary was uniform with magnitude inversely

proportional to the distance between the boundaries.

The flow fields surrounding strengtheners of different designs were analysed using streak photographs of neutral density helium bubbles, and the geometry which imparted minimum disturbance to the surrounding flow field was identified. At a distance of 0.4 m downstream from the pipes the velocity field attained a flat profile.

The phenomenon of turbulent mixing was studied for a range of conditions in the precipitator. Local dispersion coefficient values were determined by measuring the spread of an isokinetically-injected aerosol using a light scattering technique. The relevance of dispersion coefficient values was discussed, with particular emphasis on the importance of using the correct scale of scrutiny. Parameters varied in the experiments included gas velocity, presence of wall strengtheners and flow modulation pipes, applied discharge electrode voltage and position in the duct.

The presence of electric wind at low gas velocities was detected through an increase in the effective dispersion coefficient at high voltages. The electric wind is a steady-state, convective phenomenon, and as such should not be represented by a dispersion coefficient, which characterises unsteady, fluctuating properties of the flow. Also, dispute still arises in the literature as to the importance of electric wind effects at mainstream velocities as high as 2 ms^{-1}. For these reasons, the effect of electric wind has not yet been successfully incorporated into a mathematical model. A further situation not amenable to modelling using dispersion coefficients is the flow field in the downstream wakes of wall strengtheners. This problem was avoided in the mathematical models by employing a zero velocity field in this region.

Fluctuating velocity components of the flow were measured in the axial and transverse directions - u' and v' respectively. To measure the high levels of turbulence present in the precipitator duct, a phase shifter was built into the laser-Doppler photon correlation device. The results showed that turbulence levels were in general within the range 15-25%. A measure of isotropy was attained by evaluating the ratio u'/v' across the precipitator duct. In general, this ratio was found to be greater than unity, especially in the region close to the collection walls. A relationship developed between r.m.s. transverse fluctuating velocity and dispersion coefficient was provisionally verified.

The dust concentration distribution within the pilot-scale electrostatic precipitator was measured for a variety of working conditions. A sampling probe was developed which allowed particle size and concentration to be measured at seven locations across the duct simultaneously. Isokinetic sampling was achieved (where possible) through the use of valves to control the flow rate for each individual filter head. The dust captured by the sampling probe was then analysed using a Coulter Counter. The technique was shown to provide reliable results for alumina dust in the size range 2-12 μm. This size fraction is of particular interest in the study of electrostatic precipitators, since collection efficiency in this range is relatively low.

This experimental work described above provided a useful body of concentration data for comparison with mathematical models, and also for assessing the effect on collection of gas velocity, applied voltage, flow modulation pipes and wall strengtheners. The results showed that the presence of 0.1 m diameter flow modulation pipes at the precipitator inlet increased collection of larger particles, probably due to the enhanced mechanical collection caused by

increased turbulence. The increased back-mixing tended to reduce the electrically-enhanced vortex collection behind the first set of wall strengtheners. The collection of small particles was relatively unaffected. Concentration profiles were measured across the duct for a variety of electrode voltages ranging from 0 to -65KV. As the voltage was increased, concentration gradients developed which were more pronounced for larger particles. It was found that a flat concentration profile, as assumed in the Deutsch theory, was only achieved for particles less than 3 μm diameter.

Dust concentration was also measured as a function of distance downstream, both with and without wall strengtheners installed. Without strengtheners, the relationship was found to be approximately log-linear for all particle sizes within the range 2-12 μm. As mentioned previously, a concentration profile builds up quickly for large particles due to their high electrical mobility. Therefore, the qualitative agreement of the large particle concentration results with the Deutsch theory must be fortuitous. With L-shaped strengtheners installed at 0.9 m intervals, the fall in dust concentration downstream was shown to vary, with the regions of increased particle collection corresponding to the locations of the strengtheners. Subsequent analysis of mechanical deposition showed that the number of large particles collected by the wall strengtheners was approximately ten times greater than the number of fine particles. Deposition also occurred in the downstream wake of the strengtheners. Large particles would be encouraged to enter this vortex from the mainstream flow by electrical migration, whereas the fines would be thrown in by the turbulent motion of the gas.

A provisional comparison was made between the collection rates due to twisted square, axial and transverse

orientated sawtooth electrodes. The results showed that twisted square and axial sawtooth electrodes produced similar collection rates, whilst the transverse sawtooth electrodes were less efficient.

A method was developed for measuring dust deposition on the walls of the precipitator in the absence of applied voltage. The method involved attaching strips of adhesive-coated aluminium foil along the collection walls of the precipitator. The foil was later cut into strips which were Coultered individually to ascertain the number of particles in a given size range deposited during the experiment. This value was then compared with the corresponding number of particles fed into the precipitator in the same time interval, and a value for mechanical efficiency was computed. The efficiency was shown to increase from 1.74 to 16.6% as the particle size increased from 2.25 to 11.3 μm. The addition of wall strengtheners caused the efficiency values to increase by approximately 25% of their original value for all particle sizes.

As shown previously, the basic assumptions of the Deutsch equation are applicable only in the case of small particles, and a more accurate description of particle motion is obtained using the convective-diffusion equation. The numerical modelling work in this thesis employs two alternative schemes for solving the convective-diffusion equation. One method uses finite differences to solve the equation directly, whereas the second models the passage of dust down the precipitator as the progression of a series of line sources. A computer program was written to determine the electric field values in the precipitator duct, taking into account the effect of ion space charge density. Having calculated the electric field, the program then allows the user to choose either of the above methods of solution. The program also provides options for including experimentally

measured dispersion coefficient profiles and a modified velocity field which models the presence of wall strengtheners.

The theoretical predictions of both models were compared to the experimental concentration data discussed above. Whilst similar qualitative trends were observed, both models tended to underpredict collection efficiency, particularly for small particle sizes. This discrepancy could be due to a number of factors, including unrealistic modelling of small particle charging. This may result from using negative discharge electrode voltages in the experimental work, which provides free electrons for additional particle charging.

Further modifications to the mathematical models are required to improve the boundary conditions, particularly for the line-source method. It is in this region that the most significant discrepancies occurred. Also, a certain level of dependence on the density of the computational grid was observed for both models, but usually this could be suppressed and the results were in general encouraging.

Recommendations for future work include repeating some of the concentration measurements with a layer of dust on the collection walls, similar to that which would accumulate in a full-scale precipitator between rappings. This would allow the effects of reentrainment and back-ionisation to be investigated.

It is recognised that whilst the concentration measurements of alumina dust are useful in assessing mechanisms affecting particle migration in an electrostatic precipitator, different quantitative behaviour may be observed in the case of a different dust. Ideally, the tests would have been performed with a dust that is commonly

encountered in industrial situations. With this in mind, initial concentration measurements were made using flyash. Unfortunately, the size and charge properties of flyash are difficult to characterise, and it is more difficult to disperse than alumina. The shape of flyash particles tend to be irregular, and recent experimental work has shown that electrostatic charge, inherent in the particle structure, may cause discrepancies between experimental and predicted charge results.

Further investigation is also required into the variation of particle diffusivity with particle size. Whilst the difference between particle and fluid diffusivity has been shown to be negligible for the size of dust used in the work described here, this may not be the case for the large particles present in an industrial precipitator. Attempts have been made during the course of this work to measure the dispersion coefficients of narrow size fractions of flyash, using the light scattering technique described previously. Complete dispersion of the flyash in the precipitator duct required high suction velocities in the dust feeder device. Difficulties were experienced in the subsequent reduction of this velocity to 1-3 ms^{-1}, as required for isokinetic injection, without incurring significant transport losses. This problem may be overcome in future work by an alternative choice of dust feeder device.

APPENDIX A

COMPUTER PROGRAM TO CALCULATE DISPERSION COEFFICIENT

This section describes the computer algorithm used to calculate dispersion coefficient values from aerosol concentration profiles. Assuming the concentration profiles to be adequately represented by equation 4.1, a least squares fit method was applied in determining an appropriate value of dispersion coefficient as follows:

1. Concentration profile data transferred from Malvern Correlator via the IEEE interface to the PET.
2. Corresponding background data subtracted to give aerosol count values A(i).
3. Maximum aerosol count value determined, A(I).
4. Quadratic fitted to A(I-1), A(I) and A(I+1) to find height and position of curve peak. This step is particularly important when the true peak of the curve falls between experimental points.
5. Data normalised by dividing by peak height.
6. Initial value of dispersion coefficient D and step interval DD defined.
7. Theoretical concentration values calculated at positions corresponding to those measured experimentally using equation 4.1. Numerical integration over the whole width and height of the light ribbon to obtain total illumination, C(i).
8. Residue R(i) calculated as an estimate of the accuracy of curve fit, where

$$R(i) = \sum_{i} (A(i)-C(i))^2$$

9. Value of D increased by interval DD. Procedure repeated from step 7 until minimum residue R(J) is obtained.
10. Quadratic fitted to R(J-1), R(J) and R(J+1) with curve

interpolation to calculate minimum residue, R_{min}.

11. Value of D calculated corresponding to R_{min}. This value will be the best fit dispersion coefficient having r.m.s. error of curve fit given by

$$R_{min}^{1/2}/(\text{no. of expt. points})$$

APPENDIX B

THE APPROACH OF A CHARGED PARTICLE TOWARDS A FILTER

It was necessary to determine the cassette head extension length, L_c, required to eliminate the possibility of electrostatic deflection of a particle around the filter head, as described in Section 5.2.4.1. This was established by calculating the velocity of a charged particle approaching a circular filter covered with identically-charged, uniformly spaced particles. To simplify the situation, the following approximations were made;

a) only particles of a single size are present.
b) the incoming particle approaches along the central axis of the filter, and consequently the radial forces are balanced at all times.
c) the particle is carried towards the filter by a steady gas flow, which is sampled isokinetically at a velocity U_o.
d) Stokes' law may be applied to calculate the drag force of the gas flow on the particle.

The differential equation describing the particle velocity may be obtained by considering the force balance on a single particle;

$$-F_D + F_E = m_p \frac{dv}{dt} \qquad (B.1)$$

where m_p = mass of particle (Kg),
v = particle velocity (ms^{-1}).

Consider a circular filter of radius R, supporting N uniformly spaced particles of charge q. The number of particles n, in the shaded annulus of width dr, as shown in Figure B.1, is given by

$$n = \frac{N}{(\pi R^2)} (2\pi r)dr = \frac{2Nr}{R^2} dr$$

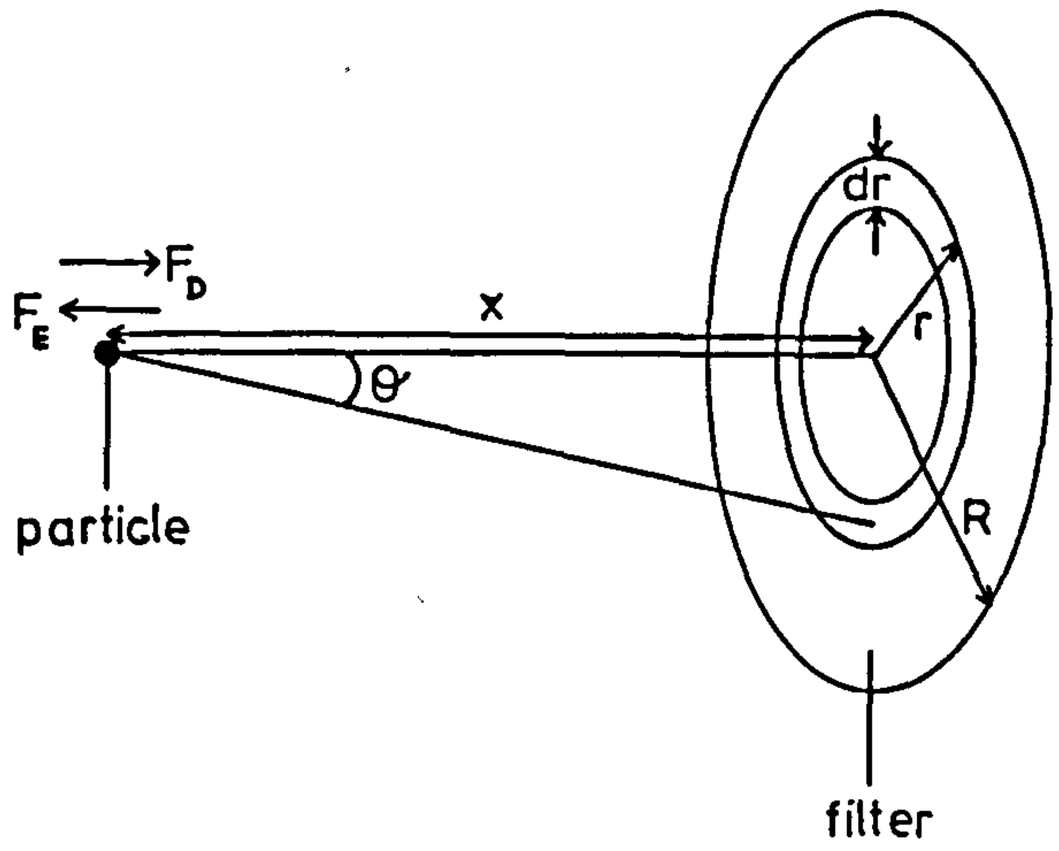

Fig. B.1 Charged particle approaching a filter

The electrostatic force, F_E, on an incoming particle forming an angle θ with the annulus is

$$(F_E)_r = \frac{nq^2}{4\pi\varepsilon_o} \frac{\cos\theta}{(x^2+r^2)} = \frac{2Nrq^2}{4\pi\varepsilon_o R^2} \frac{x}{(x^2+r^2)^{3/2}} dr$$

where x = distance of particle from filter along the x-axis (m).

To evaluate the resultant force due to all the particles on the filter, the above equation must be integrated to yield

$$(F_E)_R = \frac{Nq^2x}{2\pi\varepsilon_o R^2} \int_{r=0}^{R} \frac{r}{(x^2+r^2)^{3/2}} dr$$

Substituting $r = x\tan\theta \Rightarrow dr = x\sec^2\theta d\theta$ gives

$$(F_E)_R = \frac{Nq^2}{2\pi\varepsilon_o R^2} \int_{\theta=0}^{\tan^{-1}(R/x)} \frac{\tan\theta\sec^2\theta}{(\sec^2\theta)^{3/2}}\, d\theta$$

$$= \frac{Nq^2}{2\pi\varepsilon_o R^2} \left[-\cos\theta\right]_{\theta=0}^{\tan^{-1}(R/x)}$$

Since $\cos(\tan^{-1}(R/x)) = \dfrac{x}{(x^2+R^2)^{1/2}}$ then

$$F_E = \frac{Nq^2}{2\pi\varepsilon_o R^2}\left[1 - \frac{x}{(x^2+R^2)^{1/2}}\right] \qquad (B.2)$$

The drag force F_D may be obtained from Stoke's law thus;

$$F_D = 6\pi\mu r_p(v-U_o) \qquad (B.3)$$

Substituting F_E and F_D from equations B.2 and B.3 into the differential equation B.1 yields

$$\frac{6\pi\mu r_p(v-U_o)}{m_p v} + \frac{Nq^2}{2\pi\varepsilon_o R^2 m_p}\frac{1}{v}\left[1 - \frac{x}{(x^2+R^2)^{1/2}}\right] = \frac{dv}{dx}$$

Substituting $A=6\pi\mu r_p/m_p$ and $B=Nq^2/2\pi\varepsilon_o R^2 m_p$ gives

$$\frac{A(v-U_o)}{v} + \frac{B}{v}\left[1 - \frac{x}{(x^2+R^2)^{1/2}}\right] = \frac{dv}{dx}$$

This equation was solved using a modified version of the 4th order Runge-Kutta method. Figures B.2 and B.3 show the velocity of a particle approaching a filter for different particle sizes and a range of values of N. From the results, a value of L_c=10 mm was chosen as an acceptable

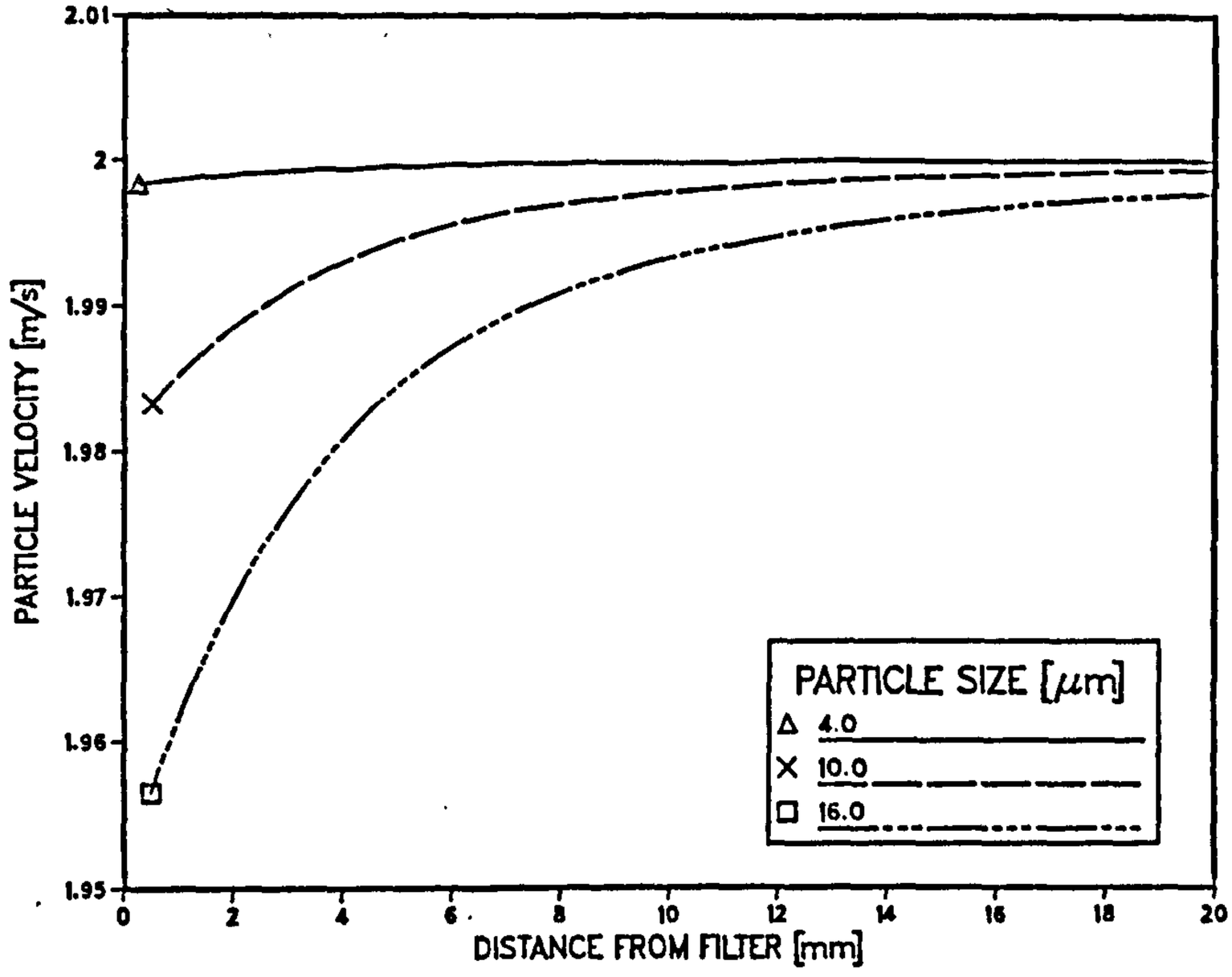

N = 50,000

Fig. B.2 Velocity of a charged particle approaching a filter for a range of particle sizes

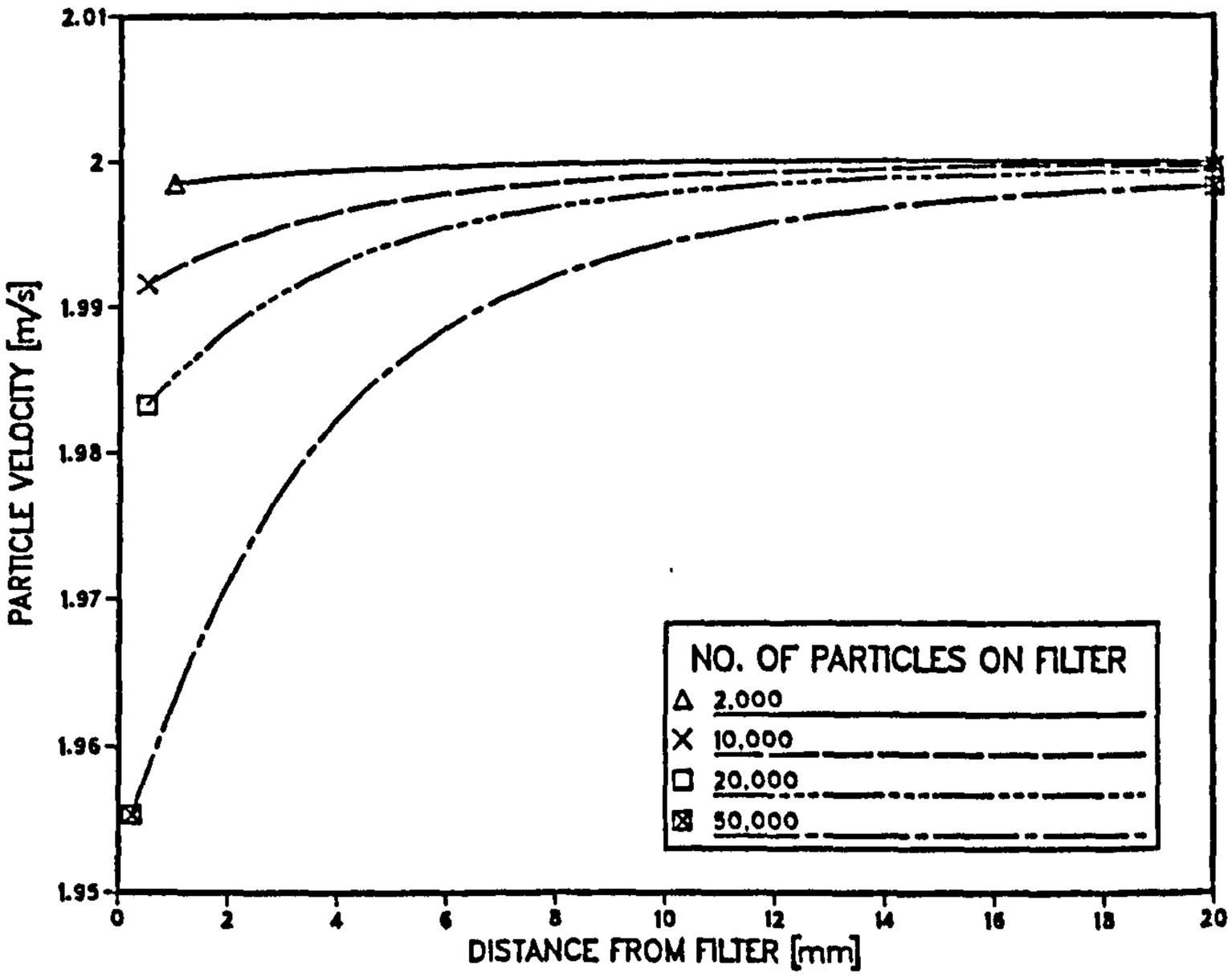

$d_p = 16\mu m$

Fig. B.3 Velocity of a charged particle approaching a filter supporting a range of particle concentrations

length for the electrostatic head extension described in Section 5.2.4.1. The effect of electrostatics on particle collection can then be ignored.

REFERENCES

1. Adam, Y., (1985), Appl. Math. Modelling, 9, 434-440.
2. Athwal, C.S., Coventry, P.F., Hughes, J.F., (1983), Inst. Phys. Conf. Ser. No.66, 167-172.
3. Barriga, A.N., (1978), PhD thesis, Washington State Univ.
4. Beal, S.K., (1970), Nucl. Sci. Engng, 40, 1.
5. Belyaev, S.P., Levin, L.M., (1974), J. Aerosol Sci., 5, 325-338
6. Bernstein, S., Crowe, C.T., (1981), Envir. Int., 6, 181-189.
7. Boothroyd, R.G., (1971), "Flowing Gas-Solids Suspensions", Powder Tech. Series, Chapman and Hall.
8. Brauer, H., (1982), "Advances in Transport Processes, Vol.3", Wiley Eastern Ltd.
9. Briller, R., Robinson, M., (1969), A.I.Ch.E. Journal, 15(5), 733-735.
10. Cleaver, J.W., Yates, B., (1975), Chem. Eng. Sci., 30, 983-992
11. Cleaver, J.W., Yates, B., (1976), Chem. Eng. Sci., 31, 147-151
12. Cooperman, G., (1984), Atmos. Envir., 18(2), 227-285.
13. Cooperman, P., (1971), Atmos. Envir., 5, 541-551.
14. Cooperman, P., (1973), Atmos. Envir., 7, 843-884.
15. Coventry, P.F., (1985), PhD thesis, Univ. of Southampton
16. Coventry, P.F., Hughes, J.F., (1982), Conf. Record I.E.E.E. Annual Meeting, 1107-1110.
17. Crank, J., (1956), "The Mathematics of Diffusion", Oxford Univ. Press.
18. Csanady, G.T., (1963), J. of Atmos. Sci., 20, 201-208
19. Darby, K., (1981), Envir. Int., 6, 191-200.
20. Davies, C.N., (1965), Ann. Occup. Hyg., 8, 235-246.
21. Davies, J.T., (1983), Chem. Eng. Sci., 38(1), 135-139.
22. Davies, J.T., (1972), "Turbulence Phenomena", Academic Press Inc. Ltd..

23. DuBard, J.L., McDonald, J.R., Sparks, L.E., (1983), J. Aerosol Sci., 14(1), 5-10.
24. Eschbach, E.J., Stock, D.E., (1981), Envir. Int., 6, 117-180.
25. Feldman, P.L., Kumar, K.S., Cooperman, G.D., (1976), A.I.Ch.E. Symp. Ser. No. 165, 73, 120-130.
26. Forney, L.J., Spielman, L.A., (1974), J. Aerosol Sci., 5, 257-271.
27. Freidlander, S.K., Johnstone, H.F., (1957), Ind. Engng. Chem., 49, 1151-1156.
28. Gooch, J.P., McDonald, J.R., (1976), A.I.Ch.E. Symp. Ser. No. 165, 73, 146-159.
29. Hauksbee, F., (1709), "Physico-Mechanical Expts. on Various Subjects", London, 46-47.
30. Hewitt, G.W., (1957), Trans. A.I.E.E., 76(2), 300-306.
31. Hinze, J.O., (1959), "Turbulence", Mc-Graw-Hill, N.Y.
32. Kalinske, A.A., Pien, C.L., (1944), Ind. and Eng. Chem., 36(3), 220-223.
33. Kim, H.T., Kline, S.J., Reynolds, W.C., (1971), J. Fluid Mech., 50(1), 133-160.
34. Koumartzakis, S., (1984), MSc thesis, Loughborough Univ. of Technology
35. Lawless, P.A., Dunn, J.W., Sparks, L.E., (1981), Trans. and Util. of Part. Cont. Tech.; 3rd Symp., EPA, US NTIS
36. Lawless, P.A., Sparks, L.E., (1980), J. Appl. Phys., 51(1), 242-256.
37. Leonard, G., Mitchner, M., Self, S.A., (1980), Atmos. Envir., 14, 1289-1299.
38. Leonard, G., Mitchner, M., Self, S.A., (1983), J. Fluid Mech., 127, 123-140.
39. Leutert, G., Bohlen, B., (1972), Staub-Reinhalt. Luft, 32(7), 27-33.
40. Liu, B.Y.H., Ilori, T.A., (1974), Envir. Sci. and Tech., 8(4), 351-356.
41. Liu, B.Y.H., Kapadia, A., (1978), J. Aerosol Sci., 9, 227-242

42. Liu, B.Y.H., Pui, D.Y.H., Rubow, K.L., (1983), "Aerosols in the Mining and Industrial Work Environments", Vol. 3, Chp 70.
43. Liu, B.Y.H., Whitby, K.T., Yu, H.H.S., (1966), J. de Recherches Atmospheriques, 397-405.
44. Liu, B.Y.H., Whitby, K.T., Yu, H.H.S., (1967), J. Appl. Phys., 38(4), 1592-1597.
45. Liu, B.Y.H., Yeh, H., (1968), J. Appl. Phys., 39(3), 1396-1402.
46. Llewelyn, R.P., (1982), Atmos. Envir., 16, 12, 2989-2997.
47. Lloyd, P.J., Stenhouse, J.I.T., Buxton, R.E., (1977), Proc. of Conf., "Particle Size Analysis", Chem. Soc., Univ. of Salford, 387-377.
48. Maclennan, A.S.M., Vincent, J.H., (1981), Conf. Gas Borne Particles, Spons. by Eng. Sci. Div. of Inst. of Mech. Eng..
49. McDonald, J.R., Smith, W.B., Spencer, H.W., Sparks, L.E., (1977), J. Appl. Phys., 48(6), 2231-2243.
50. Moseley, R.B., McDonald, J.R., Sparks, L.E., (1981), Envir. Int., 6, 1-6, 161-175.
51. Oglesby, S., Nichols, G.B., (1978), "Electrostatic Precipitation", Poll. Eng. and Tech./8, Marcel Dekker Inc.
52. Owen, P.R., (1960), Int. J. Air Water Pollut., 3, 8-25, 50-53.
53. Papavergos, P.G., Hedley, A.B., (1984), Chem. Eng. Res. Des. 62, 5, 275-295.
54. Parker, K.R., (1980), J. of Electrostatics, 8, 355-367.
55. Pauthenier, M.M., Moreau-Hanot, M., (1932), J. Phys. Radium, 3, 590
56. Peek, F.W., (1929), "Dielectric Phenomena of High Voltage Engineering", 3rd ed., McGraw-Hill, N.Y.
57. Penney, G.W., Lynch, R.D., (1957), Trans. A.I.E.E., 76(1), 294-299.

58. Penney, G.W., Matick, R.E., (1960), Trans. A.I.E.E., 79(1), 91-99.
59. Potter, E.C., (1978), J. Air Poll. Cont. Ass., 28(1), 40-46.
60. Potter, E.C., (1981), Clean Air; 7th Int. Conf., Ann. Arbor. Sci., 177-196.
61. Pude, J.R.G., Hughes, J.F., Coventry, P.F., (1983), J. Electrostatics, 14(3), 241-254.
62. Pyle, B.E., McDonald, J.R., Smith, W.B., (1981), Trans. and Util. of Part. Cont. Tech; 3rd Symp., EPA, US NTIS.
63. Pyle, B.E., Pontius, D.H., Snyder, T.R., Sparks, L.E., (1980), 73rd Annual meeting Air Poll. Cont. Ass., Paper no. 80-49.2.
64. Ramadan, O.E., Soo, S.L., (1969), Phys. Fluids, 12, 1943-1945
65. Rinard, G., Rugg, D., Patten, W., Sparks, L., (1981), Envir. Int., 6, 1-6, 153-159.
67. Robinson, M., (1967), Atmos. Envir., 1, 193-204.
68. Robinson, M., (1972), Atmos. Envir., 6, 61-63.
69. Robinson, M., (1976), PhD Thesis, The Cooper Union Univ.
Rose, H.E., Wood, A.J., (1956), "An Introduction to Electrostatic Precipitation in Theory and Practice", Constable and Co. Ltd., London.
70. Samuel, E.A., (1981), Envir. Int., 6, 1-6, 137-152.
71. Sato, T., (1980), J. Electrostatics, 8, 271-278.
72. Schlichting, H., (1962), "Boundary Layer Theory", 4th ed., McGraw Hill, chp. 23.
73. Sehmel, G.A., (1971), J. of Coll. and Int. Sci., 37, 4, 891-906.
74. Seinfeld, J.H., (1986), "Atmospheric Chemistry and Physics of Air Pollution", J. Wiley and Sons.
75. Shaw, D.T., (1978), "Fundamentals of Aerosol Science", Wiley-Interscience.
76. Singh, S., Coventry, P.F., Dalmon, J., (1981), J. Electrostatics, 10, 203-210.

77. Smith, G.D., (1978), Numerical Solution of Partial Differential Equations : Finite Difference Methods", Clarendon Press, Oxford.
78. Smith, W.B., Felix, L.G., Hussey, D.H., Pontius, D.H., Sparks, L.E., (1978), J. Aerosol Sci., 9, 101-124.
79. Smith, W.B., McDonald, J.R., (1976), J. Aerosol Sci., 7, 151-166.
80. Soo, S.L., (1967), "Fluid Dynamics of Multiphase Systems", Blaisdell Pub. Co..
81. Soo, S.L., Ihrig, H.K., El Kouh, A.F., (1960), J. Basic Eng.,609-621
82. Stenhouse, J.I.T., Lloyd, P.J., (1974), A.I.Ch.E. Symp. Ser., 70, 137.
83. Stock, D.E., (1983), Ind. Poll. Cont. Symp., ASME, 175-179.
84. Stock, D.E., Crowe, C.T., (1976), A.I.Ch.E. Symp. Ser. No. 165, 73, 131-137.
85. Stock, D.E., Eschbach, E.J., (1981), Conf. Gas Borne Part., Spons by Eng. Sci. Div. of Inst. of Mech. Eng.
86. Taylor, G., (1921), Proc. London Math. Soc., Ser. 2, 20, 196.
87. Taylor, G., (1954), Proc. of Royal Soc., Ser. A, 223, 446-468
88. Thomsen, H.P., Larsen, P.S., Christensen, E.M., Christiansen, J.V., (1982), Dept. Fluid Mech., Tech. Univ. Denmark, AFM 82-08.
89. Towle, W.L., Sherwood, T.K., (1939), Ind. and Eng. Chem., 31, 4, 459-463.
90. Vincent, J.H., (1971a), Atmos. Envir., 5, 791-799.
91. Vincent, J.H., (1971b), J. Phys. D: Appl. Phys., 4, 1499-1512.
92. Vincent, J.H., (1972), Atmos. Envir., 6, 927-942.
93. Vincent, J.H., (1980), J. Air Poll. Cont. Ass., 30(4).
94. Vincent, J.H., Maclennan, A.S.M., (1980), J. Electrostatics, 8, 325-342.
95. White, H.J., (1951), Trans. A.I.E.E., 70, 1186-1191.

96. Williams, J.C., Jackson, R., (1962), Proc. Interaction between Fluids and Particles, 282-288, (London: Instn. Chem. Engnrs.).
97. Wilson, H.A., (1904), Proc. Cambridge Phil. Soc., 12, 406
98. Wood, N.B., (1981), J. Aerosol Sci., 12(3), 275-290.
99. Yamamoto, T., Velkoff, H.R., (1981), J. Fluid Mech., 108, 1-18.